

# Nuclear and Hypernuclear Three- and Four-Body Bound States

Dissertation zur Erlangung des Grades eines  
Doktors der Naturwissenschaften  
in der Fakultät  
für Physik und Astronomie  
an der Ruhr-Universität Bochum

von  
Andreas Nogga  
aus Hagen

Bochum 2001

# Contents

<b>1</b>	<b>Introduction</b>	<b>5</b>
1.1	Overview . . . . .	5
1.2	The nuclear interaction . . . . .	6
1.3	Few-nucleon bound states . . . . .	8
1.4	Hypernuclear interactions . . . . .	9
1.5	Hypernuclear bound states . . . . .	11
1.6	Outline . . . . .	14
<b>2</b>	<b>Formalism</b>	<b>16</b>
2.1	Yakubovsky equations . . . . .	16
2.2	Representation in momentum space . . . . .	21
2.2.1	Basis systems in momentum space . . . . .	22
2.2.2	Representation of the YE's . . . . .	23
2.3	Changing the type of Jacobi coordinates . . . . .	28
2.4	The two-body $t$ -matrix in the 4-body Hilbert space . . . . .	37
<b>3</b>	<b>Numerical Realization</b>	<b>41</b>
3.1	Realization of the coordinate transformations on a massively parallel computer . . . . .	41
3.2	Realization of the $t$ -matrix application on a massively parallel computer . . . . .	45
3.3	Investigation of the numerical stability . . . . .	46
3.3.1	Numerical accuracy of the ${}^3_{\Lambda}\text{H}$ calculation . . . . .	47
3.3.2	Error estimates for the ${}^4_{\Lambda}\text{He}$ and ${}^4_{\Lambda}\text{H}$ hypernuclei . . . . .	52
<b>4</b>	<b>3N and 4N Systems</b>	<b>62</b>
4.1	Introduction to the used NN interaction models . . . . .	63
4.2	${}^3\text{H}$ and ${}^3\text{He}$ binding energies and 3NF's . . . . .	64
4.3	Properties of the 3N wave function . . . . .	71
4.4	CSB in the 3N system . . . . .	85
4.5	The $\alpha$ -particle binding energy and the size of 4NF's . . . . .	90
4.6	Properties of the 4N wave function and the influence of the 3NF on the wave function properties . . . . .	94

<b>5</b>	<b>The Light Hypernuclei</b>	<b>107</b>
5.1	Overview on YN interaction models . . . . .	108
5.2	Hypertriton binding energies . . . . .	112
5.3	Properties of the hypertriton wave function . . . . .	115
5.4	Four-body hypernuclei . . . . .	125
5.5	Properties of the four-body hypernuclear wave functions . . . . .	130
5.6	The origin of the CSB in the $\Lambda$ separation energies . . . . .	150
<b>6</b>	<b>Summary and Conclusions</b>	<b>154</b>
6.1	Summary of the technical and formal developments . . . . .	154
6.2	3N Model Hamiltonians . . . . .	155
6.3	Properties of 3N bound states . . . . .	156
6.4	$\alpha$ -particle binding energies and 4NF's . . . . .	158
6.5	Properties of the 4N wave function . . . . .	159
6.6	The hypertriton . . . . .	159
6.7	The binding energies of ${}^4_{\Lambda}\text{He}$ and ${}^4_{\Lambda}\text{H}$ . . . . .	161
6.8	The ${}^4_{\Lambda}\text{He}$ wave function . . . . .	162
6.9	The CSB in ${}^4_{\Lambda}\text{He}$ and ${}^4_{\Lambda}\text{H}$ . . . . .	162
6.10	Outlook for hypernuclear studies . . . . .	163
<b>A</b>	<b>Coordinate transformations</b>	<b>164</b>
<b>B</b>	<b>Reduction of the general Yakubovsky equations</b>	<b>167</b>
B.1	Faddeev equations for the hypertriton . . . . .	167
B.2	Yakubovsky equations for the $\alpha$ -particle . . . . .	168
B.3	Faddeev equations for the triton . . . . .	168
<b>C</b>	<b>Three-nucleon interaction</b>	<b>170</b>
C.1	Separation of the TM force in NN-like potentials . . . . .	170
C.2	Explicit form of the TM NN-like potentials . . . . .	174
C.2.1	$a$ -term and $c$ -term . . . . .	174
C.2.2	$b$ -term and $d$ -term . . . . .	176
C.3	Passage to the Urbana 3NF . . . . .	177
C.4	Explicit form of the Urbana-IX NN-like potentials . . . . .	179
<b>D</b>	<b>The calculation of the wave function</b>	<b>181</b>
D.1	The wave function of ${}^4_{\Lambda}\text{He}$ and ${}^4_{\Lambda}\text{H}$ . . . . .	181
D.1.1	(12)3, 4 coordinates . . . . .	181
D.1.2	(12)4, 3 coordinates . . . . .	183
D.1.3	(14)2, 3 coordinates . . . . .	184
D.1.4	(12)34 coordinates . . . . .	184
D.1.5	(34)12 coordinates . . . . .	185
D.2	The wave functions for the three-body system and four-nucleon system . . . . .	186
D.2.1	The $\alpha$ -particle . . . . .	186
D.2.2	The hypertriton . . . . .	188
D.2.3	The 3N system . . . . .	188

<b>E</b>	<b>Partial wave decomposition of correlation and overlap functions</b>	<b>189</b>
E.1	Correlation functions . . . . .	189
E.2	Overlap functions . . . . .	192

# Chapter 1

## Introduction

### 1.1 Overview

Though QCD for quarks and gluons is generally accepted as the underlying theory of the strong interaction, it has not been possible to derive the interactions between hadrons from the fundamental theory yet. Further, due to quark confinement, the direct experimental investigation of isolated quarks is impossible. The most simple strongly interacting objects, which one can investigate experimentally, are baryons and mesons. Therefore the interactions of baryons and mesons are of fundamental interest.

There are some attempts to derive baryon-baryon interactions from the properties of QCD, for example using chiral perturbation theory, an effective field theory, or the resonating group method (RGM). In the first case the strangeness  $S = -1$  sector (hyperon-nucleon system) has not been worked out yet and for the second case the quality of the forces is not comparable to conventional approaches, which are either based on meson exchange or just on phenomenology. These phenomenological and meson exchange based attempts are very successful to describe the baryon-baryon interaction. Our interest is to pin down failures and strengths of these models, which are often called “realistic interactions”.

This thesis deals with the exact determination of binding energies and bound state properties in three- and four-nucleon systems and additionally in systems of three and four baryons including one hyperon. Based on realistic interactions we would like to predict binding energies and compare the predictions to experimental results.

As already known since long time, the binding energies of nuclei predicted by non-relativistic calculations using pair forces only are by far too small. Two additional dynamical ingredients should be able to cure the underbinding problem. One should take relativistic effects into account, but probably more important are three-nucleon forces (3NF). We would like to start with a brief description of the present status of nucleon-nucleon (NN) interactions in Section 1.2 of the introduction. Open problems especially remain in systems with  $A > 2$ . These problems are strongly related to 3NF's. Therefore the most modern 3N interaction models are also shortly introduced in Section 1.2.

Theoretical investigations require reliable solutions of the few-nucleon Schrödinger equation. In the past many solution methods have been developed, therefore we give a short overview of the available techniques in Section 1.3. We will concentrate on investigations of bound states in this overview, because they are the subject of this thesis. This will lead us to the exiting issue, whether substantial 4N forces will be needed or whether NN and 3N forces are essentially sufficient to describe the  $\alpha$ -particle.

Another great part of this work is devoted to hypernuclear few-body systems. Therefore we would like give a brief introduction to the hyperon-nucleon (YN) interaction in Section 1.4. Even their basic properties are not understood at present days. The biggest problem is the small database for YN scattering. In the absence of a YN bound state and with the scarce scattering data, the present models are not sufficiently well constrained. Nevertheless the YN interaction opens the door to very interesting insights into the nuclear interaction, because the forces will sensitively depend on the breakdown of the SU(3) symmetry.

It is known that interaction models based on RGM predict a repulsive hyperon-nucleon interaction for all hyperons and in all spin-isospin states for short interparticle distances. In contrast the meson-theoretical interactions lead in some channels to attractive short range interactions. These qualitative differences in the interaction models are not found for NN interactions. Therefore it is of interest to find out whether the YN interactions at short distances are repulsive or attractive. This could also give important information on the range of validity for NN interaction models.

We will report in this thesis on exact bound state calculations for  ${}^3_{\Lambda}\text{H}$ ,  ${}^4_{\Lambda}\text{H}$  and  ${}^4_{\Lambda}\text{He}$  using the available YN interaction models based on meson exchange. We investigate the possibility to put constraints on the underlying interaction models. The status of such investigations is summarized in Section 1.5 of this chapter. The outline of the thesis is given in the last section of the introduction.

## 1.2 The nuclear interaction

In ordinary nuclear physics one basic interest is to work out the interaction between nucleons. Many experimental data have been collected in the last 40-50 years, which put strong constraints on the np and pp interactions. It has been observed long time ago, that the strong interaction of neutrons and protons is very similar. This led to the introduction of the isospin formalism, where protons and neutrons are seen as one kind of particle, the nucleon, and distinguished by their magnetic isospin quantum number. In good approximation the strong interaction is isospin invariant. There have been classified two aspects of the breakdown of isospin invariance. The experimentally well established differences of the np and pp interaction are commonly called charge independence breaking (CIB). The differences of the strong pp and nn interactions are less known, because there are no direct nn scattering experiments available. Those differences are called charge symmetry breaking (CSB). The difference of the  ${}^3\text{He}$  and  ${}^3\text{H}$  binding energies compared to the total potential energy of these nuclei suggests that CSB is of the order of 2 % in the nuclear force. Moreover there have been some attempts to measure the nn scattering length [1, 2, 3, 4, 5, 6, 7, 8]. The results indicate a visible CSB, but are not completely settled.

Because one is still not able to derive nuclear interactions from first principles, one depends on phenomenological models. The most prominent ones are the models of the Argonne group (AV18) [9], from the Nijmegen group (Nijm I, Nijm II and Nijm 93 [10]) and from the Bonn group (Bonn B [11], CD-Bonn [12]).

The AV18 is purely phenomenological. A certain operator structure is assumed which guarantees the symmetries of the nuclear interaction. The functional dependence is parameterized with roughly 40 parameters. With these parameters it is possible to describe the set of 4000 data nearly perfectly ( $\chi^2/\text{datum} \approx 1$ ).

The Nijmegen potentials are based on the one-boson exchange (OBE). This leads to a special operator form. The potential is parameterized by strong meson-NN form factors and coupling constants. In this form the potential can describe the data set well but not perfectly with a moderate number of 15 parameters (Nijm 93). Therefore the Nijmegen group relaxes the constraints on the operators in that

form, that the parameters are fine tuned to the data set independently for each partial wave. This results in a perfect fit, but the number of parameters also reaches about 40 (Nijm I and II). In their potential models, the nonlocal structures in the one-meson exchange are neglected. Only Nijm I keeps parts of them.

This is different in the OBE model of the Bonn group. They keep the whole Dirac structure of the OBE. Similarly to the Nijmegen group they can describe the data set quite well using the operator structure of the OBE (Bonn B), but a perfect fit can only be reached by fitting the partial waves independently (CD-Bonn) resulting in the same amount of about 40 free parameters.

Recently, chiral perturbation theory ( $\chi$ PT) has been used to derive systematically potential models [13, 14, 15]. These studies have not reached the quantitative description of the traditional models yet, but they have a lot of predictive power, because it will be possible to put also constraints on 3NF's derived in the same frame work and it is possible to estimate the contribution of higher neglected orders. Presently, 3NF's are one of the most exiting problems in low energy nuclear physics. Their appearance is the consequence of restricting the Hilbert space to purely nucleonic degrees of freedom, neglecting excitations of the nucleon, like the  $\Delta$  particle and of meson exchanges between three nucleons without intermediate free 3N propagations. Their contribution to the nuclear Hamiltonian has been considered in systems with  $A > 2$  since nearly 50 years now [16]. It has been observed that the binding energy predictions using only NN interactions of  ${}^3\text{H}$  and  ${}^3\text{He}$  differ by 500-800 keV from their experimental values. It has been shown that the underbinding problem can be solved using phenomenological 3NF models [17, 18, 19].

A systematic derivation of 3NF's has been pioneered by van Kolck [15] using  $\chi$ PT. This study has been taken up by Epelbaum [20], but one has not been able to obtain a quantitative description yet.

On a more phenomenological level the adjustment of 3NF parameters might help to clarify its structure. A natural laboratory for that is 3N scattering. But numerical calculations for the 3N continuum including 3NF's are very complicated [21]. For low energies the effects of 3NF's are generally quite small and for higher energies the calculations have to include a high number of partial waves and are even more complex. A fitting procedure for 3NF's needs the solution of scattering equations for a high number of experimental configurations and trial 3NF's. This project has to be accompanied by measurements of observables, which are sensitive to 3NF's. Those observables have to be identified. In a first step one employs two phenomenological models for 3NF's, which, however, have already a complex spin-isospin structure. With the help of these models, the identification of sensitive observables might be possible. Such theoretical investigations are an important guideline for experimental studies [22].

The first model is linked to the AV18 NN interaction. It was developed by the Urbana-Argonne collaboration and is called Urbana IX [23, 17]. Its long range tail is based on the  $\pi$ - $\pi$  exchange with an intermediate  $\Delta$  excitation. The short range behavior is parameterized by a repulsive part. Both parts have got adjustable strength parameters, which are chosen to predict the correct  ${}^3\text{H}$  binding energy and nuclear matter density in conjunction with the AV18 NN force.

The other model was developed by the Tucson-Melbourne collaboration [24] (TM-3NF). Part of it consists of the  $\pi$ - $\pi$  exchange with  $\Delta$  excitation. Other contributions of the  $\pi$ N scattering amplitude also enter. To this aim a model amplitude is adjusted to the  $\pi$ N scattering data and extrapolated to off-the-mass-shell particles. The coupling of the  $\pi$  to the nucleon is modeled by a strong form factor. This depends on one parameter, which can be used to adjust the 3NF strength [19]. In this thesis we do the adjustment for the TM 3N and each NN force separately and obtain in this way model Hamiltonians, which predict the correct triton binding energy. From our studies we know that a great part of the model dependence of the 3N observables is removed in this way, because many observables are correlated to the 3N binding energies. These observables give no new information on the structure of 3NF's. The model

Hamiltonians can be used for further investigations in the 3N continuum [25, 26, 27, 28, 22] to nail down 3NF effects in n-d scattering or, as in this work, to investigate 3NF effects on the  $\alpha$ -particle binding energy and the properties of 3N and 4N wave functions. Can the  $\alpha$ -particle be described by the modern NN and 3N forces? Is there, maybe, some indication that even 4N forces are necessary? We will address these questions in Chapter 4.

### 1.3 Few-nucleon bound states

Many other groups have already investigated the 3N and 4N bound systems. Binding energy predictions have been calculated using many computational schemes and realistic NN interactions [29, 18, 30, 31, 19, 32, 33]. In the following we will concentrate on the more demanding 4N system.

Since many years Fonseca has studied the four-nucleon bound and scattering states using Faddeev-Yakubovsky equations in momentum space. To reduce the number of independent variables his calculations rely on separable approximations of the two-body and three-body T-matrices (see for example [34]). In Ref. [35] it has been shown that 3N wave functions based on the EST approximation to the t-matrix are comparable to wave functions of full calculations. However, the separable approximation of a nucleon-nucleon interaction is in general a piece of art. There are no objective criteria, whether the approximation is reliable or not and, additionally, the separable forces are only worked out for the lower partial waves of a very restricted number of NN interactions. Therefore fully realistic calculations have never been done using this method.

In 1992 the first non-separable solutions of the Yakubovsky equations appeared. Kamada and Glöckle performed calculations in momentum space [36]. We will come back to these calculations below. In configuration space Schellingerhout presented first results in Ref. [37]. Unfortunately, the program has not been pursued further. Only in 1998 the Grenoble group came up with new solutions in configuration space using realistic NN potentials [38]. Due to their specific implementation of the algorithm, the calculations for 4N bound states are restricted to a very small number of partial waves. Also realistic 3NF's have not been implemented yet.

In addition to solution methods for the Faddeev-Yakubovsky equations, schemes have been developed, which directly solve the Schrödinger equation. First of all the Argonne-Los Alamos group developed the “Greens Function Monte Carlo” (GFMC) technique to investigate nuclear bound states up to  $A = 8$  [33]. Their scheme is restricted to the AV18+Urbana IX force model and they can deal with some parts of the NN interaction only perturbatively, but their results are nevertheless impressive. The 3N and 4N systems are described accurately. Starting from the p-state nuclei discrepancies to the experiments evolve, which are increasing with increasing  $A$ . The differences to the experiment are dependent on the spin and isospin of the nucleus. This indicates that some spin and isospin structure is missing in the 3N force. Unfortunately no other nuclear force model could be investigated in the same manner to pin down model dependences of their predictions. They are also not able to give an explicit representation of their wave function in order to build expectation values and evaluate matrix elements of electromagnetic current operators.

This is possible using the “Stochastic Variational Method” (SVM) developed by Suzuki and Varga. They also applied it to nuclear bound states [39, 40]. The results are very accurate, but up to now their method is restricted to the main parts of AV18 without any additional 3N force. At present it is possible to investigate bound states up to  $A = 4$  with their scheme and using realistic forces.

A similar representation of the wave function is used by Kamimura and Hiyama. Their “coupled-rearrangement-channel Gaussian-basis variational” (CRGBV) method can be used to find solutions for



the  $A = 3$  and  $A = 4$  systems [41, 42] and has been applied to nuclear systems and to hypernuclear systems [43] (see last section of this introduction). The usage of realistic NN and YN forces is very complicated with SVM and CRCGBV. Unfortunately, no calculation has appeared in these two schemes for realistic Hamiltonians including 3N interactions. In this point the work of the Pisa collaboration has reached a high standard.

They have developed a rigorous method using “correlated hyperspherical harmonic” expansion of the wave function. They are able to solve the Schrödinger equation for 3N and 4N bound and scattering states (at least below 3-body breakup) [44, 45]. Due to their expansion they are also restricted to the AV18 and Urbana IX potential models. 4N bound state binding energies have been published only for some older versions of the AV18 potential yet. Like for the Faddeev-Yakubovsky calculations, their results are still restricted to 3N and 4N systems.

Recently, Navrátil and Barrett developed a translationally invariant no core shell-model scheme to solve few-nucleon bound state equations [46]. The method is not restricted to local potentials and is able to handle 3N interactions. The first results are promising, especially because the scheme can be generalized to more complex systems.

In this thesis we want to continue the work of Kamada and Glöckle. Already some time ago they presented first rigorous solutions for the 4N bound state using Yakubovsky equations in momentum space without any separable and uncontrolled approximation [36]. These were the first calculations, which were able to handle realistic potentials with all their complexity, like tensor forces and momentum dependent terms. But the dimension of the linear equations were enormous and it turned out that one needs a very high number of partial waves to get converged results for the wave functions. Nowadays there are new massively parallel supercomputer systems available, which are by orders of magnitude more powerful than the “old” computers in 1992. Therefore we would like to continue the project and present calculations for the modern CIB and CSB NN potentials including realistic spin and isospin dependent 3NF’s. The investigation will result in a range of predictions for binding energies and wave function properties, which we can study to figure out the different effects of the potential models in few-nucleon systems. The wave functions are badly needed to calculate observables like form factors. Results of our investigation will be given in Chapter 4, where we investigate in detail the 3N and 4N systems. The necessary formal and technical developments are described in Chapters 2 and 3.

## 1.4 Hypernuclear interactions

While in ordinary nuclear physics the two-body interaction is already well parameterized by several realistic NN potentials, the situation in the hyperon-nucleon system is quite different. There are nearly no scattering data available and, additionally, there is no two-body bound state like the deuteron in NN physics. A purely phenomenological setup like in the case of AV18 is therefore not feasible. The very high number of free parameters cannot be fixed with the small amount of data (only 35 data given e.g. in Ref. [47]). The spin dependence and the strength of LS forces and tensor forces is to a very high degree unknown. Scattering experiments are very difficult to perform, because neither  $\Lambda$  beams nor targets are available. In the future there might be the possibility to extract YN force properties from  $K^+$  electro- and photoproduction on few-body systems like the deuteron [48]. Data are coming up [49].

From QCD and under the assumption of equal quark masses the strong interaction is invariant under flavor  $SU(3)$  rotations. But due to the different masses of the u,d and s quark, there is a rather strong breaking of this symmetry. In Fig 1.1 the octet of the lightest baryons is shown. The proton, the neutron and also the  $\Lambda$  particle belong to this octet. The baryons are distinguished by the third component of

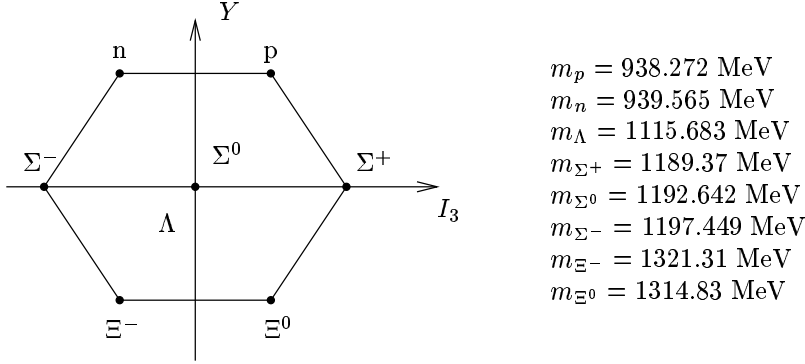


Figure 1.1: The SU(3) octet of the lightest baryons and their masses [50].

their isospin  $I_3$  and their hypercharge  $Y$ . A look to the masses of the baryons reveals that the SU(3) symmetry is broken, the masses are not equal. Whereas the isospin dependence of the masses is mild, the dependence on the hypercharge is quite strong. This reflects the similar masses of u and d quarks, and the quite different mass of the s quark. But how do the SU(3) symmetry and its breakdown manifest itself in interactions among these baryons? This is an interesting question, which is also linked to the CIB and CSB of the NN force. Mechanisms leading to isospin symmetry breaking should also be responsible for SU(3) symmetry breaking. But the strong hypercharge dependence of the baryon masses indicates, that the effects are more pronounced in the interaction between baryons of different isospin multiplets.

Current OBE models assume that the SU(3) violation mainly enters in the interaction by the mass differences of mesons and baryons of the same multiplet. However, one applies SU(3) symmetry to their coupling constants. The current models take into account the exchange of mesons from the lightest meson nonets, namely the pseudoscalar mesons and the vector mesons [51]. Additionally, the Nijmegen group assumes a nonet of scalar mesons, whereas in the Jülich model [52] the  $\sigma$  enters only as an effective parameterization of the correlated  $2\pi$  exchange. More details are given in Section 5.1.

$\Lambda\Lambda\pi$  coupling is prohibited by isospin conservation. This means that the long range part of the  $\Lambda N$  interaction is caused by the  $\Lambda$ - $\Sigma$  conversion potential, where pion exchange is possible. Therefore one can expect that this conversion potential is very important for bound states of hyperons and nucleons.

Here it is interesting to note that the Nijmegen group adds a small  $\Lambda\Lambda\pi$  coupling. They assume that the physical  $\Lambda$  and  $\Sigma_0$  is a mixture of the pure particle states. It turns out that this leads to a CSB potential. In this way the CSB of the hyperon-nucleon interaction might be linked to the properties of the  $\Lambda$  and  $\Sigma_0$  particles. We will address the contribution of this part of the force in Section 5.6.

The Nijmegen group has pursued the project for several years now [47, 53, 54, 51, 55]. Most of the coupling constants are related to each other by their meson exchange model (a flavor SU(3) invariant coupling of mesons and baryons) and can be found by fitting the interaction to NN data. There are only a few parameters left, which cannot be obtained from NN data. These constants are determined by the YN data available. In this way the interaction can even be extended to the other baryons of the octet [55]. But the choice of parameters is not unique. Therefore several parameter sets have been obtained describing the YN data equally well. The main difference within this family of YN interactions is the relative strength of the  $^1S_0$  and  $^3S_1$  interaction. We will come back to this issue in Chapter 5.

Also the Bonn-Jülich group investigated the possibility to extend their one-boson-exchange model to

hypernucleus	$J^\pi$	$E_\Lambda$ [MeV]	reference
$^3\text{H}$	$\frac{1}{2}^+$	$0.13 \pm 0.05$	[60, 63]
$^4\text{H}$	$0^+$	$2.04 \pm 0.04$	[60, 63]
$^4\text{He}$	$0^+$	$2.39 \pm 0.03$	[60, 63]
$^4\text{H}$	$1^+$	$1.00 \pm 0.06$	[61, 62, 63]
$^4\text{He}$	$1^+$	$1.24 \pm 0.05$	[61, 62, 63]

Table 1.1: Experimental  $\Lambda$  separation energies  $E_\Lambda$  of light hypernuclei with  $A \leq 4$ .

the YN system [52]. They assume SU(6) spin-flavor symmetry. This means that only the parameters of the strange form factors have to be adjusted to the YN data, all other parameters could be fitted to NN data. Similarly to the Bonn NN interaction models [11], the full Dirac structure of the OBE potentials is taken into account and the resulting YN potential is highly nonlocal. Due to the SU(6) assumption the parameters can be uniquely determined by NN and YN data. The resulting potential model is very different from the Nijmegen model in some spin observables of YN scattering [56]. Nevertheless, due to the scarce database, no conclusion about the usefulness of the approach can be drawn from present-day experimental YN data.

The two mentioned theoretical approaches use meson theory. But the fundamental degrees of freedom in QCD are quarks and gluons. The baryons are composite particles of the size of 0.7 fm. The distance of baryons within nuclei is of the same order of magnitude. Therefore the success of meson theory in describing the nuclear interaction without explicitly taking quark degrees of freedom into account seems to be astonishing. Furthermore it turns out that in contrast to the nucleon-nucleon interaction, the  $\Sigma$ -nucleon meson-theoretical interactions are attractive for short distances in some spin states. This is in contrast to predictions of interactions based on RGM. Recently YN interaction models have been developed, which take into account the quark substructure of the baryons in the short range part [57]. The result is a repulsive  $\Sigma\text{N}$  interaction for short ranges in all spin states. It will be interesting to see how the short range behavior of the meson-theoretical potentials manifest itself in bound states. In this work we will not apply the potentials based on RGM. This is left for a forthcoming study.

## 1.5 Hypernuclear bound states

In view of the Pauli principle and because of  $\Lambda$ - $\Sigma$  conversion the structure of hypernuclei is very different from ordinary nuclear bound states. Additionally, they are an important source of information on the YN interaction. Nice reviews on this interesting field can be found in Refs. [58, 59]. In the following we summarize some of the insights that could be obtained in the past to motivate our further investigations.

As we already mentioned it is very difficult to perform scattering experiments in hypernuclear physics. In contrast it has been possible to determine experimentally the binding energies of several light hypernuclei [60]. Even some excited particle stable states have been identified in the  $A = 4$  systems [61, 62].

On the other side binding energies of nuclei can be predicted accurately from underlying NN and 3N interactions for systems with  $A = 3$  and  $A = 4$ . This shows that baryon interactions can describe nuclei. Therefore it is justified to extend these techniques to hypernuclear physics and compare theoretical predictions derived from the YN interaction models to the existing  $\Lambda$  separation energy data.

Experimentally, there are five hypernuclei identified with  $A \leq 4$ . They are presented in Table 1.1.

There have been theoretical investigations of the light hypernuclei since 30 years now. To describe the

very small binding energy of the five-body hypernucleus  ${}^5_{\Lambda}\text{He}$  and the rather strong binding of the four-body hypernuclei with the same  $\Lambda\text{N}$  interaction is one of the longest standing problems in hypernuclear physics. In Ref. [64] it was realized for the first time that the strong conversion process of  $\Lambda$  to  $\Sigma$  and isospin conservation might be the reason for this puzzle. Assuming isospin conservation this process should be strongly suppressed in the  ${}^5_{\Lambda}\text{He}$  nucleus, because the  $\Sigma$  particle with isospin  $t = 1$  can only couple with a isospin  $t' = 1$  excited  ${}^4\text{He}$  core to the desired total isospin  $T = 0$ . Because this excited core state has presumably little overlap with the  ${}^4\text{He}$  ground state this mechanism is suppressed. In this way an effective medium dependent interaction arises, which is more attractive, if  $\Lambda$ - $\Sigma$  conversion is not suppressed. This effects are not as pronounced in the four-body hypernuclei leading to stronger binding. The authors of [64] realized at the same time that this  $\Lambda$ - $\Sigma$  conversion might have visible effects on strong splitting of the  ${}^4_{\Lambda}\text{H}$  and  ${}^4_{\Lambda}\text{He}$  mirror nuclei. They undertook a very simple two-body calculation of  ${}^4_{\Lambda}\text{H}$  and  ${}^4_{\Lambda}\text{He}$  treating the three nucleons as one inert  ${}^3\text{H}$  or  ${}^3\text{He}$  core. In this picture they could define a simple  $\Lambda\text{N}$ - $\Sigma\text{N}$  interaction, which simultaneously describes  ${}^5_{\Lambda}\text{He}$ ,  ${}^4_{\Lambda}\text{He}$  and  ${}^4_{\Lambda}\text{H}$ . It turned out that half of the splitting between  ${}^4_{\Lambda}\text{He}$  and  ${}^4_{\Lambda}\text{H}$  is due to the mass difference within the  $\Sigma$ -multiplet and half due to the Coulomb force between a charged  $\Sigma$  and a nucleon. This very important study already revealed many interesting aspects of the  $\text{YN}$  interaction, but it is based on a very simple two-body model, which might be misleading. An important point was already mentioned by the authors themselves. They found that a big part of the potential attraction in the four-body hypernuclei is supplied by the  $\Lambda$ - $\Sigma$  conversion. It was known at that time, that the conversion is stronger in the  ${}^3\text{S}_1$  channel. Hence they expected the full force to be somehow stronger in the  ${}^3\text{S}_1$  channel, which should lead to a  $1^+$  ground state. This is in contradiction to the experimentally found  $0^+$  ground state. The mechanism leading to the  $0^+$  ground state could not be identified at that time.

In Ref. [65] the first four-body calculation was carried out. A set of Yakubovsky equations for separable potentials were established and used to investigate the binding energy difference of the four-body mirror hypernuclei. They used the upcoming models of the Nijmegen group to fix the  $\Lambda\text{N}$  scattering lengths and effective ranges, developed a separable potential, which reproduces this parameters and applied it to the hypernuclei. Because in this calculation the  $\Sigma$ -degree of freedom could not be explicitly taken into account, they assumed that the low energy parameters of the free  $\Lambda\text{N}$  interaction can be used to determine the interaction within the 4-body medium. This means that there is essentially no conversion suppression like in  ${}^5_{\Lambda}\text{He}$ . This assumption is only valid for the  $0^+$  ground state and they had to restrict their calculation to this case. They also neglected the mass splitting of the  $\Sigma$ 's and the Coulomb interaction of the charged  $\Sigma$ 's, which from [64] are known to be important. An important point of their result was the dependence of the binding energy on the effective ranges of the potentials. The simple two-body model predicts a too big difference between the mirror nuclei, because the binding energy increases with increasing effective ranges. A full calculation reveals an increasing binding energy, if the effective range decreases. This is known as the ‘‘Thomas effect’’ [66] and was the main argument at the beginning of nuclear physics that the nuclear interaction has got a non-zero range (otherwise the triton binding energy would be infinite).

Both investigations could not study the excited states of the four-body hypernuclei. In Ref. [67] a variational calculation appeared that used a phenomenological potential to simulate the ground and excited state of the  ${}^4_{\Lambda}\text{He}$  and  ${}^4_{\Lambda}\text{H}$ . They investigated the state dependence of the splitting and connected it to the state dependence of the CSB in the  $\Lambda\text{N}$  scattering lengths. They investigated also the effect of core compression on the repulsive Coulomb force of the  ${}^3\text{He}$  core, which tends to increase the necessary CSB in the strong  $\text{YN}$  interaction. Their result was that the CSB is independent from the spin state of the hyperon and nucleon. This is in contradiction to the meson-theoretical model predictions. Therefore they rose the question, whether the CSB in  ${}^4_{\Lambda}\text{He}$  and  ${}^4_{\Lambda}\text{H}$  is an effect of the quark substructure of the baryons. The calculations of [67] neglected the  $\Sigma$ -particle, which has been shown to contribute substantially to the

CSB [64], and used only very rough approximations to the realistic potentials. Therefore no conclusion on this subject could be drawn. A realistic calculation is the aim of our study. It has not been done yet.

In 1988 Gibson and Lehman became interested in a different aspect of the four-body hypernuclei, the splitting of the  $0^+$  and  $1^+$  state [68]. The most important partial waves contributing to the YN interaction are the  $^1S_0$  and  $^3S_1$  channels. In first approximation the  $^1S_0$  and  $^3S_1$  partial waves are equally important in the  $0^+$  state, whereas in the  $1^+$  state the  $^3S_1$  dominates. In this approximation the splitting of both states should be a measure of the relative strength of the  $^3S_1$  and  $^1S_0$  YN interaction. This ratio cannot be determined from the YN scattering data. Gibson and Lehman assumed that essentially the S-wave potentials are responsible for the binding of the light hypernuclei and in view of their computational restrictions they undertook a four-body calculation using only a separable rank 1 approximation to the NN and YN interaction. They were able to address both states, because they determined matrix elements of the YN interaction for spatially symmetric four-body states (assuming a 3N core nucleus). The matrix elements for the conversion interaction contain weight factors, which effectively suppress the conversion process in the excited state. For the ground state they fitted a separable effective  $\Lambda N$  interaction to the scattering length and effective ranges from a realistic YN model including  $\Lambda$ - $\Sigma$  conversion. The idea was to use a different interaction for the  $1^+$  state. For this state they suppressed  $\Lambda$ - $\Sigma$  conversion in the full interaction using the weight factors from the four-body matrix elements. This interaction led to a “in-medium” scattering length and effective range, to which a separable effective  $\Lambda N$  interaction was fitted. This interaction entered in the bound state calculation for the excited state. In this way they could predict the correct level sequence in the hypernuclei. In contrast they predict the wrong level ordering with the “free”  $\Lambda N$  interaction. This again emphasizes the decisive role of the  $\Lambda$ - $\Sigma$  conversion process in hypernuclear physics. Due the conversion hypernuclear physics is much more than an extension of nuclear physics. There are new dynamical concepts to explore.

The mentioned investigations suggest that the CSB of the four-body hypernuclear binding energies and the splitting of the  $0^+$  and  $1^+$  states might be related to  $\Lambda$ - $\Sigma$  conversion. We will study both effects in Chapter 5 and find out, whether present-day models can explain both observables.

Up to 1990 all hypernuclear investigations were based on very rough calculations. The work of Gibson and coworkers is based on a separable approach, which only simulates the low-energy  $\Lambda N$  scattering parameters and assumes that only the S-waves contribute to the hypernuclear binding. Important dynamical ingredients like the tensor force have not been taken into account. It is well known that for example the triton binding energy is sensitive to the NN interaction model, though the modern potentials are phase-equivalent. Also higher partial waves contribute to binding energies in nuclear physics. Therefore a quantitative analysis of the YN interactions demands realistic calculations. This means that the conversion, the tensor force and also higher partial waves have to be taken into account simultaneously. All this dynamical ingredients are expected to interfere.

Since that time there has been only little progress for the four-body hypernuclei. There appeared some rough calculations with the help of the  $G$ -matrix method [69], which seem to indicate that the spin structure of the SC89 model is not correct. With the same method it was investigated, whether the new SC97 potentials have the correct spin dependence [51]. The authors claim to predict correctly the splitting of  $0^+$  and  $1^+$  states, but their method is not powerful enough to predict reliably the absolute binding energies. In this point the work of Hiyama and Kamimura is more powerful. They also investigated the four-body hypernuclei [42]. Using a Gaussian approximation to the new SC97 potentials [51], they found that the new models give a much better description of the splitting than the old interactions [70, 71]. It remains to investigate, whether the approximation to the potential is justified. Because they have got a quite restricted choice of NN and YN potentials, an investigation of the uncertainty of their conclusions still lacks. Recently a Brückner-Hartree-Fock calculation of these systems appeared [72]. This study

emphasizes again the important contribution of  $\Lambda$ - $\Sigma$  coupling to the splitting of the ground and excited state. Their results indicate that the SC97f model might supply the correct  $\Lambda$ - $\Sigma$  conversion strength. But again their calculations rely on a simple Gaussian approximation to the full meson-theoretical potential.

$\Lambda\Lambda$  hypernuclei are the only experimental approach to the interaction of the strangeness -2 system up to now. This motivated some theoretical investigations of  $\Lambda\Lambda$  hypernuclei in recent years [73, 74]. Unfortunately the lightest nucleus experimentally found is  ${}^6_{\Lambda\Lambda}\text{He}$ . Therefore theoretical calculations have to rely on many approximations. Because of the big uncertainties it is very hard to draw final conclusions on the strength and properties of the  $\Lambda\Lambda$  interaction.

In the case of the hypertriton a realistic calculation appeared in 1993 [75, 76]. Miyagawa and Glöckle developed a set of Faddeev equations for the  ${}^3_{\Lambda}\text{H}$  system including explicitly  $\Lambda$ - $\Sigma$  conversion. They solved the equations in momentum space and were able to predict directly hypertriton binding energies from the available meson-theoretical interactions. At that time the Nijm SC89 [54] and the strongly nonlocal Jülich interactions [52] were available. It turned out that only the SC89 is able to bind the hypertriton. Furthermore they showed that the binding is provided by the  $\Lambda$ - $\Sigma$  conversion potential and the hypertriton is unbound, if one artificially omits it. In Section 5.2 we will investigate whether the construction of effective  $\Lambda\text{N}$  interactions without an explicit  $\Sigma$  degree of freedom is possible and can describe the hypertriton.

Their method enabled them to calculate realistic wave functions. They found interesting correlations of hyperons and nucleons, especially it turned out that the  $\Sigma$  and the nucleon prefer to be on top of each other. This is the result of the attractive short distance  $\Sigma\text{N}$  interaction of the meson-theoretical potentials. The probability to find a  $\Sigma$  in the hypertriton is roughly 0.5 %, nevertheless its interaction contributes more than 50 % of the attraction. How does this astonishing contribution show up in the more tightly bound four-body hypernuclei? This can be clarified only with accurate and full calculations for the four-body systems. This has not been achieved yet and is the aim of this thesis.

## 1.6 Outline

We will start with an introduction into the formalism of Faddeev-Yakubovsky equations in Chapter 2. There we will derive a set of integral equations for the 4-body system of three nucleons and one hyperon. After that an explicit formulation in momentum space is given. The actual formulation makes use of a partial wave expansion. Therefore a partial wave representation of the equations is necessary and will be derived. This includes a detailed look to the partial wave representation of coordinate transformations. The dynamical input to the equations are the NN and YN potentials and a 3NF. The two-body potential enters through the two-body  $t$ -matrices. These operators have to be embedded into the 4-body Hilbert space. This is worked out together with a representation in terms of isospin quantum numbers.

Chapter 3 is devoted to the numerical realization. We outline the algorithms for the coordinate transformations and the application of the  $t$ -matrix. The code has been realized on a massively parallel supercomputer. The parallelization scheme is also described here. After that we estimate the numerical accuracy of our method and present some checks of the numerical stability and consistency of the code.

Before we turn to hypernuclei physics we investigate the three- and four-nucleon system in Chapter 4. After a brief introduction to the used NN interactions, we confirm the strong underbinding predicted for the 3N system for the most modern NN interactions. We show that 3NF's can resolve the underbinding problem. An important point of our work is the adjustment of the TM-3NF to the different NN force models. This results in a set of model Hamiltonians, which predict the same 3N binding energies. We investigate the dependence of the wave function properties, especially the momentum distributions and

correlations, on these model Hamiltonians. We also study the predictions for the CSB of the  ${}^3\text{He}$  and  ${}^3\text{H}$  binding energies based on the recently developed charge-dependent strong NN interactions. Also for this investigation the new model Hamiltonians are essential to pin down the interaction dependence of our predictions.

Chapter 4 also deals with the  $\alpha$ -particle. We present the binding energies for several interaction models. Based on the established 3N Hamiltonians with properly adjusted 3NF's, we investigate the effect of 3NF's on the  $\alpha$ -particle. This is an important step forward. From the remaining discrepancies to the experiment, we conclude on the strength of 4N interactions. This addresses the generally accepted, but never confirmed assumption, that nuclear systems can essentially be described using NN and 3N interactions only. We also obtain wave functions for the  $\alpha$ -particle. They are used to investigate the structure of the four-body bound state in comparison to the two- and three-body system  ${}^2\text{H}$ ,  ${}^3\text{H}$  and  ${}^3\text{He}$ .

Chapter 5 is devoted to the hypernuclear systems. We start with an overview on the available YN interactions. The binding energy predictions for the hypertriton are presented. For the first time converged calculations using the new SC97 YN interactions could be obtained. We use the  ${}^3_{\Lambda}\text{H}$  wave functions to get an overview on their properties. After that we turn to our new results for the hypernuclear four-body systems. We give predictions for the  $0^+$  and  $1^+$  binding energies for several YN and NN interactions and also using 3NF's. From the wave functions we read off some of their properties and identify the most important parts of the YN interaction. We are also concerned with the experimentally known CSB of the hypernuclear binding energies. Also here one observes an interplay of  $\Lambda$ - $\Sigma$  conversion and explicit CSB of the force model. Is it possible to link the interaction properties to the CSB and the  $0^+$ - $1^+$  splitting? This might help to develop new models for the YN system and this might also help to understand the mechanism of the much smaller CSB of the NN system.

We conclude and give an outlook in the last chapter.

# Chapter 2

## Formalism

Throughout this thesis we neglect relativistic effects which are presumably small for nuclear bound states. Therefore the basic equation is the nonrelativistic Schrödinger equation. It is well known that the Schrödinger equation in integral form leads to a non-connected kernel. The integral operator is non-compact on the full Hilbert space. This is in principle no problem if one searches for square integrable bound state wave functions. But it turns out that the wave function has got a complicated structure and its partial wave decomposition is very slowly converging. Instead one decomposes it into Yakubovsky components. They can be expanded more easily into partial waves. Therefore we rewrite the Schrödinger equation following Yakubovsky [77].

In this chapter we describe how the Yakubovsky equations (YE) are connected to the Schrödinger equation. We define the Yakubovsky components (YC) and derive their symmetry properties. This symmetries can be used to reduce the number of independent YC's in the case of identical particles. In the main part of this chapter, we derive an explicit partial wave decomposed representation in momentum space which can be discretized and solved numerically.

### 2.1 Yakubovsky equations

We start with the Schrödinger equation

$$\Psi = G_0 V \Psi \quad (2.1)$$

with the free four-baryon propagator

$$G_0 = \frac{1}{E - H_0} \quad (2.2)$$

and the potential  $V$  consisting of the pair potentials  $V_{ij}$  and 3-body interactions  $V_{ijk}$

$$V = \sum_{i < j} V_{ij} + \sum_{i < j < k} V_{ijk} \quad (2.3)$$

For systems with two particles this equation is well defined. The integral operator is compact for short range potentials and can be approximated numerically. For more than two particles it becomes non-connected. The operator isn't compact anymore and cannot numerically be treated in general. We would like to face the bound state problem and therefore the solution is well-behaved and square-integrable.



Therefore a direct solution of the Schrödinger equation is in principle possible. Nevertheless there are two numerical problems left. In nuclear physics realistic potentials are very repulsive at the origin whereas the  $t$ -matrices are much smoother. The introduction of the  $t$ -matrix speeds up the convergence of the iterative solution method we will describe later [78]. Additionally, it turned out that the partial wave decomposed wave function needs a lot of partial waves, especially for the high momentum components. The tremendous number of partial waves is a consequence of the antisymmetry that has to be imposed on the wave function or, like for the hypernuclei, the  $\Lambda$ -core structure. Therefore we rewrite Eq.(2.1) following the theory of Faddeev [79] and Yakubovsky [77].

In the first step we introduce the so-called Faddeev components (FC)

$$\psi_{ij} \equiv G_0 V_{ij} \Psi + G_0 (V_{ijk}^{(k)} + V_{ijl}^{(l)}) \Psi \quad (2.4)$$

with the permutation  $(ijkl)$  of  $(1234)$ . We used the fact that all available three-baryon forces (3BF) can be decomposed into three parts. Each of them is symmetric under exchange of two of the three particles. The total three-body interaction is symmetric under exchange of two arbitrary particles

$$V_{ijk} = V_{ijk}^{(i)} + V_{ijk}^{(j)} + V_{ijk}^{(k)} \quad (2.5)$$

The superscript denotes the ‘‘spectator’’ particle, in which the 3BF is not symmetric. The three parts are cyclic and anticyclic permutations of each other.

Eq. (2.4) is a decomposition of the full wave function

$$\sum_{i<j} \psi_{ij} = G_0 \sum_{i<j} (V_{ij} + V_{ijk}^{(k)} + V_{ijl}^{(l)}) \Psi \equiv \Psi \quad (2.6)$$

Therefore one can replace the wave function in Eq.(2.4) by its decomposition Eq.(2.6) and finds the Faddeev equations (FE)

$$(1 - G_0 V_{ij}) \psi_{ij} = G_0 V_{ij} (\Psi - \psi_{ij}) + G_0 (V_{ijk}^{(k)} + V_{ijl}^{(l)}) \Psi \quad (2.7)$$

It is straight forward to use the Lippmann-Schwinger equation for the off-shell  $t$ -matrix  $t_{ij}$

$$G_0 t_{ij} = G_0 V_{ij} + G_0 V_{ij} G_0 t_{ij} \quad (2.8)$$

to invert the left hand side of Eq.(2.7)

$$\psi_{ij} = G_0 t_{ij} (\Psi - \psi_{ij}) + (1 + G_0 t_{ij}) G_0 (V_{ijk}^{(k)} + V_{ijl}^{(l)}) \Psi \quad (2.9)$$

The aim of my study is a four-body system. We should note that the FE’s are still non-connected in this case. In Eq. (2.9) the two-body potentials are already replaced by the corresponding  $t$ -matrices, so the first aim of this derivation is reached.

In contrast to the three-body system, the four-body system can cluster into two kinds of structures. It can separate into a three-body cluster and a fourth particle and into two two-body clusters. Yakubovsky showed that the interaction within the clusters can be summed up to infinite order before solving the complete four-body problem [77]. His scheme leads to a decomposition of the Faddeev components into Yakubovsky components (YC).

There are two types of YC’s, which we define as

$$\psi_{(ij)k,l} \equiv G_0 t_{ij} (\psi_{ik} + \psi_{jk}) + (1 + G_0 t_{ij}) G_0 V_{ijk}^{(k)} \Psi \quad (2.10)$$

$$\psi_{(ij)kl} \equiv G_0 t_{ij} \psi_{kl} \quad (2.11)$$

They are indeed a decomposition of the Faddeev components, because they fulfill the important relation

$$\begin{aligned} & \psi_{(ij)kl} + \psi_{(ij)l,k} + \psi_{(ij)kl} \\ & = G_0 t_{ij} (\psi_{ik} + \psi_{jk} + \psi_{kl} + \psi_{il} + \psi_{jl}) + (1 + G_0 t_{ij}) G_0 (V_{ijk}^{(k)} + V_{ijl}^{(l)}) \Psi = \psi_{ij} \end{aligned} \quad (2.12)$$

Using this relation and inserting it into the definition as given in Eqs.(2.10) and (2.11), we find the set of 18 Yakubovsky equations (YE's) for four body systems

$$\begin{aligned} \psi_{(ij)kl} = & G_0 t_{ij} (\psi_{(ik)j,l} + \psi_{(ik)l,j} + \psi_{(ik)jl} \\ & \psi_{(jk)i,l} + \psi_{(jk)l,i} + \psi_{(jk)il}) + (1 + G_0 t_{ij}) G_0 V_{ijk}^{(k)} \Psi \end{aligned} \quad (2.13)$$

$$\psi_{(ij)kl} = G_0 t_{ij} (\psi_{(kl)i,j} + \psi_{(kl)j,i} + \psi_{(kl)ij}) \quad (2.14)$$

These equations are still non-connected. They can be rewritten into YE's which are connected after two iterations. In this form the non-connected parts are already summed up using a either three-body  $T$ -matrix or a  $T$ -matrix acting on the two separated two-body systems. The three-body  $T$ -matrix is the solution of a three-body off-shell Faddeev equation. It has been shown in Ref. [36] that it is more efficient to omit this step and directly solve Eqs. (2.13)-(2.14), if one searches for bound states. Only for scattering states it is mandatory to introduce those  $T$ -matrices in order to define the proper cut structures for the “3+1” and “2+2” fragmentations.

At the first glance it seems to be useless to introduce YE's, if one omits this step and give up those  $T$ -matrices, because we don't make use of the separated summation of the interaction within the clusters to infinite order. However, the YC's itself should already reflect the clustering. They should be optimal to represent a closely bound three-body cluster within the four-body system. Moreover the YE's itself also reflect both possible decompositions of a four-body system. Later on this form will naturally lead to two kinds of coordinates each describing one kind of the two possible partitions of the four-body problem optimally. It turns out that this simplifies the numerical representation of the equations.

In systems with four distinguishable particles the 18 Eqs.(2.13)-(2.14) cannot be simplified anymore. For four identical particles a simplification is possible due to the Pauli principle. In a manner we are going to show below one can reduce the number of independent YC's and YE's to two [36] (see also Appendix B.2). In the case of the  ${}^4_{\Lambda}\text{He}$  and  ${}^4_{\Lambda}\text{H}$  we would like to treat the protons and neutrons as isospin doublet of one kind of particle, the nucleon. Using the isospin formalism, the systems consist of three identical fermions, the nucleons, and a distinguishable one, the hyperon. The resulting wave function has to be antisymmetric under exchange of two nucleons. Regarding the coordinates and quantum numbers of the hyperon there is no symmetry relation. In the following we would like to establish five “fundamental” YC's and reduce the number of YE's to five. The hyperon will be the fourth particle and the nucleons the particles 1 to 3. The solution of this set will automatically fulfill the Pauli principle.

It is easy to identify the appropriate “fundamental” YC's. What are the distinguishable decompositions of my system? In the first step I decompose the 4 body system into 2 clusters. This can be done in two ways, the “3+1” and “2+2” decompositions. The three-body cluster contains either three nucleons(N) or 2N's and one hyperon(Y). In the first case there are only interacting NN systems in the three-body cluster. In the second case there might be an interacting NN or YN system. Therefore one can expect three different YC's of the “3+1” type. The decomposition into two two-body subsystems is unique. There are again two possibilities for the interacting pair and one expects two different “2+2” components. Altogether one finds five different types of YC's.

$$\psi_{1A} \equiv \psi_{(NN)N,Y} \propto \psi_{(12)3,4}, \psi_{(31)2,4}, \psi_{(23)1,4} \quad (2.15)$$

$$\psi_{1B} \equiv \psi_{(NN)Y,N} \propto \psi_{(12)4,3}, \psi_{(31)4,2}, \psi_{(23)4,1} \quad (2.16)$$

$$\begin{aligned} \psi_{1C} \equiv \psi_{(NY)N,N} \propto & \psi_{(14)2,3}, \psi_{(24)3,1}, \psi_{(34)1,2}, \\ & \psi_{(14)3,2}, \psi_{(24)1,3}, \psi_{(34)2,1} \end{aligned} \quad (2.17)$$

$$\psi_{2A} \equiv \psi_{(NN)NY} \propto \psi_{(12)34}, \psi_{(31)24}, \psi_{(23)14} \quad (2.18)$$

$$\psi_{2B} \equiv \psi_{(NY)NN} \propto \psi_{(34)12}, \psi_{(24)31}, \psi_{(14)23} \quad (2.19)$$

Eqs.(2.15)-(2.19) assign each of the 18 YC's to one of the five types. It remains to work out the relations within these groups.

Before doing this we introduce the transposition operators  $P_{ij}$ . They are defined for arbitrary identical particles and interchange the coordinates and quantum numbers of particle  $i$  and  $j$ . In our case  $i, j = 1..3$  and the antisymmetry of the wave function  $\Psi$  due to Pauli principle reads

$$P_{ij}\Psi = -\Psi \quad (2.20)$$

In the following we collect some simple properties of the applications of  $P_{ij}$ , which are very useful to relate the YC's to each other. The potential operators  $V_{ij}$ , the  $t$ -matrices  $t_{ij}$ , the free propagator and the parts of the 3BF  $V_{ijk}^{(k)}$  are symmetric with respect to  $P_{ij}$ :

$$P_{ij}V_{ij}P_{ij} = V_{ij} \quad (2.21)$$

$$P_{ij}t_{ij}P_{ij} = t_{ij} \quad (2.22)$$

$$P_{ij}G_0P_{ij} = G_0 \quad (2.23)$$

$$P_{ij}V_{ijk}^{(k)}P_{ij} = V_{ijk}^{(k)} \quad (2.24)$$

The transpositions are able to transfer the potential operators into each other

$$P_{ij}V_{ik}P_{ij} = V_{jk} \quad (2.25)$$

$$P_{ij}t_{ik}P_{ij} = t_{jk} \quad (2.26)$$

$$P_{ij}V_{jkl}^{(j)}P_{ij} = V_{ikl}^{(i)} \quad (2.27)$$

and therefore the action of  $P_{ij}$  on any YC can be derived from Eqs.(2.4), (2.10) and (2.11). These equations relate the YC's to the wave function

$$\begin{aligned} \psi_{(ij)k,l} \equiv & G_0 t_{ij} G_0 (V_{ik} + V_{jk})\Psi \\ & + G_0 t_{ij} G_0 (V_{ikl}^{(l)} + V_{ikj}^{(j)} + V_{jki}^{(i)} + V_{jkl}^{(l)}) \Psi \\ & + (1 + G_0 t_{ij}) G_0 V_{ijk}^{(k)} \Psi \end{aligned} \quad (2.28)$$

$$\psi_{(ij)kl} \equiv G_0 t_{ij} G_0 V_{kl}\Psi + G_0 t_{ij} G_0 (V_{kli}^{(i)} + V_{klj}^{(j)}) \Psi \quad (2.29)$$

and in this form the symmetry properties of  $\psi_{(ij)k,l}$  and  $\psi_{(ij)kl}$  are obvious:

$$\begin{aligned} P_{ij} \psi_{(ij)k,l} &= P_{ij} G_0 t_{ij} G_0 (V_{ik} + V_{jk})\Psi \\ &+ P_{ij} G_0 t_{ij} G_0 (V_{ikl}^{(l)} + V_{ikj}^{(j)} + V_{jki}^{(i)} + V_{jkl}^{(l)}) \Psi \\ &+ P_{ij} (1 + G_0 t_{ij}) G_0 V_{ijk}^{(k)} \Psi \\ &= G_0 t_{ij} G_0 P_{ij} (V_{ik} + V_{jk})\Psi \\ &+ G_0 t_{ij} G_0 P_{ij} (V_{ikl}^{(l)} + V_{ikj}^{(j)} + V_{jki}^{(i)} + V_{jkl}^{(l)}) \Psi \end{aligned}$$

$$\begin{aligned}
& +(1 + G_0 t_{ij}) G_0 P_{ij} V_{ijk}^{(k)} \Psi \\
= & G_0 t_{ij} G_0 (V_{jk} + V_{ik}) P_{ij} \Psi \\
& + G_0 t_{ij} G_0 (V_{jkl}^{(l)} + V_{jki}^{(i)} + V_{ikj}^{(j)} + V_{ikl}^{(l)}) P_{ij} \Psi \\
& +(1 + G_0 t_{ij}) G_0 V_{ijk}^{(k)} P_{ij} \Psi \\
= & -\psi_{(ij)k,l} \tag{2.30}
\end{aligned}$$

$$\begin{aligned}
P_{ij} \psi_{(ij)kl} = & P_{ij} G_0 t_{ij} G_0 V_{kl} \Psi \\
& + P_{ij} G_0 t_{ij} G_0 (V_{kli}^{(i)} + V_{klj}^{(j)}) \Psi \\
= & G_0 t_{ij} G_0 V_{kl} P_{ij} \Psi \\
& + G_0 t_{ij} G_0 (V_{klj}^{(j)} + V_{kli}^{(i)}) P_{ij} \Psi \\
= & -\psi_{(ij)kl} \tag{2.31}
\end{aligned}$$

$$\begin{aligned}
P_{ij} \psi_{(kl)ij} = & P_{ij} G_0 t_{kl} G_0 V_{ij} \Psi \\
& + P_{ij} G_0 t_{kl} G_0 (V_{ijk}^{(k)} + V_{ijl}^{(l)}) \Psi \\
= & -\psi_{(kl)ij} \tag{2.32}
\end{aligned}$$

$$\tag{2.33}$$

In the same manner the connections within the groups of the YC's are revealed. For example

$$\begin{aligned}
P_{23} \psi_{(14)2,3} = & P_{23} G_0 t_{14} G_0 (V_{24} + V_{12}) \Psi \\
& + P_{23} G_0 t_{14} G_0 (V_{123}^{(3)} + V_{124}^{(4)} + V_{241}^{(1)} + V_{243}^{(3)}) \Psi \\
& + P_{23} (1 + G_0 t_{14}) G_0 V_{142}^{(2)} \Psi \\
= & G_0 t_{14} G_0 P_{23} (V_{24} + V_{12}) \Psi \\
& + G_0 t_{14} G_0 P_{23} (V_{123}^{(3)} + V_{124}^{(4)} + V_{241}^{(1)} + V_{243}^{(3)}) \Psi \\
& + (1 + G_0 t_{14}) G_0 P_{23} V_{142}^{(2)} \Psi \\
= & G_0 t_{14} G_0 (V_{34} + V_{13}) P_{23} \Psi \\
& + G_0 t_{14} G_0 (V_{132}^{(2)} + V_{134}^{(4)} + V_{341}^{(1)} + V_{342}^{(2)}) P_{23} \Psi \\
& + (1 + G_0 t_{14}) G_0 V_{143}^{(3)} P_{23} \Psi \\
= & -\psi_{(14)3,2} \tag{2.34}
\end{aligned}$$

With corresponding steps, one finds several relations between the 18 YC's. In Table 2.1 we show the results.

With the knowledge of these relations, we are able to formulate the YE's for our five fundamental components now. We assume that there is only a three-body interaction between the three nucleons. In the case of the hyperon we neglect possible three-baryon interactions. Most of the hypernuclear 3BF effects should result from the  $\Lambda$ - $\Sigma$  conversion process, which we explicitly take into account. Other mechanisms have not been investigated to the best of our knowledge yet. In this case there is only in one YE a three-baryon interaction term. We choose one representative  $\psi_{1A} \dots \psi_{2B}$  given in Eqs. (2.15)-(2.19) and denote them again by  $\psi_{1A} \dots \psi_{2B}$ . It results

$$\begin{aligned}
\psi_{1A} \equiv \psi_{(12)3,4} = & G_0 t_{12} (P_{13} P_{23} + P_{12} P_{23}) (\psi_{1A} + \psi_{1B} + \psi_{2A}) \\
& + (1 + G_0 t_{12}) G_0 V_{123}^{(3)} \Psi \tag{2.35}
\end{aligned}$$

$$\begin{aligned}
\psi_{1B} \equiv \psi_{(12)4,3} = & G_0 t_{12} [(1 - P_{12})(1 - P_{23}) \psi_{1C} \\
& + (P_{12} P_{23} + P_{13} P_{23}) \psi_{2B}] \tag{2.36}
\end{aligned}$$

$$\psi_{1C} \equiv \psi_{(14)2,3} = G_0 t_{14} (\psi_{1B} + \psi_{1A} + \psi_{2A}$$

	$\psi_{1A} = \psi_{(12)3,4}$	$\psi_{1B} = \psi_{(12)4,3}$	$\psi_{1C} = \psi_{(14)2,3}$	$\psi_{2A} = \psi_{(12)34}$	$\psi_{2B} = \psi_{(34)12}$
$\psi_{(12)3,4}$	1	-	-	-	-
$\psi_{(23)1,4}$	$P_{12}P_{23}$	-	-	-	-
$\psi_{(31)2,4}$	$P_{13}P_{23}$	-	-	-	-
$\psi_{(12)4,3}$	-	1	-	-	-
$\psi_{(23)4,1}$	-	$P_{12}P_{23}$	-	-	-
$\psi_{(31)4,2}$	-	$P_{13}P_{23}$	-	-	-
$\psi_{(14)2,3}$	-	-	1	-	-
$\psi_{(24)3,1}$	-	-	$P_{12}P_{23}$	-	-
$\psi_{(34)1,2}$	-	-	$P_{12}P_{13}$	-	-
$\psi_{(14)3,2}$	-	-	$-P_{23}$	-	-
$\psi_{(34)2,1}$	-	-	$-P_{13}$	-	-
$\psi_{(24)1,3}$	-	-	$-P_{12}$	-	-
$\psi_{(12)34}$	-	-	-	1	-
$\psi_{(23)14}$	-	-	-	$P_{12}P_{23}$	-
$\psi_{(31)24}$	-	-	-	$P_{13}P_{23}$	-
$\psi_{(14)23}$	-	-	-	-	$P_{12}P_{23}$
$\psi_{(24)31}$	-	-	-	-	$P_{13}P_{23}$
$\psi_{(34)12}$	-	-	-	-	1

Table 2.1: Connection between the different YC's. The transpositions have to be applied to the YC's in the first row.

$$-P_{12}\psi_{1C} + P_{12}P_{23}\psi_{1C} + P_{13}P_{23}\psi_{2B} \quad (2.37)$$

$$\psi_{2A} \equiv \psi_{(12)34} = G_0 t_{12}((P_{12} - 1)P_{13}\psi_{1C} + \psi_{2B}) \quad (2.38)$$

$$\psi_{2B} \equiv \psi_{(34)12} = G_0 t_{34}(\psi_{1A} + \psi_{1B} + \psi_{2A}) \quad (2.39)$$

This is the system of five YE's for three identical fermions and one distinguishable particle. In the next section, we derive the momentum space representation of these equations.

The total wave function  $\Psi$  is the sum of all 18 YC's. From Table 2.1 one easily finds

$$\Psi = (1 + P)\psi_{1A} + (1 + P)\psi_{1B} + (1 - P_{12})(1 + P)\psi_{1C} + (1 + P)\psi_{2A} + (1 + P)\psi_{2B} \quad (2.40)$$

The wave function is antisymmetric under exchange of the first three particles. Its explicit form is given in Appendix D.1.

In Appendix B.2 we show how one can simplify the YE's as given in Eqs. (2.35) to (2.39) to the four-nucleon system. Because of the additional symmetry of the wave function, the number of independent YC's decreases to two. This leads to a system of two coupled YE's for the  $\alpha$ -particle.

## 2.2 Representation in momentum space

Eqs.(2.35)-(2.39) form the set of five YE's for a system of 3 identical particles and a distinguishable one in operator notation. The numerical solution requires a set of basis states, which will be introduced in this section. After that the explicit form of Eqs.(2.35)-(2.39) is derived.

### 2.2.1 Basis systems in momentum space

We describe the motion of our particles in momentum space. Momentum coordinates are very natural, especially if one uses meson-theoretical potentials or the new interactions derived with chiral perturbation theory [14, 15]. If not truncated via a  $\frac{p}{m}$  expansion, they are always nonlocal. That means that numerical investigations in configuration space are not feasible for these potentials.

The natural coordinates for the 4-body system are the Jacobi coordinates. They guarantee a kinetic energy which is independent of any angles and separate the center-of-mass (CM) motion. Without the CM motion we need three momenta. One possibility of choosing them is

$$\vec{p}_{ij} = \frac{1}{m_i + m_j} (m_j \vec{k}_i - m_i \vec{k}_j) \quad (2.41)$$

$$\vec{p}_k = \frac{m_i + m_j}{m_i + m_j + m_k} \vec{k}_k - \frac{m_k}{m_i + m_j + m_k} (\vec{k}_i + \vec{k}_j) \quad (2.42)$$

$$\vec{q}_l = \frac{m_i + m_j + m_k}{m_i + m_j + m_k + m_l} \vec{k}_l - \frac{m_l}{m_i + m_j + m_k + m_l} (\vec{k}_i + \vec{k}_j + \vec{k}_k) \quad (2.43)$$

With  $\vec{k}_i, m_i$  we denote the momentum of the particle  $i$  and its mass. The definition of Jacobi coordinates like in Eqs.(2.41)-(2.43) is not unique in four-body systems. Obviously, there are several possibilities due to the interchange of particles  $i, j, k$  and  $l$ . The example above singles out the subsystem  $(ij)$  and the 3-body cluster  $(ijk)$ . In this form they are the natural coordinates of the “3+1” YC’s  $\psi_{(ij)k,l}$ . Additionally, it is possible to define coordinates for the “2+2” partition.

$$\vec{p}_{ij} = \frac{1}{m_i + m_j} (m_j \vec{k}_i - m_i \vec{k}_j) \quad (2.44)$$

$$\vec{p}_{kl} = \frac{1}{m_k + m_l} (m_l \vec{k}_k - m_k \vec{k}_l) \quad (2.45)$$

$$\vec{q} = \frac{1}{m_i + m_j + m_k + m_l} \left( (m_i + m_j) (\vec{k}_k + \vec{k}_l) - (m_k + m_l) (\vec{k}_i + \vec{k}_j) \right) \quad (2.46)$$

These coordinates are optimal for describing the motion of two 2-body clusters. They are natural for the YC’s  $\psi_{(ij)kl}$ .

Additionally, each particle has its spin and isospin coordinates  $s_i, m_i^s$  and  $t_i, m_i^t$ . In the following we will use a partial wave decomposition to expand the angular dependence of the YC’s and wave functions. The number of continuous variables is reduced to three in this way. This introduces the orbital angular momenta  $l_{ij}, l_k, l_l$  and  $\lambda$  which replace the dependence on the direction of  $p_{ij}, p_k, q_l$  and  $q$ , respectively. The total angular momentum of the 4-body system is conserved. With a very high accuracy the same is true for the total isospin. Therefore it is useful to establish a coupling scheme for the spins and isospins introducing the total angular momentum  $J$  and isospin  $T$ . These quantum numbers are conserved. The number of partial waves is restricted by this condition. We use  $jj$ -coupling because the basic interaction, the two-body potential  $V_{ij}$ , conserves the total angular momentum  $j_{ij}$  of the relevant subsystem  $(ij)$ . For coordinate transformations it is useful that the coupling scheme reflects the kind of Jacobi coordinates. Because of this we introduce two kinds of couplings, one for the “3+1” coordinates and one for the “2+2” coordinates.

In the case of “3+1” states we couple the spins and angular momenta (isospins) to the total 2-body spin  $j_{ij}$  (2-body isospin  $t_{ij}$ ), the total 3-body spin  $j_3$  (3-body isospin  $\tau$ ) and the total spin  $J$  and its third

component  $M$  (total isospin  $T$  and  $M_T$ ).  $I_k$  and  $I_l$  are necessary intermediate spin quantum numbers. Thus we have the following sequence of couplings:

$$(((l_{ij} (s_i s_j) s_{ij}) j_{ij} (l_k s_k) I_k) j_3 (l_l s_l) I_l) J M \quad (2.47)$$

and, independently, for the isospins

$$(((t_i t_j) t_{ij} t_k) \tau t_l) T M_T \quad (2.48)$$

In short hand notation we abbreviate these sets by  $\alpha_1$ .

In the second case it is natural to introduce quantum numbers for both 2-body subsystems:  $j_{ij}$  and  $t_{ij}$ . The total angular momentum of the first subsystem couples with the angular momentum  $\lambda$  of the  $q$  motion to an intermediate spin  $I$ . The total angular momentum is the sum of  $I$  and the second 2-body spin  $j_{kl}$ .

$$(((l_{ij} (s_i s_j) s_{ij}) j_{ij} \lambda) I (l_{kl} (s_k s_l) s_{kl}) j_{kl}) J M \quad (2.49)$$

The isospin coupling is analogously defined:

$$(((t_j t_i) t_{ij} (t_k t_l) t_{kl}) T M_T \quad (2.50)$$

These sets are abbreviated by  $\alpha_2$ .

The full Hilbert space of four particles in the CM system is spanned by both kinds of basis sets:

$$|p_{ij} p_k q \alpha_1 \rangle \equiv |(ij) k, l \rangle \quad (2.51)$$

$$|p_{ij} p_{kl} q \alpha_2 \rangle \equiv |(ij) (kl) \rangle \quad (2.52)$$

## 2.2.2 Representation of the YE's

The advantage of the YE's is the possibility to introduce systematically different Jacobi coordinates into the dynamical equations. It turns out that the convergence with respect to partial waves speeds up in this case and that the YC's are best represented in their "natural" coordinates, that means in that coordinates that single out the same clusters and subsystems. Therefore we will expand the five YC's in five different basis systems.

$$\psi_{\alpha_1}^{1A}(p_{12} p_3 q_4) = \langle (12) 3, 4 | \psi_{1A} \rangle \quad (2.53)$$

$$\psi_{\alpha_1}^{1B}(p_{12} p_4 q_3) = \langle (12) 4, 3 | \psi_{1B} \rangle \quad (2.54)$$

$$\psi_{\alpha_1}^{1C}(p_{14} p_2 q_3) = \langle (14) 2, 3 | \psi_{1C} \rangle \quad (2.55)$$

$$\psi_{\alpha_2}^{2A}(p_{12} p_{34} q) = \langle (12) 34 | \psi_{2A} \rangle \quad (2.56)$$

$$\psi_{\alpha_2}^{2B}(p_{34} p_{12} q) = \langle (34) 12 | \psi_{2B} \rangle \quad (2.57)$$

In the first step we would like to derive the explicit expression for Eq. (2.35). The 3BF term is kept, but it is not worked out here. This is done in Appendix C in detail. Projecting onto  $\langle (12) 3, 4 |$  and inserting two times the unity in the form

$$I = \int |(12) 3, 4 \rangle \langle (12) 3, 4 | \quad (2.58)$$

leads to

$$\psi_{\alpha_1 A}^{1A}(p_{12} p_3 q_4) = \langle (12) 3, 4 | \psi_1 \rangle = \int' \int'' \langle (12) 3, 4 | G_0 t_{12} | (12) 3, 4' \rangle$$

$$\begin{aligned}
& \times \langle (12)3, 4' | P_{12} P_{23} + P_{13} P_{23} | (12)3, 4'' \rangle \\
& \times \langle (12)3, 4'' | \psi_{1A} + \psi_{1B} + \psi_{2A} \rangle \\
& + \langle (12)3, 4 | G_0 V_{123}^{(3)} | \Psi \rangle \\
& + \int' \langle (12)3, 4 | G_0 t_{12} | (12)3, 4' \rangle \langle (12)3, 4' | G_0 V_{123}^{(3)} | \Psi \rangle
\end{aligned} \tag{2.59}$$

In this stage it is useful to analyze the symmetry properties of the YC's as given in Eqs.(2.30)-(2.32) again. We showed that the antisymmetry of the wave function carries over to the two-body subsystems singled out by the YC's. But this property is not imposed by the YE's themselves. In principle there are spurious solutions of the YE's, which are not in agreement with Eqs.(2.30)-(2.32). It turns out that the antisymmetrized wave functions, which are connected to these solutions, are zero.

Fortunately we chose a basis system, which gives a perfect control of the subsystem symmetries to us. The application of the transposition  $P_{ij}$  to states  $|(ij)k, l \rangle$  results in a phase factor, which depends only on the angular momentum  $l_{ij}$ , the spins  $s_i, s_j$  and  $s_{ij}$  and the isospins  $t_i, t_j$  and  $t_{ij}$ :

$$P_{ij} |(ij)k, l \rangle = (-)^{l_{ij} + s_i + s_j - s_{ij} + t_i + t_j - t_{ij}} |(ij)k, l \rangle \equiv (-)^{(ij)} |(ij)k, l \rangle \tag{2.60}$$

In the following, we will restrict many times the sums in the unities of the form given in Eq. (2.58) to states, which are antisymmetric in the two-body subsystem. We just impose the additional constraint  $(-)^{(ij)} = -1$  to the partial waves and reduce the dimension by a factor 2. This implies that we omit the spurious solutions. It will turn out that we can restrict the sums always, if two nucleons are singled out by the coordinates used. Therefore we do not distinguish complete summations from summations over physical states by our notation. It remains to make sure that each of the YE's does not couple physical and spurious solutions. Before truncating the sums, we will carefully confirm this requirement for each YE.

After this remarks, we turn back to Eq. (2.59). The  $t$ -operator is symmetric in the subsystem (12), therefore we have to insure that the sum of the cyclic and anticyclic permutation also conserves that symmetry. Using Eq. (2.60), we rewrite the matrix element of the anticyclic permutation as

$$\begin{aligned}
& \langle (12)3, 4' | P_{13} P_{23} | (12)3, 4'' \rangle = \langle (12)3, 4' | P_{12} P_{12} P_{13} P_{23} | (12)3, 4'' \rangle \\
& = \langle (12)3, 4' | P_{12} P_{12} P_{23} P_{12} | (12)3, 4'' \rangle \\
& = (-)^{(12)'} (-)^{(12)''} \langle (12)3, 4' | P_{12} P_{23} | (12)3, 4'' \rangle
\end{aligned} \tag{2.61}$$

Using that Eq.(2.59) changes to

$$\begin{aligned}
\psi_{\alpha_1}^{1A}(p_{12} p_3 q_4) & = \int' \int'' \langle (12)3, 4 | G_0 t_{12} | (12)3, 4' \rangle \\
& \quad \times \left( 1 + (-)^{(12)'} (-)^{(12)''} \right) \langle (12)3, 4' | P_{12} P_{23} | (12)3, 4'' \rangle \\
& \quad \times \langle (12)3, 4'' | \psi_{1A} + \psi_{1B} + \psi_{2A} \rangle \\
& \quad + \langle (12)3, 4 | G_0 V_{123}^{(3)} | \Psi \rangle \\
& \quad + \int' \langle (12)3, 4 | G_0 t_{12} | (12)3, 4' \rangle \langle (12)3, 4' | G_0 V_{123}^{(3)} | \Psi \rangle
\end{aligned} \tag{2.62}$$

The bracket is zero, if  $(-)^{(12)'}$  and  $(-)^{(12)''}$  have opposite sign, otherwise it is two. If the summations  $\int'$  and  $\int''$  are reduced to antisymmetric states, one can replace the bracket by two and arrives at

$$\psi_{\alpha_1}^{1A}(p_{12} p_3 q_4) = 2 \times \int' \int'' \langle (12)3, 4 | G_0 t_{12} | (12)3, 4' \rangle \langle (12)3, 4' | P_{12} P_{23} | (12)3, 4'' \rangle$$



$$\begin{aligned}
& \times \langle (12)3, 4'' | \psi_{1A} + \psi_{1B} + \psi_{2A} \rangle \\
& + \langle (12)3, 4 | G_0 V_{123}^{(3)} | \Psi \rangle \\
& + \int' \langle (12)3, 4 | G_0 t_{12} | (12)3, 4' \rangle \langle (12)3, 4' | G_0 V_{123}^{(3)} | \Psi \rangle
\end{aligned} \tag{2.63}$$

The natural coordinates for  $\psi_{1B}$  and  $\psi_{2A}$  differ from the ones for  $\psi_{1A}$ . Therefore we require a conversion from the  $|(12)3, 4\rangle$  basis to the  $|(12)4, 3\rangle$  or  $|(12)(34)\rangle$  basis, respectively.

$$\begin{aligned}
\psi_{\alpha_1}^{1A}(p_{12}p_3q_4) &= 2 \times \int' \int'' \langle (12)3, 4 | G_0 t_{12} | (12)3, 4' \rangle \langle (12)3, 4' | P_{12}P_{23} | (12)3, 4'' \rangle \\
& \times \left[ \langle (12)3, 4'' | \psi_{1A} \rangle + \int''' \langle (12)3, 4'' | (12)4, 3''' \rangle \langle (12)4, 3''' | \psi_{1B} \rangle \right. \\
& \left. + \int'''' \langle (12)3, 4'' | (12)(34)'''' \rangle \langle (12)(34)'''' | \psi_{2A} \rangle \right] \\
& + \langle (12)3, 4 | G_0 V_{123}^{(3)} | \Psi \rangle \\
& + \int' \langle (12)3, 4 | G_0 t_{12} | (12)3, 4' \rangle \langle (12)3, 4' | G_0 V_{123}^{(3)} | \Psi \rangle
\end{aligned} \tag{2.64}$$

The matrix elements of the YC's can be replaced by the corresponding functions as given in Eqs. (2.53), (2.54) and (2.56):

$$\begin{aligned}
\psi_{\alpha}^{1A}(p_{12}p_3q_4) &= 2 \times \int' \int'' \langle (12)3, 4 | G_0 t_{12} | (12)3, 4' \rangle \langle (12)3, 4' | P_{12}P_{23} | (12)3, 4'' \rangle \\
& \times \left[ \psi_{\alpha_1}^{1A}(p''_{12}p''_3q''_4) + \int''' \langle (12)3, 4'' | (12)4, 3''' \rangle \psi_{\alpha_1}^{1B}(p'''_{12}p'''_4q'''_3) \right. \\
& \left. + \int'''' \langle (12)3, 4'' | (12)(34)'''' \rangle \psi_{\alpha_2}^{2A}(p''''_{12}p''''_3q''''_4) \right] \\
& + \langle (12)3, 4 | G_0 V_{123}^{(3)} | \Psi \rangle \\
& + \int' \langle (12)3, 4 | G_0 t_{12} | (12)3, 4' \rangle \langle (12)3, 4' | G_0 V_{123}^{(3)} | \Psi \rangle
\end{aligned} \tag{2.65}$$

In Eq.(2.65) one finds coordinate transformations between different sets of Jacobi momenta. These are hidden in the operator form Eq.(2.35). For a unified description we would like to rewrite the matrix element of the permutation operator as a coordinate transformation. We apply the cyclic permutation  $P_{12}P_{23}$  to one of our basis states. In a complete formulation the momenta and quantum numbers have to be accompanied by their actual meaning.

$$P_{12}P_{23}|p_{12}p_3q_4\alpha\rangle_{(12)3,4} = |p_{12}p_3q_4\alpha\rangle_{(23)1,4} \tag{2.66}$$

On the left hand side the indices  $(12)3, 4$  indicate that the momenta  $p_{12}, p_3$  and  $q_4$  describe the motion within the subsystem  $(12)$ , of the third particle and of the fourth particle, respectively. On the right side the momenta itself are unchanged. The cyclic permutation shifts the indices of the state to  $(23)1, 4$ .  $p_{12}, p_3$  and  $q_4$  change their meaning. They are the momenta of the subsystem  $(23)$ , of the first particle and of the fourth particle. In a short hand notation we write

$$P_{12}P_{23}|(12)3, 4\rangle = |(23)1, 4\rangle \tag{2.67}$$

Then Eq.(2.65) changes to

$$\begin{aligned}
\psi_{\alpha_1}^{1A}(p_{12}p_3q_4) &= 2 \times \int' \int'' \langle (12)3, 4 | G_0 t_{12} | (12)3, 4' \rangle \langle (12)3, 4' | (23)1, 4'' \rangle \\
&\quad \times \left[ \psi_{\alpha_1'}^{1A}(p_{12}''p_3''q_4'') + \int''' \langle (12)3, 4'' | (12)4, 3''' \rangle \psi_{\alpha_1''}^{1B}(p_{12}'''p_4'''q_3''') \right. \\
&\quad \left. + \int'''' \langle (12)3, 4'' | (12)(34)'''' \rangle \psi_{\alpha_2''}^{2A}(p_{12}''''p_{34}''''q''') \right] \\
&\quad + \langle (12)3, 4 | G_0 V_{123}^{(3)} | \Psi \rangle \\
&\quad + \int' \langle (12)3, 4 | G_0 t_{12} | (12)3, 4' \rangle \langle (12)3, 4' | G_0 V_{123}^{(3)} | \Psi \rangle
\end{aligned} \tag{2.68}$$

The explicit treatment of the three-nucleon interaction is explained in Appendix C. The wave function  $\Psi$  is given in Eq.(2.40), the actual calculation is outlined in Appendix D.1.

Eq.(2.36) looks a little bit more complicated. Nevertheless one finds again a very similar structure. Projecting on  $\langle (12)4, 3 |$  and inserting two times the unity one finds in a first step

$$\begin{aligned}
\psi_{\alpha_1}^{1B}(p_{12}p_4q_3) &= \int' \langle (12)4, 3 | G_0 t_{12} | (12)4, 3' \rangle \\
&\quad \left[ \int'' \langle (12)4, 3' | (1 - P_{12}) | (14)2, 3'' \rangle \langle (14)2, 3'' | (1 - P_{23}) | \psi_{1C} \rangle \right. \\
&\quad \left. + \langle (12)4, 3' | P_{12}P_{23} + P_{13}P_{23} | \psi_{2B} \rangle \right]
\end{aligned} \tag{2.69}$$

In this form it is easy to see that the YE's conserve the symmetry of the second YC. By means of the antisymmetrizer  $(1 - P_{12})$  the  $\psi_{1C}$  term is explicitly projected onto antisymmetric states. In the  $\psi_{2B}$  term the sum of the anticyclic and cyclic permutation again conserves the symmetry of  $\psi_{2B}$  which is antisymmetric in the subsystem (12) according to Eq. (2.32). In the next step we replace  $(1 - P_{12})$  by 2 and the anticyclic permutation by the cyclic one keeping in mind that  $\int'$  is restricted to antisymmetric states. Please note that  $\int''$  is not restricted in this way, because  $\psi_{1C}$  has non identical particles in its subsystem and has no symmetry.

$$\begin{aligned}
\psi_{\alpha_1}^{1B}(p_{12}p_4q_3) &= 2 \times \int' \langle (12)4, 3 | G_0 t_{12} | (12)4, 3' \rangle \\
&\quad \left[ \int'' \langle (12)4, 3' | (14)2, 3'' \rangle \langle (14)2, 3'' | (1 - P_{23}) | \psi_{1C} \rangle \right. \\
&\quad \left. + \langle (12)4, 3' | P_{12}P_{23} | \psi_{2B} \rangle \right]
\end{aligned} \tag{2.70}$$

The evaluation of the  $\psi_{1C}$  term can be done in a straight forward manner. The direct evaluation of the second term includes a coordinate transformation from  $|(12)4, 3 \rangle$  to  $|(14)23 \rangle$  coordinates. This transformation changes all three Jacobi momenta. This matrix is full in the complete 4N Hilbert space and a computational challenge, which one can not handle on today's supercomputers. In Section 2.3 we derive expressions for coordinate transformations. There we restrict ourselves to the special case, that one of the Jacobi momenta is not changed. In this case the matrix has got a block diagonal structure and numerical calculations become feasible. By the introduction of an additional transformation to  $|(14)2, 3 \rangle$

coordinates, we find a form of Eq. (2.70), where the transformations fit to our numerical requirements:

$$\begin{aligned}
\psi_{\alpha_1}^{1B}(p_{12}p_4q_3) &= 2 \times \int' \int'' \langle (12)4, 3|G_0t_{12}|(12)4, 3' \rangle \langle (12)4, 3'|(14)2, 3'' \rangle \\
&\quad \left[ \langle (14)2, 3''|\psi_{1C} \rangle - \int'''' \langle (14)2, 3''|P_{23}|(14)2, 3''' \rangle \langle (14)2, 3'''|\psi_{1C} \rangle \right. \\
&\quad \left. + \int'''' \langle (14)2, 3''|P_{12}P_{23}|(34)12''' \rangle \langle (34)12'''|\psi_{2B} \rangle \right] \quad (2.71)
\end{aligned}$$

Replacing the permutations by coordinate transformations and using the functional form of the YC's we find

$$\begin{aligned}
\psi_{\alpha_1}^{1B}(p_{12}p_4q_3) &= 2 \times \int' \int'' \langle (12)4, 3|G_0t_{12}|(12)4, 3' \rangle \langle (12)4, 3'|(14)2, 3'' \rangle \\
&\quad \left[ \psi_{\alpha_1'}^{1C}(p_{14}''p_2''q_3'') - \int'''' \langle (14)2, 3''|(14)3, 2''' \rangle \psi_{\alpha_1'''}^{1C}(p_{14}'''p_2'''q_3''') \right. \\
&\quad \left. + \int'''' \langle (34)1, 2'''|(34)12''' \rangle \psi_{\alpha_2'''}^{2B}(p_{34}'''p_{12}'''q''') \right] \quad (2.72)
\end{aligned}$$

Eq.(2.37) is a little bit more complicated, because the third YC is not antisymmetric any more. Therefore all parts of this YE have to be treated explicitly and one cannot replace any permutation by the factor two. The derivation itself is done in the same way like for the former two equations. One introduces several times the unity, changes at most two Jacobi momenta in one step and transforms to the natural coordinates of the coupled YC. The result is

$$\begin{aligned}
\psi_{\alpha_1}^{1C}(p_{14}p_2q_3) &= \int' \langle (14)2, 3|G_0t_{14}|(14)2, 3' \rangle \\
&\quad \left[ \int'' \langle (14)2, 3'|(12)4, 3'' \rangle \right. \\
&\quad \left( \psi_{\alpha_1''}^{1B}(p_{12}''p_4''q_3'') + \int'''' \langle (12)4, 3''|(12)3, 4''' \rangle \psi_{\alpha_1'''}^{1A}(p_{12}'''p_3'''q_4''') \right. \\
&\quad \left. + \int'''' \langle (12)4, 3''|(12)34''' \rangle \psi_{\alpha_2'''}^{2A}(p_{12}'''p_{34}'''q''') \right) \\
&\quad + \int'' \langle (14)2, 3'|(24)1, 3'' \rangle \\
&\quad \left( -\psi_{\alpha_1'}^{1C}(p_{24}''p_1''q_3'') + \int'''' \langle (24)1, 3''|(24)3, 1''' \rangle \psi_{\alpha_1'''}^{1C}(p_{24}'''p_3'''q_1''') \right. \\
&\quad \left. + \int'''' \langle (24)1, 3''|(24)31''' \rangle \psi_{\alpha_2'''}^{2B}(p_{24}'''p_{31}'''q''') \right) \left. \right] \quad (2.73)
\end{aligned}$$

Eqs.(2.38) and (2.39) are simpler than the first three. Since the “2+2” YC's couple only to three other ones, one only needs to treat three terms.

The  $\psi_{1C}$  term of Eq.(2.38) guarantees antisymmetric pairs (12), because of the  $P_{12} - 1$  operator. In the other terms the YC's are antisymmetrical in (12) by themselves. Again the operators don't change this symmetry. Therefore the whole set of Eqs.(2.35)-(2.39) does not couple physical and spurious states and the solution will have a definite symmetry.

The derivation of the last two equations is similar to the first three. We can replace the  $P_{12} - 1$  operator by  $(-2)$  restricting the appropriate sums to physical states. The results are

$$\begin{aligned} \psi_{\alpha_2}^{2A}(p_{12}p_{34}q) &= \int' \int'' \langle (12)34|G_0 t_{12}|(12)34' \rangle \langle (12)34'|(34)12'' \rangle \\ &\left[ (-2) \times \int''' \langle (34)12'''|(34)2, 1''' \rangle \psi_{\alpha_1'}^{1C}(p_{34}''' p_2''' q_1''') \right. \\ &\quad \left. + \psi_{\alpha_2}^{2B}(p_{34}'' p_{12}'' q'') \right] \end{aligned} \quad (2.74)$$

for Eq.(2.38) and

$$\begin{aligned} \psi_{\alpha_2}^{2B}(p_{34}p_{12}q) &= \int' \int'' \langle (34)12|G_0 t_{34}|(34)12' \rangle \langle (34)12'|(12)34'' \rangle \\ &\left[ \int''' \langle (12)34'''|(12)3, 4''' \rangle \psi_{\alpha_1'}^{1A}(p_{12}''' p_3''' q_4''') \right. \\ &\quad + \int''' \langle (12)34'''|(12)4, 3''' \rangle \psi_{\alpha_1'}^{1B}(p_{12}''' p_4''' q_3''') \\ &\quad \left. + \psi_{\alpha_2}^{2A}(p_{12}'' p_{34}'' q'') \right] \end{aligned} \quad (2.75)$$

for Eq.(2.39)

Introducing an explicit basis system, the YE's in their operator form Eqs.(2.35)-(2.39) turned into Eqs.(2.68), (2.72), (2.73), (2.74) and (2.75). In this form also the hidden coordinate transformations are seen. In the next section we are going to work more on these coordinate transformations.

## 2.3 Changing the type of Jacobi coordinates

As we briefly mentioned in the last section, we derived the YE's in a form that avoids coordinate transformations that change all three Jacobi momenta at the same time. This is necessary due to computational limitations. Restricting the transformation in this way makes it possible to relate it to a "3-body-like" operation. In Appendix A we derive a general expression for the 3-body transformation  $\langle (ab)c|(bc)a \rangle$  changing between two kinds of Jacobi coordinates of the 3-body system. In a general 3-body system we choose a basis for particles with arbitrary spins  $s_a, s_b$  and  $s_c$ , isospins  $t_a, t_b$  and  $t_c$  and masses  $m_a, m_b$  and  $m_c$ .  $p_{ab}(l_{ab})$  and  $p_c(l_c)$  are the relative momentum (angular momentum) in the subsystem (ab) and the momentum (angular momentum) of the third particle c. Similar to Eq.(2.47) the angular momenta couple to  $j_{ab}, I_c$  and the total angular momentum  $j_{abc}$  and magnetic quantum  $m_{abc}$ . The isospin coupling is similar to Eq.(2.48). The general basis state for a 3-body system reads

$$|p_{ab}q_c \alpha_3 \rangle = |p_{ab}q_c((l_{ab}(s_a s_b) s_{ab}) j_{ab}(l_c s_c) I_c) j_{abc} m_{abc}((t_a t_b) t_{ab}) t_c) \tau_{abc} m_{abc}^{\tau} \rangle \quad (2.76)$$

The transformation matrix has the form

$$\langle p_{ab}q_c \alpha_3 | p'_{bc} q'_a \alpha'_3 \rangle = \int_{-1}^1 dx \frac{\delta(p'_{bc} - \pi_{bc})}{\pi_{bc}' + 2} \frac{\delta(q'_a - \chi_a)}{\chi_a' + 2} G_{\alpha_3 \alpha'_3}^{\alpha\beta\gamma}(p_{ab}q_c x) \quad (2.77)$$

The two  $\delta$ -functions fix the momenta  $p'_{bc}$  and  $q'_a$  in terms of shifted momenta

$$\begin{aligned}\pi'_{bc}(p_{ab}q_c x) &= \sqrt{\beta^2 p_{ab}^2 + \gamma^2 q_c^2 + 2\beta\gamma p_{ab}q_c x} \\ \chi'_a(p_{ab}q_c x) &= \sqrt{p_{ab}^2 + \alpha^2 q_c^2 - 2\alpha p_{ab}q_c x}\end{aligned}\quad (2.78)$$

The mass ratios  $\alpha, \beta$  and  $\gamma$  are given as

$$\begin{aligned}\alpha &= \frac{m_a}{m_a + m_b} \\ \beta &= \frac{m_b}{m_b + m_c} \\ \gamma &= \frac{m_b(m_a + m_b + m_c)}{(m_a + m_b)(m_b + m_c)}\end{aligned}\quad (2.79)$$

The  $G$ -function is very complicated but can be divided in a momentum dependent part and a geometrical part  $g$  which depends only on the angular momentum and isospin quantum numbers

$$G_{\alpha_3 \alpha'_3}^{\alpha\beta\gamma}(p_{ab}q_c x) = \sum_k P_k(x) \sum_{\mu_1 + \mu_2 = l'_c} \sum_{\nu_1 + \nu_2 = l'_a} (-\beta p_{ab})^{\mu_1} (-\gamma q_c)^{\mu_2} p_{ab}^{\nu_1} (-\alpha q_c)^{\nu_2} g_{\alpha_3 \alpha'_3}^{k\mu_1\nu_1\mu_2\nu_2}\quad (2.80)$$

The geometrical part depends on all quantum numbers. The explicit expression is given in Appendix A. It is independent from the third components of  $j_{abc}$  and  $\tau_{abc}$  and diagonal in this quantum numbers. Of course the transformation cannot change the individual spins and isospins  $s_a, s_b, s_c$  and  $t_a, t_b, t_c$ . Please note that the introduction of this  $\delta$ -functions destroys the symmetry of the matrix elements  $\langle (ab)c | (bc)a \rangle$ . It is necessary to calculate both, the transformation and its inverse, separately.

In our transformation matrices for four particles one of the momenta is always unchanged. The corresponding quantum numbers are also conserved. Depending on the kind of matrix element one can treat the untouched subsystem as a composite particle or one simply does the transformation within the reduced subspace of the inner three particles. We will show in the following that both kinds of transformations can be led back to the general expression for three-body transformations. In this way we avoid independent, complicated partial wave decompositions for all different four-body transformations.

In Eq. (2.79) a mass dependence enters into the transformation matrix elements. In the isospin representation the individual kinds of particles are not defined. Only the isospin multiplet of the particle is fixed by the isospin coordinates  $t_i$ . Because the mass differences within the multiplets are rather small compared to the masses itself, we will use an averaged mass for each multiplet keeping in mind that this is only an approximation. We numerically checked that this approximation is reliable, because we found only a small mass dependence of the transformation matrix elements.

With this knowledge we can start to derive the expressions for the 4-body transformation matrices. There are several types, which we would like to treat separately.

#### A. Transformation within the 3-body subcluster of "3+1" coordinates

The first transformation matrix elements of Eqs.(2.68), (2.72) and (2.73) are of the type  $\langle (ij)k, l | (jk)i, l' \rangle$ . They do not change the momentum and quantum numbers of the spectator  $l$ . Clearly, the transformation can independently be done within the 3-body subcluster. It is the only task to identify the quantum numbers of  $\alpha_3$  from the coupling scheme Eq.(2.47). Taking particle  $a = i, b = j$  and  $c = k$ , the coupling within the 3-body subcluster of Eqs.(2.47) and (2.48) is the same

“3-body”	Type A	Type B	Type C	Type D
$m_a$	$m_i$	$m_k$	$m_i + m_j$	$m_l$
$s_a$	$s_i$	$s_k$	$s_{ij}$	$s_l$
$t_a$	$t_i$	$t_k$	$t_{ij}$	$t_l$
$m_b$	$m_j$	$m_i + m_j$	$m_k$	$m_k$
$s_b$	$s_j$	$s_{ij}$	$s_k$	$s_k$
$t_b$	$t_j$	$t_{ij}$	$t_k$	$t_k$
$m_c$	$m_k$	$m_l$	$m_l$	$m_i + m_j$
$s_c$	$s_k$	$s_l$	$s_l$	$j_{ij}$
$t_c$	$t_k$	$t_l$	$t_l$	$t_{ij}$
$j_{abc}$	$j_3$	$J$	$J$	$J$
$\tau_{abc}$	$\tau$	$T$	$T$	$T$
$l_{ab}$	$l_{ij}$	$l_k$	$l_k$	$l_{kl}$
$s_{ab}$	$s_{ij}$	$S$	$S$	$s_{kl}$
$j_{ab}$	$j_{ij}$	$j_3$	$j_3$	$j_{kl}$
$t_{ab}$	$t_{ij}$	$\tau$	$\tau$	$t_{kl}$
$l_c$	$l_k$	$l_l$	$l_l$	$\lambda$
$I_c$	$I_k$	$I_l$	$I_l$	$I$
$l'_{bc}$	$l'_{jk}$	$l'_l$	$l'_{kl}$	$l'_k$
$s'_{bc}$	$s'_{jk}$	$S'$	$s'_{kl}$	$S'$
$j'_{bc}$	$j'_{jk}$	$j'_3$	$j'_{kl}$	$j'_3$
$t'_{bc}$	$t'_{jk}$	$\tau'$	$t'_{kl}$	$\tau'$
$l'_a$	$l'_i$	$l'_k$	$\lambda'$	$l'_l$
$I'_a$	$I'_i$	$I'_k$	$I'$	$I'_l$

Table 2.2: Assignment of the 3-body quantum numbers of  $\alpha_3$ ,  $\alpha'_3$  to the 4-body quantum numbers for the A,B,C and D type transformations

as in Eq.(2.76) . The assignment of the quantum numbers is given in Table 2.2. Correspondingly the matrix element is given as

$$\begin{aligned}
\langle (ij)k, l | (jk)i, l' \rangle &= \delta_{JJ'} \delta_{MM'} \delta_{TT'} \delta_{M_T M'_T} \delta_{l_l l'_l} \delta_{I_l I'_l} \delta_{j_3 j'_3} \delta_{\tau \tau'} \frac{\delta(q_l - q'_l)}{q_l^2} \\
&\times \int_{-1}^1 dx \frac{\delta(p'_{jk} - \pi_{jk})}{\pi_{jk}^{l'_{jk}+2}} \frac{\delta(p'_i - \chi_i)}{\chi_i^{l'_i+2}} G_{\alpha_3 \alpha'_3}^{\alpha \beta \gamma} (p_{ij} p_k x)
\end{aligned} \tag{2.81}$$

The 3-body quantum numbers  $\alpha_3$  and  $\alpha'_3$  can be found from  $\alpha_1$  and  $\alpha'_1$  using Table 2.2. The mass ratios  $\alpha, \beta, \gamma$  and the shifted momenta are given in Eqs.(2.79) and (2.78) using the masses from Table 2.2 and identifying  $p_{ab} = p_{ij}$  and  $q_c = p_k$ .

#### B. Interchanging the third and fourth particle

Whereas the type A transformations could be done within the 3 body subspace, the matrix elements  $\langle (ij)k, l | (ij)l, k' \rangle$  transform the coordinates of the outer particles. Since all coordinates of the subsystem (ij) are not changed by the transformation, we can treat the subsystem (ij) as a composite

particle having spin  $j_{ij}$ , isospin  $t_{ij}$  and mass  $m_i + m_j$ . Unfortunately, the coupling scheme

$$[(j_{ij}(l_k s_k)I_k)j_3(l_l s_l)I_l]JM \quad (2.82)$$

differs from the form given in Eq.(2.76). A recoupling is necessary. We identify the magnitudes of the subsystem momenta  $p_{ab}$  with  $p_k$  and  $p'_{bc}$  with  $p'_l$  and the outer momenta  $q_c$  with  $q_l$  and  $q'_a$  with  $q'_k$ . (ij) belongs on both sides to the “2-body-like” subsystem. It is necessarily the particle b in the 3-body scheme  $\langle (ab)c|(bc)a \rangle$ . In consequence the particle a is equal to k and particle c is equal to l. The next step is to fix the direction of the momenta in the way, that  $p_{ab}$  points to a and  $p_{bc}$  points to b.  $p_k$  already fulfills this requirement, but the momentum  $p_l$  is just opposite to this convention. The phase  $(-)^{l_i}$  changes the direction of  $p'_l$ . Adding this phase  $p'_l$  points to the subsystem (ij), and the momentum exactly fits into the definition of  $p_{bc}$ . Using the well known definition of 6j-symbols [80] and some phase relations of the Clebsch-Gordan coefficients one finds

$$\begin{aligned} & |[(j_{ij}(l_k s_k)I_k)j_3(l_l s_l)I_l]JM \rangle \\ &= (-)^{l_k+s_k-I_k} |[(j_{ij}(s_k l_k)I_k)j_3(l_l s_l)I_l]JM \rangle \\ &= (-)^{l_k+s_k-I_k} \sum_S (-)^{j_{ij}+s_k+l_k+j_3} \sqrt{\hat{S}\hat{I}_k} \left\{ \begin{matrix} j_{ij} & s_k & S \\ l_k & j_3 & I_k \end{matrix} \right\} |[(j_{ij} s_k)S l_k]j_3(l_l s_l)I_l]JM \rangle \\ &= (-)^{l_k+s_k-I_k} \sum_S (-)^{j_{ij}+s_k+l_k+j_3} \sqrt{\hat{S}\hat{I}_k} \left\{ \begin{matrix} j_{ij} & s_k & S \\ l_k & j_3 & I_k \end{matrix} \right\} (-)^{j_{ij}+s_k-S} (-)^{S+l_k-j_3} \\ & \quad |[(l_k(s_k j_{ij})S)j_3(l_l s_l)I_l]JM \rangle \end{aligned} \quad (2.83)$$

We introduced the abbreviation  $\hat{l} = 2l + 1$ . On the right hand side, a similar recoupling is necessary. Adding the phase  $(-)^{l'_i}$  one finds

$$\begin{aligned} & (-)^{l'_i} |[(j_{ij}(l'_l s_l)I'_l)j'_3(l'_k s'_k)I'_k]JM \rangle \\ &= (-)^{l'_i} (-)^{l'_i+s_l-I'_i} |[(j_{ij}(s_l l'_l)I'_l)j'_3(l'_k s'_k)I'_k]JM \rangle \\ &= (-)^{l'_i} (-)^{l'_i+s_l-I'_i} \sum_{S'} (-)^{j_{ij}+s_l+l'_i+j'_3} \sqrt{\hat{S}'\hat{I}'_l} \left\{ \begin{matrix} j_{ij} & s'_l & S' \\ l'_l & j'_3 & I'_l \end{matrix} \right\} \\ & \quad |[(j_{ij} s_l)S' l'_l]j'_3(l'_k s'_k)I'_k]JM \rangle \\ &= (-)^{l'_i} (-)^{l'_i+s_l-I'_i} \sum_{S'} (-)^{j_{ij}+s_l+l'_i+j'_3} \sqrt{\hat{S}'\hat{I}'_l} \left\{ \begin{matrix} j_{ij} & s'_l & S' \\ l'_l & j'_3 & I'_l \end{matrix} \right\} (-)^{S'+l'_i-j'_3} \\ & \quad |[(l'_l(j_{ij} s_l)S')j'_3(l'_k s'_k)I'_k]JM \rangle \end{aligned} \quad (2.84)$$

The isospin part of the right hand side fits already to the “3-body” basis. On the left hand side one easily interchanges  $t_{ij}$  and  $t_k$

$$|(t_{ij} t_k) \tau t_l) T M_T \rangle = (-)^{t_{ij}+t_k-\tau} |(t_k t_{ij}) \tau t_l) T M_T \rangle \quad (2.85)$$

The states of Eqs.(2.83)-(2.85) have the form of Eq.(2.76). The geometrical part  $\tilde{g}$  of the matrix  $\langle (ij)k, l|(ij)l, k' \rangle$  is a linear combination of the original  $g$ . The assignment of “3-body” quantum numbers and masses to the “4-body” quantum numbers and masses is summarized in Table 2.2. Combining Eqs.(2.83),(2.84) and (2.85) one can use  $g$  to find the geometrical part from  $\langle (ij)k, l|(ij)l, k \rangle$

$$\tilde{g}_{\alpha_1 \alpha'_1}^{\mu_1 \mu_2 \nu_1 \nu_2 k} = (-)^{t_{ij}+t_k-\tau} \sum_S \sum_{S'} g_{\alpha_1 \alpha'_1}^{\mu_1 \mu_2 \nu_1 \nu_2 k}$$

$$\begin{aligned}
& (-)^{3s_k - I_k + 2j_{ij} + l_k} \sqrt{\hat{S}\hat{I}_k} \left\{ \begin{matrix} j_{ij} & s_k & S \\ l_k & j_3 & I_k \end{matrix} \right\} \\
& (-)^{2s_l - I_l + j_{ij} + S'} \sqrt{\hat{S}'\hat{I}'_l} \left\{ \begin{matrix} j_{ij} & s'_l & S' \\ l'_l & j'_3 & I'_l \end{matrix} \right\} \\
& g_{\alpha_3 \alpha'_3}^{\mu_1 \mu_2 \nu_1 \nu_2 k}
\end{aligned} \tag{2.86}$$

This  $\tilde{g}$  is necessary to define the  $G$  function in the transformation matrix element

$$\begin{aligned}
\langle (ij)k, l | (ij)l, k' \rangle &= \delta_{JJ'} \delta_{MM'} \delta_{TT'} \delta_{M_T M'_T} \delta_{l_{ij} l'_{ij}} \delta_{s_{ij} s'_{ij}} \delta_{j_{ij} j'_{ij}} \delta_{t_{ij} t'_{ij}} \frac{\delta(p_{ij} - p'_{ij})}{p_{ij}^2} \\
& \int_{-1}^1 dx \frac{\delta(p'_l - \pi'_l)}{\pi_l^{\mu'_l + 2}} \frac{\delta(q'_k - \chi'_k)}{\chi_k^{\mu'_k + 2}} G_{\alpha_1 \alpha'_1}^{\alpha \beta \gamma}(p_k q_l x)
\end{aligned} \tag{2.87}$$

The  $G$  function of Eq.(2.80) is combined with Eq.(2.86)

$$G_{\alpha_1 \alpha'_1}^{\alpha \beta \gamma}(p_k q_l x) = \sum_k P_k(x) \sum_{\mu_1 + \mu_2 = l'_l} \sum_{\nu_1 + \nu_2 = l'_k} (-\beta p_k)^{\mu_1} (-\gamma q_l)^{\mu_2} p_k^{\nu_1} (-\alpha q_l)^{\nu_2} \tilde{g}_{\alpha_1 \alpha'_1}^{k \mu_1 \nu_1 \mu_2 \nu_2} \tag{2.88}$$

The mass ratios are

$$\begin{aligned}
\alpha &= \frac{m_k}{m_k + m_i + m_j} \\
\beta &= \frac{m_l}{m_i + m_j + m_l} \\
\gamma &= \frac{(m_i + m_j)(m_i + m_j + m_k + m_l)}{(m_k + m_i + m_j)(m_i + m_j + m_l)}
\end{aligned} \tag{2.89}$$

They enter in the shifted momenta from Eq.(2.78)

$$\begin{aligned}
\pi'_l(p_k q_l x) &= \sqrt{\beta^2 p_k^2 + \gamma^2 q_l^2 + 2\beta\gamma p_k q_l x} \\
\chi'_k(p_k q_l x) &= \sqrt{p_k^2 + \alpha^2 q_l^2 - 2\alpha p_k q_l x}
\end{aligned} \tag{2.90}$$

The full partial wave decomposition of the matrices Eq. (2.87) is very complicated. It is much easier to perform carefully the recouplings of Eqs.(2.83)-(2.85) and use the general “3-body” expression for  $\langle (ab)c | (bc)a \rangle$ . Now we proceed in the same manner with the next type of transformations.

### C. Changing from “2+2” to “3+1” coordinates

In a three particle system there is only one kind of Jacobi coordinates defined. In four particle systems there are two kinds possible.  $\langle (ij)k, l | (ij)kl' \rangle$  changes from the “2+2” to the “3+1” coordinates. Again the (ij) subsystem can be treated as a composite particle. On the left hand side the composite particle (ij) belongs to the “2-body subsystem” ((ij)k). On the right hand side (ij) is the outer “particle”. Therefore the transformation is equivalent to a “3-body like” transformation  $\langle (ab)c | (bc)a \rangle$  that moves (ij) from the spectator position to the subsystem, we identify (ij) to the particle a, k to particle b and l to particle c. The transformation matrix element equals

$$\langle (ij)k, l | (ij)kl' \rangle = \delta_{JJ'} \delta_{MM'} \delta_{TT'} \delta_{M_T M'_T} \delta_{l_{ij} l'_{ij}} \delta_{s_{ij} s'_{ij}} \delta_{j_{ij} j'_{ij}} \delta_{t_{ij} t'_{ij}} \frac{\delta(p_{ij} - p'_{ij})}{p_{ij}^2}$$



$$\int_{-1}^1 dx \frac{\delta(p'_{kl} - \pi'_{kl})}{\pi'^{l'_{kl}+2}} \frac{\delta(q' - \chi')}{\chi'^{\lambda'+2}} G_{\alpha_1 \alpha_2}^{\alpha \beta \gamma} (p_k q_l x) \quad (2.91)$$

Using the masses of the particles and subsystems one finds the mass ratios

$$\begin{aligned} \alpha &= \frac{m_i + m_j}{m_k + m_i + m_j} \\ \beta &= \frac{m_l}{m_k + m_l} \\ \gamma &= \frac{m_k(m_i + m_j + m_k + m_l)}{(m_k + m_i + m_j)(m_k + m_l)} \end{aligned} \quad (2.92)$$

and the shifted momenta

$$\begin{aligned} \pi'_{kl}(p_k q_l x) &= \sqrt{\beta^2 p_k^2 + \gamma^2 q_l^2 + 2\beta\gamma p_k q_l x} \\ \chi'(p_k q_l x) &= \sqrt{p_k^2 + \alpha^2 q_l^2 - 2\alpha p_k q_l x} \end{aligned} \quad (2.93)$$

As in B. it remains to adapt carefully the direction of the momenta and the coupling scheme to Eq.(2.76) and to find the geometrical part  $\tilde{g}$ . The momentum  $p_k$  points to  $k$  and  $q'$  points to the system  $(kl)$ . This is opposite to the definition of  $p_{ab}$  and  $q'_a$  and leads to a phase  $(-)^{l_k + \lambda'}$ . For the left hand side the recoupling

$$\begin{aligned} &(-)^{l_k} |[ (j_{ij}(l_k s_k) I_k) j_3(l_l s_l) I_l ] JM \rangle \\ &= (-)^{l_k} (-)^{l_k + s_k - I_k} |[ (j_{ij}(s_k l_k) I_k) j_3(l_l s_l) I_l ] JM \rangle \\ &= (-)^{l_k} (-)^{l_k + s_k - I_k} \sum_S (-)^{j_{ij} + s_k + l_k + j_3} \sqrt{\hat{S} \hat{I}_k} \left\{ \begin{matrix} j_{ij} & s_k & S \\ l_k & j_3 & I_k \end{matrix} \right\} |[ (j_{ij} s_k) S l_k) j_3(l_l s_l) I_l ] JM \rangle \\ &= (-)^{l_k} (-)^{l_k + s_k - I_k} \sum_S (-)^{j_{ij} + s_k + l_k + j_3} \sqrt{\hat{S} \hat{I}_k} \left\{ \begin{matrix} j_{ij} & s_k & S \\ l_k & j_3 & I_k \end{matrix} \right\} (-)^{l_k + S - j_3} \\ &|[ (l_k(j_{ij} s_k) S) j_3(l_l s_l) I_l ] JM \rangle \end{aligned} \quad (2.94)$$

is necessary. For the right hand side one finds in a similar manner

$$\begin{aligned} &(-)^{\lambda'} |[ (j_{ij} \lambda') I' (l_{kl'}(s_k s_l) s'_{kl}) j'_{kl} ] JM \rangle \\ &= (-)^{\lambda'} (-)^{I' + j'_{kl} - J} |[ (l_{kl'}(s_k s_l) s'_{kl}) j'_{kl} (j_{ij} \lambda') I' ] JM \rangle \\ &= (-)^{\lambda'} (-)^{I' + j'_{kl} - J} (-)^{j_{ij} + \lambda' - I'} |[ (l_{kl'}(s_k s_l) s'_{kl}) j'_{kl} (\lambda' j_{ij}) I' ] JM \rangle \end{aligned} \quad (2.95)$$

The left hand side of the isospin matrix element couples correctly, for the right hand side  $t'_{kl}$  and  $t_{ij}$  have to be interchanged leading to the phase  $(-)^{t'_{kl} + t_{ij} - T}$ . The result for the geometrical part  $\tilde{g}$  of type C transformations is

$$\begin{aligned} \tilde{g}_{\alpha_1 \alpha_2}^{k \mu_1 \mu_2 \nu_1 \nu_2} &= (-)^{t'_{kl} + t_{ij} - T} \sum_S (-)^{2s_k - I_k + j_{ij} + S} \sqrt{\hat{S} \hat{I}_k} \left\{ \begin{matrix} j_{ij} & s_k & S \\ l_k & j_3 & I_k \end{matrix} \right\} \\ &(-)^{j'_{kl} + j_{ij} - J} g_{\alpha_3 \alpha_3}^{k \mu_1 \mu_2 \nu_1 \nu_2} \end{aligned} \quad (2.96)$$

The “3-body” quantum numbers  $\alpha_3$  and  $\alpha'_3$  can be found again in Table 2.2.

The total  $G$  function reads

$$G_{\alpha_1 \alpha'_2}^{\alpha \beta \gamma}(p_k q_l x) = \sum_k P_k(x) \sum_{\mu_1 + \mu_2 = l'_{kl}} \sum_{\nu_1 + \nu_2 = \lambda'} (-\beta p_k)^{\mu_1} (-\gamma q_l)^{\mu_2} p_k^{\nu_1} (-\alpha q_l)^{\nu_2} \tilde{g}_{\alpha_1 \alpha'_2}^{k \mu_1 \nu_1 \mu_2 \nu_2} \quad (2.97)$$

#### D. Changing from “3+1” to “2+2” coordinates

In the same way one relates the transformation  $\langle (ij)kl | (ij)k, l \rangle$  to a “3-body” operation. Transformation matrix elements are real. One might expect that the matrix elements for type C and D transformations are identical. But we chose the  $\delta$  functions asymmetrically (acting only on momenta of the right hand side), in consequence the matrix elements of C and D differ. Even the identification of the particle a,b and c does not hold any longer. The coordinates of the subsystem (ij) are not changed, the subsystem moves from the inner to the outer position and is treated as particle c. Before the transformation the motion of particle l is described by the outer coordinate and, therefore, it is particle a. Particle  $k$  is particle b of the “3-body” system. The matrix of the transformation has the form

$$\begin{aligned} \langle (ij)kl | (ij)k, l' \rangle &= \delta_{JJ'} \delta_{MM'} \delta_{TT'} \delta_{M_T M'_T} \delta_{l_{ij} l'_{ij}} \delta_{s_{ij} s'_{ij}} \delta_{j_{ij} j'_{ij}} \delta_{t_{ij} t'_{ij}} \frac{\delta(p_{ij} - p'_{ij})}{p_{ij}^2} \\ &\int_{-1}^1 dx \frac{\delta(p'_k - \pi'_k)}{\pi_k^{l'_k + 2}} \frac{\delta(q'_l - \chi'_l)}{\chi_l^{l'_l + 2}} G_{\alpha_2 \alpha'_1}^{\alpha \beta \gamma} \end{aligned} \quad (2.98)$$

Inserting the masses of a,b and c into Eq.(2.79), one finds the mass ratios

$$\begin{aligned} \alpha &= \frac{m_l}{m_l + m_k} \\ \beta &= \frac{m_i + m_j}{m_i + m_j + m_k} \\ \gamma &= \frac{m_k(m_i + m_j + m_k + m_l)}{(m_k + m_l)(m_k + m_i + m_j)} \end{aligned} \quad (2.99)$$

and the shifted momenta

$$\begin{aligned} \pi'_k(p_{kl} q x) &= \sqrt{\beta^2 p_{kl}^2 + \gamma^2 q^2 + 2\beta\gamma p_{kl} q x} \\ \chi'_l(p_{kl} q x) &= \sqrt{p_{kl}^2 + \alpha^2 q^2 - 2\alpha p_{kl} q x} \end{aligned} \quad (2.100)$$

The direction of the momenta of the right hand side already fit into the scheme of Eq.(2.76). On the left hand side  $\vec{p}_{kl}$  and  $\vec{q}$  have the wrong direction. In the partial wave decomposition changing the sign of the vectors leads to the phase  $(-)^{l_{kl} + \lambda}$ . Changing the ordering of the angular momenta one finds a coupling scheme for the spin part of the left hand side which fits into the “3-body” basis state  $|(ab)c \rangle$

$$\begin{aligned} &(-)^{l_{kl} + \lambda} |[ (j_{ij} \lambda) I(l_{kl}(s_k s_l) s_{kl}) j_{kl} ] JM \rangle \\ &= (-)^{l_{kl} + \lambda} (-)^{j_{ij} + \lambda - I} (-)^{s_k + s_l - s_{kl}} (-)^{j_{kl} + I - J} |[ (l_{kl}(s_l s_k) s_{kl}) j_{kl} (\lambda j_{ij}) I ] JM \rangle \end{aligned} \quad (2.101)$$

For the isospin part the reordering is done in a very similar manner.

$$|[t_{ij}(t_k t_l) t_{kl}] T M_T \rangle$$

$$= (-)^{t_{ij}+t_{kl}-T} (-)^{t_k+t_l-t_{kl}} |[(t_l t_k) t_{kl} t_{ij}] T M_T \rangle \quad (2.102)$$

For the right hand side a recoupling is necessary.

$$\begin{aligned} & |[(j_{ij}(l'_k s_k)) I'_k] j'_3(l'_i s_l) I'_i] J M \rangle \\ &= (-)^{l'_k+s_k-I'_k} \sum_{S'} (-)^{j_{ij}+l'_k+s_k+j'_3} \sqrt{\hat{S}' \hat{I}'_k} \left\{ \begin{matrix} j_{ij} & s_k & S' \\ l'_k & j'_3 & I'_k \end{matrix} \right\} |[(j_{ij} s_k) S' l'_k] j'_3(l'_i s_l) I'_i] J M \rangle \\ &= (-)^{l'_k+s_k-I'_k} \sum_{S'} (-)^{j_{ij}+l'_k+s_k+j'_3} \sqrt{\hat{S}' \hat{I}'_k} \left\{ \begin{matrix} j_{ij} & s_k & S' \\ l'_k & j'_3 & I'_k \end{matrix} \right\} (-)^{j_{ij}+s_k-S'} (-)^{S'+l'_k-j'_3} \\ & \quad |[(l'_k(s_k j_{ij}) S') j'_3(l'_i s_l) I'_i] J M \rangle \end{aligned} \quad (2.103)$$

The isospin part of the right hand side needs only one additional phase

$$|[(t_{ij} t_k) \tau' t_l] T M_T \rangle = (-)^{t_{ij}+t_k-\tau'} |[(t_k t_{ij}) \tau' t_l] T M_T \rangle \quad (2.104)$$

Therefore the geometrical part of the general transformations are combined to

$$\begin{aligned} \tilde{g}_{\alpha_2 \alpha'_1}^{k\mu_1 \mu_2 \nu_1 \nu_2} &= (-)^{t_{ij}+t_{kl}-T} (-)^{t_k+t_l-t_{kl}} (-)^{t_{ij}+t_k-\tau'} \\ & \quad (-)^{l'_k+3s_k-I'_k} \sum_{S'} \sqrt{\hat{S}' \hat{I}'_k} \left\{ \begin{matrix} j_{ij} & s_k & S' \\ l'_k & j'_3 & I'_k \end{matrix} \right\} \\ & \quad (-)^{l_{kl}+j_{ij}+s_k+s_l-s_{kl}+j_{kl}-J} g_{\alpha_3 \alpha'_3}^{k\mu_1 \mu_2 \nu_1 \nu_2} \end{aligned} \quad (2.105)$$

Again one finds the “3-body” quantum numbers in Table 2.2. The total  $G$  function can be expressed as

$$G_{\alpha_2 \alpha'_1}^{\alpha \beta \gamma}(p_{kl} q x) = \sum_k P_k(x) \sum_{\mu_1+\mu_2=l'_k} \sum_{\nu_1+\nu_2=l'_i} (-\beta p_{kl})^{\mu_1} (-\gamma q)^{\mu_2} p_{kl}^{\nu_1} (-\alpha q)^{\nu_2} \tilde{g}_{\alpha_2 \alpha'_1}^{k\mu_1 \mu_2 \nu_1 \nu_2} \quad (2.106)$$

#### E. Interchanging the 2-body subclusters

$\langle (ij)kl | (kl)ij' \rangle$  interchanges the two 2-body subclusters. There is no change in the magnitudes of the momenta. The direction of  $\vec{q}$  is reversed leading to a phase  $(-)^{\lambda}$ . Nevertheless a recoupling is necessary because the coupling scheme Eqs.(2.49) and (2.50) is non-symmetric in the subsystems  $(ij)$  and  $(kl)$ . Therefore we recouple the right hand side of the matrix element

$$\begin{aligned} & (-)^{\lambda'} |(kl)ij' \rangle = (-)^{\lambda'} |((j'_{kl} \lambda') I' j'_{ij}) J' \rangle \\ &= (-)^{\lambda'} (-)^{j'_{kl}+\lambda'-I'} (-)^{I'+j'_{ij}-J} \\ & \quad \sum_{\tilde{I}} \sqrt{\hat{I} \tilde{I}} (-)^{j'_{kl}+\lambda'+j'_{ij}+J} \left\{ \begin{matrix} j'_{ij} & \lambda' & \tilde{I} \\ j'_{kl} & J' & I' \end{matrix} \right\} |((j'_{kl} \lambda') I' j'_{ij}) J \rangle \end{aligned} \quad (2.107)$$

Due to the interchange of the isospins  $t'_{ij}$  and  $t'_{kl}$  there occurs a factor  $(-)^{t'_{ij}+t'_{kl}-T'}$ . The left hand side of the matrix element projects the sum of Eq.(2.107) on fixed quantum numbers. The transformation matrix has got the form

$$\langle (ij)kl | (kl)ij' \rangle = \delta_{JJ'} \delta_{TT'} \delta_{MM'} \delta_{M_T M'_T} \delta_{\lambda \lambda'} \delta_{j_{ij} j'_{ij}} \delta_{l_{ij} l'_{ij}} \delta_{s_{ij} s'_{ij}} \delta_{t_{ij} t'_{ij}} \delta_{j_{kl} j'_{kl}} \delta_{l_{kl} l'_{kl}} \delta_{s_{kl} s'_{kl}} \delta_{t_{kl} t'_{kl}}$$

matrix element	phase	type	$i$	$j$	$k$	$l$
$\langle (12)3, 4 (12)4, 3' \rangle$	—	B	1	2	3	4
$\langle (12)3, 4 (12)34' \rangle$	—	C	1	2	3	4
$\langle (12)3, 4 (23)1, 4' \rangle$	—	A	1	2	3	4
$\langle (14)2, 3 (14)3, 2' \rangle$	—	B	1	4	2	3
$\langle (34)1, 2 (34)12' \rangle$	—	C	3	4	1	2
$\langle (12)4, 3 (14)2, 3' \rangle$	$(-)^{(12)}$	A	2	1	4	3
$\langle (12)4, 3 (12)3, 4' \rangle$	—	B	1	2	4	3
$\langle (12)4, 3 (12)34' \rangle$	$(-)^{(34')}$	C	1	2	4	3
$\langle (24)1, 3 (24)31' \rangle$	$(-)^{(31')}$	C	2	4	1	3
$\langle (14)2, 3 (12)4, 3' \rangle$	$(-)^{(14)}$	A	4	1	2	3
$\langle (14)2, 3 (24)1, 3' \rangle$	$(-)^{(24')}$	A	1	4	2	3
$\langle (34)12 (34)2, 1' \rangle$	$(-)^{(12)}$	D	3	4	2	1
$\langle (12)34 (34)12' \rangle$	—	E	1	2	3	4
$\langle (12)34 (12)3, 4' \rangle$	—	D	1	2	3	4
$\langle (12)34 (12)4, 3' \rangle$	$(-)^{(34)}$	D	1	2	4	3
$\langle (34)12 (12)34' \rangle$	—	E	3	4	1	2

Table 2.3: List of all necessary transformation matrix elements in Eqs.(2.68), (2.72), (2.73), (2.74) and (2.75). The explicit assignment of the particle numbers and additional phases are given. Please note that  $\langle (24)1, 3|(24)3, 1' \rangle$  is identical to  $\langle (14)2, 3|(14)3, 2' \rangle$

$$\frac{\delta(p_{ij} - p'_{ij})}{p_{ij}p'_{ij}} \frac{\delta(p_{kl} - p'_{kl})}{p_{kl}p'_{kl}} \frac{\delta(q - q')}{qq'} (-)^{t_{ij}+t_{kl}-T} (-)^{\lambda\sqrt{\hat{I}\hat{I}'}} \left\{ \begin{array}{ccc} j_{ij} & \lambda & I \\ j_{kl} & J & I' \end{array} \right\} \quad (2.108)$$

The matrix is diagonal in all quantum numbers except the intermediate spin  $I$ . It is sparse. Its numerical realization is simple compared to the former four transformation matrices.

This finishes the definition of all necessary kinds of transformation matrices. A closer look to Eqs.(2.68), (2.72), (2.73), (2.74) and (2.75) reveals that some transformations do not fit exactly into the forms A-E. For example the transformation  $\langle (12)4, 3|(12)34' \rangle$  from the second Yakubovsky equation Eq.(2.72) does not fit into the actual definition of the transformations of kind C. Particle  $k$  fits to particle 4 on the left hand side while it fits to the third particle on the right hand side. We can adjust the matrix element by interchanging particle 3 and 4 on the right hand side. Because 3 and 4 form a two-body subsystem and because of the partial wave representation, the interchange only leads to an additional phase

$$(-)^{(34')} \equiv (-)^{t'_{34}+s_3+s_4-s'_{34}+t_3+t_4-t'_{34}} \quad (2.109)$$

according to Eq.(2.60). Using this relation one finds

$$\langle (12)4, 3|(12)34' \rangle = (-)^{(34')} \langle (12)4, 3|(12)43' \rangle \quad (2.110)$$

The right hand side of Eq.(2.110) fits exactly into the definition of transformations of type C. The actual assignments of the particles are  $i = 1$ ,  $j = 2$ ,  $k = 4$  and  $l = 3$ . In Table 2.3 we list all necessary matrix elements and their connection to the general forms A-E. The necessary phase factors are also given.

In the next section we have to deal with the matrix element of the  $t$ -matrix. This will conclude the derivation of the explicit form of the Yakubovsky equations.

## 2.4 The two-body $t$ -matrix in the 4-body Hilbert space

The last missing ingredient of the Yakubovsky equations is the explicit form of the  $t$ -matrix, which is defined in Eq. (2.8). This equation is embedded in the four particle Hilbert space. It can be solved using the “3+1” or the “2+2” coordinates, but it turns out that the dependence on the outer particles enters only by means of an off-shell energy. The equations in “2+2” and “3+1” representation are essentially the same.

In the last section the individual particle masses are replaced by averaged masses of the isospin multiplet. In the free propagator this approximation might be less accurate. The masses are subtracted and the resulting difference is of the order of the binding energy. The splitting in the multiplet is of the same order of magnitude. Therefore we would like to avoid the former approximation in this part of the equation and treat the individual masses correctly. Because of this we introduce “pure” particle states

$$|n\rangle \equiv |t_i m_i^t\rangle |t_j m_j^t\rangle |t_k m_k^t\rangle |t_l m_l^t\rangle \quad (2.111)$$

Combining these states with the angular momenta of Eq. (2.47) and the Jacobi momenta we define a new kind of “3+1” representation  $|(ij)k, l\rangle^n$ . In this representation the Lippmann-Schwinger equation reads

$$\begin{aligned} {}^n \langle (ij)k, l | G_0 t_{ij} | (ij)k, l' \rangle^n &= {}^n \langle (ij)k, l | G_0 V_{ij} | (ij)k, l' \rangle^n \\ &+ \int'' {}^n \langle (ij)k, l | G_0 V_{ij} | (ij)k, l'' \rangle^n {}^n \langle (ij)k, l'' | G_0 t_{ij} | (ij)k, l' \rangle^n \end{aligned} \quad (2.112)$$

The kernel of equation Eq. (2.112)

$$\begin{aligned} {}^n \langle (ij)k, l | G_0 V_{ij} | (ij)k, l' \rangle^n &= \frac{\delta(p_k - p'_k)}{p_k p'_k} \frac{\delta(q_l - q'_l)}{q_l q'_l} \delta_{kl, kl'} \\ &\frac{1}{E - m_l - m_k - \frac{p_k^2}{2\mu_k} - \frac{q_l^2}{2\mu_l} - m_i - m_j - \frac{p_{ij}^2}{2\mu_{ij}}} V_{t_i m_i^t m_i^{t'} t_j m_j^t t_j^{t'} m_j^{t'}}^{l_{ij} l'_{ij} s_{ij} j_{ij}}(p_{ij}, p'_{ij}) \end{aligned} \quad (2.113)$$

has got a very simple dependence on the outer coordinates. It is absorbed in the off-shell energy of the two-body subsystem

$$E' = E - m_l - m_k - \frac{p_k^2}{2\mu_k} - \frac{q_l^2}{2\mu_l} \quad (2.114)$$

The three reduced masses are defined as

$$\begin{aligned} \frac{1}{\mu_{ij}} &\equiv \frac{1}{m_i} + \frac{1}{m_j} \\ \frac{1}{\mu_k} &\equiv \frac{1}{m_k} + \frac{1}{m_i + m_j} \\ \frac{1}{\mu_l} &\equiv \frac{1}{m_l} + \frac{1}{m_i + m_j + m_k} \end{aligned} \quad (2.115)$$

The matrix element of the kernel is diagonal in the outer momenta and the outer angular momentum quantum numbers which is abbreviated by  $\delta_{kl, kl'}$ . This includes the total angular momenta of the three-body subsystem and the full four-body system, because the potential conserves itself the angular momentum of the two-body system. Please note the non diagonal structure in the isospin quantum numbers. It reflects

the possibility of strong  $\Lambda$ - $\Sigma$  conversion in the hyperon-nucleon channels. All these properties carry over to the  $t$ -matrix and the Lippmann-Schwinger equation reduces to a two-body equation

$$\begin{aligned}
(G_0 t_{ij})_{t_i m_i^t m_i^{t'} t_j m_j^t m_j^{t'}}^{l_{ij} l'_{ij} s_{ij} j_{ij}}(p_{ij}, p'_{ij}, E') &= \frac{1}{E' - m_i - m_j - \frac{p_{ij}^2}{2\mu_{ij}}} V_{t_i m_i^t m_i^{t'} t_j m_j^t m_j^{t'}}^{l_{ij} l'_{ij} s_{ij} j_{ij}}(p_{ij}, p'_{ij}) \\
+ \sum_{l''_{ij}} \sum_{t''_j m''_j} \int d p''_{ij} p''_{ij}{}^2 &\frac{1}{E' - m_i - m_j - \frac{p''_{ij}{}^2}{2\mu_{ij}}} V_{t_i m_i^t m_i^{t''} t_j m_j^t m_j^{t''}}^{l_{ij} l''_{ij} s_{ij} j_{ij}}(p''_{ij}, p'_{ij}) \\
(G_0 t_{ij})_{t_i m_i^{t''} m_i^{t''} t_j m_j^{t''} m_j^{t''}}^{l''_{ij} l'_{ij} s_{ij} j_{ij}} &(p''_{ij}, p'_{ij}, E')
\end{aligned} \tag{2.116}$$

The dependence on the particles  $k$  and  $l$  is absorbed in the energy variable  $E'$ .  $E'$  includes the individual particle masses of the subsystem. By the definition Eq. (2.114) it is insured that

$$\Delta = E' - m_i - m_j \tag{2.117}$$

is smaller equal than the binding energy of the four-body system  $\epsilon_B$ . The full energy  $E = M + \epsilon_B$  is the sum of the binding energy and the sum of the lightest possible particles  $M$  of the four-baryon system. Therefore the sum of all the individual masses  $m_i$  in Eq. (2.114) and Eq. (2.117) is equal or bigger than  $M$ . This implies that  $\Delta \leq \epsilon_B < 0$ . The denominator in the Lippmann-Schwinger equation is finite and in this energy range there are no homogenous solutions indicating bound states in the two-body system anymore.

Eq. (2.116) is the same for “2+2” coordinates. The dependence of the energy on the momenta changes to

$$E' = E - m_k - m_l - \frac{p_{kl}^2}{2\mu_{kl}} - \frac{q^2}{2\mu} \tag{2.118}$$

in this case. Additionally, the reduced masses of the “2+2” partition appear

$$\begin{aligned}
\frac{1}{\mu_{kl}} &\equiv \frac{1}{m_k} + \frac{1}{m_l} \\
\frac{1}{\mu} &\equiv \frac{1}{m_k + m_l} + \frac{1}{m_i + m_j}
\end{aligned} \tag{2.119}$$

The form of Eq. (2.116) differs from the one chosen in the previous work [75]. There the authors employ the Lippmann-Schwinger equation in the form

$$t_{ij} = V_{ij} + V_{ij} G_0 t_{ij} \tag{2.120}$$

The free propagator has to be calculated for intermediate states, which because of the strong  $\Lambda$ - $\Sigma$  conversion have to be calculated for different kinds of hyperons in the subsystem. The reduced masses  $\mu_{kl}$ ,  $\mu_k$ ,  $\mu_l$  and  $\mu$  which are necessary for the calculation of  $E'$  are not well defined in this case. They depend on the reduced masses of the *intermediate four-body* states. In equation Eq. (2.116) we avoid this problem, because the free propagator has to be explicitly evaluated only for the outgoing state. In this state all reduced masses are well defined and the off-shell energy is uniquely given. In Ref. [75] the authors deal with a three-body problem. They used the momentum of the outer particle as parameter for the Lippmann-Schwinger equation. This defines the energy  $E'$  again uniquely. But in four-body calculations, there are two spectator momenta. Our formulation avoids a dependence of the Lippmann-Schwinger equation on two parameters and saves computational resources.

In the formulation of the Yakubovsky equations we use the isospin representation. To a very high accuracy the nuclear and hypernuclear bound states have a well defined total isospin. This reduces the dimension of the problem by a factor two or three. In the last paragraph we introduced the  $t$ -matrix in the “pure” particle representation. The inclusion of the  $t$ -matrix in the YE’s needs a transformation from isospin to “pure” particle states. This transformation is different for the “3+1” and the “2+2” isospin coordinates.

Neglecting all spins and momenta and concentrating on the isospin quantum numbers one finds for the “3+1” states

$$\begin{aligned}
& \langle ((t_i t_j) t_{ij} t_k) \tau t_l \rangle T M_T | G_0 t_{ij} | \langle ((t_i t'_j) t'_{ij} t_k) \tau' t_l \rangle T' M'_T \rangle \\
&= \sum_{\substack{m_i^t m_j^t m_k^t m_l^t \\ m_i^{t'} m_j^{t'}}} \langle ((t_i t_j) t_{ij} t_k) \tau t_l \rangle T M_T | t_i m_i^t \rangle | t_j m_j^t \rangle | t_k m_k^t \rangle | t_l m_l^t \rangle \\
&\quad \times \langle t_i m_i^{t'} | \langle t'_j m_j^{t'} | \langle t_k m_k^t | \langle t_l m_l^t | \langle ((t_i t'_j) t'_{ij} t_k) \tau' t_l \rangle T' M'_T \rangle \\
&\quad \times (G_0 t_{ij})_{t_i m_i^t m_i^{t'} t_j m_j^t t_j^{t'} m_j^t} (E - m_l - m_k - \frac{p_k^2}{2\mu_k} - \frac{q_l^2}{2\mu_l}) \\
&= \sum_{\substack{m_i^t m_j^t m_k^t m_l^t \\ m_i^{t'} m_j^{t'}}} (t_i t_j t_{ij}, m_i^t m_j^t m_i^t + m_j^t) (t_{ij} t_k \tau, m_i^t + m_j^t m_k^t m_i^t + m_j^t + m_k^t) \\
&\quad (\tau t_l T, m_i^t + m_j^t + m_k^t m_l^t M_T) \\
&\quad \times (t_i t'_j t'_{ij}, m_i^{t'} m_j^{t'} m_i^{t'} + m_j^{t'}) (t_{ij} t_k \tau, m_i^{t'} + m_j^{t'} m_k^t m_i^{t'} + m_j^{t'} + m_k^t) \\
&\quad (\tau' t_l T', m_i^{t'} + m_j^{t'} + m_k^t m_l^t M_{T'}) \\
&\quad \times (G_0 t_{ij})_{t_i m_i^t m_i^{t'} t_j m_j^t t_j^{t'} m_j^t} (E - m_l - m_k - \frac{p_k^2}{2\mu_k} - \frac{q_l^2}{2\mu_l}) \\
&\equiv \sum_{nn'} M_{3+1}^{iso}(\alpha_I, \alpha'_I, n, n') (G_0 t_{ij})_{nn'}(E'(n)) \tag{2.121}
\end{aligned}$$

In the last step we defined the recoupling coefficient  $M_{3+1}^{iso}$  in 3+1 representation which depends on the isospin channels  $\alpha_I$  and  $\alpha'_I$  and pure particle channels  $n$  and  $n'$ . Because of the reduced masses the energy  $E'$  also depends on the kind of particles given by  $n$ .

In the case of the “2+2” coordinates there are different couplings. The expression changes to

$$\begin{aligned}
& \langle ((t_i t_j) t_{ij} (t_k t_l) t_{kl}) T M_T | G_0 t_{ij} | \langle ((t_i t'_j) t'_{ij} (t_k t_l) t'_{kl}) T' M'_T \rangle \\
&= \sum_{\substack{m_i^t m_j^t m_k^t m_l^t \\ m_i^{t'} m_j^{t'}}} \langle ((t_i t_j) t_{ij} (t_k t_l) t_{kl}) T M_T | t_i m_i^t \rangle | t_j m_j^t \rangle | t_k m_k^t \rangle | t_l m_l^t \rangle \\
&\quad \times \langle t_i m_i^{t'} | \langle t'_j m_j^{t'} | \langle t_k m_k^t | \langle t_l m_l^t | \langle ((t_i t'_j) t'_{ij} (t_k t_l) t'_{kl}) T' M'_T \rangle \\
&\quad \times (G_0 t_{ij})_{t_i m_i^t m_i^{t'} t_j m_j^t t_j^{t'} m_j^t} (E - m_l - m_k - \frac{p_{kl}^2}{2\mu_{kl}} - \frac{q^2}{2\mu}) \\
&= \sum_{\substack{m_i^t m_j^t m_k^t m_l^t \\ m_i^{t'} m_j^{t'}}} (t_i t_j t_{ij}, m_i^t m_j^t m_i^t + m_j^t) (t_k t_l t_{kl}, m_k^t m_l^t m_k^t + m_l^t) \\
&\quad (t_{ij} t_{kl} T, m_i^t + m_j^t m_k^t + m_l^t M_T) \\
&\quad \times (t_i t'_j t'_{ij}, m_i^{t'} m_j^{t'} m_i^{t'} + m_j^{t'}) (t_k t_l t'_{kl}, m_k^t m_l^t m_k^t + m_l^t)
\end{aligned}$$

$$\begin{aligned}
& (t'_{ij} t'_{kl} T', m_i^{t'} + m_j^{t'} m_k^t + m_l^t M_T') \\
& \times (G_0 t_{ij})_{t_i m_i^t m_i^{t'} t_j m_j^t m_j^{t'}} (E - m_l - m_k - \frac{p_{kl}^2}{2\mu_{kl}} - \frac{q^2}{2\mu}) \\
& \equiv \sum_{nn'} M_{2+2}^{iso}(\alpha_I, \alpha'_I, n, n') (G_0 t_{ij})_{nn'}(E'(n))
\end{aligned} \tag{2.122}$$

Also in the 2+2 basis the transformation from isospin to particle basis is given by a recoupling coefficient  $M_{2+2}^{iso}$ .

This concludes the derivation of the explicit form of the YE's. In the next chapters these equations are applied to the three- and four-nucleon systems and the strangeness  $S = -1$  three- and four-baryon bound systems. It is possible to solve them numerically without any uncontrolled approximation. Because the YE's are three dimensional integral equations, their numerical realization is a very high dimensional eigenvalue equation. The actual solution is possible only on massively parallel supercomputers. The algorithms used are described in the next chapter.



## Chapter 3

# Numerical Realization

The Yakubovsky equations Eqs. (2.68), (2.72), (2.73), (2.74) and (2.75) represent a set of three-dimensional homogenous integral equations, which after discretization turns into a huge matrix eigenvalue equation. The dimension of the problem is of the order  $10^8$ . A direct solution is out of question, the problem calls for an iterative solution method. Since some time a Lanczos-like scheme, the “method of iterated orthonormal vectors” (IOV), has proved to be very efficient for nuclear few-body problems [81]. This scheme is also applied in our case. Therefore the numerical and technical challenge reduces to the application of the kernel to a set of trial YC’s. Because of the huge dimension, the calculation of the kernel matrix would be not feasible, the storage of  $10^8 \times 10^8$  numbers would be impossible and the application of this full matrix would even be inefficient, because it would not make use of the block diagonal structures which are implied in our formulation of the Yakubovsky equations. As already pointed out, all transformations leave one of the momenta unchanged. Therefore the matrix is diagonal in this variable. The application of the kernel decomposes naturally into the application of separate coordinate transformations and the  $t$ -matrix. The numerical realization of these tasks is described in the next two sections. We will start with the treatment of the coordinate transformations and turn to the application of the  $t$ -matrices afterwards. The solution requires the usage of a massively parallel supercomputer. The parallization has to be made manually. We decided to distribute the momentum grid points. This parallization is also described. The last section deals with the investigation of the numerical stability of our method. It is divided into two parts. One is devoted to the hypertriton and the other one to the four-body system. Apart from investigating the numerical accuracy of the binding energy, we put a special emphasis on the development of an accurate and fast algorithm to calculate the wave function.

### 3.1 Realization of the coordinate transformations on a massively parallel computer

The numerical realization of the five different types of transformations of Section 2.3 is very similar. We will exemplify the algorithm for the type A transformations only.

Using the transformation as given in Eq. (2.81), one can express the application on a state vector  $\psi$  as

$$\tilde{\psi}_{\alpha_1}(p_{12}p_3q_4) = \int' \langle (12)3, 4|(23)1, 4' \rangle \langle (12)3, 4'|\psi \rangle$$

$$= \sum_{\alpha'_1} \int_{-1}^1 dx G_{\alpha_1 \alpha'_1}(p_{12} p_3 x) \frac{\psi_{\alpha'_1}(\pi_{23}(p_{12} p_3 x) \chi_1(p_{12} p_3 x) q_4)}{\pi_{23}^{l'_{23}} \chi_1^{l'_1}} \quad (3.1)$$

To simplify the notation, we omitted the superscripts  $\alpha, \beta, \gamma$  of  $G$  and replaced the “three-body” channels  $\alpha_3$  by “four-body” channels  $\alpha_1$ . The  $\delta$ -functions remove all momentum integrations. There is only the integration over the angular variable  $x$  left. The numerical solution requires the definition of grids for the three momentum variables. The functions  $\tilde{\psi}$  and  $\psi$  are defined on grid points  $p_{12}^k, p_3^l$  and  $q_4^m$ . The grid points for  $\psi$  and  $\tilde{\psi}$  are chosen to be equal. But they differ in general from the shifted momenta  $\pi_{23}$  and  $\chi_1$ . Therefore the evaluation of Eq. (3.1) needs an efficient interpolation scheme from the grid points to the shifted momenta  $\pi$ . This has been developed in Ref. [82]. The interpolation of an arbitrary function  $f$  is reduced to a sum over  $f$  at four sample grid points  $N(\pi, i)$  multiplied by spline functions  $S_i(\pi)$ . The spline function  $S$  and the sample points  $N$  do not depend on  $f$  itself, they only depend on the grid points and shifted momenta  $\pi$ .

$$f(\pi) = \sum_{i=1}^4 S_i(\pi) \cdot f(p^{N(\pi, i)}) \quad (3.2)$$

The explicit definition of  $S$  is given in Appendix B of [82]. Using this interpolation Eq. (3.1) can be discretized in the form

$$\begin{aligned} \tilde{\psi}_{\alpha_1}(p_{12}^l p_3^m q_4^n) &= \sum_{\alpha'_1} \sum_{x^i} G_{\alpha_1 \alpha'_1}(p_{12}^l p_3^m x^i) w_{x^i} \\ &\sum_{s_{12}, s_3=1}^4 S_{s_{12}}(\pi_{23}(p_{12}^l p_3^m x^i)) \tilde{S}_{s_3}(\chi_1(p_{12}^l p_3^m x^i)) \frac{\psi_{\alpha'_1}(p_{12}^{N(\pi_{23}, s_{12})} p_3^{\tilde{N}(\chi_1, s_3)} q_4^n)}{(p_{12}^{N(\pi_{23}, s_{12})})^{l'_{23}} (p_3^{\tilde{N}(\chi_1, s_3)})^{l'_1}} \end{aligned} \quad (3.3)$$

Here we introduced a grid  $x^i$  of angular points and their integration weights  $w_{x^i}$  and the spline functions  $S$  and  $\tilde{S}$  for the grids of  $p_{12}$  and  $p_3$ , respectively. The next step is to insert the definition of  $G$  given in Eq. (2.80) and Table 2.2.

$$\begin{aligned} \tilde{\psi}_{\alpha_1}(p_{12}^l p_3^m q_4^n) &= \sum_{\alpha'_1} \sum_{\mu_1 + \mu_2 = l'_{23}} \sum_{\nu_1 + \nu_2 = l'_1} (-\beta p_{12}^{\mu_1})^{\mu_1} (-\gamma p_3^{\mu_2})^{\mu_2} (p_{12}^{\nu_1})^{\nu_1} (-\alpha p_3^{\nu_2})^{\nu_2} \\ &\sum_k g_{\alpha_1 \alpha'_1}^{k \mu_1 \nu_1 \mu_2 \nu_2} \sum_{x^i} w_{x^i} P_k(x^i) \\ &\sum_{s_{12}, s_3=1}^4 S_{s_{12}}(\pi_{23}(p_{12}^l p_3^m x^i)) \tilde{S}_{s_3}(\chi_1(p_{12}^l p_3^m x^i)) \frac{\psi_{\alpha'_1}(p_{12}^{N(\pi_{23}, s_{12})} p_3^{\tilde{N}(\chi_1, s_3)} q_4^n)}{(p_{12}^{N(\pi_{23}, s_{12})})^{l'_{23}} (p_3^{\tilde{N}(\chi_1, s_3)})^{l'_1}} \end{aligned} \quad (3.4)$$

In this way the transformation turns out to be a matrix times vector multiplication.

The sum of the number of partial waves of the five YC's is roughly 5500. Each of the three momentum grids has to be discretized using  $\approx 40$  grid points. Therefore we estimate the dimension of the discretized kernel of the eigenvalue equation to

$$40^3 \times 5500 \approx 4 \cdot 10^8 \quad (3.5)$$

This eigensystem is non-symmetric and has no band structure. The numerical solution is a challenge for today's supercomputers.

In order to have a feeling on the necessary computer resources for the solution of our numerical problem, we would like to give a rough estimate of the necessary operations. It turns out that the most

time consuming step in Eq. (3.4) is the application of  $g$ . We assume that we have already performed the interpolation and  $x$  summation. The intermediate result depends on  $k$ , the three momenta and on  $\alpha'_1$ . Again we estimate the number of momentum grid points per momentum to 40. A converged calculation requires up to 2000 partial waves for one of the YC's.  $g_{\alpha_1 \alpha'_1}^{k \mu_1 \nu_1 \mu_2 \nu_2}$  is not a full matrix. Because some of the quantum numbers are conserved in the application of a coordinate transformation,  $g$  couples each channel to no more than 50 other ones. The number of necessary summations in  $\mu_i, \nu_i$  and  $k$  depends on the partial waves  $\alpha_1$  and  $\alpha'_1$ . In the following we assume a typical number of 60  $\mu_i, \nu_i$  and  $k$  combinations. The calculation of each summand requires at least one multiplication and one addition. Therefore we need

$$40^3 \times 2000 \times 50 \times 60 \times 2 \approx 10^{12} \text{ operations} \quad (3.6)$$

This is only a rough estimate for one transformation. The application of the kernel of the eigenvalue equation needs several transformations and, additionally, the application of the  $t$ -Matrix. The iterative solution method needs 5-10 iterations to compute the biggest eigenvalue and eigenvector. The aim is to find an eigenstate in roughly 4 CPU-h. To reach this aim no more than 200 CPU-sec are available for the operations in Eq. (3.4). This means that the sustained performance of the computer should be of the order of 5 GFlops (five billion floating point operations per second).

This computer requirements are nowadays available on massively parallel supercomputers. We have access to a Cray installation in the NIC in Jülich [83]. The available Cray T3E fulfills our needs, but the architecture is of the “distributed memory” type. Therefore the programmer himself has to distribute the numerical tasks and the necessary arrays in a suitable manner. In the moment there are no tools available, which can parallize programs automatically and generate efficient codes. The algorithm has to make sure that most data are available on the local node and that the processor load is balanced. In Jülich one is able to access 256 nodes (PE's) each with 512 MB of memory.

One possibility to distribute the operations and the arrays is to calculate each partial wave on a different node. But in our case the number of partial waves is strongly dependent on the physical problem. Furthermore the computational effort is in general very different for each partial wave. It is very hard to obtain a balanced load. Therefore we decided to distribute the momentum grids. Because the number of grid points per variable is roughly 40, much smaller than the number of nodes available, it is necessary to distribute simultaneously more than one momentum variable. This has been done. We used all three momenta. In order to do this, we distribute the available PE's logically on a three-dimensional grid. Each PE is identified by a triple of indices  $(pe_{12}, pe_3, pe_4)$ . The part of the  $\{p_{12}^k\}$ ,  $\{p_3^l\}$  or  $\{q_4^m\}$  momentum grid, which is kept local on the PE, depends on its index  $pe_{12}$ ,  $pe_3$  or  $pe_4$ , respectively. In this way all processors obtain a nearly equal number of local grid points. In this three-dimensional ordering of PE's, it is easy to build groups of processors, which have got the same grid points in one or two of the momenta. The implementation has been carried out using the “MPI message passing interface” [84]. This library for the communication between nodes already supports groups of processors, they are called “communicators”.

Let us turn to Eq. (3.4) now. We perform the calculation for each pair of incoming and outgoing partial wave  $\alpha_1$  and  $\alpha'_1$  separately. We divide the calculation in three parts.

- 1) In the first step we carry out the interpolation of  $\psi$ .

$$\tilde{\psi}^1(p_{12}^l p_3^m q_4^n x^i) = \sum_{s_{12}, s_3=1}^4 S_{s_{12}}(\pi_{23}(p_{12}^l p_3^m x^i)) \tilde{S}_{s_3}(\chi_1(p_{12}^l p_3^m x^i)) \frac{\psi_{\alpha'_1}(p_{12}^{N(\pi_{23}, s_{12})} p_3^{\tilde{N}(\chi_1, s_3)} q_4^n)}{(p_{12}^{N(\pi_{23}, s_{12})})'_{23} (p_3^{\tilde{N}(\chi_1, s_3)})'_{12}} \quad (3.7)$$

The calculation is done for local grid points of the outgoing state. The grid points, which are necessary for the interpolation, are given by the index fields  $N(\pi_{23}, s_{12})$  and  $\tilde{N}(\chi_1, s_3)$ . Because the shifted momenta are  $x$  dependent, the necessary sample points are in general spread over the entire momentum grid. These are not available on the local PE. We use a broadcast command of the MPI library to collect all  $p_{12}$  and  $p_3$  grid points on the local processor for the actual partial wave channel  $\alpha_1$ . Because the operation is diagonal in the  $q_4$  momentum, we need only local grid points in  $q_4$  for the interpolation. In this situation a communication within the group of processors, which have got the same  $q_4$  points and therefore the same  $pe_4$  index, is necessary. The MPI standard supports these communications.

- 2) Using  $\tilde{\psi}^1(p_{12}^l p_3^m q_4^n x^i)$ , which is also given at the local grid points, the  $x$ -integration can be performed:

$$\tilde{\psi}^2(p_{12}^l p_3^m q_4^n k) = \sum_{x^i} w_{x^i} P_k(x^i) \tilde{\psi}^1(p_{12}^l p_3^m q_4^n x^i) \quad (3.8)$$

In this step there is no communication necessary. The results can be stored locally.

- 3) The most time consuming part is the application of the geometrical  $g$ -matrix to the intermediate result  $\tilde{\psi}^2$ .  $\tilde{\psi}^2$  is given at local points and the result should be calculated for the same grid points. However, the extremely high number of partial waves, which we can expect, made it necessary to distribute also the  $g$ -coefficients over the PE's. Remembering that we treat each partial wave combination  $\alpha_1, \alpha'_1$  of Eq. (3.4) separately, we put a copy of  $g$  for the specific  $\alpha_1, \alpha'_1$  on all PE's by a MPI broadcasting operation. After that all  $g$ -numbers for the summation over  $\mu_i, \nu_i$  and  $k$  are locally present, the operations necessary for  $\alpha_1$  and  $\alpha'_1$  can be finished.

In summary there is parallization overhead in two steps

- 1) a broadcasting operation to collect the data for all grid points for a certain  $\alpha'_1$  on every PE.
- 2) a broadcasting operation which copies the necessary  $g$ -coefficients to the local memory.

Table 3.1 exemplifies the dependence of the performance on the number of PE's. One can see a visible loss of performance of roughly 30 %, if one increases the number of PE to 128. With this PE number the total performance is more than 10 GFlops. This means more than 10 $\times$  the performance of a well vectorized code on a Cray T90 and two times the performance we estimated as minimal requirement for our problem (see above in this section).

In the same table one can also find our memory needs. Because of the distributed memory architecture each node needs a certain amount of local memory for the copy of the code and some local arrays. For our code this amounts to 80 MB, which is independent of the number of partial waves. Apart from this unavoidable and fixed amount of memory, we carefully distributed all arrays. This is a very important feature of the code, because it enables us to make efficient usage of the core memory for a very high number of PE's. For a realistic calculation the set of five Yakubovsky components needs roughly

$$40^3 \times 2000 \text{ channels} \times 5 \text{ YC's} \times 4 \text{ Byte per floating point number} = 2.5 \text{ GB} \quad (3.9)$$

The application of our Lanczos-like method requires the storage of roughly 10 sets of YC's. These 10 vectors form the basis system for the diagonalization procedure. The storage of these 10 vectors requires the whole memory of 62 PE's of the installation of the NIC, Jülich. This is by far the most memory consuming array. Therefore the performance and the core memory size of the T3E complex in Jülich is sufficient for the solution of realistic hypernuclear problems. In the next section we would like to describe briefly the application of the  $t$ -matrix.

# PE's	MFlops per node	total GFlops	memory usage per node
8	126	1.01	296 MB
16	118	1.89	208 MB
32	115	3.70	144 MB
64	106	6.76	104 MB
128	88	11.27	88 MB
192	82	15.68	80 MB

Table 3.1: Dependence of the performance on the number of used PE's on the T3E-1200 of the NIC. The averaged single node performance, the resulting total performance and the used memory per node is given.

### 3.2 Realization of the $t$ -matrix application on a massively parallel computer

In the following we would like to describe the numerical realization of the  $t$ -matrix, which appears in the form  $\langle (ij)k, l | G_0 t_{ij} | \psi \rangle$ . Because the algorithm is essentially identical for “3+1” and “2+2” coordinates, we will take (12)3,4 coordinates as an example.

As outlined in Section 2.4, we insert a complete set of states between  $t$  and  $\psi$  and transform from the isospin to the pure particle state basis. Using the form of Eq. (2.121) and splitting the  $\alpha'_1$  sum in an  $\alpha'_S$  spin sum and an  $\alpha'_I$  isospin sum, one finds

$$\begin{aligned} \tilde{\psi}(p_{12}^l p_3^m q_4^n) &= \sum_{\alpha'_S \alpha'_I} \sum_{nn'} \int dp_{12}^l p_{12}^{\lambda 2} M_{3+1}^{iso}(\alpha_I, \alpha'_I, n, n') \\ &\quad (G_0 t_{12})_{nn'}^{\alpha_S \alpha'_S}(p_{12}^l, p_{12}^\lambda, E'(p_3^m q_4^n, nn')) \psi_{\alpha'(\alpha'_S, \alpha'_I)}(p_{12}^l p_3^m q_4^n) \end{aligned} \quad (3.10)$$

The integration has to be discretized. Its discretization grid is the same as for the state vectors. We call the integration weights  $w_{p_{12}}^\lambda$ .

$$\begin{aligned} \tilde{\psi}(p_{12}^l p_3^m q_4^n) &= \sum_{\alpha'_S \alpha'_I} \sum_{nn'} \sum_{p_{12}^\lambda} w_{p_{12}}^\lambda p_{12}^{\lambda 2} M_{3+1}^{iso}(\alpha_I, \alpha'_I, n, n') \\ &\quad (G_0 t_{12})_{nn'}^{\alpha_S \alpha'_S}(p_{12}^l, p_{12}^\lambda, E'(p_3^m q_4^n, n)) \psi_{\alpha'(\alpha'_S, \alpha'_I)}(p_{12}^\lambda p_3^m q_4^n) \end{aligned} \quad (3.11)$$

Here we point out that  $E'$  depends on two momentum variables and the kind of particles of the outgoing state. The number of different energies, where the  $t$ -matrix is needed, is quadratic in the number of momentum grid points. The  $t$ -matrix would be extremely huge, if we kept the dependence on both momenta. On the other side the energy dependence of  $t$  is mild (except near the bound state poles of the two-body subsystem). Therefore we introduce an additional energy grid  $\{E^i\}$  and insert an interpolation step from this grid to  $E'$ . It turns out that one can obtain stable results using 50 energy points. This reduces the memory and computing time necessary for the  $t$  matrix tremendously.

$$\begin{aligned} \tilde{\psi}(p_{12}^l p_3^m q_4^n) &= \sum_{s_E} \sum_{\alpha'_S \alpha'_I} \sum_{nn'} \sum_{p_{12}^\lambda} w_{p_{12}}^\lambda p_{12}^{\lambda 2} M_{3+1}^{iso}(\alpha_I, \alpha'_I, n, n') \hat{S}_{s_E}(E') \\ &\quad (G_0 t_{12})_{nn'}^{\alpha_S \alpha'_S}(p_{12}^l, p_{12}^\lambda, E^{\hat{N}(E', s_E)}) \psi_{\alpha'(\alpha'_S, \alpha'_I)}(p_{12}^\lambda p_3^m q_4^n) \end{aligned} \quad (3.12)$$

The introduction of the energy grid improves the efficiency of our code drastically. Because of the introduction of this energy grid, the Lippmann-Schwinger equation as given in Eq. (2.112) must be solved without knowledge of the actual momenta of the outer particles. This is only possible, because we solve for the combined operators  $G_0 t_{12}$  (see Section 2.4).

In this point the actual implementation differs from the one in Ref. [75] and [36] for the hypertriton and the  $\alpha$  particle, respectively. For the hypertriton the authors could keep the dependence of the  $t$ -matrix on the outer momentum, because they only treat a three-body system. The authors of [36] restricted themselves to the four-nucleon system. In their case there is no particle conversion and the off-shell energy is well defined also for the intermediate propagator.

In bound state problems  $G_0$  is finite, because of the negative binding energies. The matrix elements are defined for all desired  $E'$ .

However, still the  $t$ -matrix in its discretized form needs a visible amount of 170 MB of core memory and, hence, has to be distributed over the PE's. In our implementation we use the distribution of  $p_{12}$  momenta of the state vectors also for the first  $p_{12}$  momentum grid of  $t$ . It has no  $q_4$  and  $p_3$  dependence. Therefore we use the group of  $(pe_3, pe_4)$  PE's for the distribution of the energy grid points. Again the index fields  $\hat{N}(E', s_E)$  spread the sample grid points over the complete energy grid. That's why Eq. (3.12) requires the  $t$ -matrix at all energy grid points on the local PE. The algorithm is easily read off from Eq. (3.12):

- a) For all channels  $\alpha$  one collects  $\psi$  for the complete  $p_{12}$ -grid on the local PE. The calculation is done for the local  $p_3$  and  $q_4$  points. Communication is necessary only in the group of PE's with the same  $pe_3$  and  $pe_4$  coordinates.
- b) The partial waves are arranged in a way, that the angular momentum quantum numbers of the outer particles change more quickly than the two-body angular momentum quantum numbers. The isospin quantum numbers change fastest. We make available in this step a local copy of the  $t$ -matrix for all energy points. Because of the size of the array, we collect all data, which are necessary for the actual two-body subsystem channel. In the case that consecutive partial waves have the same two-body subsystem quantum numbers, this communication can be avoided.
- c) After all data are locally available, the summation is carried out for the actual  $\alpha, \alpha'$  channels.

This concludes the brief description of our algorithm. Its performance and memory requirements are sufficient for an accurate solution of the very high dimensional Yakubovsky equations. The numerical stability of our method shall be investigated in the next section.

### 3.3 Investigation of the numerical stability

In this section we investigate the numerical stability of our calculation. It is divided into two subsections. One deals with the hypertriton, the other one with the four-body system.

We start with a systematic estimate of our numerical errors in the binding energies. Here we emphasize that one of the advantages of our method is the possibility to control all numerical errors. Therefore the results are reliable and physical conclusions can safely be drawn from them.

Afterwards we turn to the calculation of the wave function. Here it becomes clear that the introduction of different Jacobi coordinates is highly advisable. In addition the calculation of the energy expectation value is a good check for the code and the numerical accuracy.

The second part is devoted to the four-body system. The estimate of the error in the binding energy is done in a straight forward manner, but the calculation of the wave function is much more involved. Generalizing the experience from the hypertriton, we look for an efficient and accurate way to calculate the wave function. A successful solution of this problem requires a careful analysis of the accuracy of several transformations. We will carry this out and present the expectation value of  $H$  as a very impressive consistency check.

The triton and  $\alpha$ -particle calculations have been checked correspondingly. These checks are not explicitly outlined in this thesis. Because the physical problem is much simpler, converged calculations could be obtained much easier.

### 3.3.1 Numerical accuracy of the ${}^3_{\Lambda}\text{H}$ calculation

In this subsection we will present in some detail the numerical checks, that we performed for the solution of the two coupled Faddeev equations for the hypertriton. The derivation of the equations is outlined in Ref. [75] and in Appendix B.1. The definition of the wave function is given in Appendix D.2.

As already shown we have to solve a linear eigenvalue problem.

$$\eta \psi = K(E) \psi \quad (3.13)$$

The kernel of the linear equation is energy dependent.  $\psi$  represents the set of Faddeev components (FC).

Therefore finding the physical solution requires an energy search. For the physical binding energy  $\eta = 1$  appears in the spectrum. The corresponding eigenstate is the physical set of FC's.

We solve the equations in a partial wave representation. To obtain a finite set of linear equations, we truncate the partial wave basis. For the three-body system it is sufficient to restrict the total two-body angular momentum  $j_{ij}$  of Eq. (2.47) (omitting the angular momenta of the fourth particle). Provided that the total three-body angular momentum  $j_3$  is fixed, the number of channels is finite in this case. In Table 3.2 we present the allowed angular momenta couplings with  $j_{12} \leq 1$  for the quantum numbers of the hypertriton  $j_3^{\pi} = \frac{1}{2}^{+}$ .

Finding a suitable grid for the momenta and the angular integration is our first task. For the angular integration it turned out that Gauss quadrature points are most efficient. For the momentum grid we also use a point distribution, which is based on Gaussian points, but we change the distribution by a hyperbolic transformation [85]. The momentum integration has to be performed in the interval  $[0, \infty[$ . Because the functions drop sufficient rapidly we limit the integration to  $[0, p^c]$ . This interval is divided into three parts:  $[0, p^a]$ ,  $[p^a, p^b]$  and  $[p^b, p^c]$ . By the hyperbolic transformation we distribute  $np^a/2$  grid points in the first and second interval. In the last interval a simple linear distribution of  $np^b$  Gaussian points turned out to be suitable.  $p^a = 1.0 \text{ fm}^{-1}$  and  $p^b = 4.0 \text{ fm}^{-1}$  are reasonable choices for the interval boundaries. The last cut-off  $p^c$  will be chosen differently for the two momentum grids of the Faddeev equation and the momentum grid  $p_t$ , which we use for the solution of the Lippmann-Schwinger equation Eq. (2.8). We derive the energy grid for the  $t$ -matrix from an auxiliary momentum grid  $p_e$ . With the negative starting energy  $E_0$ , which is smaller than the lowest bound state pole of the  $t$ -matrix, we obtain the energy grid points as

$$E_i = E_0 - \frac{p_e^i{}^2}{\bar{m}} \quad (3.14)$$

$\bar{m}$  is an averaged baryon mass. For  $p_e$  we use similar grid points as for the other momenta. We choose  $p_e^a = 0.5 \text{ fm}^{-1}$ ,  $p_e^b = 4.0 \text{ fm}^{-1}$  and  $p_e^c = 10.0 \text{ fm}^{-1}$ . The actual values of  $p_e^c$  and  $\bar{m}$  make sure that the energy interval includes all energies, which are needed in the Faddeev calculation.

#	$l_{12}$	$s_{12}$	$j_{12}$	$l_3$	$I_3$	$j_3^\pi$
1	0	0	0	0	$\frac{1}{2}$	$\frac{1}{2}^+$
2	1	1	0	1	$\frac{1}{2}$	$\frac{1}{2}^+$
3	1	0	1	1	$\frac{1}{2}$	$\frac{1}{2}^+$
4	1	0	1	1	$\frac{3}{2}$	$\frac{1}{2}^+$
5	1	1	1	1	$\frac{1}{2}$	$\frac{1}{2}^+$
6	1	1	1	1	$\frac{3}{2}$	$\frac{1}{2}^+$
7	0	1	1	0	$\frac{1}{2}$	$\frac{1}{2}^+$
8	0	1	1	2	$\frac{3}{2}$	$\frac{1}{2}^+$
9	2	1	1	0	$\frac{1}{2}$	$\frac{1}{2}^+$
10	2	1	1	2	$\frac{3}{2}$	$\frac{1}{2}^+$

Table 3.2: Angular momentum quantum numbers for total  $j_3^\pi = \frac{1}{2}^+$  with the two-body angular momenta  $j_{12} \leq 1$ .

In Tables 3.3 to 3.7 we present the eigenvalue results for different grids and investigate their stability. For this investigation we use the Nijm 93 NN potential [10] and the Nijm SC89 YN interaction [54]. The momentum cut-offs are fixed to  $p_{12}^c = 15.0 \text{ fm}^{-1}$ ,  $p_3^c = 10.0 \text{ fm}^{-1}$  and  $p_t^c = 30.0 \text{ fm}^{-1}$ .

For this calculations we restrict the partial waves with  $j_{12} \leq 2$  and choose a reasonable trial binding energy of  $E_B = -2.360 \text{ MeV}$  below the breakup into three free baryons. Our results are stable within  $\Delta\eta = 0.0005$  for  $np_{12}^a = 32$ ,  $np_{12}^b = 8$ ,  $np_3^a = 32$ ,  $np_3^b = 4$ ,  $np_t^a = 32$ ,  $np_t^b = 20$ ,  $np_e^a = 36$ ,  $np_e^b = 10$  and  $nx = 16$ . Please note that most of the error is due to the truncation for the  $x$ -points. This behavior is very different in a  ${}^3\text{H}$  calculation, which requires a much smaller number of  $x$ -points. We consider this as a signal that there is a strong dependence on the angle between the relative momentum in the YN subsystem and the momentum of the outer nucleon. Such a behavior is very natural, if one assumes that the hyperon is loosely bound to an unperturbed deuteron.

Next we check whether the cut-offs  $p_{12}^c = 15.0 \text{ fm}^{-1}$ ,  $p_3^c = 10.0 \text{ fm}^{-1}$  and  $p_t^c = 30.0 \text{ fm}^{-1}$  are sufficiently high. In Table 3.8 results for different cut-offs are shown. It turns out that above cut-offs are sufficient to obtain stable results.

Now we are ready to search for the physical binding energy. This is outlined in Table 3.9. From this table we estimate a roughly linear dependence of  $\eta$  on the trial energies with the gradient  $\left|\frac{dE}{d\eta}\right| \approx 3.02 \text{ MeV}$ . Because we claimed an error below  $\Delta\eta = 0.0005$  for the eigenvalues, we calculate an error of  $\Delta E \approx 1.5 \text{ keV}$  for the energy because of the discretization. The discretization error is far below the experimental error. The grids are sufficiently dense.

In the next step we take the higher partial waves into account. The binding energy results for different truncations of the partial wave decomposition are shown in Table 3.10. Our best calculation involves partial waves up to  $j_{12} = 6$ . From the table we estimate that the binding energy is converged within



$np_{12}^a$	$np_{12}^b$	$\eta$
28	8	0.99834
32	8	0.99823
36	8	0.99822
32	4	0.99785
32	8	0.99823
32	12	0.99822

Table 3.3: Dependence of the eigenvalue of the hypertriton Faddeev equation on the number of  $np_{12}$  grid points. For the calculation we have chosen  $np_3^a = 32$ ,  $np_3^b = 4$ ,  $np_t^b = 32$ ,  $np_t^b = 20$ ,  $np_e^a = 36$ ,  $np_e^b = 10$  and  $nx = 16$ .

$np_3^a$	$np_3^b$	$\eta$
28	4	0.99829
32	4	0.99823
36	4	0.99819
32	4	0.99823
32	8	0.99832
32	12	0.99834

Table 3.4: Dependence of the eigenvalue of the hypertriton Faddeev equation on the number of  $np_3$  grid points. For the calculation we have chosen  $np_{12}^a = 32$ ,  $np_{12}^b = 8$ ,  $np_t^b = 32$ ,  $np_t^b = 20$ ,  $np_e^a = 36$ ,  $np_e^b = 10$  and  $nx = 16$ .

1 keV. Together with the discretization error we claim converged results within  $\Delta E = \sqrt{1.5^2 + 1.0^2}$  keV = 1.8 keV. For the used potential combination Nijm 93 and Nijm SC89 our binding energy result is  $E = 2.367$  MeV. This compares well with the result from [76] of  $E = 2.36$  MeV.

At this point we emphasize once more that all necessary approximations can be check systematically in this way. The solution of Faddeev equations in momentum space allows to estimate numerical errors reliably.

With the binding energy and the Faddeev components in hand, we are able to calculate also the wave function of the hypertriton as given in Appendix D.2. We will show below that the partial wave decomposition of the wave function has got a different convergence behavior than the Faddeev calculation itself. The quality of the partial wave decomposition of the wave function is easily estimated, because of some features of the three-body calculation:

- 1) The truncation of the two-body channels by a maximum two-body total angular momentum  $j_{12}^{\max}$  results in a finite number of partial waves. Equivalently, a fully converged calculation for a NN and YN potential, which is truncated to these lower partial waves, requires only a finite number of partial waves for the Faddeev components. Nevertheless, the number of partial waves for the wave function is not restricted in this case.
- 2) Assuming that the potentials are zero for  $j_{12} > j_{12}^{\max}$  we can calculate the exact partial wave decomposition of the Faddeev components. From these components we can, in principle, calculate any partial wave of the wave function accurately. However, because the number of partial waves

$np_t^a$	$np_t^b$	$\eta$
28	20	0.99829
32	20	0.99823
36	20	0.99829
40	20	0.99827
32	16	0.99834
32	20	0.99823
32	24	0.99821

Table 3.5: Dependence of the eigenvalue of the hypertriton Faddeev equation on the number of  $np_t$  grid points. For the calculation we have chosen  $np_{12}^a = 32$ ,  $np_{12}^b = 8$ ,  $np_3^b = 32$ ,  $np_3^b = 4$ ,  $np_e^a = 36$ ,  $np_e^b = 10$  and  $nx = 16$ .

$nx$	$\eta$
12	0.99743
16	0.99823
20	0.99849
24	0.99861
28	0.99866

Table 3.6: Dependence of the eigenvalue of the hypertriton Faddeev equation on the number of  $nx$  grid points. For the calculation we have chosen  $np_{12}^a = 32$ ,  $np_{12}^b = 8$ ,  $np_3^b = 32$ ,  $np_3^b = 4$ ,  $np_e^a = 36$ ,  $np_e^b = 10$ ,  $np_t^b = 32$  and  $np_t^b = 20$ .

$ne^a$	$ne^b$	$\eta$
32	10	0.99827
36	10	0.99823
40	10	0.99825
36	10	0.99823
36	20	0.99823

Table 3.7: Dependence of the eigenvalue of the hypertriton Faddeev equation on the number of  $ne$  grid points. For the calculation we have chosen  $np_{12}^a = 32$ ,  $np_{12}^b = 8$ ,  $np_3^b = 32$ ,  $np_3^b = 4$ ,  $np_t^b = 32$ ,  $np_t^b = 20$  and  $nx = 16$ .

$p_{12}^c$ [fm $^{-1}$ ]	$p_3^c$ [fm $^{-1}$ ]	$p_t^c$ [fm $^{-1}$ ]	$\eta$
15.0	10.0	30.0	0.99823
12.0	10.0	30.0	0.99823
15.0	10.0	25.0	0.99821
15.0	10.0	30.0	0.99832
15.0	8.0	30.0	0.99834

Table 3.8: Dependence of the eigenvalue of the Faddeev equation on the cut-offs  $p_{12}^c, p_3^c$  and  $p_t^c$ . To clearly see the dependence on  $p_3^c$ , the last two rows show calculations with  $np_3^b = 8$ .

$E$ [MeV]	$\eta$
2.360	0.99823
2.380	0.99160
2.355	1.00000

Table 3.9: Eigenvalues  $\eta$  as a function of the trial energies  $E$ .

$j_{12}^{\max}$	$E$ [MeV]
1	2.323
2	2.355
3	2.365
4	2.366
5	2.367
6	2.367

Table 3.10: Binding energies of the hypertriton dependent on the maximal  $j_{12}$  we consider in the calculation.

contributing to the wave function is infinite, we can never obtain an exact decomposition of the wave function.

- 3) Using the antisymmetry with respect to the interchange of particles 1 and 2, one easily finds from the wave function  $\Psi$  given in Eq. (B.9) that matrix elements of a symmetric operator  $\hat{O}$  can be expressed by mixed matrix elements with the Faddeev components  $\psi_{1B}$  and  $\psi_{1C}$

$$\langle \Psi | \hat{O} | \Psi \rangle = \langle \Psi | \hat{O} | \psi_{1B} \rangle + 2 \langle \Psi | \hat{O} | \psi_{1C} \rangle \quad (3.15)$$

We can calculate the mixed matrix elements without any error from the partial wave decomposition, because the Faddeev components project out a finite number of partial waves. This holds especially for the norm of the wave function.

$$\langle \Psi | \Psi \rangle = \langle \Psi | \psi_{1B} \rangle + 2 \langle \Psi | \psi_{1C} \rangle \quad (3.16)$$

- 4) Similarly, we can give expectation values of the potentials  $V_{NN}$  and  $V_{YN}$  only with discretization errors, because the potentials do the same projection.

Because 3) holds especially for the kinetic energy  $T$ , which is symmetric under permutation of the identical nucleons, we can calculate the expectation value of  $H = T + V$  without any error of the missing partial waves. This is exemplified in Table 3.11. Indeed, the expectation value of the Hamiltonian agrees with the binding energy within the discretization error.

Nevertheless the representation of the wave function in partial waves is by far not perfect. We define the ratio

$$R_N = \frac{\langle \Psi | \Psi \rangle}{\langle \Psi | \psi_{1B} \rangle + 2 \langle \Psi | \psi_{1C} \rangle} \quad (3.17)$$

The difference of  $R_N$  to 1 is a measure for the error of the antisymmetrization of the nucleons. This error is the consequence of the missing higher partial waves. Therefore we investigate the dependence of this

$T$ [MeV]	$V_{NN}$ [MeV]	$V_{YN}$ [MeV]	$H$ [MeV]	$E$ [MeV]
23.61	-22.24	-3.73	-2.366	-2.367

Table 3.11: Expectation values of the kinetic energy  $T$ , the NN potential  $V_{NN}$ , the YN potential  $V_{YN}$  and the Hamiltonian  $H$  compared to the binding energy result  $E$ .

$j_{12}^{\max}$	$R_N^{1B}$	$R_N^{1C}$
2	0.9986	0.7962
3	0.9993	0.8569
4	0.9996	0.8937
5	0.9997	0.9165
6	0.9998	0.9315
8	0.9999	0.9479
10	1.0000	0.9551

Table 3.12: Ratios  $R_N$  as defined in the text for different partial waves truncations and both kinds of Jacobi coordinates of the hypertriton. The behavior of  $R_N$  is exemplified for a calculation using the Nijm SC97f and Nijm 93 interactions.

ratio on the partial wave truncation in Table 3.12. This is done in both representations of the hypertriton wave function: in the left column the hyperon is the outer particle and in the right column one of the nucleons is the outer particle. You can see a good convergence for the first norm ratio, but a very slow one for the second one. As will be shown Section 5.3 the hypertriton is essentially a deuteron to which a hyperon is loosely bound. The  $1C$  representation is not suitable at all to describe this state. A lot of partial waves are necessary to describe a bound state of the two nucleons in a representation which singles out one of them. Nevertheless, we have proved above that the Faddeev calculation is converged. This shows once more that the Faddeev decomposition speeds up the partial wave convergence by the systematic introduction of all different Jacobi coordinates.

In the case of a four-body system the situation is quite different. Firstly there are also explicit truncations necessary for one of the outer angular momenta and secondly an exact calculation of the lower partial waves of the wave function is not possible any more, because we require intermediate states in the calculation which are subject of a truncated partial wave decomposition. At the end of the next section we will come back to these problems. Before that we exemplify the numerical stability of the four-body calculation.

### 3.3.2 Error estimates for the ${}^4_{\Lambda}\text{He}$ and ${}^4_{\Lambda}\text{H}$ hypernuclei

The calculation of a four-body system is much more involved. The dimension of the discretized eigensystem increases not only because of one more momentum grid, but also because of a tremendously higher number of partial waves. One outstanding new complication is the need of an additional constraint on the partial wave decomposition. In the case of the three-body system, the truncation of the total angular momentum of the two-body subsystem together with a fixed total angular momentum restricted the partial wave decomposition to a finite sum. As already outlined this means that expectation values of the wave function can be calculated without the knowledge of the higher partial waves in some cases.

$l_{sum}^{max}$	$N_{1A}$	$N_{1B}$	$N_{1C}$	$N_{2A}$	$N_{2B}$	$\Sigma$
2	57	57	115	57	57	343
4	200	200	400	200	200	1200
6	472	472	945	472	472	2833
8	915	915	1830	915	915	5490
10	1567	1567	3135	1567	1567	9403
12	2456	2456	4905	2441	2441	14699
14	3440	3440	6845	3236	3236	20197

Table 3.13: Number of partial waves contributing to different kinds of Jacobi coordinates for  $J^\pi = 0^+$  dependent on  $l_{sum}^{max}$ .  $\Sigma$  is the total number of channels.

$l_{sum}^{max}$	$N_{1A}$	$N_{1B}$	$N_{1C}$	$N_{2A}$	$N_{2B}$	$\Sigma$
2	134	134	270	134	134	806
4	532	532	1065	532	532	3193
6	1311	1311	2640	1311	1311	7916
8	2617	2617	5235	2617	2617	15703
10	4544	4544	9090	4544	4544	27266

Table 3.14: Number of partial waves contributing to different kinds of Jacobi coordinates for  $J^\pi = 1^+$  dependent on  $l_{sum}^{max}$ .  $\Sigma$  is the total number of channels.

This feature holds no longer in four-body systems. The investigation of the stability is therefore more complicated.

The angular momentum coupling scheme is given in Eq. (2.47) for the “3+1” and Eq. (2.49) for the “2+2” representation. We put two constraints on orbital angular momenta. First we require  $j_{ij}, j_{kl} \leq 6$  and  $l_k, l_l, \lambda \leq 8$ . But this restriction is not sufficient, because it still leads to a tremendous number of partial waves. In the following we will not change any of this truncations. Instead of working with constraints for the individual quantum numbers, we restrict the sum of them. Namely we demand additionally that

$$\begin{aligned} l_{ij} + l_k + l_l &\leq l_{sum}^{max} \\ l_{ij} + l_{kl} + \lambda &\leq l_{sum}^{max} \end{aligned} \quad (3.18)$$

We use the same  $l_{sum}^{max}$  for the 3+1 and 2+2 partitions. With  $l_{sum}^{max}$  we can systematically control the number of partial waves by one parameter. This makes stability investigations easier.

To give a feeling of the number of partial waves for a given  $l_{sum}^{max}$ , we summarize in Table 3.13 and 3.14 the number of the channels, which contribute to the partial wave decomposition, for five kinds of Jacobi coordinates. The dimension of the linear equation is driven by the sum  $\Sigma$ . The number strongly depends on  $l_{sum}^{max}$  and is more than one order of magnitude higher than corresponding numbers for the three-body system.

Before we investigate the stability of our calculation with respect to the partial wave truncation, we fix our momentum grid.

$np_{12}^a$	$np_{12}^b$	$\eta$
28	8	1.00167
32	8	1.00164
36	8	1.00166
32	4	1.00142
32	8	1.00164
32	12	1.00161

Table 3.15: Stability of the eigenvalue  $\eta$  of the Yakubovsky kernel with respect to the number of grid points in  $p_{12}$ . The calculations have been done using  $l_{sum}^{max} = 2$  and  $np_t^a = np_{34}^a = np_3^a = nq_4^a = nq^a = 32$ ,  $np_{34}^b = np_3^b = nq_4^b = nq^b = 4$ ,  $np_t^b = 20$ ,  $np_e^a = 36$ ,  $np_e^b = 10$  and  $nx = 16$

We start with similar grids as in the case of the hypertriton and choose

$$p_{12}^a = p_{34}^a = p_t^a = p_3^a = q_4^a = q^a = 1.0 \text{ fm}^{-1} \quad (3.19)$$

and

$$p_{12}^b = p_{34}^b = p_t^b = p_3^b = q_4^b = q^b = 4.0 \text{ fm}^{-1} \quad (3.20)$$

The last boundary depends on the kind of momentum. We will start with  $p_{12}^c = 15.0 \text{ fm}^{-1}$ ,  $p_{34}^c = 12.0 \text{ fm}^{-1}$ ,  $p_t^c = 30.0 \text{ fm}^{-1}$ ,  $p_3^c = 10.0 \text{ fm}^{-1}$ ,  $q_4^c = 8.0 \text{ fm}^{-1}$  and  $q^c = 8.0 \text{ fm}^{-1}$ .

As in the case of the hypertriton we calculate the eigenvalue of a Yakubovsky kernel for a realistic trial energy  $E = -7.300 \text{ MeV}$  using the Bonn B NN [11] and Jülich  $\tilde{A}$  YN [52] interactions. We truncate the partial wave decomposition using  $l_{sum}^{max} = 2$  and investigate the stability with respect to the number of grid points in Tables 3.15-3.22 for the  $0^+$  state of  ${}^4_\Lambda\text{He}$ . From the tables we read off that a number of grid points of

$$\begin{array}{ll}
np_{12}^a = 32 & np_{12}^b = 8 \\
np_t^a = 32 & np_t^b = 20 \\
np_{34}^a = 32 & np_{34}^b = 4 \\
np_3^a = 32 & np_3^b = 4 \\
nq_4^a = 32 & nq_4^b = 4 \\
nq^a = 32 & nq^b = 4 \\
np_e^a = 36 & np_e^b = 10 \\
nx = 16 &
\end{array}$$

leads to eigenvalues, which are converged within  $\Delta\eta = 0.0003$ . We will use these grids in the following.

The convergence with respect to the cut-offs of the momentum grids is checked in Table 3.23. We find that the values previously chosen are sufficiently high.

Now we can turn to an energy search with the same truncation of the partial wave decomposition. In Table 3.24 one sees the dependence of the eigenvalue  $\eta$  on the trial energy  $E_B$ . In our preliminary partial wave truncation, we find a binding energy of  $E = 7.335 \text{ MeV}$ . From the table we estimate the gradient  $\left| \frac{dE}{d\eta} \right| \approx 21.3 \text{ MeV}$  and conclude an error of the binding energy  $\Delta E = \left| \frac{dE}{d\eta} \right| \cdot \Delta\eta = 21.3 \cdot 0.0003 = 6.4 \text{ keV}$  due to the discretization. This error is below the experimental error in the binding energy. Therefore we are very satisfied with this accuracy.

$np_{34}^a$	$np_{34}^b$	$\eta$
28	4	1.00164
32	4	1.00164
36	4	1.00167
32	4	1.00164
32	8	1.00164
32	12	1.00165

Table 3.16: Stability of the eigenvalue  $\eta$  of the Yakubovsky kernel with respect to the number of grid points in  $p_{34}$ . The calculations have been done using  $l_{sum}^{max} = 2$  and  $np_{12}^a = np_t^a = np_3^a = nq_4^a = nq^a = 32$ ,  $np_3^b = nq_4^b = nq^b = 4$ ,  $np_{12}^b = 8$ ,  $np_t^b = 20$ ,  $np_e^a = 36$ ,  $np_e^b = 10$  and  $nx = 16$

$np_3^a$	$np_3^b$	$\eta$
28	4	1.00174
32	4	1.00164
36	4	1.00162
32	4	1.00164
32	8	1.00159
32	12	1.00159

Table 3.17: Stability of the eigenvalue  $\eta$  of the Yakubovsky kernel with respect to the number of grid points in  $p_3$ . The calculations have been done using  $l_{sum}^{max} = 2$  and  $np_{12}^a = np_t^a = np_{34}^a = nq_4^a = nq^a = 32$ ,  $np_{34}^b = nq_4^b = nq^b = 4$ ,  $np_{12}^b = 8$ ,  $np_t^b = 20$ ,  $np_e^a = 36$ ,  $np_e^b = 10$  and  $nx = 16$

To complete the calculation we increase the number of partial waves and report on the convergence of the binding energies  $E({}_\Lambda^4\text{He})$  and  $E({}^3\text{He})$  for  ${}_\Lambda^4\text{He}$  and its core nucleus  ${}^3\text{He}$  with respect to the full break-up threshold. We also show their difference, the  $\Lambda$  separation energy  $E_{sep}^\Lambda = E({}^3\text{He}) - E({}_\Lambda^4\text{He})$ . For  ${}^3\text{He}$  we restricted the grids and partial waves in the same way as for  ${}_\Lambda^4\text{He}$  ( $l_{sum}^{max}$  restricts the sum of  $l_{ij}$  and  $l_k$ ). We hope that the difference converges faster, because it might be less sensitive to numerical errors of the core state. The results in Table 3.25 show that this is the case.

Because of our computational restrictions, we cannot increase the number of partial waves for the four-body system further. Unfortunately the change of the binding energy is nearly equal in the last two steps. Therefore we cannot estimate the accuracy of the four-body calculation directly. But we would like to point out that the  ${}^3\text{He}$  binding energies behaves similar. Its calculation is converged with  $l_{sum}^{max} = 8$ . Therefore we expect that the four-body calculation is also converged with  $l_{sum}^{max} = 8$ .

The physical observable is the  $\Lambda$  separation energy. As you can see in the table, its convergence is more obvious than that of the individual binding energies. We estimate an error of about 10 keV here. Together with the discretization error we find

$$\Delta E_{sep}^\Lambda = \sqrt{6.4^2 + 10^2} \text{ keV} \approx 12 \text{ keV} \quad (3.21)$$

Again the error is smaller than the error of the experimental data. We are very satisfied with this accuracy. Later on we will see that the predictions of the force models differ by more than this 12 keV. Therefore the accuracy is high enough to draw conclusion on the underlying model Hamiltonians.

$nq_4^a$	$nq_4^b$	$\eta$
28	4	1.00165
32	4	1.00164
36	4	1.00163
32	4	1.00164
32	8	1.00164
32	12	1.00163

Table 3.18: Stability of the eigenvalue  $\eta$  of the Yakubovsky kernel with respect to the number of grid points in  $q_4$ . The calculations have been done using  $l_{sum}^{max} = 2$  and  $np_{12}^a = np_t^a = np_{34}^a = np_3^a = nq^a = 32$ ,  $np_{34}^b = np_3^b = nq^b = 4$ ,  $np_{12}^b = 8$ ,  $np_t^b = 20$ ,  $np_e^a = 36$ ,  $np_e^b = 10$  and  $nx = 16$

$nq^a$	$nq^b$	$\eta$
28	4	1.00164
32	4	1.00164
36	4	1.00163
32	4	1.00164
32	8	1.00164
32	12	1.00164

Table 3.19: Stability of the eigenvalue  $\eta$  of the Yakubovsky kernel with respect to the number of grid points in  $q$ . The calculations have been done using  $l_{sum}^{max} = 2$  and  $np_{12}^a = np_t^a = np_{34}^a = np_3^a = nq_4^a = 32$ ,  $np_{34}^b = np_3^b = nq_4^b = 4$ ,  $np_{12}^b = 8$ ,  $np_t^b = 20$ ,  $np_e^a = 36$ ,  $np_e^b = 10$  and  $nx = 16$

This closes the investigation of the numerical stability of the binding energies. The rest of this subsection is devoted to the investigation of the accuracy of the wave function.

It turned out that especially for the hypernuclear four-body system an accurate calculation of the wave function requires a careful choice of the sequence of the numerical coordinate transformations. In Table 3.12 we saw already that the accuracy of the partial wave expansion crucially depends on the choice of the Jacobi coordinates. Jacobi momenta based on a YN subsystem seem to fail to describe a loosely bound hypernuclear state. We will see later that this is still true for the four-body bound states. This problem has to be taken very seriously now, because our whole algorithm relies on coordinate transformations, which conserve one of the momenta. This implies that many transformations must be divided in several steps. That introduces intermediate states, which themselves are expanded in partial waves. An accurate calculation of the wave function requires a minimum of intermediate states. Additionally we should avoid transformations that moves the hyperon from the two-body subsystem to one of the outer particles and vice versa as far as possible. In this way we are able propose an “optimal” way of the calculation. However, it requires a very high number of transformations. This algorithm is outlined in Appendix D.1. One gains a representation of the wave function for each of the five kinds of Jacobi coordinates independently. Later on we will also learn about a practical short-cut with a reasonable numerical error and a small requirement of CPU-time.

Our truncation of the partial wave decomposition introduces numerical errors in the YC’s and intermediate states. These errors also influence the lower partial waves of the wave function. This is different to the three-body system, where we could obtain exact lower partial waves of the wave function, if we



$np_t^a$	$np_t^b$	$\eta$
28	20	1.00137
32	20	1.00164
36	20	1.00161
32	16	1.00164
32	20	1.00164
32	24	1.00164

Table 3.20: Stability of the eigenvalue  $\eta$  of the Yakubovsky kernel with respect to the number of grid points in  $p_t$ . The calculations have been done using  $l_{sum}^{max} = 2$  and  $np_{12}^a = np_{34}^a = np_3^a = nq_4^a = nq^a = 32$ ,  $np_{34}^b = np_3^b = nq_4^b = nq^b = 4$ ,  $np_{12}^b = 8$ ,  $np_e^a = 36$ ,  $np_e^b = 10$  and  $nx = 16$

$np_e^a$	$np_e^b$	$\eta$
28	20	1.00166
32	20	1.00164
36	20	1.00164
32	16	1.00164
32	20	1.00164
32	24	1.00164

Table 3.21: Stability of the eigenvalue  $\eta$  of the Yakubovsky kernel with respect to the number of grid points in  $p_e$ . The calculations have been done using  $l_{sum}^{max} = 2$  and  $np_{12}^a = np_t^a = np_{34}^a = np_3^a = nq_4^a = nq^a = 32$ ,  $np_{34}^b = np_3^b = nq_4^b = nq^b = 4$ ,  $np_{12}^b = 8$ ,  $np_t^b = 20$  and  $nx = 16$

assume a finite number of partial waves for the Faddeev component.

We start with a study of the accuracy of the wave function, which we calculated according to Appendix D.1. We use again the Bonn B NN and Jülich  $\tilde{A}$  YN interactions. For the solution of the YE's, we truncated the partial waves with  $l_{sum}^{max} = 8$ . Therefore the YC's are restricted to these partial waves. Nevertheless, we increase the number of partial waves for the calculation of the wave function. Because we take more partial waves for the intermediate states into account, also the accuracy of the lower partial waves of the wave function should increase in this case.

From Eq. (2.40) one can establish again a simple relation for the expectation value of symmetric operators  $O$  (like the norm and the kinetic energy)

$$\langle \Psi | O | \Psi \rangle = 3 \langle \psi_{1A} | O | \Psi \rangle + 3 \langle \psi_{1B} | O | \Psi \rangle + 6 \langle \psi_{1C} | O | \Psi \rangle + 3 \langle \psi_{2A} | O | \Psi \rangle + 3 \langle \psi_{2B} | O | \Psi \rangle \quad (3.22)$$

To get a feeling of the accuracy of the wave function in different representations, we define again a norm ratio

$$R_N = \frac{\langle \Psi | \Psi \rangle}{3 \langle \psi_{1A} | \Psi \rangle + 3 \langle \psi_{1B} | \Psi \rangle + 6 \langle \psi_{1C} | \Psi \rangle + 3 \langle \psi_{2A} | \Psi \rangle + 3 \langle \psi_{2B} | \Psi \rangle} \quad (3.23)$$

Theoretically the denominator and the nominator should be equal. In practice  $R_N$  deviates from one. The size of the deviation is a measure of the quality of the partial wave decomposition. In Table 3.26 we display the results for  $R_N$  for different representations of our wave function. We learn that the 1A

$nx$	$\eta$
12	1.00167
16	1.00164
20	1.00163
24	1.00162

Table 3.22: Stability of the eigenvalue  $\eta$  of the Yakubovsky kernel with respect to the number of grid points in  $x$ . The calculations have been done using  $l_{sum}^{max} = 2$  and  $np_{12}^a = np_t^a = np_{34}^a = np_3^a = nq_4^a = nq^a = 32$ ,  $np_{34}^b = np_3^b = nq_4^b = nq^b = 4$ ,  $np_{12}^b = 8$ ,  $np_t^b = 20$ ,  $np_e^a = 36$  and  $np_e^b = 10$

$p_{12}^c$	$p_t^c$	$p_{34}^c$	$p_3^c$	$q_4^c$	$q^c$	$\eta$
15.0	30.0	12.0	10.0	8.0	8.0	1.00158
12.0	30.0	12.0	10.0	8.0	8.0	1.00158
15.0	25.0	12.0	10.0	8.0	8.0	1.00155
15.0	30.0	10.0	10.0	8.0	8.0	1.00158
15.0	30.0	12.0	8.0	8.0	8.0	1.00160
15.0	30.0	12.0	10.0	7.0	8.0	1.00157
15.0	30.0	12.0	10.0	8.0	7.0	1.00158

Table 3.23: Dependence of the eigenvalue on the last interval boundary. The calculations have been performed with a slightly increased the number of mesh points in  $p_3$  and  $p_{12}$ . We used  $l_{sum}^{max} = 2$  and  $np_{12}^a = np_t^a = np_{34}^a = np_3^a = nq_4^a = nq^a = 32$ ,  $np_{34}^b = nq_4^b = nq^b = 4$ ,  $np_{12}^b = 12$ ,  $np_3^b = 8$ ,  $np_t^b = 20$ ,  $np_e^a = 36$ ,  $np_e^b = 10$  and  $nx = 16$ . The boundaries are given in  $\text{fm}^{-1}$ .

$E_B$ [MeV]	$\eta$
7.300	1.0016
7.348	0.9993
7.337	0.9999
7.335	1.0000

Table 3.24: Dependence of the eigenvalue  $\eta$  on the trial energy.

$l_{sum}^{max}$	$E(\Lambda\text{He})$	$E(^3\text{He})$	$E_{sep}^\Lambda$
2	-7.335	-6.908	0.427
4	-7.712	-7.232	0.480
6	-7.731	-7.240	0.491
8	-7.751	-7.256	0.495
10	—	-7.256	—

Table 3.25: Convergence of the binding energies  $E(\Lambda\text{He})$  and  $E(^3\text{He})$  with respect to increasing  $l_{sum}^{max}$ . The  $\Lambda$  separation energy  $E_{sep}^\Lambda$  is also given. All energies are given in MeV

$l_{sum}^{max}$	1A	1B	1C	2A	2B
8	0.9968	0.9831	0.9350	0.9648	0.9648
10	0.9984	0.9899	0.9502	0.9767	0.9767

Table 3.26: Norm ratio  $R_N$  for different representations of the  ${}^4_\Lambda\text{He}$  wave function.

representation seems to be optimal. For this representation we can achieve a converged  $R_N$  within 0.2 %. In contrast the 1C, 2A and 2B representations do not reproduce accurately the ideal value 1. There are still more partial waves necessary to obtain a converged wave function for these types of Jacobi coordinates. Unfortunately, we cannot use the 1A representation to calculate matrix elements of YN operators like the YN potential, because these calculations rely on coordinates which single out a YN subsystem. For such calculations the 1C, 2A or 2B representation is needed.

The wave functions used for Table 3.26 are calculated according to Appendix D.1. This means that each representation is directly derived from the YC's. This needs a lot of CPU time, therefore a further increase of the number of partial waves is not practical anymore. We decided to give up this direct calculation of all representations and have chosen the 1A and 2B representations as most suitable. For these calculations we can increase the number of partial waves further. Nevertheless we would like to make use of Eq. (3.22) for the calculation of the kinetic energy and other symmetric operators. Therefore we create the other representations of the wave function using the results given in 1A and 2B coordinates. It is natural to interchange the two subsystems to find the 2A representation from the 2B wave function. The necessary transformation can be done in one step and has been introduced in Chapter 2. Similarly, we get the 1B wave function from the 1A representation. However, the situation is less clear in the case of 1C coordinates. It turns out that the accuracy of wave functions in 1C coordinates strongly depends on the way, in which one calculates them. To illustrate this problem and to justify our choice, we give in Table 3.27 the expectation value of the YN potential in three ways.

- A) We calculate all representations of the wave function directly as explained in Appendix D.1. The results for the 1C and 2B representations agree very well. This is a good check of the consistency of our transformation codes. This is surely the most accurate way, but it is very CPU-time consuming.
- B) We calculate only the 1A and 2B representations directly from the YC's. The wave functions in 1B(2A) coordinates are obtained using the result in 1A(2B) coordinates. The 1C representation is obtained in a second step from the 1B result. There is no good agreement. The accuracy of the 1C wave function is very low.
- C) Because we are not satisfied with this accuracy, we decided to choose the 2B representation as starting point. In this way we can obtain a very high accuracy even for the 1C wave function. The agreement we found for  $l_{sum}^{max} = 10$  is not accidental. We will show later, that this result is almost converged. In this manner we are able to increase the number of partial waves keeping the accuracy of the wave function.

With C) we found an optimal algorithm to find an accurate wave function in all representations. We can increase the number of partial waves further and investigate the convergence of the five different wave functions.

This shall be done now. In Table 3.28 the convergence of the norm ratio  $R_N$  is exemplified. We can confirm Eq. (3.22) for the norm to at least 2 %. From the hypertriton we learned that this error might

way	1C	2B
A	-13.5	-13.6
B	-11.0	-13.6
C	-13.5	-13.6

Table 3.27: Expectation value of the YN potential energy calculated in 1C and 2B coordinates. The wave functions are calculated in the ways A,B and C as explained in the text. The YC's (wave functions) are restricted to partial waves with  $l_{sum}^{max} = 8$  ( $l_{sum}^{max} = 10$ ). The results are based on the Bonn B and Jülich  $\tilde{A}$  interactions. All energies are in MeV.

$l_{sum}^{max}$	1A	1B	1C	2A	2B
8	0.9958	0.9810	0.9520	0.9638	0.9638
10	0.9974	0.9882	0.9682	0.9757	0.9757
12	0.9987	0.9924	0.9777	0.9824	0.9824
14	0.9991	0.9949	0.9817	0.9840	0.9840

Table 3.28: Norm ratio  $R_N$  for different representations of the  ${}^4_{\Lambda}\text{He}$  wave function. In contrast to Table 3.26 the wave functions are not calculated independently. There are also small changes for the 1A and 2B representation, because all representations contribute to the denominator of the norm ratio.

result from missing higher partial waves. However, this is not clear here.

Therefore we investigate the convergence of the potential energy and the kinetic energy with respect to the number of partial waves used for the wave function in Table 3.29. To the kinetic energy only partial waves with  $l_{sum}^{max} = 8$  contribute, because we used Eq. (3.22) to evaluate the symmetric kinetic energy. This means that the lower partial waves are almost converged in all cases in Table 3.29 and that the number of partial waves for the intermediate states is sufficiently high. The potential energies show the same convergence behavior. All numbers are converged within 4 digits. Additionally we calculated the expectation value of the Hamiltonian. For the considered wave function, we obtained a binding energy of  $E = -7.751$  MeV from the solution of the YE's. The expectation value of  $H$  agrees to that result within 0.8 % of the binding energy and within 0.1 % of the kinetic energy. Again the calculations turned out to be consistent.

We already emphasized a few times that the YE's introduce in a natural manner all different kinds of Jacobi coordinates. We mentioned that in the case of a bound state calculation, one could in principle solve directly the simpler Schrödinger equation choosing one of the coordinates. In Table 3.30 we exemplify that the YC's converge much faster than the wave function. Especially the high momentum components, which contribute quite a lot to the kinetic energy, converge very slowly. While one obtains a converged kinetic energy using the "mixed" matrix elements of Eq. (3.22), it is not converged even in the 1A representation. Therefore a direct solution of the Schrödinger equation in a partial representation seems to be not feasible. The potential energy in the 1A representation is converged as can be seen from Table 3.29. But one finds a sizable disagreement to the NN potential calculated in the other coordinates which is in line with the differences of the norms given in Table 3.28. The agreement of the YN potential expectation values is perfect. In Table 3.28 we find considerable differences to Eq. (3.22) also for the 1C and 2B representations. Therefore we consider the perfect agreement as an accident.

This concludes the investigation of our numerical stability. In the next chapter we use the established

$l_{sum}^{max}$	$T$	$V_{NN}$	$V_{YN}$	$H$
8	49.75	-43.84	-13.57	-7.663
10	49.76	-43.86	-13.58	-7.679
12	49.77	-43.87	-13.59	-7.684
14	49.77	-43.87	-13.59	-7.687

Table 3.29: Expectation values of the kinetic energy  $T$ , the YN potential  $V_{YN}$ , the NN potential  $V_{NN}$  and the Hamilton operator  $H$ . The YC's were obtained using the Bonn B and Jülich  $\tilde{A}$  interactions. The YE's were solved for  $l_{sum}^{max} = 8$ . The wave functions were normalized using Eq. (3.22). The NN(YN) interaction was evaluated in the 1A(2B) representation. The kinetic energy is also based on Eq. (3.22). The energies are given in MeV.

operator	1A	1B	1C	2A	2B	“mixed”
$T$	49.10	47.52	44.80	45.49	45.51	49.77
$V_{NN}$	-43.87	-43.75	—	-43.38	—	—
$V_{YN}$	—	—	-13.59	—	-13.59	—

Table 3.30: Expectation values of the kinetic energy  $T$ , the YN potential  $V_{YN}$  and the NN potential  $V_{NN}$ . If possible, results are given for all representations of the wave function and in the case of  $T$  compared to the “mixed” result based on Eq. (3.22). The energies are given in MeV.

methods to get some insights into nuclear and hypernuclear bound states with  $A \leq 4$ . We need no uncontrolled approximations to solve the YE's. Because we are not restricted to local or simplified potentials, our method is suitable to investigate the underlying models of the strong interaction.

## Chapter 4

# 3N and 4N Systems

In this chapter we apply the techniques developed in Chapters 2-3 to the 3N and 4N systems.

In recent years several realistic NN force models have been developed. In Section 4.1 we give a brief overview of those NN interactions, which we use in this thesis. Then we start with a study of the 3N bound state and figure out the dependence of the  ${}^3\text{H}$  and  ${}^3\text{He}$  binding energies on those interactions in Section 4.2. We confirm that all models underpredict the 3N binding energies.

There are two dynamical ingredients, which are missing: relativity and 3NF's. We comment on possible relativistic effects in the 3N bound state. Because of the complexity of relativistic Hamiltonians and insufficiently solved conceptual problems, we are forced to neglect these effects in the present study. Instead of introducing relativity, we concentrate on 3NF's.

Therefore we add the Tucson-Melbourne 3NF to our NN interactions and motivate a phenomenological adjustment of these force combinations to the experimental  ${}^3\text{H}$  binding energy. This culminates in a set of 3N model Hamiltonians, which predict by definition the experimental  ${}^3\text{H}$  binding energy. Additionally we study the 3N model Hamiltonian proposed by the Argonne-Urbana-Los Alamos collaboration: the AV18 NN interaction in conjunction with the Urbana IX 3NF model.

In Section 4.3 we illustrate some simple 3N wave function properties. We present nucleon momentum distributions and NN correlations. It is interesting to figure out the dependence of these properties on the NN and 3N interactions.

We conclude the investigations of the 3N system with a look to the CSB of the  ${}^3\text{H}$  and  ${}^3\text{He}$  nuclei in Section 4.4. The most sophisticated NN force models distinguish the pp and nn interaction. The AV18 force is supplied with an electromagnetic interaction, which goes beyond the static Coulomb force between protons. We would like to study the contribution of these individual parts of the interaction to the CSB in the 3N system.

After that, in Section 4.5, we turn to the  $\alpha$ -particle. We present our fully converged binding energy predictions. Again the binding energy is underpredicted by all present day NN interaction models. Our results confirm the strong correlation between the 3N and 4N binding energies.

This leads to a study of the  $\alpha$ -particle binding energy predictions of our model Hamiltonians, which predict by definition the experimental 3N binding energies. Our binding energy results are only slightly dependent on the Hamiltonian. They are close to the experimental value. This can be considered as an indication for at most a small contribution of 4N forces to the binding energy of the  $\alpha$ -particle. This is an important new insight.

We obtain accurate wave functions and investigate some of their properties with respect to their

Potential	$E$	$T$	$P_D$
AV18	-2.225	19.81	5.760 %
Nijm 93	-2.224	19.30	5.755 %
Nijm I	-2.225	17.61	5.678 %
Nijm II	-2.225	20.25	5.652 %
CD-Bonn	-2.223	15.48	4.833 %
CD-Bonn 2000	-2.223	15.60	4.854 %
Bonn B	-2.225	15.65	4.987 %
Exp.	-2.225	—	—

Table 4.1: Deuteron binding energy predictions  $E$  of several NN interaction models. We also display the expectation values of the kinetic energy  $T$  and the D-state probabilities  $P_D$ . The energies are given in MeV.

dependence on the force model. We also reveal similarities and differences of the wave functions of the four lightest nuclei:  $^2\text{H}$ ,  $^3\text{H}$ ,  $^3\text{He}$  and  $^4\text{He}$ . The results of this study are presented in Section 4.6. Especially, we are interested in the dependence of the 3N and 4N wave functions on the 3NF.

## 4.1 Introduction to the used NN interaction models

Unfortunately, the strong NN interaction cannot be derived from QCD yet. To get some insights into nuclear dynamics, many phenomenological and meson theoretical parameterizations of the NN interaction have been developed. In the following we summarize some aspects of the NN interaction models used in this thesis.

The most prominent interaction models nowadays are the Argonne model AV18 [9], the three Nijmegen models Nijm 93, Nijm I and Nijm II [10] and the CD-Bonn interaction [12] which is a refined Bonn B model [11]. All these models reach a very accurate description of the deuteron and the pp and np scattering data up to about 350 MeV nucleon lab energy. For completeness we summarize the deuteron binding energy predictions of the different NN interactions in Table 4.1. One can see that the calculations for all models result (by construction) in the experimental deuteron binding energy. Additionally, we give the model predictions for the unobservable kinetic energies  $T$  and D-state probabilities  $P_D$ . From the range of results one sees that the interaction models are quite different.

Because we will study the CIB and CSB of the strong interaction in the 3N system later on, we display in Table 4.2 the  $^1\text{S}_0$  scattering lengths predicted by the different interaction models and compare them to the data. The scattering lengths refer to the strong part of the interaction. The experimental  $pp$  scattering length is Coulomb corrected to allow for a meaningful comparison. These scattering lengths are the most prominent experimental verification of CSB and CIB of the strong interaction in the two-nucleon system. The measurement of the nn scattering length is very complicated, because neutron targets are not available. nn scattering can only be studied in final state interactions (FSI) [1, 2, 3, 4, 5, 6, 7, 8]. This leads to a quite large error bar in the datum. Moreover also the strong pp scattering lengths cannot be determined accurately, because the Coulomb correction introduces a model dependence. Please note in this context the different predictions of the AV18 model to all other realistic interactions for the np and pp scattering lengths. The full AV18 interaction includes an electromagnetic force. In conjunction with this electromagnetic force the AV18 model describes the scattering data with the same quality as

the other models. The differences in the np and pp scattering length predictions of AV18 to the other models exemplify that the “strong part” of the interaction is not uniquely defined.

The AV18 interaction has been developed by the Argonne collaboration. It is based on a purely phenomenological ansatz supplemented with a pion tail motivated by the one-boson-exchange (OBE) model. Its functional form guarantees complete locality of the interaction. Locality is crucial for many few-body techniques in configuration space. Therefore this model has been widely used for few-nucleon calculations in the past. There are roughly 40 parameters needed, which are fitted to the deuteron, the np and pp scattering data and, additionally, to the nn scattering length. This results in a np, pp and nn interaction. Its built-in electromagnetic interaction, which goes beyond the static Coulomb force of two protons, is the special feature of this model. We again look into its electromagnetic part in Section 4.4, where we study the CSB in more detail.

The family of Nijmegen interactions is based on the OBE model. It is also fitted to the deuteron and the np and pp scattering data. So far no nn interaction has been developed by the Nijmegen group, which is able to predict the difference of the nn and pp scattering lengths (see Table 4.2). The Nijm 93 potential keeps most of the meson theoretical structure. The potential is mildly nonlocal. There are only 15 free parameters, which can be adjusted to the NN database. The resulting description of the NN data is quite good, but not perfect. Therefore the Nijmegen group invented two additional models: Nijm I and Nijm II. They are based on a slight adjustment of the parameter set separately for each partial wave. In Nijm II the nonlocal part of the interaction is also omitted and the parameters are refitted. In both models the number of parameters is comparable to the number of parameters in the Nijmegen phase shift analysis (40-50 parameters) [86]. Both interactions reach a very accurate description of the np and pp database. The nn scattering length is not considered in the fit. Therefore the nn interaction does not predict the experimental nn scattering length (see Table 4.2).

The last modern NN potential family has been developed from the Bonn B interaction [11], which is also based on the OBE. In Ref. [12] a new charge-dependent fit to the NN database led to the CD-Bonn interaction. Because also the Bonn B model doesn’t provide enough freedom to find a highly accurate description of the NN data, the parameters have been slightly adjusted separately for each partial wave. Also this model can describe the NN data very accurately. It is highly nonlocal, because the full Dirac structure of the OBE is kept. Recently the model has been updated to the CD-Bonn 2000 potential [87]. In Ref. [88] the full Bonn potential model, which includes also the multi meson exchanges, has been used to estimate the CSB in the NN phaseshifts. Using these results realistic nn phaseshifts have theoretically been predicted. The nn force of CD-Bonn 2000 model has been fitted to those phaseshifts. Therefore this model might give a realistic description of the nn interaction. Later on we will investigate, whether the effects on the  ${}^3\text{H}$ - ${}^3\text{He}$  binding energy difference visibly differ for this nn interaction and the old ones.

In the next section we report on our 3N binding energy results using these NN interactions and introduce 3NF’s, which complete our 3N Hamiltonians.

## 4.2 ${}^3\text{H}$ and ${}^3\text{He}$ binding energies and 3NF’s

Realistic calculations of the 3N bound state can be performed since several years [29, 18, 30, 31, 19, 32]. However, many techniques are restricted to local potentials or separable approximations to the NN interactions and are not flexible enough to investigate the dependence of the bound state properties on the interaction model.

For this reason we started with an investigation of the  ${}^3\text{H}$  binding energy in Ref. [19]. Since that time we have improved our algorithms to include completely the isospin breaking parts in the strong



Potential	pp	np	nn
AV18	-17.16	-23.08	-18.82
CD-Bonn	-17.47	-23.74	-18.80
CD-Bonn 2000	-17.46	-23.74	-18.97
Nijm I	-17.50	-23.74	-17.54
Nijm II	-17.40	-23.75	-17.42
Nijm 93	-17.56	-23.75	-17.51
Exp.	-17.3±0.4	-23.75±0.01	-18.8 ±0.3

Table 4.2:  $^1S_0$  scattering lengths for several interaction models compared to the experimental values [8]. For the pp force only the strong part of the interaction has been taken into account. The experimental pp scattering length is Coulomb corrected. All scattering lengths are given in fm.

interaction, the proton-neutron mass difference and also the Coulomb interaction.

These calculations require a Fourier transformed Coulomb potential, which is known to be singular. This singularity is very uncomfortable in practical calculations. It arises because of the long range part of the interaction. But the nuclear bound state wave functions very rapidly drop and do not feel this long range part. Therefore we truncate the Coulomb force for pp distances  $r > r_{max} \approx 15$  fm. The resulting Fourier transformed potential is non-singular and can easily be implemented in our Faddeev scheme. We carefully checked the numerical stability and found fully converged bound state results with respect to the cut-off value  $r_{max}$ . Please note that the truncated Fourier transform itself is not converged with respect to  $r_{max}$ . It is only equivalent to the complete Coulomb interaction in bound state calculations. In this way we are able to introduce also long range interactions into our scheme.

In Table 4.3 we summarize our 3N binding energy results for the modern NN interactions and compare them to the experimental binding energies. The energies are given relative to the 3N break-up threshold. We present results for the phase-equivalent interactions CD-Bonn, AV18 and Nijm I and II. The Bonn B and Nijm 93 potentials do not describe the NN scattering data with the same accuracy as the other potentials. We only included them, because we will study the hypernuclear systems using those interactions in Chapter 5. The theoretical results are accurate within 2 keV. The calculations are fully charge dependent and take the total isospin  $T = \frac{1}{2}$  and  $T = \frac{3}{2}$  components into account. We also distinguish the neutron and proton masses. For all calculations we use partial waves up to  $j_{12} = 6$ . As expected all potentials underpredict both 3N binding energies. However, there are remarkably different results, which underline the differences of the NN force models. The smallest binding energies are predicted by the local potentials AV18 and Nijm II. The non-local interactions CD-Bonn and Nijm I lead to somewhat bigger binding energies.

For completeness, we also give the kinetic energies and the differences of the  $^3\text{H}$  and  $^3\text{He}$  binding energy. The CSB splitting between both nuclei is small compared to the kinetic energy. One expects that the effect of the different pp and nn force can perturbatively be calculated. We will see in Section 4.4 that this is indeed possible to a large extent. Comparing the kinetic energies of the mirror nuclei, one finds sizable differences of the wave function due to the Coulomb repulsion. This repulsion decreases the magnitude of the binding energy of  $^3\text{He}$  by roughly 600-700 keV. The  $^3\text{He}$  nucleus becomes less dense than the  $^3\text{H}$  nucleus. This reduces its kinetic energy visibly. The kinetic energy is a first property of the wave function, which in parts is correlated to the predicted binding energy. For the kinetic energy the correlation is not strict, as one sees comparing the results for  $^3\text{H}$  for AV18 and CD-Bonn, where the

	${}^3\text{H}$		${}^3\text{He}$		$\Delta E_B$
	$E_B$	$T$	$E_B$	$T$	
CD-Bonn 2000	-8.005	37.64	-7.274	36.81	0.731
CD-Bonn	-8.013	37.43	-7.288	36.62	0.725
AV18	-7.628	46.76	-6.917	45.69	0.711
Nijm I	-7.741	40.74	-7.083	40.01	0.658
Nijm II	-7.659	47.55	-7.008	46.67	0.651
Bonn B	-7.915	38.13	-7.256	37.43	0.659
Nijm 93	-7.668	45.65	-7.014	44.79	0.654
Exp.	-8.482	—	-7.718	—	0.764

Table 4.3: 3N binding energies  $E_B$  for different NN interactions compared to the experimental values. Results are shown for  ${}^3\text{H}$ ,  ${}^3\text{He}$  and their binding energy difference  $\Delta E_B$ . Additionally, we show the kinetic energies  $T$ . All results are given in MeV

kinetic energies are driven by the NN force. We will find other properties of the wave functions and also 3N scattering observables, which are strictly correlated.

In the following we would like to pin down the dependence of wave function properties on the NN interaction model. We can expect that parts of the differences are only the consequence of different binding energy predictions. Those differences are correlated to the binding energy and do not give independent information on the quality or properties of the underlying interaction model. For a meaningful comparison to experimental results the models should correctly predict the experimental binding energy. Before we phenomenologically develop Hamilton operators, which fulfill this requirement, we would like to see the possible origins of the missing binding energy.

So far we neglected two dynamical ingredients in our calculations: relativistic effects and 3NF's. Both are not fully understood at present. Whereas we are going to investigate 3NF's in the following, we do not want to include relativity. Nevertheless, we would like to summarize the status of relativistic quantum mechanics to get a feeling of the size of the inaccuracies in our non-relativistic approach.

There are in general two ideas to include relativity into the dynamical equations. Most work is based on the Bethe-Salpeter equation. The solution of the Bethe-Salpeter equation is technically very complicated. A direct solution has only be obtained using a separable approximation to the underlying interaction and neglecting the Dirac spin structure of the nucleons [89]. The authors predict an attractive relativistic effect of about 300 keV. In Ref. [90] the three dimensional approximation of the Bethe-Salpeter equation proposed by Blankenbecler and Sugar has be used. The interaction model (Bonn B) is also based on this ansatz. The work predicts a gain of binding energy due to relativity by 200 keV. A different approach to the field theoretical model underlying the Bethe-Salpeter equation has been proposed by Gross: the spectator or Gross equation. In Ref. [91, 92] this formulation has been worked out and applied to a meson exchange model. They found that their meson exchange model can predict the experimental binding energy, though the quality of the description of the NN data is not comparable to that of the "realistic" models. However, they showed that relativistic dynamics also include interaction terms, which do not influence the 2N system but have a big impact on the 3N system. These are off-mass-shell parts of the strong meson-nucleon form factors. They are linked to 3NF's. In this view 3NF's and relativistic effects are related to each other.

The second approach to include relativity is based on the Poincaré algebra of a relativistic quantum

mechanical system. There are several forms to build up relativistic dynamical operators [93]. The instant form is the closest to the well known Schrödinger equation. Momentum and angular momentum operators are not interaction dependent. The generators of Lorentz transformations to moving systems, called boost operators, and the Hamiltonian depend on the interactions. The dynamical modifications of the NN interaction are in general called boost corrections. They depend on the total momentum of the NN subsystem. In Ref. [94] this framework has been investigated for a simple three-boson system. In contrast to the estimates based on the Bethe-Salpeter equation, the authors found repulsive corrections of 200 keV. But they also revealed that this effect is the sum of an attractive contribution of 1 MeV from the kinetic energy and a repulsive contribution of 1.2 MeV from the potential. Therefore the result might depend on the interaction model. A study of realistic spin dependent interactions has been undertaken in Ref. [95]. The authors also found a repulsive contribution of 300 keV. Because of the technical restrictions in that work, the boost corrections have only been included in a  $p/m$  expansion. The reliability of this expansion has still to be investigated. However, their results indicate only a small change of the wave function properties due to relativistic effects.

This closes the small survey on relativistic approaches to few-body quantum mechanics. The problem is not solved yet, the contribution of relativistic effects to the binding energy seems to be of the order of 200 keV. Therefore it is not negligible, but even the sign of this contribution has not clearly been established yet. Though a solution is highly desirable, it is far beyond the scope of this work. Unfortunately, we have to neglect this interesting dynamical ingredient in our present investigation. For our further investigations it is important that the wave functions seem to be only slightly affected by relativity. This justifies the usage of non-relativistic wave functions in the following studies.

Now we would like to concentrate on the second missing dynamical ingredient. These are 3NF's.

The Argonne-Urbana collaboration developed a purely phenomenological model with an attractive part inspired by the  $\pi$ - $\pi$  exchange 3NF and enriched with a simple short range repulsive part [96]. The model has been adjusted in conjunction with the AV18 model to predict the experimental triton binding energy and nuclear matter density [17]. In this manner the Argonne-Urbana collaboration established a model Hamiltonian, which predicts the correct 3N binding energy. It can be used to investigate properties of the 3N and more complex nuclear systems. The Argonne group has already applied their interaction model to bound states up to  $A = 8$  and could obtain a fairly good agreement of theoretical predictions and experimental binding energies as well as the low lying spectra [33].

However, so far only one such realistic model Hamiltonian has been developed. For many studies of few-nucleon systems it is important to pin down the model dependence of the theoretical predictions. Such investigations require a set of trial Hamiltonians.

Therefore we started to establish a series of realistic model Hamiltonians in Ref. [19], which predict at least the experimental 3N binding energies. These trial interactions should be as realistic as possible. To establish such a series of interactions, we start from the modern NN forces and augment them by 3NF's. Because we combine quite different NN interactions with several 3NF's, we obtain a series of 3N Hamiltonians, which cover a wide range of 3N models. All the models describe the NN system with very high accuracy. However, the 3NF's depend on parameters, which are not fixed by the underlying theory. The 3N binding energies are quite sensitive to those parameters. Therefore we adjust the strength of these 3NF's using the parameters and phenomenologically construct 3N Hamiltonians, which predict 3N binding energies more or less correctly. In this way, we obtain a series of realistic model Hamiltonians, which are very useful for further investigations.

To justify these phenomenological ansatz, we give a small overview on the current status of 3NF's.

In many physical problems it is economic to eliminate degrees of freedom, which are not the subject of the investigated process. In general one simulates their physical effects by interactions, which are ex-

pressed in terms of the degrees of freedom considered. In multi particle systems the elimination procedure naturally leads to three-body forces. For example, the movement of a satellite in the gravitational field of the moon and the earth is slightly affected by the tides of the seas. The problem can be successfully solved using a rigid earth and replacing its deformability due to the gravitational field of the moon by additional two-body and three-body interactions.

In the same manner 3NF's arise in nuclear physics. It is in general very economic to describe nuclei in terms of nucleons. This neglects for example resonance states of the nucleons and the mesons (we do not consider quark and gluonic degrees of freedom). These degrees of freedom are eliminated and their effects can be simulated by nuclear interactions. From the  $A = 2$  system one obtains the NN forces. Hamiltonians for systems with  $A > 2$  are based on the sum of those interactions over all NN pairs. The difference of this sum to the correct nuclear interaction is by definition a 3NF (or possibly higher order interaction).

In contrast to the gravitational example from above, the contribution of these higher order interactions cannot be estimated in advance, because the fundamental theory of the strong interaction of hadrons, the QCD, has not been solved yet. In the 3N system one assumes in general that the 3NF contributes the missing binding energy to the triton (roughly 10 % of the binding energy). At present it is not clear, whether higher order nuclear forces are negligible or whether they contribute visibly to the 4N and more complex systems. We will study this problem in Section 4.5.

To get some insights into the mechanisms leading to 3NF's, many investigations used meson-theoretical models to estimate the 3NF strength and its possible functional form [97, 98]. Very often one considers the process, where the pion, which is exchanged between two nucleons, is scattered on its way by the third nucleon. This naturally leads to a 3NF.

This mechanism is still the basis of the modern 3NF's and leads to the commonly used  $\pi$ - $\pi$  exchange 3NF's. It requires a continuation of the fairly well known  $\pi$ N scattering amplitude to off-the-mass-shell momenta. This continuation is model dependent. Based on this idea, the authors of Ref. [16] estimated the contribution of a 3NF to the  ${}^3\text{H}$  binding energy to 220 keV attraction.

Because the  $\Delta$  particle is a resonance of the  $\pi$ N system, a great part of this scattering process can also be understood in terms of an intermediate  $\Delta$  particle. However, explicitly considering the  $\Delta$  degrees of freedom in the wave function decreases the triton binding energy. Dispersive effects of the propagating intermediate  $\Delta$  particles repulsively contribute to the two-body interaction in the 3N system [99]. This is one example showing that the mechanisms of 3NF's have not been understood in all aspects.

Nevertheless, the work in Ref. [16] has been refined using the partially conserved axial vector current hypothesis (PCAC) and current algebra to constrain the off-shell  $\pi$ N scattering amplitude [24]. This led to the often used Tucson-Melbourne (TM) 3NF. Based on this interaction the contribution of 3NF's to the 3N binding energy has been investigated. One finds that

- a 3NF cannot be treated perturbatively and has to be considered in the dynamical equations [100, 101, 102] and
- the contribution strongly depends on a cut-off parameter  $\Lambda$ , which parameterizes the  $\pi$ NN vertex [18]. Therefore the TM model cannot be used to predict uniquely a theoretical triton binding energy.

Later on the TM model has been augmented by  $\pi$ - $\rho$  and  $\rho$ - $\rho$  exchange mechanisms [103]. The cut-off dependence could not be resolved [104]. Moreover it became clear that cut-offs, which lead to correct predictions for the triton binding energy, are inconsistent with similar cut-offs in the NN interaction models. A consistent description of NN and 3N forces is highly desirable. An attempt to find a consistent

model has been worked out in Ref. [105]. Unfortunately, this study has not been developed further and cannot compete in accuracy with the modern NN interactions. Maybe upcoming interaction models based on chiral perturbation theory can overcome the standstill in this field [15, 20].

Because of the unsolved conceptual problems, we think that our phenomenological approach is justified. We combine the different NN interactions with the TM 3NF. We use the cut-off parameter  $\Lambda$  to adjust the binding energy prediction to the experimental result separately for each combination of NN interaction and TM force. The corresponding adjustment is also made for a modified TM model, called TM' in the following, which has been proposed in Ref. [106, 107], because the operator form of the TM model is inconsistent with chiral perturbation theory. We also include this modified interaction in our studies, because the modification has some impact on the structure of our wave functions and on Nd scattering observables [108]. Additionally, we include the Urbana IX model proposed by the Argonne-Los Alamos collaboration into your studies. In this way, we obtain a wide range of interaction models, which describe the NN system with a very high accuracy and predict the experimental 3N binding energy by construction.

In Table 4.4 we display the most recent results of this procedure. Because of an implementation error in our version of the Nijmegen potentials, we correct the results in [19]. The CD-Bonn and AV18 interactions include a nn interaction, which correctly parameterizes the nn scattering length. Therefore, we also decided to refine the calculations of Ref. [19] and to include in our new fits the full charge dependence of the interaction. The resulting cut-off parameters have been published in Ref. [109]. They have been obtained in calculations, which neglect the  $T = \frac{3}{2}$  components and the proton-neutron mass difference in the 3N calculations. In the table we give the resulting cut-off parameters  $\Lambda$  together with the binding energy results for  ${}^3\text{He}$  and  ${}^3\text{H}$ . Because the CD-Bonn and AV18 interactions provide a nn interaction, we adjusted  $\Lambda$  using the  ${}^3\text{H}$  binding energy. The combinations of Nijm I or II and TM have been adjusted to the  ${}^3\text{He}$  binding energy, because the models do not provide an accurate nn interaction. For the studies of the hypernuclear systems in Chapter 5, the TM model has also been adapted to the slightly less accurate Nijm 93 interaction using the  ${}^3\text{H}$  binding energy.

Because we improved our algorithms, we are able to consider also the proton-neutron mass difference and the  $T = \frac{3}{2}$  components now. Therefore the  $\Lambda$  parameters of Ref. [19] do not lead to a perfect agreement between our binding energy results and the experimental values. Because the agreement is sufficient for further investigations, we did not correct these differences. Instead of this, we will build up new trial models based on a recently published version of the TM model [110]. This is left for a forthcoming study.

Additionally, we display in Table 4.4 the results, which we obtained using the Argonne-Urbana model. In this case we can compare our results to calculations of the Pisa group [111]. The Pisa calculation is fully charge-dependent, but neglects the proton-neutron mass difference. For the comparison, we added the perturbatively calculated contribution of the mass difference to the binding energy. The agreement is nearly perfect. The slight difference to the Argonne result, which is also given in the table, has not been understood yet.

In Table 4.4 we also display the predictions for the CSB splitting of the binding energies of  ${}^3\text{H}$  and  ${}^3\text{He}$  of our model Hamiltonians. We will investigate the contribution of the strong and electromagnetic interaction to this difference in Section 4.4. Here we only note that the Nijmegen interactions do not provide a realistic description of the nn interaction. Therefore these models underpredict the CSB splitting sizably, whereas the CSB splitting predictions of CD-Bonn, CD-Bonn 2000 and AV18 are close to the experimental value.

In Tables 4.5 and 4.6, we summarize expectation values of the kinetic energies, the NN and the 3N interactions for the different Hamiltonians. Now there are only small differences in the binding energy

Model	$\Lambda$	$E(^3\text{H})$	$E(^3\text{He})$	$\Delta E_B$
CD-Bonn+TM	4.784	-8.478	-7.735	0.743
CD-Bonn 2000 +TM	4.795	-8.482	-7.732	0.750
AV18+TM	5.156	-8.478	-7.733	0.744
Nijm I+TM	5.035	-8.398	-7.719	0.679
Nijm II+TM	4.975	-8.388	-7.714	0.674
Nijm 93+TM	5.212	-8.497	-7.817	0.680
AV18+TM'	4.756	-8.448	-7.706	0.742
AV18+Urb IX	—	-8.484	-7.739	0.745
AV18+Urb IX (Pisa) [111]	—	-8.485	-7.742	0.743
AV18+Urb IX (Argonne) [33]	—	-8.47(1)	—	—
Exp.	—	-8.482	-7.718	0.764

Table 4.4: 3N binding energy results for different combinations of NN and 3N interactions together with the adjusted form factor parameters  $\Lambda$  in units of  $m_\pi$ . The binding energies for  $^3\text{H}$   $E(^3\text{H})$  and  $^3\text{He}$   $E(^3\text{He})$  are shown. For completeness also the splitting  $\Delta E_B$  is displayed. All energies are given in MeV.

Model	$E$	$\langle H \rangle$	$T$	$V_{NN}$	$V_{3N}$
CD-Bonn+TM	-8.478	-8.475	39.11	-46.52	-1.067
CD-Bonn 2000 +TM	-8.482	-8.480	39.39	-46.78	-1.081
AV18+TM	-8.478	-8.477	50.76	-57.80	-1.441
Nijm I+TM	-8.398	-8.396	43.37	-50.43	-1.336
Nijm II+TM	-8.388	-8.388	51.05	-58.14	-1.297
Nijm 93+TM	-8.497	-8.494	49.37	-56.37	-1.496
AV18+TM'	-8.448	-8.448	50.58	-58.04	-0.989
AV18+Urb IX	-8.484	-8.484	51.32	-58.68	-1.129

Table 4.5: Expectation values with respect to the  $^3\text{H}$  wave functions for various potential combinations. The expectation values  $\langle H \rangle$  of the Hamiltonians are compared to the binding energy results from the Faddeev equations. Additionally, we present the kinetic energy  $T$ , the NN potential energy  $V_{NN}$  and the expectation value of the 3NF  $V_{3N}$ . All energies are given in MeV.

predictions. Therefore the spread in the expectation values is a direct consequence of the properties of the force models. One also sees that the differences are less pronounced regarding Hamiltonians, which are based on the same NN interaction and only differ in their 3NF part. We conclude that the kinetic energy only slightly depends on the 3NF.

The expectation values of the 3NF's of about  $-1.0$  to  $-1.5$  MeV are much bigger in magnitude than the change of the binding energy due to the 3NF of about  $0.5$  to  $0.8$  MeV. This shows that in contrast to the Coulomb interaction, the 3NF's cannot be treated perturbatively. This is astonishing, because their contributions to the binding energies are comparable to the Coulomb force effects. The impact of 3NF's on the wave function is studied in Section 4.6 in more detail.

In the remaining part of this section, we would like to summarize some investigations in the 3N continuum using our new phenomenological Hamiltonians. The Hamiltonians have been applied to Nd scattering in the low- and intermediate energy regime (up to 200 MeV nucleon lab energy). It is generally

Model	$E$	$\langle H \rangle$	$T$	$V_{NN}$	$V_{3N}$
CD-Bonn+TM	-7.735	-7.732	38.29	-45.00	-1.017
CD-Bonn 2000 +TM	-7.732	-7.730	38.54	-45.24	-1.031
AV18+TM	-7.733	-7.733	49.68	-56.03	-1.382
Nijm I+TM	-7.719	-7.717	42.63	-49.06	-1.289
Nijm II+TM	-7.714	-7.713	50.17	-56.63	-1.252
Nijm 93+TM	-7.817	-7.814	48.51	-54.88	-1.446
AV18+TM'	-7.706	-7.705	49.50	-56.25	-0.953
AV18+Urb IX	-7.739	-7.739	50.22	-56.87	-1.086

Table 4.6: Expectation values with respect to the  ${}^3\text{He}$  wave functions for various potential combinations. The expectation values  $\langle H \rangle$  of the Hamiltonians are compared to binding energy result from the Faddeev equations. Additionally, we present the kinetic energy  $T$ , the NN potential energy  $V_{NN}$  and the expectation value of the 3NF  $V_{3N}$ . All energies are given in MeV.

known that 3NF effects in low-energy Nd scattering are rather small [21]. Nevertheless, some low energy Nd scattering observables were identified, which exhibit a scaling behavior with the triton binding energy [112, 113]. Predictions for these observables without using 3NF's are in general dependent on the NN interaction and therefore they seem to be sensitive to the properties of the NN forces model. Using the new model Hamiltonians including 3NF's it turned out that these differences disappear. Thus the NN force dependence is misleading and only an indirect effect due to the triton binding energy differences.

Recently, there has been a lot of effort to pin down 3NF effects at intermediate energies [25, 26, 27, 28, 114]. It is expected that for those higher energies Nd scattering is more sensitive to the 3NF. In general our 3N and NN force combinations are able to predict the experimental differential Nd cross section, whereas the NN forces alone are not able to describe its minimum. In contrast spin observables are not always correctly predicted by the new Hamiltonians. This led to the investigations presented in Ref. [22]. With the help of the wide range of 3N and NN interaction combinations, spin observables have been identified, which are sensitive to the used types of 3NF's and insensitive to the NN interaction. These are considered as probes for the spin structure of a 3NF. Measurements of these observables will be able to test the used 3NF models as well as new upcoming ones. The experiments will inspire theoretical work on the interaction models. In this sense the phenomenological Hamiltonians contribute to the theoretical understanding of the strong interaction. At present they are an important tool to guide experimental investigations in this field.

In the next section we present properties of the 3N wave functions. We will exemplify the different predictions of the force models in more detail.

### 4.3 Properties of the 3N wave function

In this section we investigate the dependence of the 3N wave function properties on the interaction model. For this study we choose two NN forces: the CD-Bonn and the AV18 interactions. From Tables 4.3 and 4.1 one reads off that they are quite different in their structure. Nevertheless they both provide realistic descriptions of the NN data including the CSB between nn and pp forces. We think that they are good candidates to find sensitivities of 3N properties to the NN interaction model, which cannot be led back to differences in the description of the NN data base. As described in the preceding section, these models

model	$S$	$S'$	$P$	$D$	$P_{T=\frac{3}{2}}$
CD-Bonn 2000	91.62	1.30	0.047	7.02	0.0047
CD-Bonn 2000+TM	91.72	1.20	0.102	6.97	0.0048
CD-Bonn	91.65	1.30	0.046	6.99	0.0037
CD-Bonn+TM	91.76	1.20	0.100	6.94	0.0037
AV18	90.13	1.29	0.066	8.51	0.0024
AV18+TM	89.99	1.07	0.153	8.78	0.0025
AV18+TM'	89.59	1.07	0.133	9.21	0.0024
AV18+Urb IX	89.51	1.05	0.135	9.30	0.0024

Table 4.7:  $S$ ,  $S'$ ,  $P$  and  $D$  state probabilities for the  ${}^3\text{H}$  wave functions. The probability of the  $T = \frac{3}{2}$  state is also given. All probabilities are in %.

model	$S$	$S'$	$P$	$D$	$P_{T=\frac{3}{2}}$
CD-Bonn 2000	91.35	1.56	0.047	7.04	0.0098
CD-Bonn 2000+TM	91.46	1.42	0.100	7.01	0.0096
CD-Bonn	91.38	1.55	0.046	7.02	0.0086
CD-Bonn+TM	91.50	1.42	0.098	6.97	0.0084
AV18	89.93	1.53	0.065	8.46	0.0082
AV18+TM	89.83	1.26	0.150	8.75	0.0077
AV18+TM'	89.44	1.26	0.130	9.16	0.0077
AV18+Urb IX	89.37	1.24	0.132	9.25	0.0076

Table 4.8:  $S$ ,  $S'$ ,  $P$  and  $D$  state probabilities for the  ${}^3\text{He}$  wave functions. The probability of the  $T = \frac{3}{2}$  state is also given. All probabilities are in %.

are augmented by suitably adjusted 3NF's.

Wave functions are no observables. Therefore we summarize our predictions for the wave function properties without any comparison to experimental results. Though one can link e.g. momentum distributions within the nuclei to observable quantities in electron scattering experiments, a complete analysis of these experiments requires taking into account FSI's and meson exchange currents (MEC's). In this thesis we restrict ourselves to the identification of sensitive and insensitive parts of the wave function with respect to the model Hamiltonian. To this aim we will give momentum distributions and correlations within the 3N system and pin down there differences varying the interaction models. These results might indicate observables, which depend on the NN and 3N interactions. We do not intend to describe quantitatively these physical observables neglecting FSI and MEC and refer to complete calculations at this point [115].

We start with a look in Tables 4.7 and 4.8. There we give the probabilities to find the symmetric orbital  $S$  (principal  $S$ -state), the mixed symmetric  $S'$ ,  $P$  and  $D$ -state components in our wave functions as defined in [116].

One sees that, as expected, the dominant part of the wave function is the symmetric  $S$ -state. Due to the tensor force there is a visible contribution of the  $D$ -states. The size of this component is linked to the tensor force and, therefore, it is strongly related to the  $D$ -state probability of the deuteron as



given in Table 4.1. The P-wave parts of the wave functions are quite small. Please note that their size increases by a factor of about two in the presence of 3NF's. This indicates their importance for 3NF matrix elements. Comparing the  $S'$ -state results in Tables 4.7 and 4.8, one sees a quite big dependence on the charge of the 3N system of roughly 20 %.

We present these results because of two reasons. First of all they can serve as benchmarks, because they allow a simple comparison of different calculational schemes. We compared our predictions for AV18 and AV18+Urbana IX to the results of the Pisa group and found a nearly perfect agreement [111]. Additionally we would like to note that the one body approximation to the Gamov Teller matrix element of the  ${}^3\text{H}$  decay can be estimated by

$$\langle GT \rangle \approx \sqrt{3} (P_S + P_D/3 - P_{S'}/3) \quad (4.1)$$

It has been shown in [117] that this estimate is reliable and that the  $S$ -,  $S'$ - and  $D$ -state probabilities as given in Table 4.7 underpredict the experimental matrix element by 2 % to 4 %. There seems to be some dependence of the underprediction on the interaction model. A complete analysis in [117] revealed that weak two-body currents can be adjusted to contribute the missing transition strength to the  $\beta$  decay. Moreover, the adjustment is model independent and, therefore, the model dependence of the predictions is removed. This shows that one cannot make judgments on the wave function properties without a complete analysis of the dynamical system and that a complete calculation (at least according to the present state of art) removes spurious model dependences in some cases.

In Tables 4.7 and 4.8 the probabilities to find the three nucleons in a total isospin  $T = \frac{3}{2}$  state are also given. Although the values are smaller than 0.01 %, we found a visible contribution of 25 keV to binding energy of  ${}^3\text{He}$ . This is a consequence of the non-negligible transition matrix elements of the Coulomb interaction between  $T = \frac{1}{2}$  and  $T = \frac{3}{2}$  states. Because the truncation to  $T = \frac{1}{2}$  is not uniquely defined and depends on the calculational scheme [111], the results of incomplete calculations depend on the solution method and cannot be used for reliable benchmarks. Therefore we only give results of complete calculations for the 3N systems.

Now we turn to the spin averaged nucleon momentum distribution functions of  ${}^3\text{H}$ . They are defined as

$$D_{p/n}(p) = \frac{\mathcal{N}}{2J+1} \sum_M \langle \Psi JM | \delta(p-p_3) P_{p/n} | \Psi JM \rangle \quad (4.2)$$

The  $\delta$  function fixes the magnitude of the momentum  $p_3$  of the third particle to  $p$ . The isospin projection operator  $P_{p/n}$  also acts on the third particle

$$P_{p/n} = |tm_t \rangle_3 \langle tm_t| \quad (4.3)$$

and singles out proton or neutrons for isospin  $t = \frac{1}{2}$  and its third component  $m_t = \pm \frac{1}{2}$ . The function is averaged over all directions  $M$  of the total spin  $J = \frac{1}{2}$  of the 3N bound state. The probabilities to find neutrons or protons in the 3N bound state are different. For a better comparison we introduce a normalization constant  $\mathcal{N}$ , which guarantees that the individual proton and neutron distributions are normalized in the same way

$$\int_0^\infty D_{n/p}(p) dp = \frac{1}{4\pi} \quad (4.4)$$

The dependence of these functions on the NN interaction is shown in Fig. 4.1. One sees that the predictions of all models are very similar for momenta below  $p \approx 1.5 \text{ fm}^{-1}$ . It sticks out that the results around  $p \approx 0.4 \text{ fm}^{-1}$  are in perfect agreement for AV18+TM (dotted lines) and CD-Bonn+TM (dashed

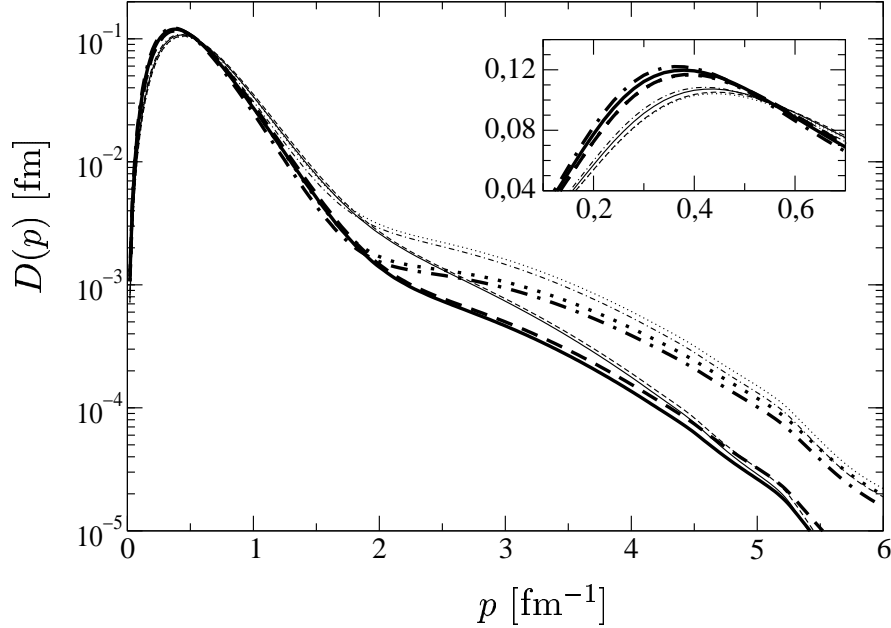


Figure 4.1: Neutron (thick lines) and proton (thin lines) momentum distributions in  ${}^3\text{H}$  on a logarithmic scale. The distribution functions are based on calculations using the CD-Bonn (solid lines), CD-Bonn+TM (dashed lines), AV18 (dashed dotted lines) and AV18+TM (dotted lines) potentials. The inset shows more details of the low momentum region on a linear scale. The functions are normalized to  $\int D(p)dp = \frac{1}{4\pi}$ .

lines). By definition both models predict the same  ${}^3\text{H}$  binding energy. Therefore we expect a scaling behavior of the distribution functions for low momenta with the triton binding energy. This means that the small differences in the momentum distributions based on pure NN forces are a consequence of different binding energies.

This scaling behavior is also visible in Fig. 4.2. There we compare the momentum distributions of wave functions, which are based on the AV18 NN interaction and several 3NF's. For small momenta the Hamiltonians including 3NF's predict identical distributions. Only the calculation based on AV18 without 3NF sticks out a little bit. This is caused by the underbinding predicted by pure NN interactions.

Fig. 4.1 also exemplifies the strong dependence of the high momentum tail ( $p \geq 2 \text{ fm}^{-1}$ ) on the NN interaction. The results of CD-Bonn are far below the predictions of AV18 in this momentum region. In contrast one sees in Fig. 4.2 only a minor dependence of the results on the 3N interaction. The distribution functions are non-sensitive to the 3N interaction.

In summary we found model independent predictions for the distribution functions at low momenta. There is strong sensitivity to the NN interaction model for momenta above  $2 \text{ fm}^{-1}$ . We would like to point out that in this region  $p/m$  already reaches 0.4 and higher values. For those high momenta we cannot claim a quantitative description of the momentum distribution functions because of our non-relativistic calculation. Nevertheless we expect sensitivity to the interaction model in this momentum region, which might be quantitatively explored with relativistic calculations.

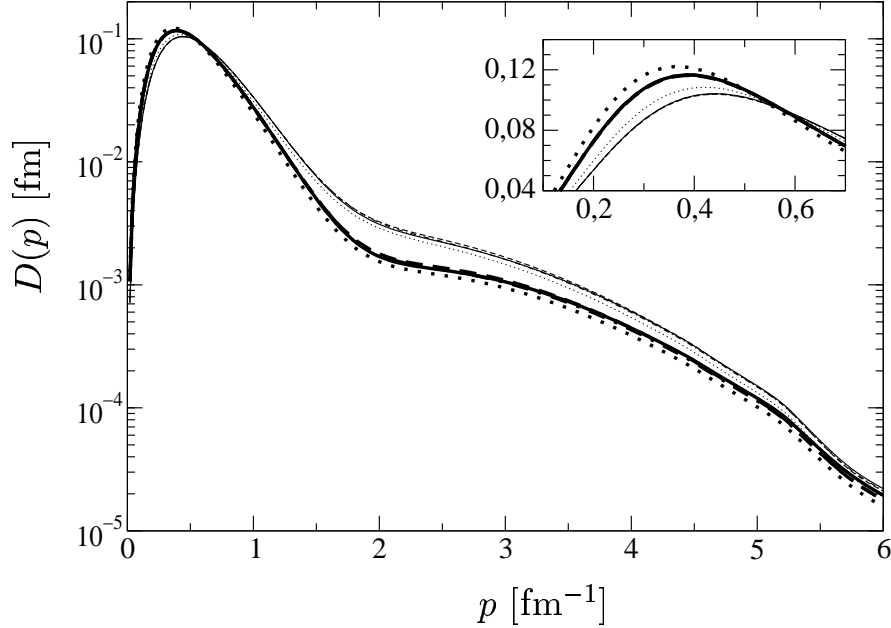


Figure 4.2: Neutron (thick lines) and proton (thin lines) momentum distributions in  ${}^3\text{H}$  on a logarithmic scale. The distribution functions are based on calculations using the AV18+TM (solid lines), AV18+Urbana IX (dashed lines), AV18+TM' (dashed dotted lines) and AV18 (dotted lines) potentials. The inset shows more details of the low momentum region on a linear scale. The functions are normalized to  $\int D(p)dp = \frac{1}{4\pi}$ .

Both figures show that the neutron and proton distributions are quite different. This is a consequence of the Pauli principle, which restricts the quantum numbers of the nn pairs. This is no manifestation of CSB. The effects of CSB on the momentum distributions are shown in Section 4.4.

The next interesting wave function properties are NN correlation functions. Traditionally one extracts from the wave functions the probability that pairs of nucleons have got a fixed interparticle distance (see for example Refs. [118, 19]). Though this is a very instructive picture, it is very hard to relate the results to physical observables. The approach via the Coulomb sum rule is blurred by MEC and relativistic effects [119, 120]. Therefore we choose a different way in this thesis. In the following we define correlation functions in momentum space, which are essentially the probabilities to find two nucleons with a fixed relative momentum. These momentum correlations are related to experiments, where one nucleon is knocked out for instance in  $e^-$  scattering on  ${}^3\text{He}$  and the relative momentum of the remaining two is detected. It has still to be investigated under which conditions this simple picture is realized in nature and not obscured by FSI and MEC. Nevertheless we think that these “momentum correlations” are interesting properties of the wave functions and might help to understand the structure of 3N bound states.

The definition of the correlation functions follows the idea presented in Ref. [118]. They are defined

as an expectation value of the wave function  $\Psi$

$$\mathcal{C}_{s m_s}^{q=pp, np, nn}(\vec{p}) = \frac{1}{2J+1} \sum_M \langle \Psi JM | \delta^3(\vec{p} - \vec{p}_{12}) P_{12}^S(s m_s) P_{12}^T(q) | \Psi JM \rangle \quad (4.5)$$

In this form the correlation is averaged over all spin directions  $M$  of the 3N bound state with total spin  $J = \frac{1}{2}$ . The  $\delta$ -function fixes the momentum within the subsystem of particles 1 and 2 to  $\vec{p}$ . The definition includes a projection  $P_{12}^T(q)$  to nn, np or pp pairs. The spin projection operator  $P_{12}^S(s m_s)$  on pairs of nucleons with total spin  $s$  and spin orientation  $m_s$  is introduced to investigate the spin dependence of the correlation. It acts only on the intrinsic spins of the two nucleons in the 12 subsystem and is defined independently from orbital angular momenta.  $m_s$  is related to a quantization axis. Therefore  $\mathcal{C}$  becomes angular dependent.

In Ref. [118] it has numerically been observed that the angular dependence is quite simple and given by a Legendre polynomial of second order

$$\mathcal{C}_{s m_s}^q(\vec{p}) = \frac{1}{p^2} \left[ C_s^q(p) + P_2(x) \tilde{C}_{s m_s}^q(p) \right] \quad (4.6)$$

where  $x$  is given by the angle between  $\vec{p}$  and the quantization axis  $\hat{e}_z$ :  $x = \hat{p} \cdot \hat{e}_z$ . Please note that the angular independent part of  $\mathcal{C}$  differs from  $C$  by a factor  $\frac{1}{p^2}$ . The scalar part  $C$  is independent from the spin orientation  $m_s$ .

In Appendix E we derive explicit representations of  $\mathcal{C}$  using partial waves. In this form we could analytically confirm Eq. (4.6).

The normalization of  $\mathcal{C}$  and  $C$  is given by Eqs. (4.5) and (4.6):

$$\sum_{q,s,m_s} \int d^3p \mathcal{C}_{s m_s}^q(\vec{p}) = 4\pi \sum_{q,s,m_s} \int dp C_{s m_s}^q(p) = \frac{1}{2J+1} \sum_M \langle \Psi JM | \Psi JM \rangle \equiv 1 \quad (4.7)$$

From the definition of  $\mathcal{C}$  and Eq. (4.6) one derives the probabilities to find a NN pair with charge  $q$  in a certain spin state  $s$  as

$$P_s^q = (2s+1) 4\pi \int dp C_s^q(p) \quad (4.8)$$

Our theoretical predictions for those probabilities are presented in Tables 4.9 and 4.10.

One sees that the probabilities do not significantly differ for  ${}^3\text{H}$  and  ${}^3\text{He}$ . They are also nearly independent from the 3NF's and are only slightly dependent on the NN interaction. For a comparison we included the analytically given probabilities for 3N waves functions, which are completely determined by the principal  $S$ -state. The results are in rough agreement with this approximation. This shows that the characteristic differences of  $P_s^q$  for different  $s$  and  $q$  values are caused by the dominance of the principal  $S$ -state in the 3N wave function. The differences to this rough picture are a consequence of the admixtures of the  $P$  and  $D$  waves and the mixed symmetric  $S'$ -state.

In the following we will show the functional dependences of two kinds of momentum correlations: charge independent, but spin dependent correlations

$$\mathcal{C}_{s m_s}(\vec{p}) = \sum_q \mathcal{C}_{s m_s}^q(\vec{p}) \quad (4.9)$$

and charge dependent, but spin independent correlations

$$\mathcal{C}^q(\vec{p}) = \sum_{s m_s} \mathcal{C}_{s m_s}^q(\vec{p}) \quad (4.10)$$

	$s = 0$			$s = 1$		
	nn	np	NN	nn	np	NN
CD-Bonn 2000	30.79	15.70	46.49	2.54	50.97	53.51
CD-Bonn 2000+TM	30.81	15.69	46.51	2.52	50.97	53.49
CD-Bonn	30.80	15.71	46.51	2.53	50.96	53.49
CD-Bonn+TM	30.82	15.70	46.52	2.51	50.97	53.51
AV18	30.30	15.46	45.76	3.03	51.21	54.24
AV18+TM	30.22	15.38	45.60	3.11	51.29	54.40
AV18+TM'	30.08	15.31	45.39	3.25	51.36	54.61
AV18+Urb IX	30.02	15.30	45.35	3.28	51.37	54.65
pri. S-state	33.33	16.67	50.00	0.00	50.00	50.00

Table 4.9: Probabilities  $P_s^q$  to find NN pairs in spin  $s = 0$  and  $s = 1$  states in  ${}^3\text{H}$  as given in Eq. (4.8). We give separate results for nn and np pairs and the sum of both contributions denoted by NN. The predictions for the principal S-state wave function are also included. All probabilities are given in %.

	$s = 0$			$s = 1$		
	pp	np	NN	pp	np	NN
CD-Bonn 2000	30.76	15.72	46.48	2.57	50.95	53.52
CD-Bonn 2000+TM	30.78	15.71	46.49	2.55	50.96	53.51
CD-Bonn	30.77	15.73	46.50	2.56	50.94	53.50
CD-Bonn+TM	30.79	15.72	46.51	2.54	50.95	53.49
AV18	30.29	15.49	45.78	3.03	51.18	54.22
AV18+TM	30.22	15.40	45.62	3.11	51.27	54.38
AV18+TM'	30.08	15.34	45.42	3.25	51.33	54.58
AV18+Urb IX	30.06	15.32	45.38	3.27	51.35	54.62
pri. S-state	33.33	16.67	50.00	0.00	50.00	50.00

Table 4.10: Probabilities  $P_s^q$  to find NN pairs in spin  $s = 0$  and  $s = 1$  states in  ${}^3\text{He}$  as given in Eq. (4.8). We give separate results for pp and np pairs and the sum of both contributions. The predictions for the principal S-state wave function are also included. All probabilities are given in %.

Due to the summation over all orientations of the spin, the second one is angular independent. The decomposition of the first one into angular dependent and angular independent parts can be performed analogously to Eq. (4.6). As can be expected the explicit expressions show, that the  $s = 0$  part is angular independent. There is only one spin orientation  $m_s = 0$  in this case. For  $s = 1$  we always choose  $m_s = 0$  in the following. This determines the full  $m_s$  dependence, because  $C$  is independent from  $m_s$  and the  $\tilde{C}$  just differ by an overall  $m_s$ -dependent factor (see Appendix E).

In order to compare the different  $C^q$  and  $C_{s m_s}$  we normalize them separately for all charges  $q$  and spins  $s m_s$

$$\int d^3p C_{s m_s}(\vec{p}) = \int d^3p C^q(\vec{p}) \equiv 1 \quad (4.11)$$

The individual importance of each of these correlations can be found in Tables 4.9 and 4.10.

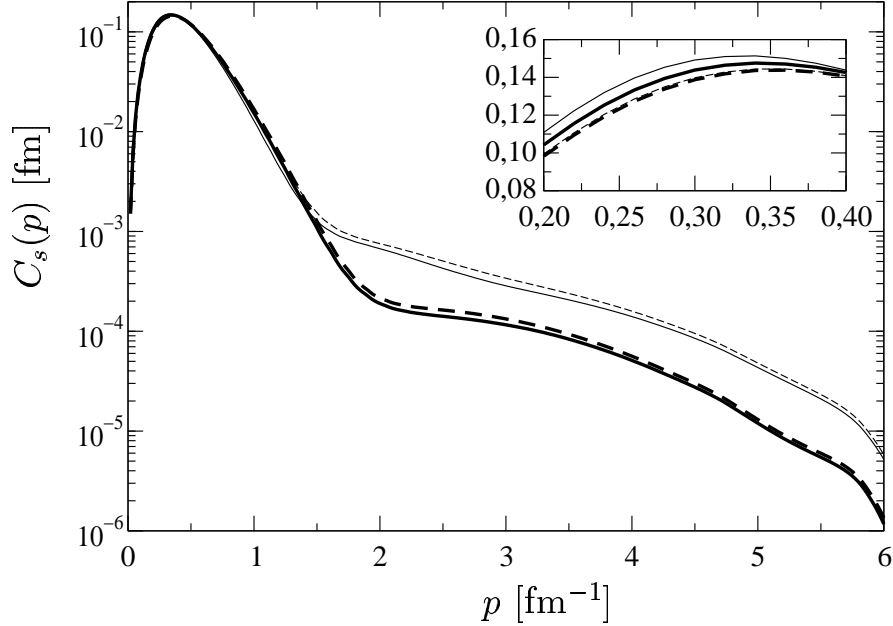


Figure 4.3: NN correlations  $C_s(p)$  in  ${}^3\text{H}$  for spin  $s = 0$  compared for different 2N potentials with and without TM 3NF on a logarithmic scale. The correlation functions are based on calculations using the CD-Bonn (thick solid line), CD-Bonn+TM (thick dashed line), AV18 (thin solid line), AV18+TM (thin dashed line) potentials. The inset shows more details of the low momentum region on a linear scale. The functions are normalized to  $\int C(p)dp = \frac{1}{4\pi}$ .

In Fig. 4.3 we present  $C_{s=0}(p)$  for calculations based on the CD-Bonn and AV18 NN interactions with and without TM 3NF. Again we find only a minor dependence of the function on the models below  $p = 1.5 \text{ fm}^{-1}$ . Moreover, we see for  $s = 0$  a perfect scaling behavior. Our predictions are identical in the low momentum region for the two models, which include the TM 3NF and predict the same 3N binding energies (thick and thin dashed lines). Therefore we assume that the slight deviations of the calculations using no 3NF can be led back to the different binding energy predictions of these models. Around  $2 \text{ fm}^{-1}$  and above strong differences between the CD-Bonn and AV18 results become visible (thick and thin lines). We also see that the TM 3NF only slightly affects the  $s = 0$  correlation (solid and dashed lines).

This is also true for other 3NF's. In Fig. 4.4 we exemplify the 3NF dependence for calculations using the AV18 NN interaction. All calculations including 3NF's perfectly agree in the whole momentum range shown. Due to the scaling effect with the 3N binding energy, there is a slight difference to the prediction without 3NF (thin dashed line).

In Fig. 4.5 we turn to  $C_{s=1}$ . Again we find a small dependence on the interaction model below  $1.5 \text{ fm}^{-1}$ . The enlargement reveals that very small differences are left comparing the calculations of AV18 and CD-Bonn including the TM force (dashed lines). Because both model Hamiltonians nearly predict the same binding energies, we find an extremely small model dependence, which cannot be led back to a scaling effect.

Above  $2.0 \text{ fm}^{-1}$  our theoretical predictions depend strongly on the NN interaction (thick and thin

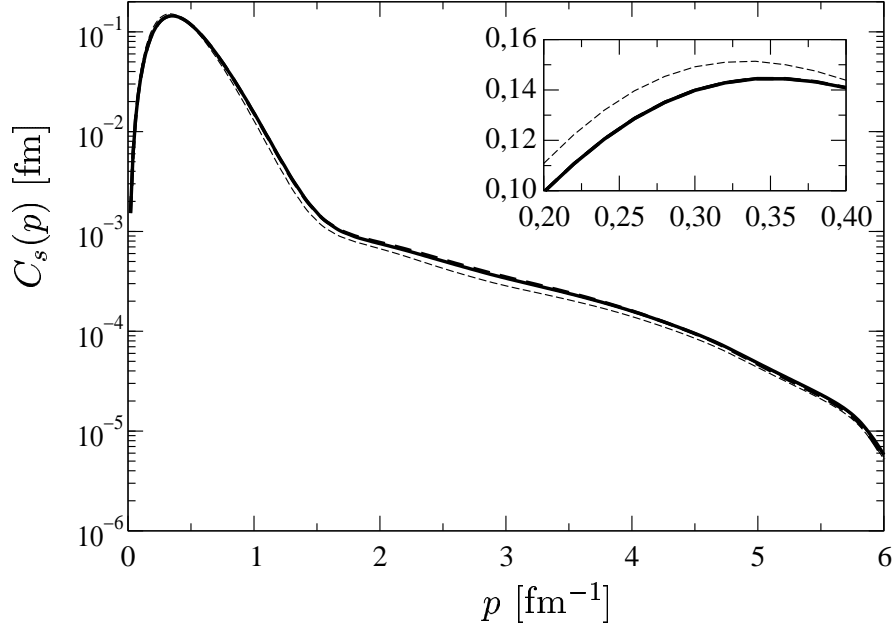


Figure 4.4: NN correlations  $C_s(p)$  in  ${}^3\text{H}$  for spin  $s = 0$  and AV18 compared for different 3NF's on a logarithmic scale. The correlation functions are based on calculations using the TM (thick solid line), Urbana IX (thick dashed line), TM' (thin solid line) 3NF's or no 3NF (thin dashed line). The inset shows more details of the low momentum region on a linear scale. The functions are normalized to  $\int C(p)dp = \frac{1}{4\pi}$ .

lines in Fig. 4.5) and only slightly on the TM 3NF (dashed and solid lines).

Similarly to the  $s = 0$  case, there is no dependence on the used 3NF in the correlation function. This is exemplified for AV18 in Fig. 4.6. Again only the prediction without 3NF (thin dashed line) differs from the calculations including TM, TM' and Urbana IX.

Therefore we can summarize that the predictions for the momentum correlation functions  $C_s$  are nearly model independent for  $p \leq 1.5 \text{ fm}^{-1}$  and strongly depend on the NN interaction above  $2 \text{ fm}^{-1}$ . The model dependence is very similar for momentum distribution functions as we saw earlier in this section. We think that this clear separation of momentum ranges with and without model dependence is the main advantage of correlations in momentum space. Unfortunately, we cannot claim a quantitative description of the correlations above  $2 \text{ fm}^{-1}$ . Quantitative descriptions in this momentum region are left for a relativistic study of the 3N problem. Nevertheless we expect that our results are qualitatively correct also in this range. For momenta below  $1.5 \text{ fm}^{-1}$  we are able to describe the properties of the correlations model independently.

Having this in mind we turn to a comparison of the correlations for different spins and charges. In Fig. 4.7 we start with the spin dependence of  $C$ . There is a remarkably slower decrease of the correlation for  $s = 1$  than for  $s = 0$  for higher momenta. This leads to a visibly smaller correlation for  $s = 1$  for momenta below  $0.6 \text{ fm}^{-1}$ . This behavior is a consequence of the strong  ${}^3\text{D}_1$  component in the partial wave decomposition of the wave function due to the tensor force. For  $s = 0$  the  ${}^3\text{D}_1$  partial wave does

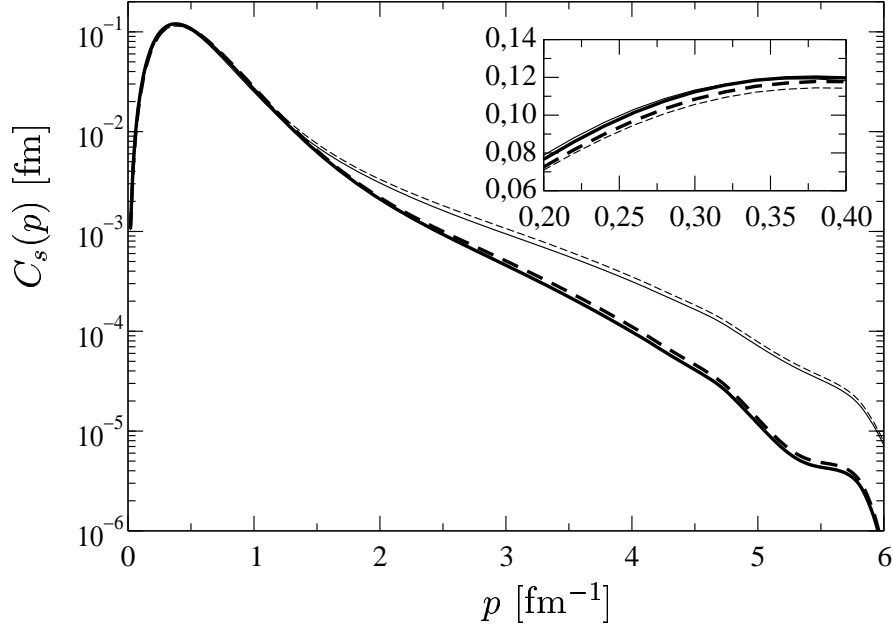


Figure 4.5: NN correlations  $C_s(p)$  in  ${}^3\text{H}$  for spin  $s = 1$  compared for different 2N potentials with and without TM 3NF on a logarithmic scale. The correlation functions are based on calculations using the CD-Bonn (thick solid line), CD-Bonn+TM (thick dashed line), AV18 (thin solid line), AV18+TM (thin dashed line) potentials. The inset shows more details of the low momentum region on a linear scale. The functions are normalized to  $\int C(p)dp = \frac{1}{4\pi}$ .

not contribute. This causes the much faster decrease of the correlation in the spin state  $s = 0$ .

The dependence on the charge of the NN subsystem is shown in Fig. 4.8. From Table 4.9 we read off that the nn correlation is dominated by the  $s = 0$  part. Therefore we find a similar behavior of the nn correlations (thick lines in Fig. 4.8) and  $s = 0$  correlations (thick lines in Fig. 4.7), especially in the low momentum region. The admixture of  $s = 0$  to the np correlation is considerably bigger than the  $s = 1$  contribution to nn pairs. From Fig. 4.8 we see that the differences of nn and np correlations are less pronounced around  $0.5 \text{ fm}^{-1}$  than the differences of  $s = 0$  and  $s = 1$  correlations.

Up to now we only looked at the angular independent parts of the correlation functions for  $s = 1$ . In [118] it has been observed that configuration space correlations show a strong angular dependence in the region around 1 fm distance. Does this angular dependence carry over to momentum space? To answer this question we show the magnitudes of the functions  $\tilde{C}_{sm_s}$  for  $s = 1$  and  $m_s = 0$  in Fig. 4.9. We find that there is really a considerable angular dependence of the correlation around  $p = 1 \text{ fm}^{-1}$ . In this momentum region the  $\tilde{C}$ 's are only slightly model dependent. Therefore also the angular dependence can be predicted nearly model independently in this region. The functions are positive and negative and in a certain  $p$  range bigger than  $C_s$ . We would like to note that the Legendre polynomials  $P_2(x)$  vary between  $-\frac{1}{2}$  and 1. We checked carefully that the sign of  $\tilde{C}$  and its size insures that the combination  $\mathcal{C}$  is positive for all momenta. This concludes our survey on correlations in momentum space.

In the following we introduce overlap functions, which combine the NN and 3N wave functions. They



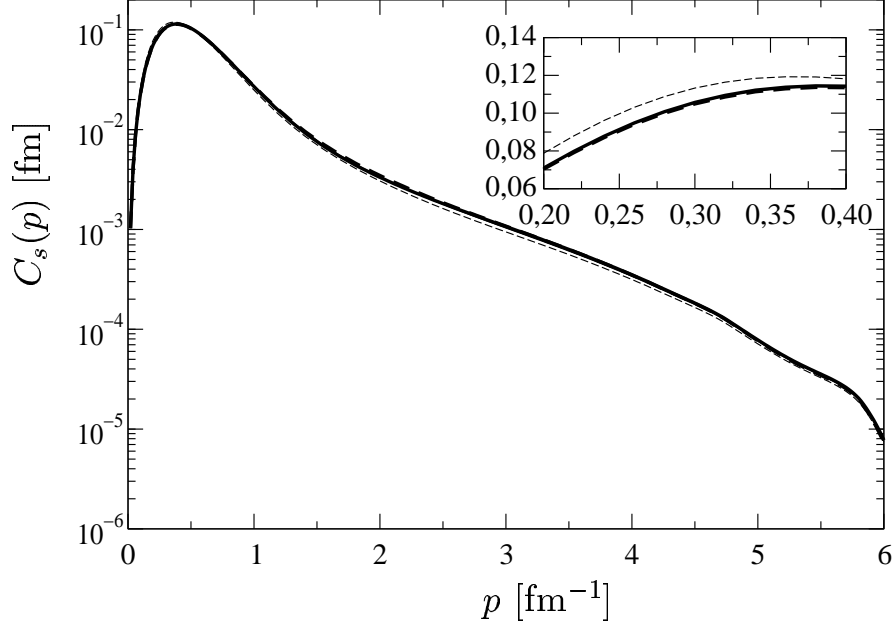


Figure 4.6: NN correlations  $C_s(p)$  in  ${}^3\text{H}$  for spin  $s = 1$  compared for different 3NF's in conjunction with the AV18 NN interaction on a logarithmic scale. The correlation functions are based on calculations using the TM (thick solid line), Urbana IX (thick dashed line), TM' (thin solid line) 3NF's or no 3NF (thin dashed line). The inset shows more details of the low momentum region on a linear scale. The functions are normalized to  $\int C(p)dp = \frac{1}{4\pi}$ .

might give insights, in which way the properties of the deuteron are visible in 3N bound states. Therefore we define the d- ${}^3\text{H}$  or d- ${}^3\text{He}$  overlap functions as

$$\hat{D}_{m_j}(\vec{p}_3) = \frac{1}{2J+1} \sum_M \langle \Psi JM | \phi_d j m_j \rangle_{12} | \vec{p}_3 \rangle_3 \langle \vec{p}_3 |_{12} \langle \phi_d j m_j | \Psi JM \rangle \quad (4.12)$$

They are the expectation values of the projection operator onto the deuteron bound state  $\phi_d$  with spin  $j = 1$  and spin orientation  $m_j$ . The momentum  $\vec{p}_3$  of the third particle is also fixed. The expectation values of the 3N bound state wave function  $\Psi$  with total angular momentum  $J = \frac{1}{2}$  are averaged over all orientations of the 3N angular momentum  $M$ . The polarization of the deuteron state introduces a dependence on the angle  $x = \hat{p}_3 \cdot \hat{e}_z$  between the quantization axis and the momentum of the third particle  $\vec{p}_3$ . As explicitly shown in Appendix E the angular dependence is given in a similar form as for the correlation functions and can be expressed in terms of an angular independent part and a Legendre polynomial of second order

$$\hat{D}_{m_j}(\vec{p}_3) = \frac{1}{p_3^2} \left[ \mathcal{D}(p_3) + P_2(x) \tilde{D}_{m_j} \right] \quad (4.13)$$

Again the scalar part  $\mathcal{D}$  does not depend on the spin orientation  $m_j$ . The dependence of  $\tilde{D}_{m_j}$  on  $m_j$  is given by a Clebsch-Gordan coefficient and therefore analytically known. Below we present results for a fixed  $m_j = 0$ .

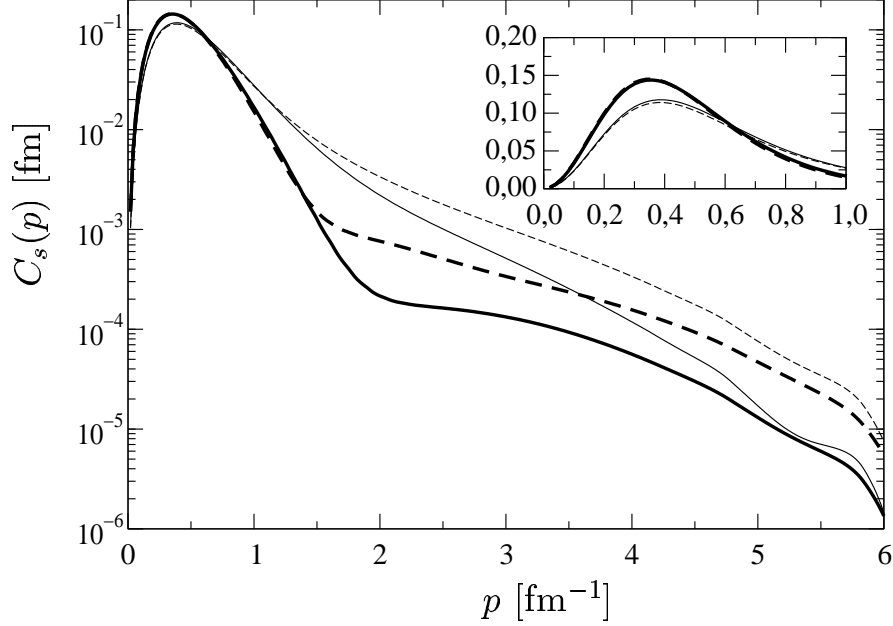


Figure 4.7: NN correlations  $C_s(p)$  in  ${}^3\text{H}$  compared for 2N spin  $s = 0$  (thick lines) and  $s = 1$  (thin lines) in momentum space on a logarithmic scale. The correlation functions are based on calculations using the CD-Bonn+TM (solid lines) and AV18+TM (dashed lines) potentials. The inset shows more details of the low momentum region on a linear scale. The functions are normalized to  $\int C(p)dp = \frac{1}{4\pi}$ .

The overlap functions are the probability to find two nucleons in a deuteron state and the third one with a fixed momentum  $\vec{p}_3$ . The integral over  $\vec{p}_3$  and sum over the orientations of the deuteron spin  $m_j$  result in the probability  $N_d$  to find a deuteron in the 3N bound state

$$N_d = \sum_{m_j} \int d^3 p_3 \hat{\mathcal{D}}_{m_j}(\vec{p}_3) = 3 \cdot 4\pi \int_0^\infty dp_3 \mathcal{D}(p_3) \quad (4.14)$$

Our predictions for  $N_d$  are given in Table 4.11 for different model Hamiltonians. We found that  $N_d$  is roughly 45 % for all models considered. There is a small dependence on the interaction model. Both, the NN interaction and the 3N interaction, have got a small impact on  $N_d$ . The small size of  $N_d$  could be expected from the results in Tables 4.9 and 4.10. The deuteron spin state is  $s = 1$ . Therefore the relation  $N_d \leq P_1^{np}$  holds. The dominance of the principal  $S$ -state causes a roughly equal contribution of the NN  $s = 0$  and  $s = 1$  states to the 3N bound state. Therefore the spin structure of  ${}^3\text{He}$  causes already a reduction of  $N_d$  to roughly 50 %. In this view the results in Table 4.11 indicate that the  $s = 1$  states of a NN pair in  ${}^3\text{He}$  are similar to the deuteron states. The similarities and differences of NN correlations in the 2N, 3N and 4N systems are shown in Section 4.6. Here we continue with the presentation of the relative motion of the third nucleon to a NN pair in a deuteron state.

For this aim we normalize the overlap functions to one separately for all orientations of the deuteron

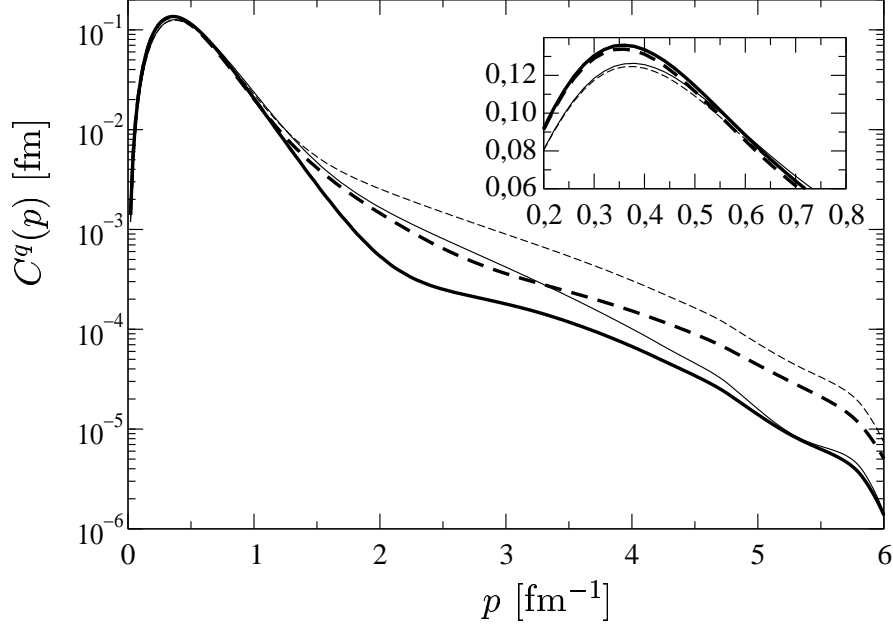


Figure 4.8: Spin averaged nn (thick lines) and np (thin lines) correlation  $C^q(p)$  in  ${}^3\text{H}$  on a logarithmic scale. The correlation functions are based on calculations using the CD-Bonn 2000+TM (solid lines), and AV18+TM (dashed lines) potentials. The inset shows more details of the low momentum region on a linear scale. The functions are normalized to  $\int C(p)dp = \frac{1}{4\pi}$ .

interaction	$N_d({}^3\text{He})$	$N_d({}^3\text{H})$
CD-Bonn	45.13	44.96
CD-Bonn +TM	44.72	44.53
AV18	45.06	44.88
AV18+TM	44.33	44.13
AV18+Urbana IX	44.36	44.16
AV18+TM'	44.42	44.22
CD-Bonn 2000	45.13	44.96
CD-Bonn 2000+TM	44.71	44.52

Table 4.11: Normalization constants  $N_d$  of the deuteron-nucleon overlap distributions in  ${}^3\text{H}$  and  ${}^3\text{He}$ . Results are given in %.

spin  $m_j$

$$\int d^3p_3 \hat{\mathcal{D}}_{m_j}(\vec{p}_3) = \int_0^\infty dp_3 \mathcal{D}(p_3) \equiv 1 \quad (4.15)$$

In Fig. 4.10 our results for  $\mathcal{D}$  are shown. Again we find a scaling behavior with the triton binding energy. The enlargement shows that the predictions for CD-Bonn+TM (dashed line) and AV18+TM

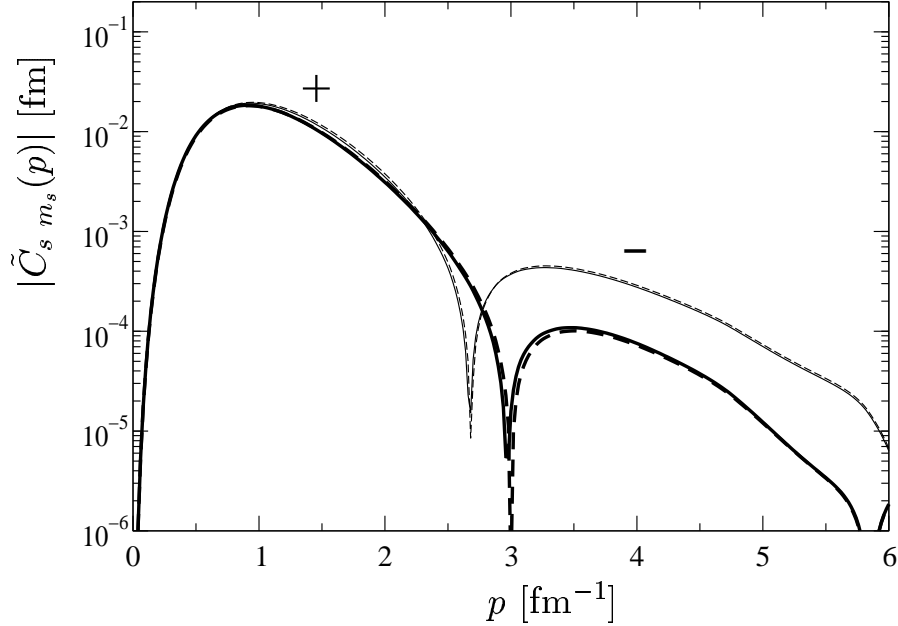


Figure 4.9: Angular dependent part of the NN correlations  $\tilde{C}_{s m_s}$  in  ${}^3\text{H}$  for spin  $s = 1$  and its third component  $m_s = 0$  as defined in the text compared for different interactions on a logarithmic scale. The correlation functions are based on calculations using the CD-Bonn (thick solid line), CD-Bonn+TM (thick dashed line), AV18 (thin solid line), AV18+TM (thin dashed line) potentials. The functions are normalized correspondingly to the angular independent part  $C$  shown in Fig. 4.5. The magnitude  $|\tilde{C}|$  is shown.  $+(-)$  indicates positive (negative)  $\tilde{C}$ .

(dotted) lines are identical in the low momentum region. The high momentum tail is sensitive to the NN interaction. Interestingly, we find a structure around  $5.5 \text{ fm}^{-1}$  in calculations without 3NF, which disappears in the presence of a 3N interaction. That structure is the consequence of a node in the s-wave part of  $\mathcal{D}$ . The 3NF's increase the d-wave contribution in this momentum range. This leads to the removal of the dip structure. Without exemplifying in a figure, we note that  $\mathcal{D}$  has got only a slight dependence on the kind of 3NF.

This is different for the angular dependent part  $\tilde{\mathcal{D}}_{m_j}$  of the overlap function given in Fig. 4.11. In the low momentum region, there is again only a slight sensitivity on the model Hamiltonian. In the figure we compare the results for AV18 without and with different 3N interactions. The interesting point is the dip structure around  $5 \text{ fm}^{-1}$ . The position of this structure moves from  $5 \text{ fm}^{-1}$  for a calculation without 3NF to  $4.5 \text{ fm}^{-1}$  for a calculation with TM' and Urbana IX. The calculation using TM predicts the dip at  $4 \text{ fm}^{-1}$ . Of course this momenta are relativistic and we cannot claim a quantitative description. But these differences indicate that 3N wave functions show some dependence on the 3NF interaction model. This is remarkable because correlations and momentum distributions are insensitive to 3NF's as shown earlier in this section.

This concludes our presentation of 3N bound state properties. We saw that the low momentum properties are nearly independent from the model Hamiltonian, especially if the models predict the

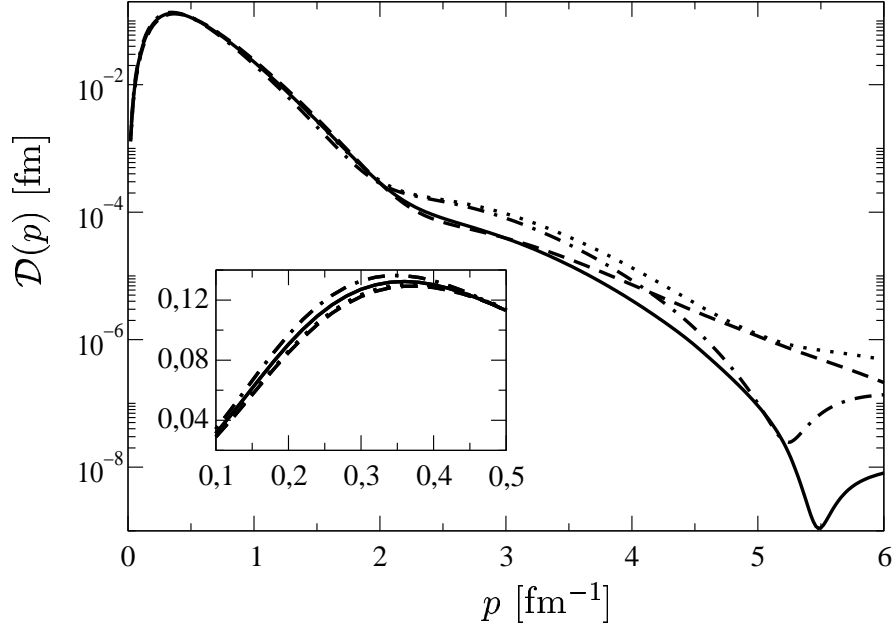


Figure 4.10: Deuteron-nucleon momentum distributions  $\mathcal{D}$  in  ${}^3\text{H}$  on a logarithmic scale. The distribution functions are based on calculations using the CD-Bonn (solid line), CD-Bonn+TM (dashed line), AV18 (dashed dotted line) and AV18+TM (dotted line) potentials. The inset shows more details of the low momentum region on a linear scale. The functions are normalized to  $\int \mathcal{D}(p) dp = \frac{1}{4\pi}$ .

experimental triton binding energy. In the next section we study the  ${}^3\text{H}$ - ${}^3\text{He}$  binding energy difference using the model Hamiltonians. In this section we will also reveal the CSB effects on the wave function properties.

#### 4.4 CSB in the 3N system

In Section 4.2 we presented the predictions for the  ${}^3\text{He}$  and  ${}^3\text{H}$  binding energies. These results are based on a fully charge-dependent calculation, which includes the  $T = \frac{3}{2}$  components of the wave function and the neutron and proton mass difference. In this section we want to investigate in some detail the origin of this binding energy difference. A similar investigation has already been performed in Ref. [31] using charge-independent NN interactions and meson-theoretical models of the CIB and CSB parts. The new charge-dependent NN interactions [12, 9] were not available at that time. We think that a new look into this problem is in order to confirm that the new forces can describe  $\Delta E_B$  accurately and that the results from [31] were not obscured by failures in the description of the NN data.

In Ref. [121] a scaling behavior of the Coulomb repulsion in  ${}^3\text{He}$  with the  ${}^3\text{He}$  binding energy has been established. Hence a complete analysis of  $\Delta E_B$  requires model Hamiltonians, which predict at least the experimental  ${}^3\text{H}$  binding energy. Those Hamilton operators are to our disposal now.

In the following we will use the models based on CD-Bonn, CD-Bonn 2000 and AV18 augmented by

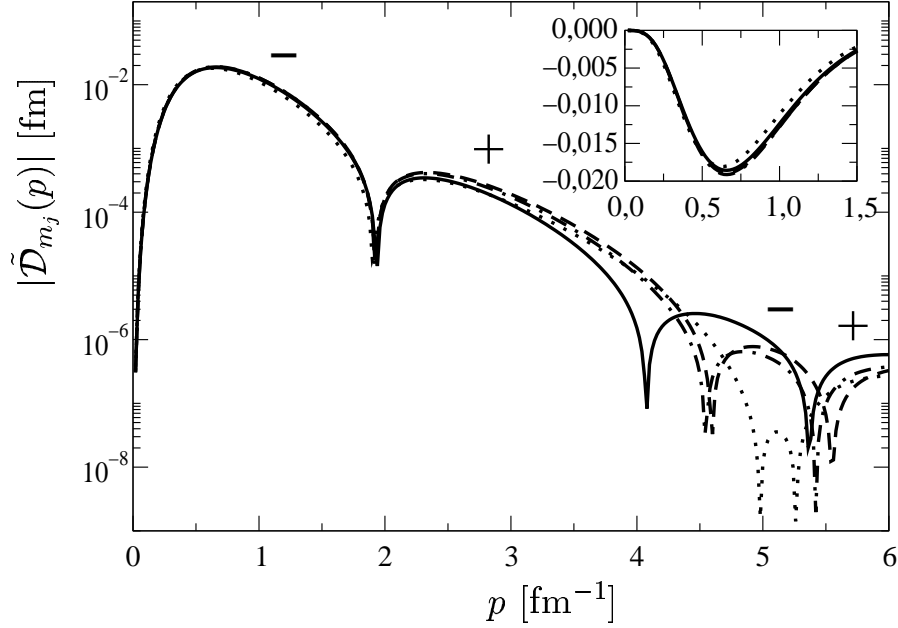


Figure 4.11: Angular dependent parts of the deuteron-nucleon momentum distributions  $\tilde{D}_{m_j}$  in  ${}^3\text{H}$  on a logarithmic scale. The distribution functions are based on calculations using the AV18+TM (solid line), AV18+Urbana IX (dashed line), AV18+TM' (dashed dotted line) and AV18 (dotted line) potentials. The inset shows more details of the low momentum region on a linear scale. The functions are normalized according to the angular independent part presented in Fig. 4.10. The figure shows the magnitude  $|\tilde{D}_{m_j}|$ , the sign of  $\tilde{D}$  is indicated by + and -.

3NF's. The 3NF's are charge-independent. The chosen NN interactions nearly perfectly describe the np and pp scattering data and predict the experimental nn scattering length as given in Table 4.2. However, the charge-dependence is implemented in the CD-Bonn models and AV18 quite differently: whereas AV18 is fitted to the NN data in conjunction with an electromagnetic interaction, which goes beyond the Coulomb force and takes finite size effects of the nucleons into account, the CD-Bonn models are combined with a simple Coulomb interaction for point-like protons. Both models can describe the NN data with the same accuracy. Nevertheless one sees from Table 4.2 that the strong parts of the interaction predicts quite different pp and np scattering lengths. Therefore the strong and electromagnetic contribution to the CSB is quite different in both models.

The CSB of the CD-Bonn 2000 interaction sticks out as its description of the nn system is not based on the experimental scattering length datum. Its nn force is fitted to theoretical phaseshifts, which are derived from pp scattering data and CSB predictions of the full Bonn model [88]. In this way CSB is included not only in the  ${}^1\text{S}_0$  partial wave, but also in other partial waves. From Table 4.2 we learn that the theoretical prediction for the nn scattering length differs slightly from the CD-Bonn and AV18 results, which are close to the central value of the currently accepted experimental range.

Table 4.4 shows our predictions for the  ${}^3\text{H}/{}^3\text{He}$  binding energy differences  $\Delta E_B$ . To our surprise the models based on CD-Bonn and AV18 predict within our numerical accuracy the same  $\Delta E_B$ . In view

interaction	AV18+TM	AV18+Urb IX	Ref. [31] Table 5
$\Delta T$	15	15	11
$\Delta V_{NN,nucl}$	66	66	77
$\Delta V_{C1}$	653	653	648
$\Delta V_{C2}$	-1	-1	—
$\Delta V_{DF}$	-2	-2	—
$\Delta V_{VP}$	4	4	4
$\Delta V_{MM}$	19	19	11
$\Delta E_B(\text{pert})$	754	754	751
$\Delta E_B(\text{non-pert})$	744	745	—
Exp.	764	764	764

Table 4.12: Perturbative estimate of the contribution of various parts of the AV18 interaction to the CSB of the  ${}^3\text{H}$  and  ${}^3\text{He}$  nuclei. The contributions from the kinetic energy  $\Delta T$ , the nuclear NN interaction  $\Delta V_{NN,nucl}$ , the one and two photon Coulomb terms  $\Delta V_{C1}$  and  $\Delta V_{C2}$ , the Darwin-Foldy term  $\Delta V_{DF}$  and the magnetic moment interaction  $\Delta V_{MM}$  are distinguished. The expectation values of the CSB breaking parts of the operators are based on the wave function of  ${}^3\text{H}$  obtained from the AV18+TM and AV18+Urb IX model Hamiltonians. The sum  $\Delta E_B(\text{pert})$  is compared to the non-perturbative binding energy difference  $\Delta E_B(\text{non-pert})$  from Table 4.4 and the experimental value. All energies are given in keV.

of their different electromagnetic interactions, we conclude that model independent predictions for  $\Delta E_B$  are possible, if the models can describe the NN data accurately. We also see that the 3NF models do not have any impact on  $\Delta E_B$ . In comparison to the experimental datum all models underpredict  $\Delta E_B$ .

Interestingly, the new CD-Bonn 2000 interaction leads to a slightly improved description of the binding energy difference.

In the following we would like to study three points in more detail.

- 1) We pin down the individual contributions of the electromagnetic part, the strong part and the kinetic energy to  $\Delta E_B$  and see their importance.
- 2) We study for CD-Bonn 2000, whether the different nn scattering length is the only reason for the improved description of  $\Delta E_B$ .
- 3) We look at the momentum distributions and correlations to see the size of CSB effects on these properties of the wave function

In Table 4.12 we summarize our perturbative estimates of the contribution of various parts of the AV18 interaction model and compare them to corresponding predictions from Ref. [31]. Details of the different electromagnetic contributions are outlined in [9]. We do not include the “orbit-orbit” interaction into our study, which has been introduced to simulate an energy dependence of the Coulomb interaction. From our point of view, there are some conceptual problems including this term. Its contribution to  $\Delta E_B$  has been estimated to 9 keV [31, 122]. The electromagnetic interactions take finite-size effects of the nucleons into account. The contribution of the kinetic energy  $\Delta T$  due to the mass difference of proton and neutron is also given. Corresponding numbers for the CD-Bonn models are given in Table 4.13. In this case we distinguish the contribution of the kinetic energy, the strong and the Coulomb interactions.

interaction	${}^3\text{H}$		${}^3\text{He}$
	CD-Bonn+TM	CD-Bonn 2000+TM	CD-Bonn+TM
$\Delta T$	12	12	12
$\Delta V_{NN,nucl}$	53	60	50
$\Delta V_C$	689	690	673
$\Delta E_B(\text{pert})$	754	762	736
$\Delta E_B(\text{non-pert})$	743	750	743
Exp.	764	764	764

Table 4.13: Perturbative estimate of the contribution of the CD-Bonn and point Coulomb interaction to the CSB of the  ${}^3\text{H}$  and  ${}^3\text{He}$  nuclei. The contributions from the kinetic energy  $\Delta T$ , the nuclear NN interaction  $\Delta V_{NN,nucl}$  and the static Coulomb force for point protons  $\Delta V_C$  are distinguished. The expectation values of the CSB breaking parts of the operators are based on the wave function of  ${}^3\text{H}$  for the CD-Bonn+TM and CD-Bonn 2000+TM models and of  ${}^3\text{He}$  for the CD-Bonn+TM model. The sum  $\Delta E_B(\text{pert})$  is compared to the non-perturbative binding energy difference  $\Delta E_B(\text{non-pert})$  from Table 4.4 and the experimental value. All energies are given in keV.

A look to Tables 4.12 and 4.13 reveals that a perturbative estimate of  $\Delta E_B$  differs from the non-perturbative by  $\approx 10$  keV. Perturbative calculations based on the  ${}^3\text{H}$  wave functions overestimate the result, whereas the use of  ${}^3\text{He}$  wave functions leads to an underprediction (right column of Table 4.13). Nevertheless we would like to estimate the different contributions to  $\Delta E_B$  perturbatively.

Table 4.12 shows that all parts do not depend on the kind of 3NF model used. Comparing our results with Ref [31], we find differences in the individual contributions. In contrast the summed up estimate is roughly equivalent to our findings. We observe a similar behavior comparing the results of Table 4.12 and 4.13. For CD-Bonn the total  $\Delta E_B$  equals the predictions of AV18, though the electromagnetic interactions and the strong part of the interaction contribute differently. The AV18, the CD-Bonn and the model of Ref. [31] are all fitted in conjunction with their specific electromagnetic interaction to the same pp, nn and np scattering lengths. Therefore we argue that  $\Delta E_B$  is sensitive to the scattering length differences and does not depend on details of the interaction. Especially the definition of a detailed electromagnetic part is not required to describe  $\Delta E_B$  as long as the strong and electromagnetic parts predict the NN data. A similar observation was found in Ref. [123] comparing the predictions of CSB model interactions based on  $\rho - \omega$  mixing and nucleon mass splitting.

Table 4.13 also shows the results for the new CD-Bonn 2000 model. We investigated for this model the dependence of  $\Delta E_B$  on the nn scattering length  $a_{nn}$ . To this aim we changed the  ${}^1\text{S}_0$  nn force by a factor  $\lambda$ . Together with the TM force adjusted to  ${}^3\text{H}$  in conjunction with  $\lambda = 1$ , we obtained model Hamiltonians which predict the same  ${}^3\text{He}$  binding energy of -7.732 MeV, but differ in their  ${}^3\text{H}$  binding energy and  $a_{nn}$  predictions. The results are given in Table 4.14. Fig. 4.12 reveals a linear dependence of  $\Delta E_B$  on the scattering length  $a_{nn}$ . The dashed dotted lines mark the prediction of  $\Delta E_B$  for today's generally accepted experimental  $a_{nn}$ . The corresponding  $\Delta E_B$  is an independent prediction based on the modified CD-Bonn 2000 interaction, which agrees with the CD-Bonn and AV18 results. This confirms that the deviation in  $\Delta E_B$  of CD-Bonn 2000 can be led back to its different  $a_{nn}$  value. The dashed lines mark the experimental  $\Delta E_B$  and the corresponding  $a_{nn} \approx 19.3$  fm. This is well outside the experimental error bar of  $a_{nn}$  (shaded region). We note that the small discrepancy between the theoretical and experimental  $\Delta E_B$  cannot be resolved by an adjustment of the nn forces to an  $a_{nn}$  within the experimental error bar.



$\lambda$	$E_b(^3\text{H})$ [MeV]	$a_{nn}$ [fm]
0.9990	-8.474	-18.75
0.9995	-8.478	-18.86
1.0000	-8.482	-18.97
1.0005	-8.486	-19.08
1.0010	-8.491	-19.19
1.0020	-8.499	-19.42

Table 4.14: Strength factor  $\lambda$  for the  $^1\text{S}_0$  nn force, resulting  $^3\text{H}$  binding energy  $E_b$  and nn scattering length  $a_{nn}$ . The calculations are based on the CD-Bonn 2000 potential modified by the strength factor in the  $^1\text{S}_0$  partial wave and the TM 3NF with  $\Lambda = 4.795 m_\pi$  adjusted to the original CD-Bonn 2000 interaction.

Summarizing we found predictions of  $\Delta E_B$ , which do not depend on the interaction model. We confirmed the sensitivity to  $a_{nn}$ . Moreover we showed that there is a small discrepancy to the experiment, which cannot be resolved by an adjustment of the nn forces to  $a_{nn}$ 's within the error bar of the experimental scattering length. We expect that one or more of the following improvements should resolve the problem:

- We neglected relativistic effects in our calculations. Because the differences are very small ( $\approx 10$  keV), they might visibly contribute to the discrepancy.
- The experimental  $a_{nn}$  is not completely settled. A remeasurement might resolve the problem. In this context we note that a recent determination resulted in  $a_{nn} = 16.3$  fm [6, 7], which would completely wipe out our current understanding of  $\Delta E_B$ .
- The most likely reason for the small difference of theory and experiment is a small CSB in the 3N interaction. Our current understanding of 3NF's is not sufficient to understand CSB effects on this level

In the remaining part of this section, we will look on the dependence of momentum distributions and correlations on the CSB interactions.

To this aim we compare in Fig. 4.13 the neutron momentum distributions in  $^3\text{H}$  to the proton momentum distributions in  $^3\text{He}$  for CD-Bonn+TM and AV18+TM. On the logarithmic scale we cannot distinguish both distributions (thick and thin lines) in the whole momentum range. Only the detailed look in the inset reveals a small shift of the neutron momentum distributions (thick lines) to slightly higher momenta. This effect can be expected due to the higher binding energy of  $^3\text{H}$ . Because the differences are very small compared to expected experimental error bars, we state that the momentum distributions are not significantly affected by CSB forces.

We performed a similar comparison of the momentum correlations of nn pairs in  $^3\text{H}$  and pp pairs in  $^3\text{He}$ . Also this comparison showed that both correlations agree to a very high accuracy. Only in the low momentum region we observed a small shift of the nn pair prediction to higher momenta. Also these differences are non-significant.

This closes our investigations of the 3N system. In the next section we apply our model Hamiltonians to the 4N system. A look to the 4N binding energies will reveal, whether our models can be successfully applied to the 4N system at least in its ground state.

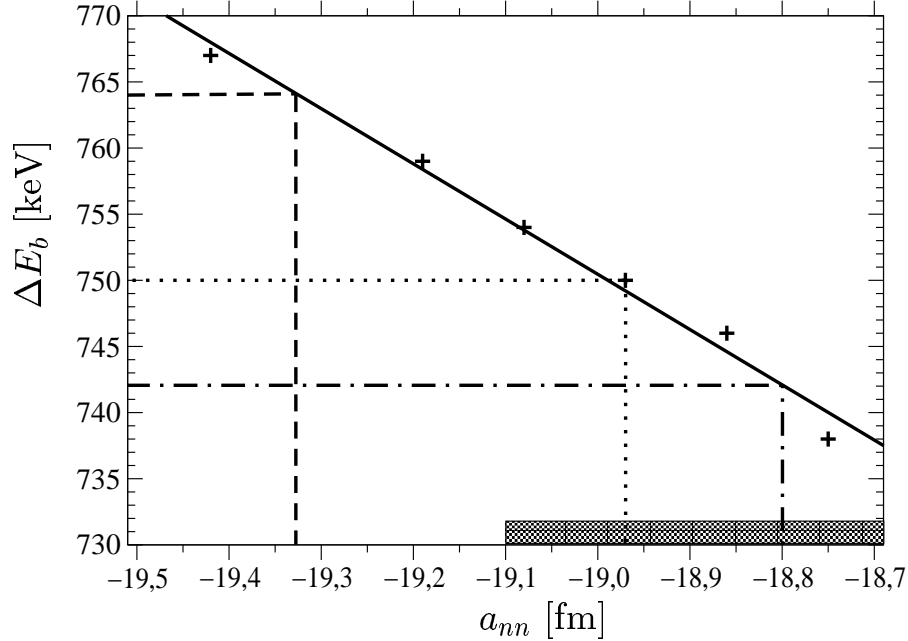


Figure 4.12: Difference of the  ${}^3\text{He}$  and  ${}^3\text{H}$  binding energies  $\Delta E_b$  dependent on the nn scattering lengths  $a_{nn}$ . The crosses are based on the calculations shown in Table 4.14, the solid line is a linear fit to the crosses and the shaded region on the  $a_{nn}$ -axis indicates the experimental error bar of  $a_{nn}$ . The dashed, the dotted and the dashed dotted lines mark pairs of  $\Delta E_b$  and  $a_{nn}$ , which belong to the experimental  $\Delta E_b$ , the predictions of CD-Bonn 2000 and today's experimental  $a_{nn}$  value, respectively.

## 4.5 The $\alpha$ -particle binding energy and the size of 4NF's

In Section 4.2 we developed model Hamiltonians, which are able to describe the binding energies of the 3N system with very high accuracy. They are based on NN interactions, which provide an accurate description of the NN observables. In this section we will apply the Hamilton operators purely based on the modern NN pair interactions and our model Hamiltonians including 3NF's to the  $\alpha$ -particle. We would like to find out, to what extent these models are able to describe the 4N system at least in its ground state. Especially, we are interested in the question, whether 4N interactions are necessary for a description of the  $\alpha$ -particle binding energy. This is not a trivial question. The strong coupling constant is too big to estimate perturbatively the contribution of higher order diagrams to the interaction. The assumption, that the importance of higher order forces is small, cannot be established analytically.

The numerical calculations are based on the partial wave decomposition described in Chapters 2 and 3. For the  $\alpha$ -particle calculations we restrict  $l_{sum}^{max}$  to 14 and obtain binding energies, which are converged within 50 keV. For the 4N system we do not make fully charge dependent calculations. We only take total isospin  $T = 0$  states into account. Based on truncated calculations with  $l_{sum}^{max} = 4$  we estimated the contribution of the  $T = 1$  and  $T = 2$  channels to 10 keV, which is non-significant in view of our numerical accuracy. Our results are based on equal neutron and proton masses of  $m_N = 938.943$  MeV.

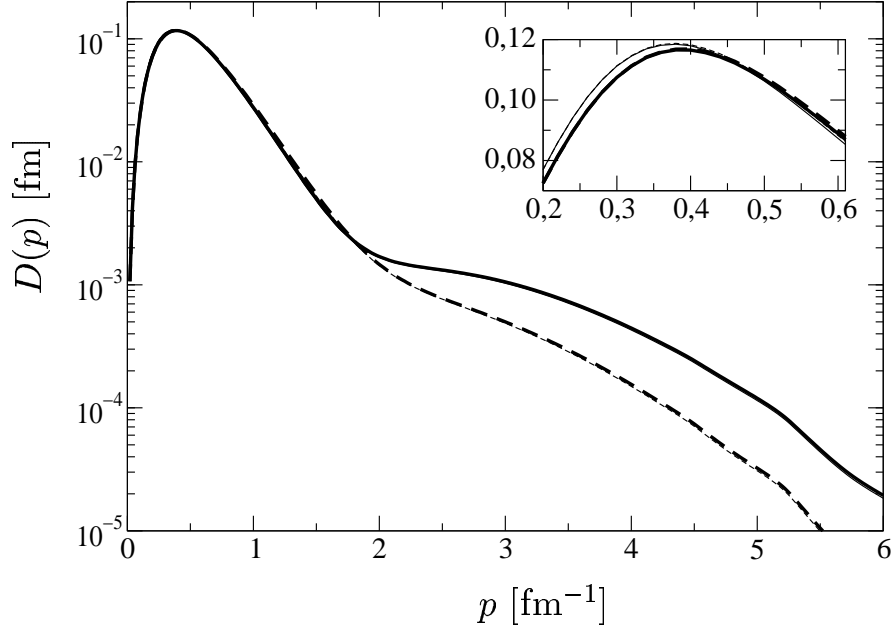


Figure 4.13: Neutron momentum distributions in  ${}^3\text{H}$  (thick lines) compared to the proton momentum distributions in  ${}^3\text{He}$  (thin lines) on a logarithmic scale. The distribution functions are based on calculations using the AV18+TM (solid lines) and CD-Bonn+TM (dashed lines) potentials. The inset shows more details of the low momentum region on a linear scale. The functions are normalized to  $\int D(p)dp = \frac{1}{4\pi}$ .

Perturbatively we checked that the neutron-proton mass difference contributes not more than 2 keV. Therefore we are able to determine the  $\alpha$ -particle binding energy from realistic non-relativistic Hamilton operators within 50 keV.

In Table 4.15 we present our results for the most modern NN interactions and compare them to the experimental result and a NCSM calculation [46]. The binding energy prediction for CD-Bonn agrees in both schemes. One sees that present day NN potential models underpredict the 4N binding energy. The deviation from the experimental value varies between  $\approx 2$  MeV and  $\approx 4$  MeV. As in the 3N system the binding energies strongly depend on the NN interaction.

In Ref. [124] a strong correlation of the  ${}^3\text{H}$  and  ${}^4\text{He}$  binding energy predictions for different potential models has been observed. In Fig. 4.14 this correlation is shown for our new results, which are based on nearly phase equivalent potentials. One sees that there is to a high accuracy a linear relation between the predictions of the  ${}^3\text{H}$  and  ${}^4\text{He}$  binding energies for all modern NN interactions (crosses). One also observes that a linear fit (so called Tjon-line) to our predictions does not hit the experimental point (star) exactly. Does this linear correlation still hold, if we include 3NF's into our Hamiltonian? This would lead to an overprediction of the  $\alpha$ -particle binding energy by the model Hamiltonians, which are adjusted to the 3N binding energy.

Again the difference to the experimental result might be the result from relativistic effects, 3NF's and, additionally in the 4N system, 4N forces (4NF's). We have to neglect relativistic effects.

We apply the model Hamiltonians developed in Section 4.2 to the 4N system to see the effects of 3NF's

interaction	$E_\alpha$	$H$	$T$	$V_{NN}$
Nijm 93	-24.53	-24.55	95.34	-119.89
Nijm I	-24.98	-24.99	84.19	-109.19
Nijm II	-24.56	-24.55	100.31	-124.86
AV18	-24.28	-24.25	97.83	-122.08
CD-Bonn	-26.26	-26.23	77.15	-103.38
CD-Bonn [46]	-26.4(2)	—	—	—
Exp.	-28.30	—	—	—

Table 4.15:  $\alpha$ -particle binding energy predictions  $E_\alpha$  of several NN potential models compared to the experimental value and the “no-core shell model” result [46]. The expectation values of the kinetic energy  $T$ , the NN interaction  $V_{NN}$  and the Hamilton operator  $H$  are also shown. All energies are given in MeV.

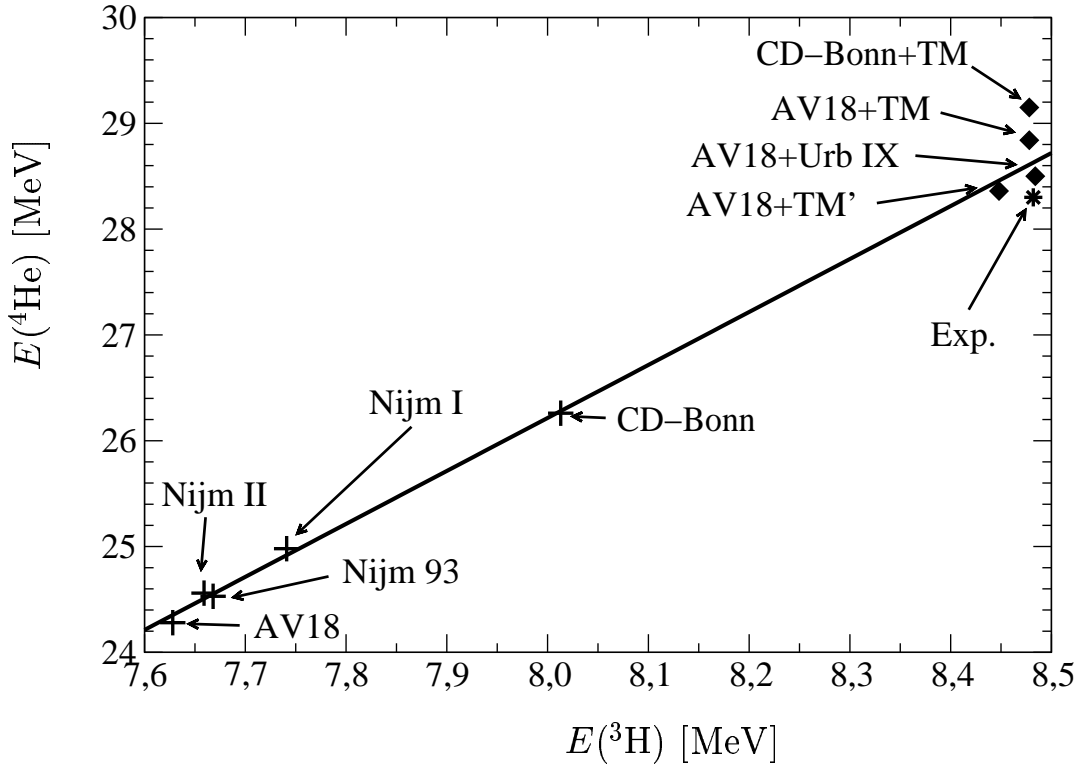


Figure 4.14: Tjon-line:  $\alpha$ -particle binding energy predictions  $E(^4\text{He})$  dependent on the prediction of the  $^3\text{H}$  binding energy for several realistic interaction models. Predictions of interaction models without (crosses) and with (diamonds) 3NF are shown. The experimental point is marked by a star. The line represents a least square fit to the predictions of models without 3NF.

interaction	$E_\alpha$	$H$	$T$	$V_{NN}$	$V_{3NF}$
CD-Bonn+TM	-29.15	-29.09	83.92	-106.16	-6.854
AV18+TM	-28.84	-28.81	111.84	-132.62	-8.033
AV18+TM'	-28.36	-28.40	110.14	-133.36	-5.178
AV18+Urbana IX	-28.50	-28.53	113.21	-135.81	-5.929
AV18+Urbana IX (Argonne) [33]	-28.34(4)	—	110.7(7)	-135.3(7)	-6.3(1)
Exp.	-28.30	—	—	—	—

Table 4.16:  $\alpha$ -particle binding energy predictions  $E_\alpha$  of the CD-Bonn and AV18 interactions in conjunction with various 3NF's compared to the experimental value and the Argonne-Los Alamos result. The expectation values of the kinetic energy  $T$ , the NN interaction  $V_{NN}$ , the 3NF  $V_{3NF}$  and the Hamilton operator  $H$  are also shown. All energies are given in MeV.

to the 4N binding energy. Table 4.16 shows the results and the experimental value. For AV18+Urbana IX we can compare to a calculation using GFMC [33]. We find a small deviation, which we cannot explain. Similar differences show up in the 3N system (see Table 4.4). However, both results agree within 0.7 % of the binding energy.

As expected 3NF's contribute to the binding energy attractively. The model Hamiltonians overpredict the experimental binding energy by up to 850 keV. In Fig. 4.14 we also marked these results (diamonds). It is noticeable that the TM' and Urbana IX results are quite close to the Tjon-line. Both 3NF's overpredict the  $\alpha$ -particle binding energy only slightly. Their predictions are slightly below the Tjon-line. In contrast the Hamiltonians based on the TM-3NF visibly overpredict the 4N binding energy.

Unfortunately, the predictions of our various NN and 3N force combinations are not completely model independent, but vary in a certain range changing its NN or 3N interaction. We note that the inclusion of 3N interactions reduces the model dependence from  $\approx 2$  MeV in Table 4.15 to 0.8 MeV in Table 4.16. For the following considerations, we do not take the AV18+TM' result into account, because its fit to the  ${}^3\text{H}$  binding energy is less accurate (see Section 4.2) than for the other interactions. Moreover its prediction is similar to the Urbana IX result, if one considers the deviation of the results from the Tjon-line in Fig. 4.14. The average  $\alpha$ -particle binding energy of the remaining three model Hamiltonians is -28.83 MeV. Our predictions change in a range of width  $\pm 320$  keV. The difference of the average to the experimental result is 530 keV. Assuming that the range covered by our model calculations is a measure of the uncertainty due to failures in our 3N Hamiltonians, we conclude that we overpredict the 4N binding energies by 530 keV with an uncertainty of 320 keV.

For a judgment on the size of possible 4NF's, we assume that those 530 keV overprediction are removed by a repulsive effect of 4NF's. This means the effect of 4NF's is 1.87 % of the  $\alpha$ -particle binding energy. Comparing the calculations with and without 3NF's, we find an average attraction of 3NF's in the 4N system of 3.89 MeV, which is roughly 13.75 % of the  $\alpha$ -particle binding energy.

This strong decrease of the importance of 4NF's compared to 3NF's is an indication that 4NF's are small at least in the 4N system for angular momentum  $J = 0$  and isospin  $T = 0$ . To the best of our knowledge this is the first estimate of the effect of 4N interactions based on realistic model calculations for the 4N system. The decrease of importance going from 2N to 3N to 4N interactions confirms the generally accepted picture that nuclei can be described in terms of NN interactions and small contributions of 3N interactions. This justifies the program of the Argonne-Los Alamos collaboration using a Hamiltonian consisting of NN and 3N interactions to describe bound and resonance states up to  $A = 8$  [33].

model	$S$	$P$	$D$
CD-Bonn	89.06	0.22	10.72
CD-Bonn+TM	89.65	0.45	9.90
AV18	85.89	0.35	13.76
AV18+TM	85.36	0.77	13.88
AV18+TM'	83.58	0.75	15.67
AV18+Urb IX	83.23	0.75	16.03

Table 4.17:  $S$ ,  $P$  and  $D$  state probabilities for the  ${}^4\text{He}$  wave functions. All probabilities are in %.

## 4.6 Properties of the 4N wave function and the influence of the 3NF on the wave function properties

In this section we generalize the investigations of Section 4.3 to the  $\alpha$ -particle. The possibility to obtain accurate descriptions of the 4N wave function for several realistic NN interactions is one of the main advantages of the Faddeev-Yakubovsky scheme. It turned out that the partial wave expansion of the  $\alpha$ -particle wave function needs a tremendous number of partial waves. Therefore it was not possible to obtain wave functions for the  $\alpha$ -particle in Ref. [36]. With the increased computational resources of today's supercomputers we are able to give also results for converged wave functions now.

To demonstrate the reliability of our calculations we present the expectation value for the Hamilton operators  $H$  in Tables 4.15 and 4.16. In all cases we can confirm the binding energy derived from the eigenvalues of the Yakubovsky equations within 60 keV (0.2 % of the binding energy and 0.06 % of the kinetic energy). We consider this as a great success of the numerical method applied in this thesis.

In the same tables we give the individual contributions of the kinetic energy  $T$ , the NN potential energy  $V_{NN}$  and in Table 4.16 of the 3NF  $V_{3NF}$  to the expectation value  $H$ . We see that the predictions for  $T$  and  $V$  strongly depend on the used NN interaction. We also note that the dependence of  $T$  on the 3NF is less striking. Similar to the 3N system CD-Bonn predicts remarkably smaller kinetic and potential energies.

The expectation values of the 3NF's shown in Table 4.16 are significantly bigger than their contribution to the binding energy. This excludes a perturbative treatment of 3NF's in the 4N system.

The ratio of 3N potential energy and NN potential energy increases going from 3N to the 4N systems (e.g. from  $\approx \frac{1}{40}$  to  $\approx \frac{1}{16}$  for CD-Bonn+TM). Therefore we expect that 3NF effects are more pronounced in the 4N system. At the end of this section we will investigate effects of the 3NF's in more detail.

Now we turn to a look to the  $S$ -,  $P$ - and  $D$ -state probabilities. In Table 4.17 our results are given. Again the numbers represent a simple and effective possibility to compare wave function properties in benchmarks.

As expected the  $S$ -state is the dominant part the  $\alpha$ -particle wave function. In the 4N system the  $P$ -wave component is slightly more important than in the 3N system. Again we find roughly twice as large  $P$ -components for calculations including a 3NF. Also the  $D$ -waves are more important in the 4N than in the 3N system. Our values indicate that their size also depends on the interplay of NN and 3N interactions. In conjunction with CD-Bonn the  $D$ -state probability decreases in the presence of the TM-3NF. In contrast there is a slight increase in conjunction with AV18. It is noticeable that TM' and Urbana IX lead to a stronger increase of the  $D$ -state probability than TM.

Correspondingly to Eq. (4.2), one defines the momentum distributions of protons and neutrons in

the 4N system (replacing  $p_3$  by  $q_4$ ). Because we neglect isospin  $T = 1$  and 2 components in the wave function, we cannot distinguish the proton and neutron distributions and define the nucleon momentum distribution

$$D(p) \equiv D_n(p) = D_p(p) \quad (4.16)$$

Again we normalize the momentum distribution functions to

$$\int_0^\infty D(p) dp = \frac{1}{4\pi} \quad (4.17)$$

The interaction dependence of  $D(p)$  is very similar to the 3N system. We find that the distributions are equal for low momenta smaller  $1.5 \text{ fm}^{-1}$  as long as the model interaction predicts roughly the correct binding energies (3N and 4N). The high momentum tail above  $2 \text{ fm}^{-1}$  depends on the NN interaction. We do not exemplify this behavior here.

Instead of this we have a look to the 3NF dependence of  $D(p)$  in Fig 4.15. Again we find the scaling behavior with the binding energy: the prediction of AV18 (dotted line) differs in the low momentum region from the identical results of the interaction models including 3NF's. In the region around  $p = 2.5 \text{ fm}^{-1}$  we observe a slight deviation of the calculations based on AV18+TM (solid line) and AV18+TM'/Urbana IX. Because we see no differences in the low momentum region (see inset), this is no effect of the slightly different 4N binding energies. Though the size of the effect is extremely small, we note that the different structures in the TM, TM' and Urbana IX interactions seem to be visible in the momentum region around  $p = 2.5 \text{ fm}^{-1}$ .

In Fig. 4.16 a comparison of the  $^3\text{H}$  and  $^4\text{He}$  momentum distributions is shown. We see a shift of the maximum of  $D(p)$  from  $p = 0.4 \text{ fm}^{-1}$  for  $^3\text{H}$  (solid and dashed lines) to  $p = 0.6 \text{ fm}^{-1}$  for  $^4\text{He}$  (dashed dotted lines). The  $\alpha$ -particle distributions are broader than the 3N ones. From the higher binding energy and the higher nuclear density of the  $\alpha$ -particle we can expect these results. We note that the differences in the momentum distributions of neutrons and protons in  $^3\text{H}$  are in size comparable to the differences to the nucleon distribution in the 4N system. In the enlargement in the inset one clearly sees that the distribution functions of CD-Bonn+TM and AV18+TM overlap in the low momentum region for both nuclei,  $^3\text{H}$  (solid lines and dashed lines) and  $^4\text{He}$  (dashed dotted lines). This confirms the model independence of the low momentum distribution functions.

The definition of correlation functions as given in Eq. (4.5) is easily generalized to the  $\alpha$ -particle. In the same way we define configuration space correlation as the probability to find two nucleons with fixed charge  $q$  and spin state  $s m_s$  at a certain interparticle distance  $r$ :

$$C_{s m_s}^{q=pp,np,nn}(\vec{r}) = \frac{1}{2J+1} \sum_M \langle \Psi JM | \delta^3(\vec{r} - \vec{r}_{12}) P_{12}^S(s m_s) P_{12}^T(q) | \Psi JM \rangle \quad (4.18)$$

Also for configuration space correlations we find the simple angular dependence underlying the separation given in Eq. (4.6) (see Appendix E). Spin- and charge-dependent functions in configuration space can be defined correspondingly to the momentum space versions from Eqs. (4.9) and (4.10).

Because of an interesting similarity of configuration space correlation functions for different nuclei, we present a comparison for the  $^2\text{H}$ ,  $^3\text{H}$  and  $^4\text{He}$  correlations in the spin  $s = 1$  state in Fig. 4.17. We normalized the functions to the same peak height. In this normalization one observes that the correlations do not depend on the nucleus for interparticle distances  $r \leq 1.6 \text{ fm}$ . In this region the correlations depend on the NN interaction used. CD-Bonn (thin lines) predicts an increased probability to find two nucleons with small distances. In contrast the long distance behavior is ruled by the binding energy. Therefore

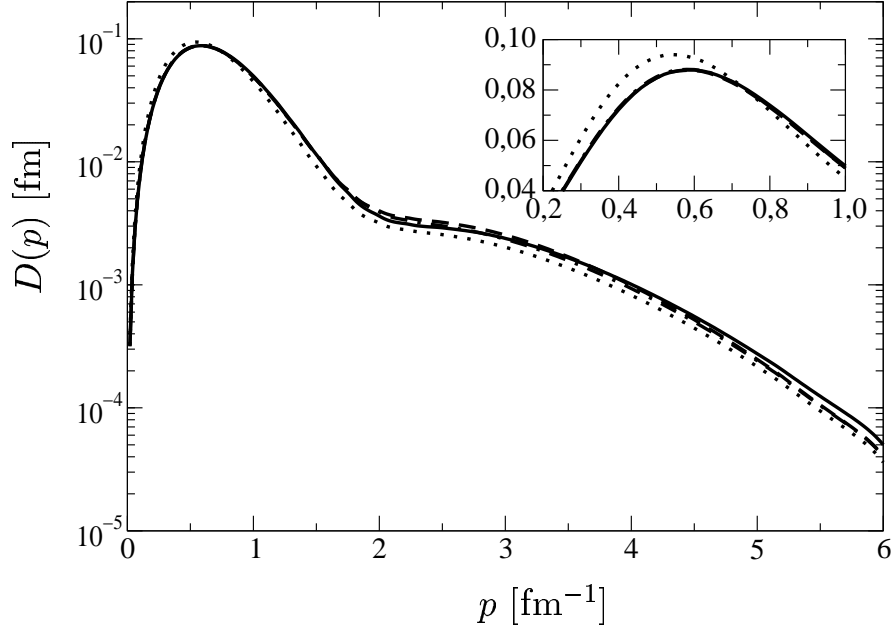


Figure 4.15: Nucleon momentum distributions in  ${}^4\text{He}$  on a logarithmic scale. The distribution functions are based on calculations using the AV18+TM (solid lines), AV18+Urbana IX (dashed lines), AV18+TM' (dashed dotted lines) and AV18 (dotted lines) potentials. The inset shows more details of the low momentum region on a linear scale. The functions are normalized to  $\int D(p)dp = \frac{1}{4\pi}$ .

we see that the tail above  $r = 1.6$  fm differs for the various nuclei, but is independent from the used interaction as long as the predicted binding energies are similar (the thick and thin lines overlap in this region). We do not show the  $s = 0$  correlation, but we confirmed a similar behavior.

As we have already argued in Section 4.3, the relation between experimental observables and correlations in configuration space is not direct. Therefore we prefer the presentation of momentum space correlations in this thesis. In the following we present spin-dependent and charge-dependent correlations as given in Eqs. (4.9) and (4.10). Again we normalize the correlation functions for each spin- or charge-state separately as outlined in Eq. (4.11).

The individual importance of the different spin- and charge-states is given by the probability  $P_s^q$  to find two nucleons with charge  $q$  and in spin state  $s$  from Eq. (4.8). For the  $\alpha$ -particle we summarize  $P_s^q$  in Table 4.18. Our restriction to isospin  $T = 0$  states implies that nn and pp correlations are equal. The small  $P_s^q$  values for nn and pp pairs in spin  $s = 1$  states are again a consequence of the Pauli principle. The important two nucleon  ${}^3\text{S}_1$ -state cannot contribute for nn and pp pairs. To our surprise the contribution of the higher partial waves to  $P_1^{nn/pp}$  is smaller for the  $\alpha$ -particle than for  ${}^3\text{H}$  (see Table 4.9). The unbalance between  $s = 0$  and  $s = 1$  states is slightly increased in the 4N system compared to the 3N system. We also observe that the effect of the TM forces on the difference between  $s = 0$  and  $s = 1$  states depends on the NN interaction. This behavior didn't show up in the 3N wave functions and indicates a stronger 3NF dependence of 4N wave functions in comparison to 3N wave functions.

We start with a study of the interaction dependence in Fig. 4.18. The figure shows the NN correlation



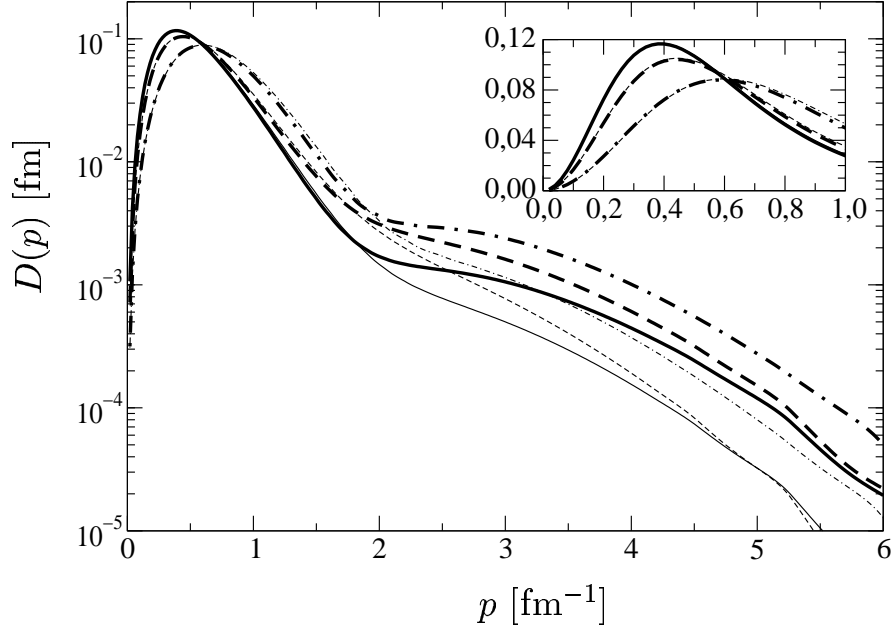


Figure 4.16: Neutron (solid lines) and proton momentum distributions in  ${}^3\text{H}$  (dashed lines) compared to the nucleon momentum distributions in  ${}^4\text{He}$  (dashed dotted lines) on a logarithmic scale. The distribution functions are based on calculations using the AV18+TM (thick lines) and CD-Bonn+TM (thin lines) potentials. The inset shows more details of the low momentum region on a linear scale. The functions are normalized to  $\int D(p)dp = \frac{1}{4\pi}$ .

for spin  $s = 0$  for the CD-Bonn and AV18 interactions without and with TM 3NF. For momenta below  $p = 1.5 \text{ fm}^{-1}$  we observe the same scaling behavior as in the 3N system: the predictions are identical for both NN interactions, if they are accompanied by 3NF's and the interaction models predict roughly the experimental binding energy. For higher momenta we find a strong dependence of the correlation on the NN interaction. The 3NF does not have a comparable strong effect in this region.

In Fig. 4.19 we present the same comparison for spin  $s = 1$  states. Though the differences in the low momentum region ( $p \leq 1.5 \text{ fm}^{-1}$ ) are small, we do not find the same scaling behavior. Compared to the 3N system, the differences of the CD-Bonn+TM and AV18+TM predictions are more pronounced. For the higher momenta we see the usual dependence on the NN interaction. The inclusion of the TM force has only slight effects on  $C_s$ .

In the whole range of momenta and for both spins we found no sensitivity on the 3NF model applied. Because the curves overlap in the whole momentum range, we omit the corresponding figures.

This leads us to a comparison of momentum correlations for different nuclei. We compare our spin  $s = 1$  predictions for  ${}^2\text{H}$ ,  ${}^3\text{H}$  and  ${}^4\text{He}$  in Fig. 4.20. In momentum space one finds clear differences in the correlations. With increasing mass number  $A$  the maximum of the correlations shifts to higher momenta and the peak is broaden. From Fig. 4.17 we know that the long range correlations in configuration space are quite different for different  $A$ , but the short range correlations are very similar. Therefore the peak position and peak width in momentum space seem to be related to the long range correlations. In the

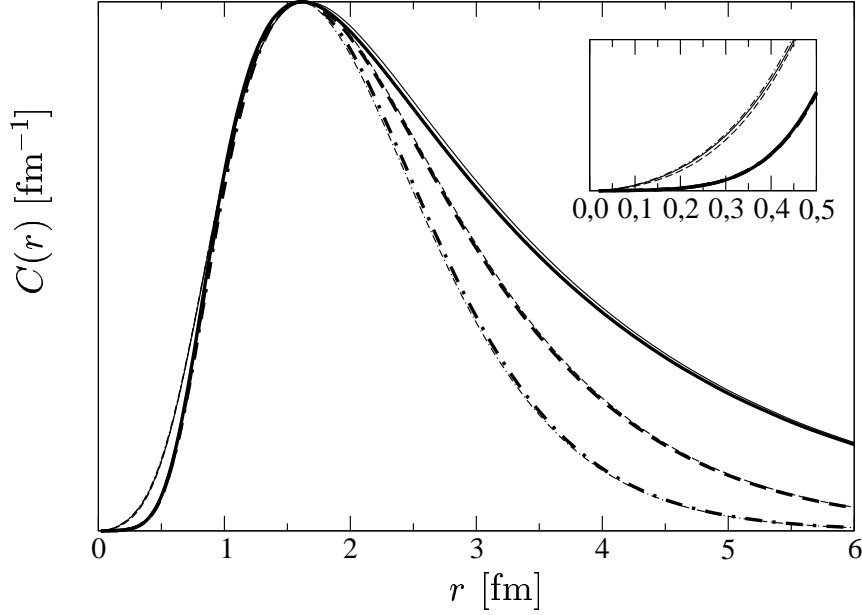


Figure 4.17: NN correlations in  ${}^2\text{H}$  (solid lines),  ${}^3\text{H}$  (dashed lines) and  ${}^4\text{He}$  (dotted dashed lines) for spin  $s = 1$  in configuration space. The correlation functions are based on calculations using the AV18+TM (thick lines) and the CD-Bonn+TM (thin lines) interaction. The inset shows more details of the small distance region. The functions are normalized to the same peak height. They are given in arbitrary units on a linear scale.

	$s = 0$			$s = 1$		
	nn/pp	np	NN	nn/pp	np	NN
CD-Bonn	14.82	14.97	44.60	1.85	51.70	55.40
CD-Bonn+TM	14.94	15.09	44.98	1.72	51.57	55.02
AV18	14.31	14.45	43.07	2.36	52.21	56.93
AV18+TM	14.27	14.41	42.95	2.40	52.25	57.05
AV18+TM'	13.96	14.13	42.05	2.71	52.54	57.95
AV18+Urb IX	13.91	14.06	41.87	2.76	52.60	58.13

Table 4.18: Probabilities  $P_s^q$  to find NN pairs in spin  $s = 0$  and  $s = 1$  states in  ${}^4\text{He}$  as given in Eq. (4.8). We give separate results for nn/pp and np pairs and the sum (NN) of the nn, pp and np contributions. Our restriction to  $T = 0$  states implies that  $P_s^{pp} = P_s^{nn}$ . All probabilities are given in %.

figure we give results for the CD-Bonn+TM interaction, we checked that the same behavior also holds for other interaction models and spin  $s = 0$  states (comparing  ${}^3\text{H}$  and  ${}^4\text{He}$ ).

A comparison of the spin dependence of the correlation reveals a similar behavior as in the 3N System. In Fig. 4.21 we compare  $C_s$  for  $s = 1$  and  $s = 0$  states. Again we find a strong spin dependence of the correlation functions in the low momentum region. The model dependence of the  $s = 1$  results is much

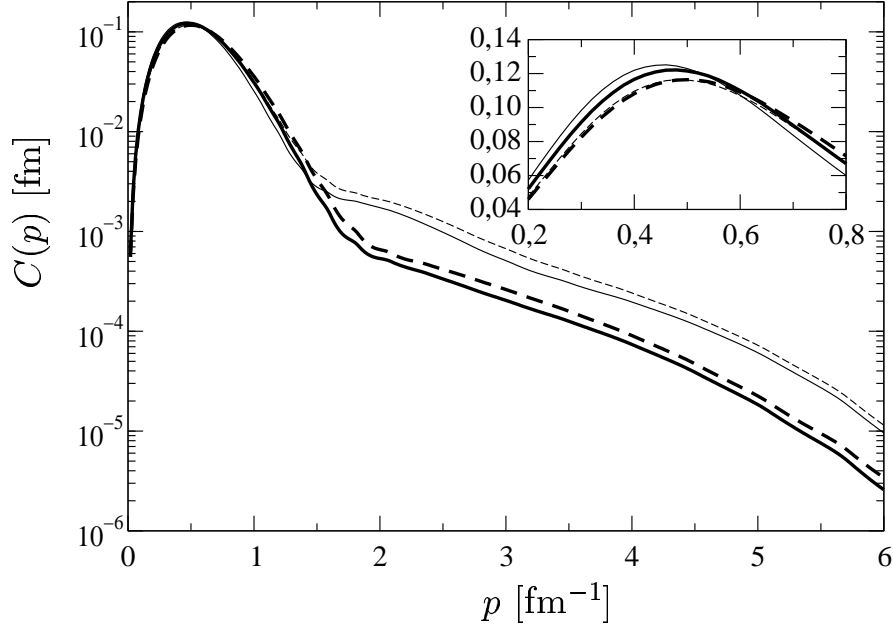


Figure 4.18: NN correlations in  ${}^4\text{He}$  for spin  $S = 0$  compared for different 2N potentials with and without TM 3NF on a logarithmic scale. The correlation functions are based on calculations using the CD-Bonn (thick solid line), CD-Bonn+TM (thick dashed line), AV18 (thin solid line), AV18+TM (thin dashed line) potentials. The inset shows more details of the low momentum region on a linear scale. The functions are normalized to  $\int C(p)dp = \frac{1}{4\pi}$ .

smaller than the differences of  $s = 1$  and  $s = 0$  results. For higher momenta the  $s = 1$  correlations drop very slowly. This holds for both interaction models shown. Nevertheless, the predictions for momenta above  $p = 1.5 \text{ fm}^{-1}$  are quite NN interaction dependent. In this region the spin dependence of the correlation cannot be separated from the interaction dependence.

We already emphasized that we cannot distinguish nn and pp pairs in our approximation to  $T = 0$  isospin states. Therefore the charge dependent correlations  $C^q$  are indistinguishable for pp and nn pairs. From the results shown in Table 4.18 we would expect that the nn/pp momentum correlations are driven by the  $s = 0$  and the np correlations by  $s = 1$  contributions. As in the 3N system the results do not confirm this expectation. From Fig. 4.22 we learn that the nn/pp and np correlations are very similar in the low momentum region. The inset shows that the interaction dependence is more visible than the np and nn/pp differences. For momenta between  $p = 2.5 \text{ fm}^{-1}$  and  $p = 3.0 \text{ fm}^{-1}$  the deviations are most clear. As could be expected the np correlations, which get more contributions from  $s = 1$ , drop slower than the nn/pp one. However the differences are not as pronounced as for the spin dependence and are only visible in momentum regions, where the correlations are model dependent.

The angular dependent parts  $\hat{C}_{s m_s}$  are similar in shape and magnitude as for  ${}^3\text{H}$ . Therefore we omit their presentation for  ${}^4\text{He}$ .

This closes our survey on momentum distributions and correlations. The results for the 4N system are qualitatively very similar to the 3N system. We nearly find model independence in the low momentum

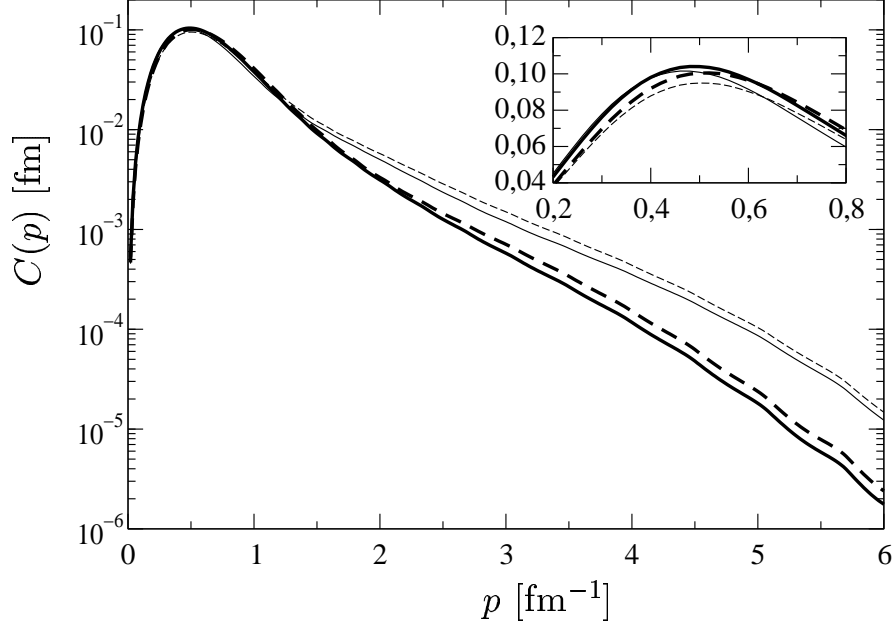


Figure 4.19: NN correlation in  ${}^4\text{He}$  for spin  $s = 1$  compared for different 2N potentials with and without TM 3NF on a logarithmic scale. The correlation functions are based on calculations using the CD-Bonn (thick solid line), CD-Bonn+TM (thick dashed line), AV18 (thin solid line), AV18+TM (thin dashed line) potentials. The inset shows more details of the low momentum region on a linear scale. The functions are normalized to  $\int C(p)dp = \frac{1}{4\pi}$ .

region below  $p = 1.5 \text{ fm}^{-1}$ . An interesting point to us is the spin dependence of the correlation function, which is visible in the low and high momentum region and which is very similar for 3N and 4N systems. We also note that 3NF's do not significantly affect the distributions and correlations. Our predictions for different 3NF models are very similar. In this view we expect that observables, which are sensitive to NN correlations or momentum distributions are not sensitive to the 3N force model. Nevertheless, we observed a scaling behavior with the binding energy in some cases. This means that quantitative comparisons of interaction models require the inclusion of 3NF's to obtain results, which are not obscured by wrong predictions for the 3N and 4N binding energies.

In recent years the  ${}^3\text{H}/{}^4\text{He}$ -overlap functions received much attention [125, 126, 127, 128]. They are defined as

$$\hat{T}_{m_t}(\vec{p}) = \frac{1}{2J+1} \sum_M \langle \Psi JM | \delta^3(\vec{q}_4 - \vec{p}) | \phi_t j_t m_t \rangle \langle \phi_t j_t m_t | \Psi JM \rangle \quad (4.19)$$

$\hat{T}$  is the projection of the  $\alpha$ -particle wave function  $\Psi$  on the  ${}^3\text{H}$  bound state  $\phi_t$  with its angular momentum  $j_t m_t$ . The momentum of the fourth nucleon is fixed to  $\vec{p}$ . We average the overlap function over all possible spin orientations  $M$ . In the special case of the  $\alpha$ -particle with  $J = 0$ , there is no averaging necessary. In Appendix E we give explicit expressions for  $\hat{T}$  using our partial wave decomposition. It turns out that  $\hat{T}$  is independent from  $m_t$  and from the angle of  $\vec{p}$ . To our surprise this also holds for other angular

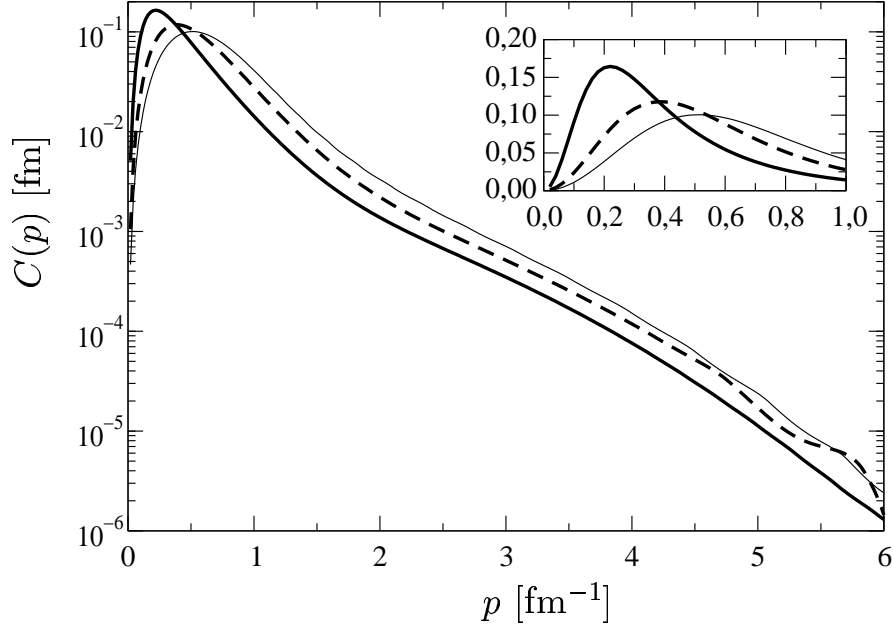


Figure 4.20: NN correlation in  ${}^2\text{H}$  (thick solid line),  ${}^3\text{H}$  (thick dashed line) and  ${}^4\text{He}$  (thin solid line) for spin  $s = 1$  on a logarithmic scale. The correlation functions are based on calculations using the CD-Bonn+TM interaction. The inset shows more details of the low momentum region on a linear scale. The functions are normalized to  $\int C(p)dp = \frac{1}{4\pi}$ .

momenta than  $J = 0$ . One finds that only the relative S-wave of the nucleon and the 3N bound state can contribute to  $\hat{\mathcal{T}}$ , because of the angular momenta and parities of the  $\alpha$ -particle and  ${}^3\text{H}$ . This is an important feature. It clearly distinguishes the properties of  $\hat{\mathcal{T}}$  from  $\hat{\mathcal{D}}$  as given in Eq. (4.12). The relative S-wave contribution in both cases has got a node, which can be led back clearly to short range correlations [129]. Therefore the node position is interaction dependent. This node is clearly visible in  $\hat{\mathcal{T}}$ , but washed out in  $\hat{\mathcal{D}}$ , because of D-wave contributions. There are ideas to measure the node position in proton knock-out  ${}^4\text{He}(e,e'p){}^3\text{H}$  experiments. However, the reaction mechanism is not as clearly dominated by the plane wave impulse approximation (PWIA) as it is necessary for an extraction of the node position from electron scattering data. A recent measurement of the knock-out reaction at NIKHEF [125] did not show the expected dip structure in the cross sections. This could be explained by strong FSI and MEC effects in the momentum region considered. New theoretical calculations using the “generalized eikonal approach (GEA)” [130] predicted kinematical regions, in which the FSI and MEC contributions are suppressed. For those kinematics a new experiment is approved at TJLab [126]. In the following we present our results for  $\hat{\mathcal{T}}$ . This is the first time that the overlap-function could be calculated for *several* realistic 4N Hamiltonians including 3NF’s. We are interested in a confirmation of the model dependence based on Hamiltonians, which predict the same 3N and 4N binding energies and are phase equivalent in the NN system. We would also like to see whether the results show a dependence on the 3NF model.

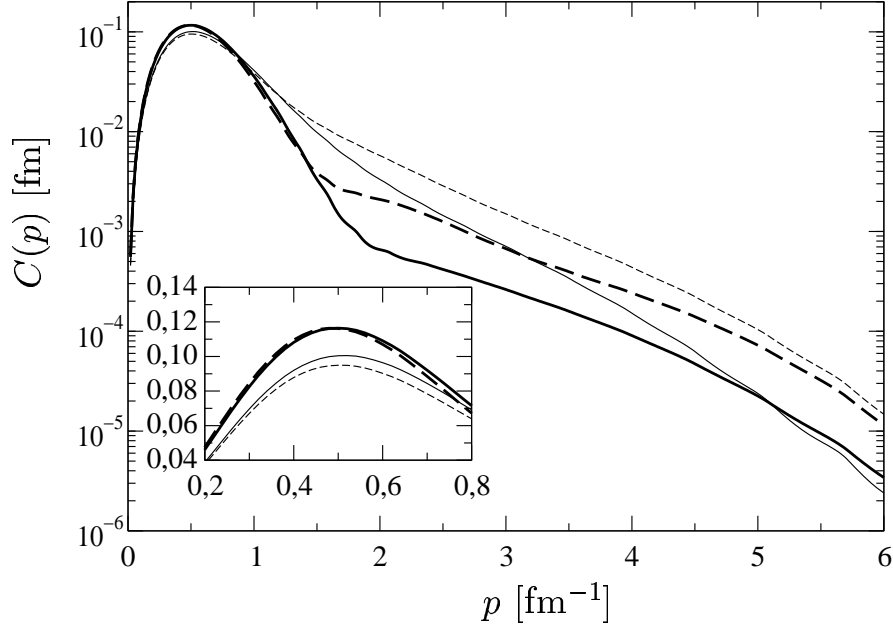


Figure 4.21: NN correlations in  ${}^4\text{He}$  compared for 2N spin  $s = 0$  (thick lines) and  $s = 1$  (thin lines) in momentum space on a logarithmic scale. The correlation functions are based on calculations using the CD-Bonn+TM (solid lines) and AV18+TM (dashed lines) potentials. The inset shows more details of the low momentum region on a linear scale. The functions are normalized to  $\int C(p)dp = \frac{1}{4\pi}$ .

In Table 4.19 we present the normalization constants

$$N_t = \int d^3p \hat{\mathcal{T}}(p) \quad (4.20)$$

They give the probability to find a  ${}^3\text{H}$  bound state within  ${}^4\text{He}$ . In contrast to similar results for the  ${}^2\text{H}/{}^3\text{H}$  overlap shown in Table 4.11, the results are bigger now. The  ${}^3\text{H}$  and  ${}^4\text{He}$  wave functions have got a similar spin structure. The contributions of  $s = 0$  and  $s = 1$  pairs is roughly equal in both nuclei. This distinguishes them from the purely  $s = 1$  2N bound state.  $N_t$  ranges from 80 % to 85 %. It is remarkable that the results depend on the NN interaction as well as on the kind of 3NF.

Therefore we look at the NN interaction dependence in Fig. 4.23. For a better comparison we defined a normalized overlap function  $\mathcal{T}(p) = \frac{N}{p^2} \hat{\mathcal{T}}(p)$ . As usual the normalization is chosen as

$$\int_0^\infty dp \mathcal{T}(p) = \frac{1}{4\pi} \quad (4.21)$$

The figure reveals a scaling behavior for momenta below  $p \leq 1 \text{ fm}^{-1}$  (see dashed and dotted line in the inset). We also find the expected dependence of the position of the node around 2-2.5  $\text{fm}^{-1}$  on the NN interaction. One sees that CD-Bonn and CD-Bonn+TM predicts the node around 2.5  $\text{fm}^{-1}$ , whereas AV18 and AV18+TM lead to slightly smaller  $p$ 's. The deviations in the node position only slightly

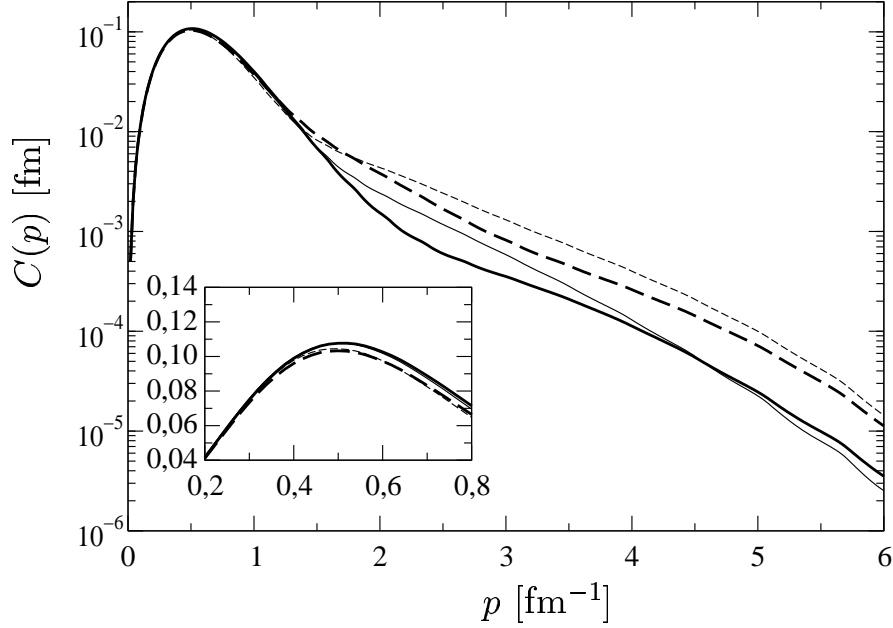


Figure 4.22: Spin averaged nn (thick lines) and np (thin lines) correlations in  ${}^4\text{He}$  on a logarithmic scale. The correlation functions are based on calculations using the CD-Bonn+TM(solid lines), and AV18+TM (dashed lines) potentials. The inset shows more details of the low momentum region on a linear scale. The functions are normalized to  $\int C(p)dp = \frac{1}{4\pi}$ .

interaction	$N_t({}^4\text{He})$
CD-Bonn	84.46
CD-Bonn +TM	83.49
AV18	82.40
AV18+TM	80.84
AV18+Urbana IX	80.33
AV18+TM'	80.54

Table 4.19: Normalization constants  $N_t$  of the  ${}^3\text{H}$ -p overlap distributions in  ${}^4\text{He}$ . Results are given in %.

depend on the action of a 3NF. The height of the second maximum around  $3 \text{ fm}^{-1}$  is sensitive to the NN interaction and to the presence of a 3NF.

Fig. 4.24 compares the predictions for various 3NF models. We see that for momenta below  $5 \text{ fm}^{-1}$   $\mathcal{T}$  does not significantly depend on the 3NF chosen. We conclude that both, the node position and the height of the second maximum are sensitive to the NN interaction. The inclusion of 3NF's is indispensable to guarantee correct binding energies though the used model has nearly no influence on  $\mathcal{T}$ . We admit that our predictions are based on non-relativistic calculations. In the momentum region of the node  $p/m$  reaches already 0.5. Relativistic effects might become important in this region. However, the predictions

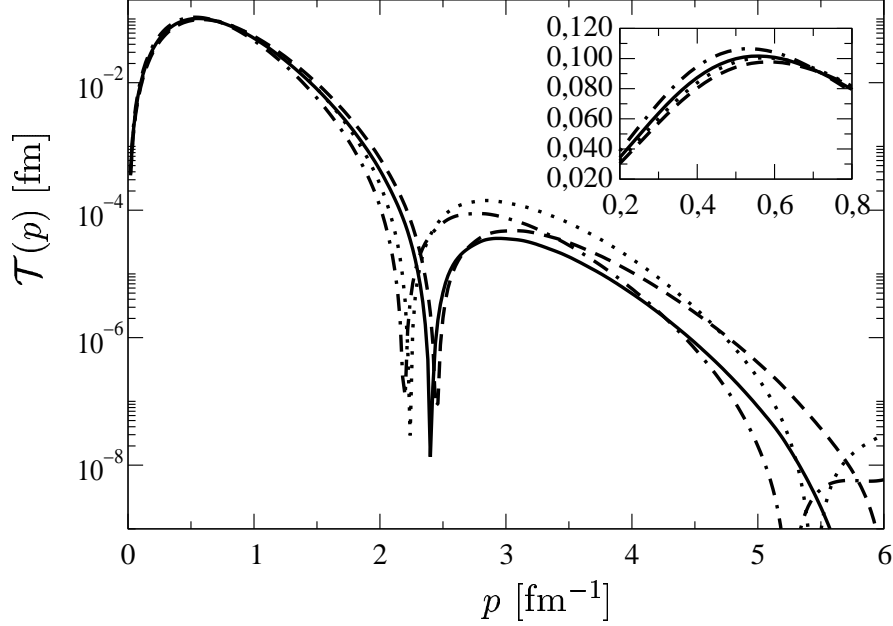


Figure 4.23:  ${}^3\text{H}$ - $p$  momentum distribution  $\mathcal{T}$  in  ${}^4\text{He}$  on a logarithmic scale. The distribution functions are based on calculations using the CD-Bonn (solid line), CD-Bonn+TM (dashed line), AV18 (dashed dotted line) and AV18+TM (dotted line) potentials. The inset shows more details of the low momentum region on a linear scale. The functions are normalized to  $\int \mathcal{T}(p)dp = \frac{1}{4\pi}$ .

for height of the second maximum differ by a factor of 3. We expect that the NN interaction dependence is more pronounced than possible relativistic effects and that the shown results are significant. A relativistic calculation is highly desirable to confirm this assumption.

In this section we presented various wave function properties, which hardly show any dependence on the kind of 3NF. In contrast we found that the expectation values of the different 3NF's given in Table 4.16 are strongly 3NF dependent. For a more detailed look to these expectation values, we expanded the wave functions in states of fixed total orbital angular momenta. For the  $\alpha$  particle  $S$ ,  $P$  and  $D$  states contribute.

$$|\Psi\rangle = |\Psi_S\rangle + |\Psi_P\rangle + |\Psi_D\rangle = \sum_L |\Psi_L\rangle \quad (4.22)$$

Correspondingly, the expectation value of the 3NF separates into  $3 \times 3 = 9$  overlaps for each  $L$  and  $L'$  combination:  $\langle \Psi_L | V_{123} | \Psi_{L'} \rangle$ . Numerically we find that the most important contributions arise from the S-S, S-P/P-S, S-D/D-S and D-D matrix elements. Table 4.20 shows these matrix elements for the Urbana IX and TM 3NF's. For each 3NF we present two results. One is based on a wave function calculated from the AV18 interaction only. The other result is based on a wave function calculated from AV18 and the 3NF in focus.

First we compare the results based on the AV18 wave functions for the Urbana IX and TM 3NF. We see strong differences in the contributions of the different partial waves, which show that the two 3NF's tremendously differ in their structure. The diagonal S-S and D-D matrix elements for Urbana-IX are



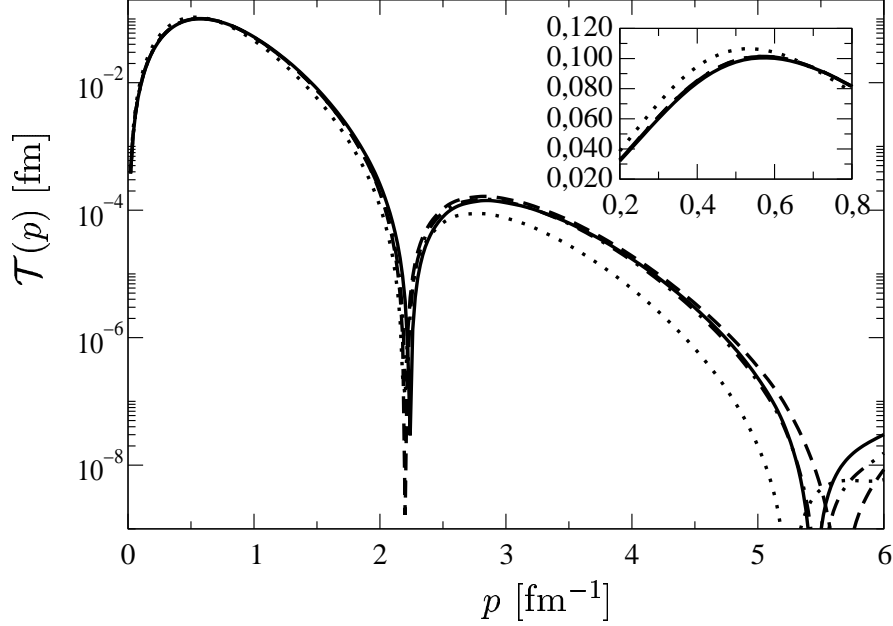


Figure 4.24:  ${}^3\text{H}$ - $p$  momentum distribution  $\mathcal{T}$  in  ${}^4\text{He}$  on a logarithmic scale. The distribution functions are based on calculations using the AV18+TM (solid line), AV18+Urbana IX (dashed line), AV18+TM' (dashed dotted line) and AV18 (dotted line) potentials. The inset shows more details of the low momentum region on a linear scale. The functions are normalized to  $\int \mathcal{T}(p)dp = \frac{1}{4\pi}$ .

	Urbana IX		TM	
	(AV18)	(AV18+Urb IX)	(AV18)	(AV18+TM)
S-S	+3.16	+2.74	-2.34	-4.09
S-P/P-S	-0.96	-2.10	-1.22	-3.56
S-D/D-S	-5.44	-7.46	+2.08	-0.14
D-D	+0.59	+0.85	+0.01	+0.06

Table 4.20: Contribution of different total orbital angular momenta in the wave functions to the expectation values of the Urbana IX and TM 3NF's. All energies are given in MeV.

strongly repulsive. In contrast the S-S part of TM is attractive and the D-D matrix element only gives a minor contribution. We argue that this is a result of the phenomenological repulsive part of Urbana IX, which conserves the orbital angular momentum. This means of course that this part dominates the S-S interaction. The contribution of the  $2\pi$  exchange is less important for this matrix element. For TM the S-S contribution gives most of the attraction. In this point the 3NF models are very different. The overall attraction of Urbana IX is supplied by the very strong S-D contribution. We state that this comparison shows the very different action of the TM and Urbana IX forces in the 4N system.

Next we regard the Urbana IX results going from the AV18 to the AV18+Urbana IX wave function.

We see that the individual contributions change visibly. There is a remarkable increase of the S-P/P-S and S-D/D-S attraction. The summed up repulsive contributions of S-S and D-D slightly decrease.

For TM we find very interesting changes comparing the results based on AV18 and AV18+TM wave functions. The S-S and S-P/P-S attraction is increased. It is very remarkable that the strong S-D/D-S repulsion predicted by the AV18 wave function turns to an attractive contribution for the AV18+TM wave function. In the presence of the TM interaction the 4N configuration is changed qualitatively. The differences cannot be explained by a small shift to higher momentum components. It is also remarkable that this qualitative difference in the wave function is not visible in the NN correlations and momentum distributions.

This closes the investigation of 4N bound state properties. To a great extent we found model independent predictions also for 4N wave functions. We emphasize that there are still model dependences for higher momenta. Those are predominately caused by the NN interactions. The kind of 3NF does not significantly affect correlations, momentum distributions and overlap functions. This is an important insight, because it allows reliable investigation of NN force effects on e.g. short correlations in few-nucleon bound states without exact knowledge of the 3NF. This isn't a trivial statement, because we showed that the 3NF's affect the wave function in a very subtle, but significant way and that the observed effects strongly depend on the used 3NF interaction model.

In the next chapter we will turn to the hypernuclear bound states. In contrast to ordinary nuclear physics, the underlying YN interactions are not settled. It will be interesting to compare the predictions of the various, very different interaction models.

## Chapter 5

# The Light Hypernuclei

In this chapter we turn to the light hypernuclear few-body systems.

Hypernuclear interactions are still not settled. Because there are nearly no YN scattering data, it has not been possible yet to determine unambiguously the spin structure of the YN interaction. Several interaction models have been proposed. In Section 5.1 we start with a brief introduction into the meson-theoretical models used in this thesis and work out their very different predictions for  $\Lambda\text{N}$  scattering observables. Nevertheless all these models are consistent with the measured YN scattering observables.

Do the model differences show up in the hypernuclear few-body bound states? In Section 5.2 we look at the lightest hypernuclear bound system: the hypertriton. We confirm that only the Nijmegen models provide enough attraction to form a bound state. For the first time we present converged calculations for the new Nijmegen SC97 interactions. We also rise the question, whether effective  $\Lambda\text{N}$  interactions without conversion can describe the hypertriton accurately. Section 5.3 deals with the properties of the hypertriton wave function. We describe the different structures predicted by the SC89 and SC97 models.

Unfortunately, the hypertriton is very weakly bound. This complicates experimental investigations tremendously. Moreover, we found that many interaction models do not bind the hypertriton. We expect a different situation for the four-body hypernuclei.  ${}^4_{\Lambda}\text{He}$  and  ${}^4_{\Lambda}\text{H}$  possess two experimentally verified bound states with different spins. The binding energies of both states are considerably higher than the hypertriton binding energy. Therefore they are an ideal laboratory to check the spin structure of the existing YN models. In Section 5.4 we present the, to the best of our knowledge, first binding energy predictions for  ${}^4_{\Lambda}\text{H}$  and  ${}^4_{\Lambda}\text{He}$  based on realistic NN, YN and 3N interactions. We do not rely on simplified approximations to the YN potentials. The wide range of forces enables us to investigate the dependence of the binding energy on the YN interaction and also on the NN interaction and 3NF. Unfortunately, there are no three-baryon force (3BF) models for the ANN system available, which would enable us to estimate numerically their contribution to the binding energies. Instead of this we generalize our experience in the 3N and 4N system and make rough estimations on their strength. We find that they might visibly affect the predicted  $0^+-1^+$  splitting.

Because we expect that the properties of the wave function are less affected by those ANN interactions, we summarize our insights into the structure of  ${}^4_{\Lambda}\text{He}$  bound state based on calculations without 3BF in Section 5.5. Here we can pin down some characteristic differences of the predictions for different YN interaction models. We also observe the effects of the attractive short range interaction in some  $\Sigma\text{N}$  channels.

In Section 5.6 we more closely look to the binding energy differences of  ${}^4\text{He}$  and  ${}^4\text{H}$ . We argue that

they are strongly related to  $\Lambda$ - $\Sigma$  conversion and that our predictions are less obscured by missing ANN interactions. Therefore these binding energy differences can give important new insights on the validity of the current YN interaction models.

## 5.1 Overview on YN interaction models

In this section we give a brief overview on the YN interaction models used in this thesis. We compare the underlying theoretical input and show some of their predictions for YN scattering. Because the potentials of the Nijmegen group seem to describe the available scattering data slightly more accurate than the Jülich interactions, there is some emphasis on their work. Nevertheless we also address a model proposed by the Jülich group. The model is able to give interestingly different predictions especially in the four-body systems. Unfortunately, its prescription of the YN data is slightly less accurate. All models are based on the OBE.

The Nijmegen group has got a longstanding experience in modeling the YN interaction based on the OBE [47, 53, 54, 51, 55]. In this thesis we only apply their more recent soft core models: the original soft core model SC89 [54] and the series of models SC97a-f [51]. SC89 and SC97 are based on very similar theoretical assumptions.

OBE models of nuclear interactions involve a set of parameters, which have to be determined from the available scattering data. In general these are coupling constants of the baryon-baryon-meson (BBM) vertices and cut-off parameters of BBM form factors. In contrast to the NN system, these parameters cannot be fixed by the scarce YN scattering data. The physical idea is to impose flavor SU(3) constraints on the coupling constants and adjust their size by fits to NN data. Also the strong  $\Lambda$ - $\Sigma$  coupling naturally arises in this framework. In the Nijmegen models pseudoscalar ( $\pi$ ,  $\eta$ ,  $\eta'$ ,  $K$ ), vector ( $\rho$ ,  $\phi$ ,  $K^*$ ,  $\omega$ ) and scalar ( $a_0(962)$ ,  $f_0(760)$ ,  $f_0(993)$ ,  $\kappa$ ) mesons are considered. Each of the three kinds of mesons is treated as a flavor SU(3) nonet of mesons. Additionally the model includes the Pomeron exchange, which provides additional short range repulsion. Three mechanisms introduce flavor SU(3) symmetry breaking:

1. The physical hadron masses are used
2. Mixing of the isoscalar meson of the octets and the singlet meson is assumed. The mixing angle is a new parameter.
3.  $\Lambda$ - $\Sigma_0$  mixing provides a long range  $\Lambda N$  interaction due to  $\Lambda\Lambda\pi$  coupling.

Up to now, all dynamical input is the same for the SC89 and SC97 models. But there are a few conceptual differences. First, the form factor cut-offs are related to YN channels in SC89, whereas SC97 assumes that the form factors are attached to the BBM vertices. Second, the  $\frac{F}{F+D}$  ratio  $\alpha_V^m$  related to the vector meson couplings is constrained by weak decay data in SC89. In SC97 this parameter takes six different values for the six models of the series SC97a-f. It is used as a strength parameter for the spin-spin interaction in SC97. And third, the SC97 models include additional SU(3) breaking based on the so called  $^3P_0$  model (see [51]).

Unfortunately, it turned out that all SC97 models predict a spurious  $\Lambda N$  bound state at  $\approx 500$  MeV. This property tremendously slowed down the convergence of our numerical calculations. Therefore we had to remove the spurious bound state from the potentials and perform the diagonalization of our kernel with “corrected” potentials. In the case of the hypertriton we could check the equivalence of both potentials by comparing calculations with the original and the corrected interactions. For four-body

systems we compared our binding energy results to the expectation values of the Hamiltonians based on the full interaction and found agreement.

For nuclear structure calculations an approximation to the SC97f model has been developed [131], to which we refer as SC97f-sim. This interaction simulates the SC97f low energy phaseshifts with a Gaussian form of the interaction. The potential includes a Gaussian approximation to the  $\Lambda$ - $\Sigma$  conversion potential of SC97f. For this interaction we performed benchmarks to other existing schemes. The results are presented in Sections 5.2 and 5.4.

The Jülich group also invented a series of models, from which we chose the Jülich  $\tilde{A}$  interaction [52] for our calculations. This model impose SU(6) flavor-spin symmetry on the coupling constants, which also fix the  $\frac{F}{F+D}$  ratios. In this way all coupling constants are determined by NN data. The model also includes the  $\Lambda$ - $\Sigma$  conversion process. The conceptual difference to the Nijmegen models is the treatment of the scalar mesons. The model only considers the  $\sigma$  meson. It is seen as an effective parameterization of the correlated two-meson exchange. This is inspired by the multi-meson exchange Bonn model of the NN interaction. In consequence no symmetry constraints apply to its coupling constants. They are free parameters to be also fitted to the YN data. In contrast to the Nijmegen interaction, the potential keeps the full Dirac structure of the baryons and is strongly non-local. We refer to Ref. [56] for a detailed comparison of the Jülich models to the SC89 model.

In Fig. 5.1 the  $\Lambda p$  cross section predictions below the  $\Sigma$  threshold are shown. We give results for three SC97 models, the SC89 interaction and the Jülich  $\tilde{A}$  model. The Jülich model sticks out, because it cannot accurately describe the data around 35 MeV. This can be led back to a resonance in the  $^1S_0$  state. The available data are quite accurate in this energy region. Therefore we consider that as a failure of the model.

The Nijmegen interactions predict in this region comparable results. Differences become visible below 20 MeV, but all Nijmegen models are consistent with the available data. It is remarkable that the cross sections for zero energy are different. The group of SC97 models predict considerably higher cross sections than SC89. It seems that the SC89 model provides less attraction than the new models. We will see later, that this is not true for the hypernuclear bound states. Again Jülich  $\tilde{A}$  sticks out as it leads to very small cross sections near zero energy.

In Table 5.1 the scattering lengths and effective ranges for  $\Lambda p$  and  $\Lambda n$  scattering are presented. They provide a more detailed look into the spin dependence of low energy scattering. From the scattering lengths  $a$  we read off that the relative strength of the  $^1S_0$  and  $^3S_1$  channels covers a wide range of values.

Especially the series of SC97 models provides interactions, which predict similar  $\Lambda p$  total cross sections, but differ in the relative strength of their  $^1S_0$  and  $^3S_1$  potentials. This confirms that their spin structure is not constrained by the available scattering data and the dynamical input into the underlying models. We point out that the series of SC97 models allows investigations of this spin structure in few-body systems, which are not obscured by a different overall strength of the interactions.

The SC89 and SC97f interactions give comparable  $^1S_0$  scattering lengths. However, we find a very small  $^3S_1$  scattering length for SC89. We note that our predictions for the SC89 scattering lengths slightly differ from the published results in Ref. [54]. We cannot explain these differences. We did not find similar differences for the SC97 models comparing to Ref. [51].

The Jülich interaction predicts very small scattering lengths in both states. Surprisingly for us, we observe extremely small  $\Lambda N$  effective ranges in  $^1S_0$ , which are strongly dependent on the charge of the YN system. According to the arguments of Ref. [65], these small effective ranges should lead to higher binding energies in few-body calculations. We will see later, whether this effect is visible in our results for three- and four-body hypernuclei.

We note that the scattering lengths indicate a visible CSB of the  $\Lambda p$  and  $\Lambda n$  interaction, which is

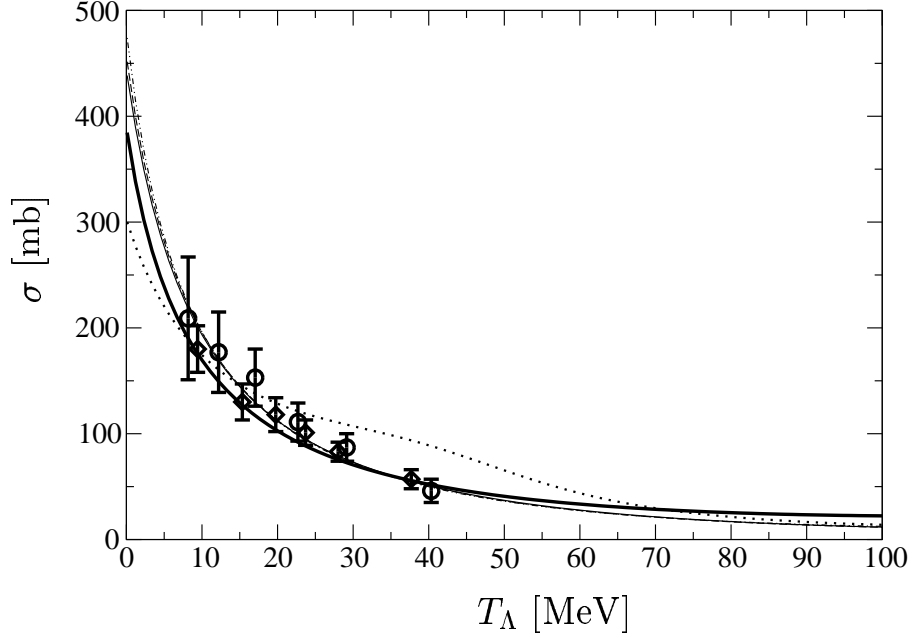


Figure 5.1: Total  $\Lambda p$  elastic cross section  $\sigma$  dependent on the  $\Lambda$  laboratory energy. The predictions of Nijm SC97d (thin solid line), Nijm SC97e (thin dashed line), Nijm SC97f (thin dashed dotted line), Nijm SC89 (thick solid line) and Jülich  $\tilde{A}$  (dotted line) are compared to data from [132] (circles) and [133] (diamonds).

model dependent. The SC97 scattering lengths predict more attraction in  $^1S_0$  in the  $\Lambda n$  than in the  $\Lambda p$  system. In contrast we find smaller  $a$ 's for  $^3S_1$  in  $\Lambda n$  scattering. This is different for SC89. Whereas the  $^1S_0$  predictions are similar in  $\Lambda p$  and  $\Lambda n$ , the  $^3S_1$  force results in much smaller  $a$ 's for  $\Lambda n$ . For the Jülich interaction we already mentioned the strong difference in the effective ranges of  $\Lambda p$  and  $\Lambda n$ . In addition we see that the  $^1S_0$  scattering length is charge dependent. For  $^3S_1$  we only observe a small CSB.

In Figs. 5.2 to 5.4 the most important  $\Lambda p$  phaseshifts below the  $\Sigma$  threshold for SC97d-f and SC89 are presented. In Fig. 5.2 we show the  $^1S_0$  phaseshifts. Their shape is very similar in all cases and the size of the phaseshifts is consistent with the scattering lengths of Table 5.1.

This is very different for the  $^3S_1$  phaseshifts in Fig 5.3. Again the size of the phases for energies below 30 MeV is consistent with the scattering lengths, but we observe an unexpectedly rising tail in the case of SC89. It indicates a very attractive  $^3S_1$  interaction near the  $\Sigma$  threshold.

These differences do not show up in the total cross section. The missing attraction in the  $^3S_1$  channel of SC97 is equalized by additional attraction in  $^3D_1$  as one can see in Fig. 5.4. We note that the SC97 interactions predict very similar shapes for the phaseshifts, whereas the old SC89 interaction visibly deviates from the shape predicted by SC97.

Summarizing we see that the spin dependence of YN low energy scattering is completely undetermined by present day data and models. We saw that the SC97 models have got the very interesting feature to describe the total cross sections nearly equally and, in the same time, to differ in their spin structure.

potential	$\Lambda p$				$\Lambda n$			
	$^1S_0$		$^3S_1$		$^1S_0$		$^3S_1$	
	$a$	$r$	$a$	$r$	$a$	$r$	$a$	$r$
SC97a	-0.70	5.90	-2.15	2.76	-0.76	6.13	-2.11	2.72
SC97b	-0.90	4.95	-2.11	2.83	-0.96	5.11	-2.06	2.80
SC97c	-1.20	4.13	-2.06	2.92	-1.28	4.23	-2.04	2.87
SC97d	-1.70	3.47	-1.93	3.03	-1.82	3.53	-1.91	3.02
SC97e	-2.10	3.19	-1.83	3.20	-2.24	3.24	-1.78	3.15
SC97f	-2.51	3.03	-1.73	3.33	-2.68	3.07	-1.64	3.35
SC89	-2.59	2.90	-1.38	3.17	-2.62	3.02	-1.18	3.45
Jülich $\tilde{A}$	-2.07	0.48	-1.33	3.90	-1.74	0.97	-1.32	3.92

Table 5.1: Scattering lengths  $a$  and effective ranges  $r$  in fm for different YN potentials.

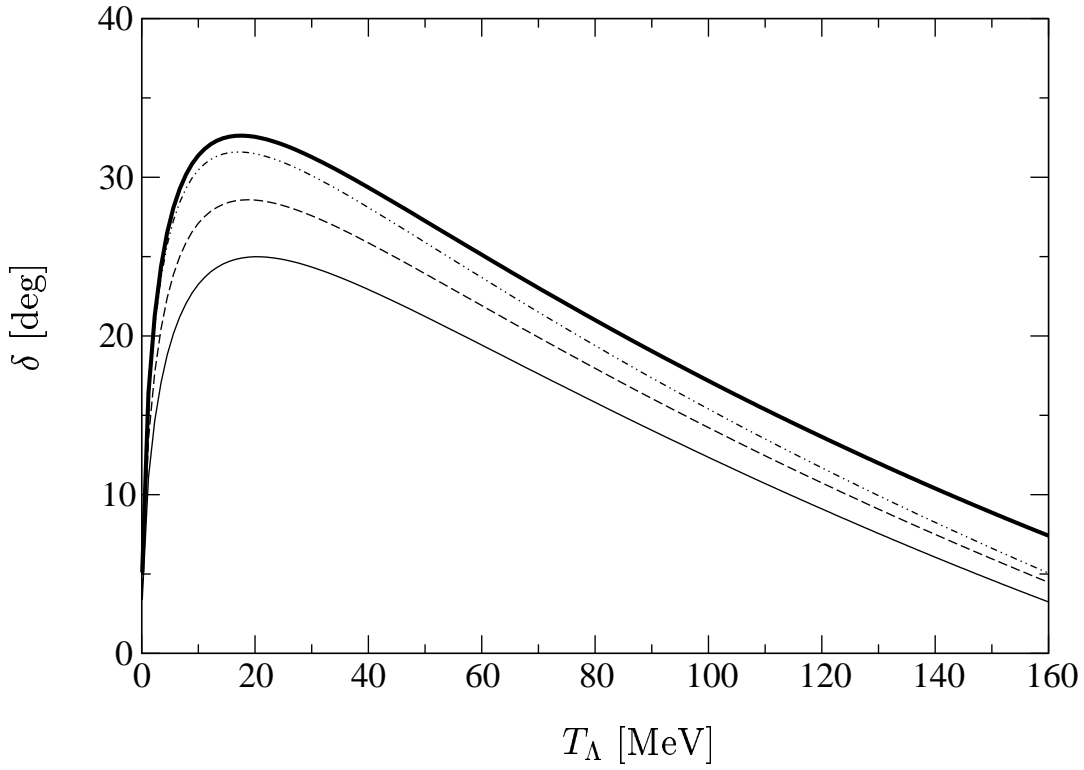


Figure 5.2:  $^1S_0$   $\Lambda p$  phaseshifts dependent on the  $\Lambda$  laboratory energy. The predictions of Nijm SC97d (thin solid line), Nijm SC97e (thin dashed line), Nijm SC97f (thin dashed dotted line) and Nijm SC89 (thick solid line) are compared.

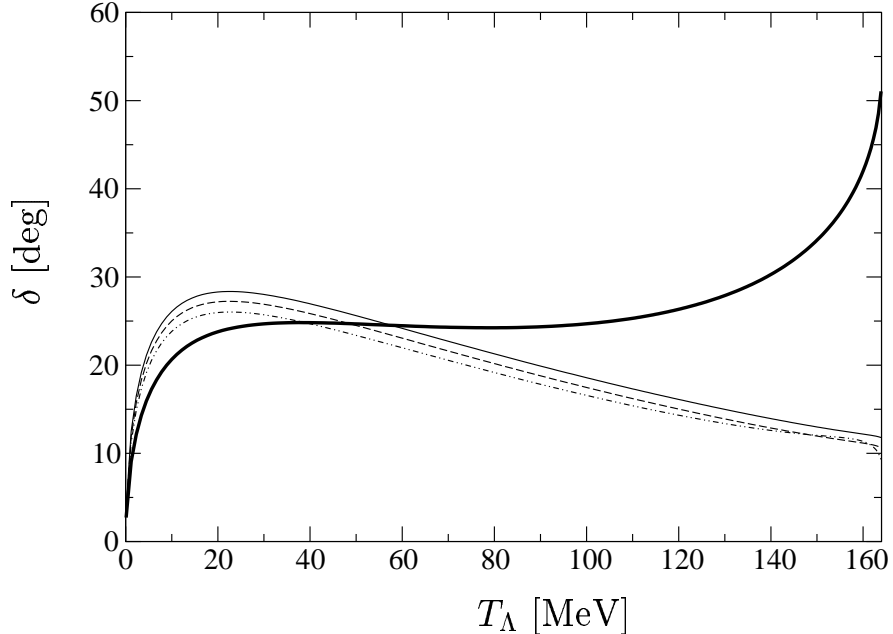


Figure 5.3:  ${}^3S_1$   $\Lambda p$  phaseshifts dependent on the  $\Lambda$  laboratory energy. The predictions of Nijm SC97d (thin solid line), Nijm SC97e (thin dashed line), Nijm SC97f (thin dashed dotted line) and Nijm SC89 (thick solid line) are compared.

As we shall see, SC97f provides the most realistic hypertriton binding energy of the SC97 series (see Section 5.2). Because SC97d is the closest model to SC97f, which predicts a larger scattering length in  ${}^3S_1$  than  ${}^1S_0$ , we choose the SC97 models d, e and f for further investigations and compare their results to SC89 and the Jülich  $\tilde{A}$  interactions.

We start with a look to the hypertriton binding energies in the next section.

## 5.2 Hypertriton binding energies

In this section we summarize our binding energy results for  ${}^3_\Lambda\text{H}$ .

Our results have been obtained by solving the Faddeev equations for  ${}^3_\Lambda\text{H}$ . Very similar to Ref. [76, 75] we take the  $\Lambda$ - $\Sigma$  conversion fully into account. The estimate of our numerical uncertainty in Section 3.3.1 showed that the results are converged within 1.8 keV. To this aim we take partial waves up to  $j_{12}^{max} = 6$  into account.

Additionally to the former work [76, 75], our calculations include the full charge dependence of the interaction. We consider isospin  $T = 0$  and  $T = 1$  states, the Coulomb force of  $pp$  and  $p\Sigma^-$  pairs created by  $\Lambda$ - $\Sigma$  conversion and mass differences of the nucleons and  $\Sigma$  particles. However, a perturbative estimate showed that the Coulomb force and the mass difference negligibly contribute to the binding energy. We found for Bonn B and SC89 1.0 keV Coulomb repulsion in  $pp$  pairs and -0.8 keV attraction in  $p\Sigma^-$  pairs. The mass differences changed the kinetic energy by less than 1 keV.



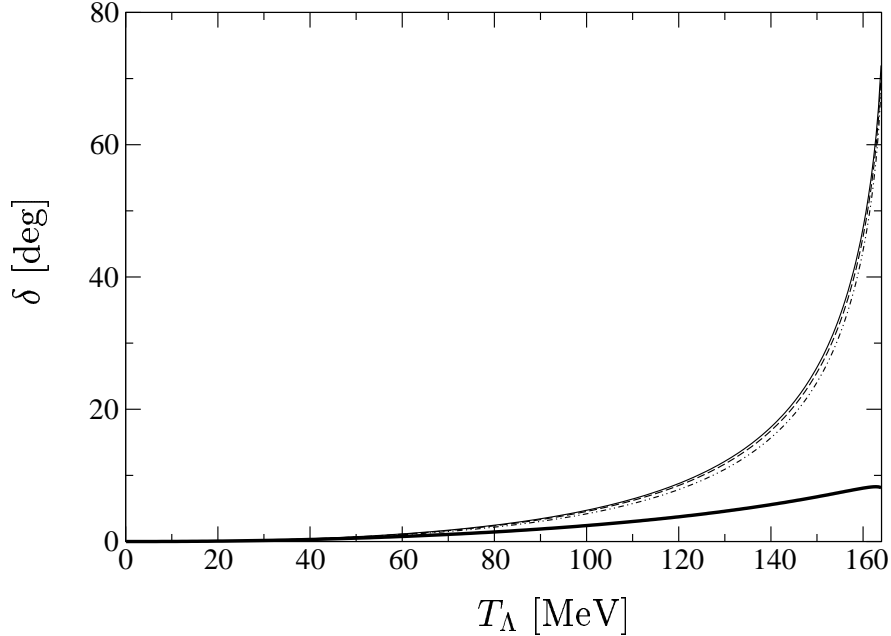


Figure 5.4:  ${}^3D_1$   $\Lambda p$  phaseshifts dependent on the  $\Lambda$  laboratory energy. The predictions of Nijm SC97d (thin solid line), Nijm SC97e (thin dashed line), Nijm SC97f (thin dashed dotted line) and Nijm SC89 (thick solid line) are compared.

Our results are presented in Table 5.2. They are in good agreement with the Bonn B+SC89 (Nijm 93 +SC89) binding energies of -2.37 (-2.36) found in Ref. [76]. Using for the NN interaction the AV8' approximation to AV14 [134] and the SC97f-sim YN potential, we also performed a benchmark in comparison to a “coupled-rearrangement-channel Gaussian-basis variational” (CRCGBV) calculation [71]. We found -2.413 MeV binding energy, which is in satisfactory agreement with the CRCGBV result of -2.406 MeV. For the full SC97f only unconverged calculations using the most important  ${}^1S_0$  and  ${}^3S_1$ - ${}^3D_1$  channels are available. We find in conjunction with Nijm 93 -2.338 MeV. This agrees perfectly with -2.34 MeV obtained by Miyagawa [135]. Summarizing we could find agreement with other rigorous calculations of the  ${}^3_\Lambda\text{H}$  binding energy. A comparison of our binding energy results with the expectation value of the Hamilton operator is outlined in Section 5.3.

Table 5.2 shows our binding energy results for several combinations of NN and YN interaction. We always give binding energies with respect to the break-up in neutron, proton and  $\Lambda$ , which includes the deuteron binding energy of -2.234 MeV. In the table we compare two SC89 results obtained with the Bonn B and Nijm 93 NN interactions. Both binding energies only differ by 13 keV. The functional form of both NN interactions is very different. Nevertheless the agreement of both results is quite good. Therefore we state that the hypertriton binding energy is insensitive to the NN interaction and confirm the same conclusion obtained in Ref. [76]. This justifies that we restrict our  ${}^3_\Lambda\text{H}$  calculations to Nijm 93 in the following.

As shown in the table, the hypertriton is only very weakly bound. Experimentally the binding energy

potential	$E_B$	$E_\Lambda$	$T$	$V_{NN}$	$V_{YN}$	$H$
SC97e+Nijm 93	-2.247	-0.023	20.93	-21.67	-1.51	-2.246
SC97f+Nijm 93	-2.304	-0.080	22.43	-21.81	-2.93	-2.305
SC89+Nijm 93	-2.367	-0.143	23.61	-22.24	-3.73	-2.366
SC89+Bonn B	-2.380	-0.155	20.02	-18.52	-3.88	-2.379
SC97e+Nijm 93 w/o $\Sigma$	-2.232	-0.008	20.02	-21.60	-0.65	—
SC89+Nijm 93 w/o $\Sigma$	-2.251	-0.027	20.53	-21.70	-1.08	—
Deuteron Nijm 93	-2.224	—	19.30	-21.53	—	-2.224
Deuteron Bonn B	-2.225	—	15.65	-17.87	—	-2.225
Exp.	-2.354(50)	-0.130(50)	—	—	—	—

Table 5.2: Binding energies of  ${}^3_\Lambda\text{H}$  for different YN and NN force combinations compared to the deuteron results and the experimental value. The theoretical expectation values of the NN potential  $V_{NN}$ , the YN potential  $V_{YN}$ , the kinetic energy  $T$  and the total Hamiltonian  $H$  is also given. All energies are in MeV. The threshold of the binding energy  $E_B$  is the total break-up in 2 nucleons and a  $\Lambda$ -particle and for  $E_\Lambda$  the break-up in  ${}^2\text{H}$  and a  $\Lambda$ -particle.

is  $-130\pm 50$  keV against break-up in a deuteron and a  $\Lambda$  particle. The calculations showed that only SC97e, SC97f and SC89 from the realistic potentials are able to bind the hypertriton. The binding energy of SC89 is in agreement with the experimental one. For the SC97f the agreement has not the same quality as in SC89. Taking into account the uncertainty of 13 keV caused by the dependence on the NN interaction, brings the found binding energy in better agreement with the experimental result. SC97e clearly underbinds the hypertriton. The action of SC89 in  ${}^3_\Lambda\text{H}$  is clearly stronger than the one of SC97. This is remarkable, because the total cross sections for zero energy scattering are bigger for the SC97 models.

We emphasize that these conclusions are based on fully converged calculations using the full interactions. From the SC97f benchmark mentioned above [135] we learned that a calculation with a truncated number of partial waves predicts a slightly increased binding energy of -2.338 MeV. Taking into account P-waves decreases the binding energy visibly. We also state that the SC97f-sim potential overbinds the hypertriton by 109 keV. A simulation of the SC97f interaction by Gaussians seems to be very complicated and might be misleading.

Because we are especially interested in the importance of the  $\Lambda$ - $\Sigma$  conversion, we made truncated calculations, without the  $\Sigma$  contribution in the Faddeev components. To this aim we solved the Lippmann-Schwinger equation for the YN  $t$ -matrix  $t$  without approximation including the  $\Sigma$  components. We manually removed the  $\Lambda\text{N}$ - $\Sigma\text{N}$  conversion and  $\Sigma\text{N}$ - $\Sigma\text{N}$  matrix elements of  $t$  and obtained a truncated  $t$ -matrix  $t_{trunc}$ . The truncated  $t$ -matrix does not couple the  $\Lambda$ - and  $\Sigma$ -parts of the Faddeev component. Nevertheless we can analytically continue  $t_{trunc}$  from our negative off-shell energies to positive on-shell energies. The  $\Lambda\text{N}$ - $\Lambda\text{N}$  matrix elements for negative energies are exactly equal to the original matrix  $t$ . This implies that the analytical continuations of  $\Lambda\text{N}$ - $\Lambda\text{N}$  matrix elements to positive energies of  $t$  and  $t_{trunc}$  are also equal. Both  $t$  matrices describe  $\Lambda\text{N}$  scattering equivalently.

$t_{trunc}$  is related to an effective  $\Lambda\text{N}$  potential, which describes the  $\Lambda\text{N}$  data equivalently to the original one. Does this interaction predict the same hypertriton binding energies?

In Table 5.2 the results of these truncated calculations are labeled by “w/o  $\Sigma$ ”. We performed truncated calculations for SC89 and SC97e. In both cases the binding energy is decreased comparing to

potential	$\eta(E_1)$	$\eta(E_2)$	$\eta(E_3)$
SC97a+Nijm 93	0.7605	0.7519	0.7425
SC97b+Nijm 93	0.8147	0.8079	0.8038
SC97c+Nijm 93	0.8806	0.8703	0.8622
SC97d+Nijm 93	0.9669	0.9556	0.9482
Jülich $\tilde{A}$ +Nijm 93	0.9333	0.9248	0.9181

Table 5.3: Eigenvalues of the Faddeev kernel for three different trial energies  $E_1 = 2.230$ ,  $E_2 = 2.240$  and  $E_3 = 2.250$  MeV.

the full calculations. Whereas for SC97e the decrease is moderate (15 keV), we find a significant decrease of 116 keV in the case of SC89. We note that both truncated calculations agree within 19 keV, though the full calculations clearly reveal the different predictions of both potential models.

First, we observe that the very different AN phase shifts of SC89 and SC97e (see Section 5.1), which also show up in the truncated interactions, do not show up in the “truncated” binding energies considerably. We also state that the effect of the  $\Sigma$  component is model dependent. And maybe most importantly: with our scheme we defined a truncated AN interaction without  $\Lambda$ - $\Sigma$  conversion, which exactly predicts the same AN data as SC89. This truncated potential underpredicts the hypertriton binding energy by 116 keV. We consider this value as an estimate of the systematical error in the hypertriton binding energies predicted by effective AN interactions models, which neglect explicit  $\Lambda$ - $\Sigma$  conversion and three-body forces due to this mechanism. Our calculations show that this mechanism is attractive for the hypertriton. We think this is a strong indication that realistic interactions of the YN system have to consider the conversion process for a realistic description of the few-body hypernuclei, directly or by means of corresponding three-body forces.

Now we turn to the SC97a-d and Jülich models. We would like to document that these models do not bind the hypertriton. To this aim we show in Table 5.3 the biggest eigenvalue  $\eta$  of the Faddeev kernel for the mentioned YN interactions in conjunction with Nijm 93. We used three different trial energies  $E$  near the  $\Lambda$ -deuteron threshold at  $-2.224$  MeV. For physically binding energies  $\eta$  should reach 1.

In Fig. 5.5 the dependence of the eigenvalues on the trial energies is shown. The crosses mark the calculated eigenvalue/energy pairs and the curves represent linear fits to these eigenvalues. The eigenvalues depend with high accuracy linearly on  $E$ . The linear extrapolation to the deuteron threshold energy (vertical line) confirms that the eigenvalues do not reach 1 for all considered potentials. The interactions do not bind the hypertriton.

Summarizing we emphasize that complete and converged solutions of the hypertriton Schrödinger equation are necessary to conclude safely on the failures or strengths of the YN interaction. From the meson-theoretical model interactions studied only SC89, SC97e and SC97f predict a bound hypertriton. While the binding energies for SC89 and SC97f agree with the experiment, this is not the case for SC97e.

In the next section we will look in some detail into the properties of the predicted bound states.

### 5.3 Properties of the hypertriton wave function

In this section we describe the properties of the hypertriton wave functions in more detail.

We start with a look towards the expectation values of the kinetic energy  $T$ , the NN and YN potential energies  $V_{NN}$  and  $V_{YN}$  and the Hamiltonian  $H$  in Table 5.2. For the truncated calculations labeled by

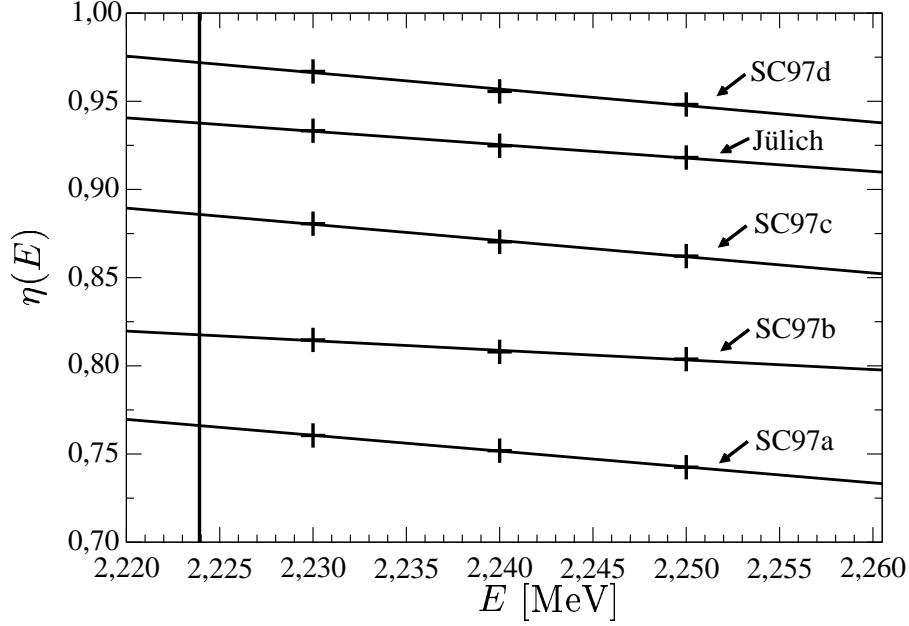


Figure 5.5: Dependence of the eigenvalue  $\eta$  of the Faddeev kernel from the trial energy  $E$  for various YN potentials in conjunction with the Nijm 93 NN interaction. The deuteron binding energy prediction of Nijm 93 is marked by the vertical line, eigenvalue results by crosses. The curves are linear fits to the eigenvalue results.

“w/o  $\Sigma$ ” we cannot give independent results for  $H$ , because we have not evaluated the effective  $\Lambda N$  interaction from the truncated  $t$ -matrix. Instead of this we assume directly  $H = E_B$  and calculate the expectation value of the YN potential from the known binding energy, NN potential energy and the kinetic energy using  $V_{\Lambda N} = E_B - V_{NN} - T$ . For the full calculations we could independently obtain the expectation values and check the consistency of  $H$  with  $E_B$ . We find agreement of  $H$  and the binding energy  $E_B$  within our numerical accuracy of 1.8 keV.

The NN potential energy contributes the major part to the total potential energy. In  ${}^3_\Lambda\text{H}$  the YN interaction is not comparable in strength to the NN interaction. We see a strong dependence of the expectation value of  $V_{YN}$  on the used YN model. It is remarkable that the difference of the SC97f and SC97e predictions is stronger than the difference of the SC97f and SC89 expectation values. We also find that the truncated effective YN interactions lead to remarkably smaller expectation values than the corresponding full interactions.

For the NN potential energy, we can compare to the corresponding expectation values of the deuteron wave functions. We find that the  $V_{NN}$  expectation values of  ${}^3_\Lambda\text{H}$  and  ${}^2\text{H}$  only slightly differ. This is in agreement with the assumption of a deuteron core in  ${}^3_\Lambda\text{H}$ . We come back to this issue below.

In Table 5.4 we give our results for the orbital  $S$ -,  $P$ - and  $D$ -wave probabilities. The  $S$ -state is the dominant part of the wave function. The  $D$ -state probability is slightly smaller than for the  ${}^3\text{H}$  wave functions (see Table 4.7). As in  ${}^3\text{H}$  we find a very small admixture of the  $P$ -waves to the wave function.

In contrast to this total orbital  $S$ -state dominance, we find very important contributions of the higher

model	$S$	$P$	$D$
SC97e+Nijm 93	94.19	0.00	5.81
SC97f+Nijm 93	94.15	0.00	5.84
SC89+Nijm 93	94.02	0.01	5.97
SC89+Bonn B	94.80	0.01	5.19

Table 5.4:  $S$ ,  $P$  and  $D$  state probabilities for the  ${}^3_\Lambda\text{H}$  wave functions. All probabilities are given in %.

	NN				YN			
	${}^1S_0$	${}^3S_1$	P	other	${}^1S_0$	${}^3S_1$	P	other
SC97e+Nijm 93	0.03	99.83	0.05	0.09	32.79	12.00	20.68	34.53
SC97f+Nijm 93	0.05	99.67	0.10	0.17	42.35	15.35	18.63	23.68
SC89+Nijm 93	0.26	99.36	0.18	0.20	47.13	17.21	17.06	18.60
SC89+Bonn B	0.27	99.34	0.18	0.21	47.87	17.44	16.78	17.91

Table 5.5: Probabilities to find a NN or YN pair in a fixed relative partial wave for the  ${}^3_\Lambda\text{H}$  wave functions. We distinguish  ${}^1S_0$ ,  ${}^3S_1$ - ${}^3D_1$ , P-waves ( ${}^3P_0$ ,  ${}^1P_1$ ,  ${}^3P_1$ ,  ${}^3P_2$ - ${}^3F_2$ ) and other partial waves. All probabilities are given in %.

partial waves to the *relative* motion of the hyperon and one of the nucleons as shown in Table 5.5. We see that in the YN subsystem the relative  $S$ -states contribute only 40 % to 60 % to the total partial wave decomposition of the relative motion. This behavior is very different from the one in purely nucleonic bound states. This is also reflected in the very slow convergence of the partial wave decomposed wave function in the 1C representation (see Table 3.12). In the NN subsystem we find a dominance of the relative  ${}^3S_1$ - ${}^3D_1$  states, which again indicates a deuteron core of the hypertriton.

A more detailed look to the wave function can be obtained by various momentum distributions and correlation functions. The definitions of momentum distributions as given in Eq. (4.2), correlation functions as given in Eqs. (4.5) and (4.6) and deuteron overlap functions as given in Eqs. (4.12) and (4.13) can be easily generalized to the hypernuclei. We added a projection operator for the hyperon to be in a  $\Lambda$  state in the definition of the overlap function. In the following we will present our results for angular independent parts of these functions, namely the momentum distributions  $D_i(p)$  ( $i=\Lambda, N, \Sigma$ ), the  $\Lambda$ - ${}^2\text{H}/{}^3_\Lambda\text{H}$ -overlaps  $\mathcal{D}_\Lambda(p)$  and the correlation functions  $C_s^q(p)$ .

For all these distributions and correlations, we have not found any CSB effect. Therefore we look in the following only to nucleons,  $\Lambda$  and  $\Sigma$ -particles and do not distinguish their different charge states. Corresponding isospin projection operators are easily introduced in Eqs. (4.2), (4.5) and (4.12). In Table 5.6 the probability  $P_T$  for the total isospin  $T = 1$  part of the wave function is given. It is extremely small for the considered interactions and confirms our observation of a small CSB in  ${}^3_\Lambda\text{H}$ .

We start with a look to the momentum distributions  $D_i(p)$  and the overlaps  $\mathcal{D}_\Lambda(p)$  in Fig. 5.6. All distributions are normalized to

$$\begin{aligned}
\int_0^\infty dp D_i(p) &= \frac{1}{4\pi} \text{ for } i = \Lambda, N, \Sigma \\
\int_0^\infty dp \mathcal{D}_\Lambda(p) &= \frac{1}{4\pi}
\end{aligned} \tag{5.1}$$

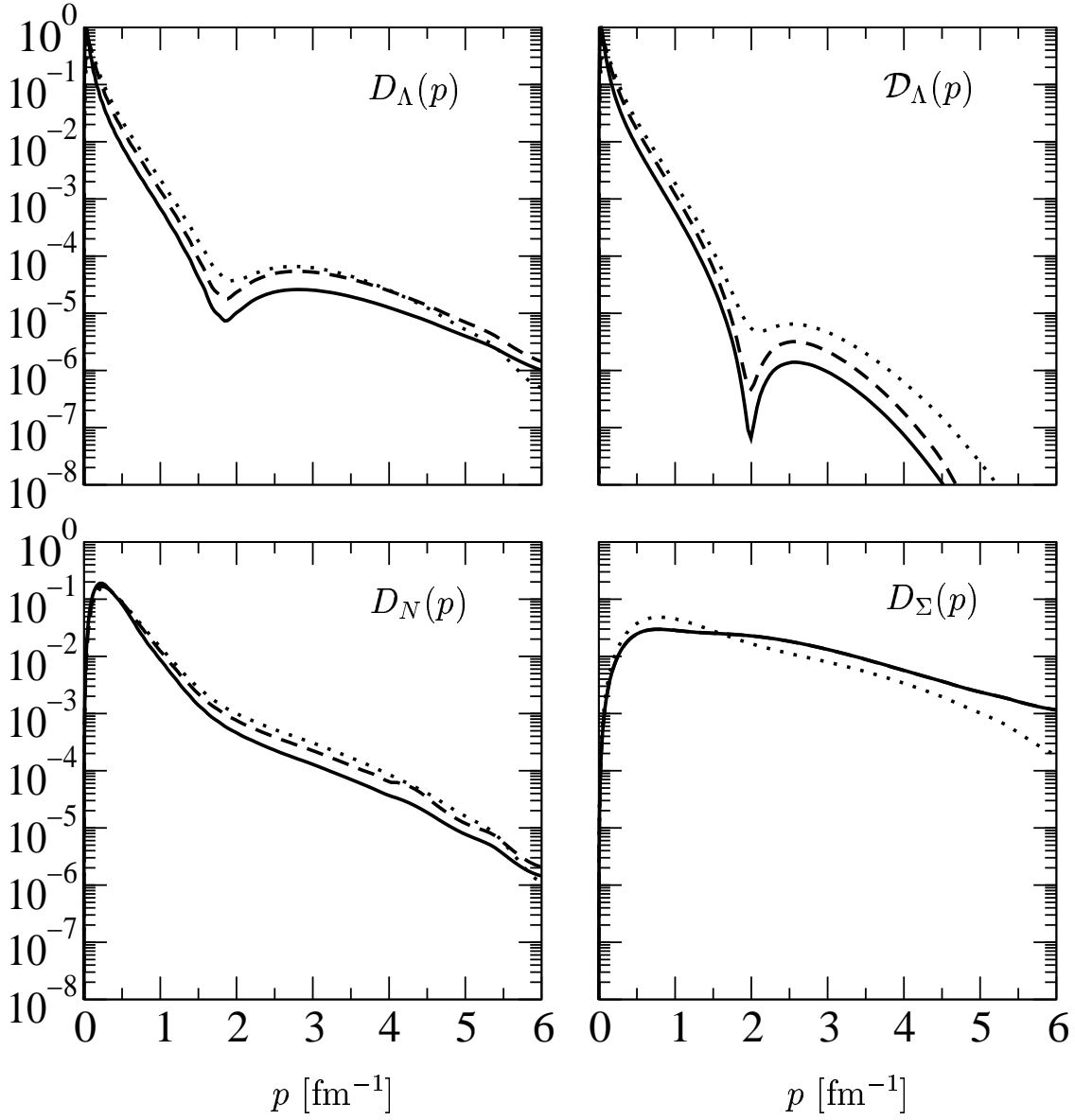


Figure 5.6:  $\Lambda$  momentum distributions  $D_\Lambda(p)$ ,  $\Lambda^{-2}\text{H} / {}^3_\Lambda\text{H}$  overlaps  $\mathcal{D}_\Lambda(p)$ , nucleon momentum distributions  $D_N(p)$  and  $\Sigma$  momentum distributions  $D_\Sigma(p)$  compared for different YN interactions on a logarithmic scale. The functions are based on calculations using the Nijm 93 NN interaction and the SC97e (solid line), SC97f (dashed line), the SC89 (dotted line) YN interactions. They are normalized to  $\int C(p)dp = \frac{1}{4\pi}$  and given in fm.

potential	$N_D$	$P_\Sigma$	$P_{T=1}$
SC97e+Nijm 93	99.65	0.10	0.0003
SC97f+Nijm 93	99.30	0.18	0.0011
SC89+Nijm 93	98.71	0.47	0.0026
SC89+Bonn B	98.65	0.49	0.0027
SC89+Nijm 93 w/o $\Sigma$	99.72	—	0.0007

Table 5.6: Theoretical predictions of the probability to find a deuteron ( $N_D$ ) or a  $\Sigma$  particle ( $P_\Sigma$ ) within the hypertriton. The size of the total isospin  $T = 1$  contribution is also given ( $P_{T=1}$ ). All probabilities are given in %.

The original sizes of the  $\Lambda$  and  $\Sigma$  distributions can be found using the probabilities  $P_\Sigma$  to find the hyperon in a  $\Sigma$ -state. They are shown in Table 5.6.  $P_\Sigma$  is quite small and ranges from 0.1 % for SC97e to 0.5 % for SC89. It is only slightly dependent on the NN interaction.

The importance of the deuteron overlap  $\mathcal{D}_\Lambda(p)$  is given by the probability  $N_D$  that the two nucleons form a deuteron bound state within  ${}^3_\Lambda\text{H}$  and the hyperon is in a  $\Lambda$  state. As shown in Table 5.6,  $N_D$  nearly reaches 100.0 %. The small deviations from 100.0 % are also dependent on the YN interaction, but less dependent on the NN force. Because of the high probability of the two nucleons to form a bound state, we expect that  $D_\Lambda$  and  $\mathcal{D}_\Lambda$  are very similar. Indeed, we find this behavior for low momenta as shown in Fig. 5.6.

There we give results for SC97f (solid lines), SC97e (dashed lines) and SC89 (dotted lines) in conjunction with Nijm 93.  $D_{\Lambda,\Sigma}(p)$  and  $\mathcal{D}_\Lambda(p)$  do not depend on the NN interaction. Therefore we omit a fourth curve in the figures and only display Nijm 93 results.

The left upper figure shows the  $\Lambda$  momentum distribution  $D_\Lambda(p)$ . We find a very pronounced and sharp peak close to  $p = 0 \text{ fm}^{-1}$  and a dip structure near  $p = 2 \text{ fm}^{-1}$ . The differences of SC89 and SC97f are comparable in magnitude to the differences of SC97f and SC97e.

In the right upper figure the  $\Lambda$ - ${}^2\text{H}/{}^3_\Lambda\text{H}$ -overlaps  $\mathcal{D}_\Lambda$  are presented. In the low momentum region the behavior of  $\mathcal{D}_\Lambda$  and  $D_\Lambda$  are very similar and consistent with the deuteron probability  $N_d \approx 100 \%$  in  ${}^3_\Lambda\text{H}$ . Differences show up for the high momentum components. These are much more important in  $D_\Lambda(p)$ . Nevertheless  $\mathcal{D}_\Lambda$  shows a similar structure around  $2 \text{ fm}^{-1}$ . In contrast to  $D_\Lambda$  the high momentum tail of  $\mathcal{D}_\Lambda$  above  $2 \text{ fm}^{-1}$  drops very rapidly. We note that  $D_\Lambda$  and  $\mathcal{D}_\Lambda$  strongly depend on the YN force also in the low momentum region. For completeness we give the maxima of the  $\Lambda$  distributions. They reach 1.0 fm for SC97e, 0.55 fm for SC97f and 0.4 fm for SC89 for both functions,  $D_\Lambda(p)$  and  $\mathcal{D}_\Lambda(p)$ .

The lower left figure of Fig. 5.6 shows the nucleon momentum distribution  $D_N(p)$ . It is much smoother than  $D_\Lambda(p)$ . Compared to  $D_\Lambda(p)$ , the peak near  $p = 0 \text{ fm}^{-1}$  is shifted to higher momenta and its tail drops more slowly and does not have any dip structure. Its shape is similar to the momentum distributions in  ${}^3\text{H}$  and  ${}^4\text{He}$  shown in Chapter 4. We do not show the dependence on the NN interaction. It is similar to the one found in  ${}^3\text{H}$  and  ${}^4\text{He}$ . We refer to the discussions in Chapter 4 at this point.

In the lower right figure the  $\Sigma$  momentum distributions are shown. For the  $\Sigma$  particle the momentum distributions are very broad. We confirmed that they are not NN interaction dependent. It sticks out that the predictions of SC97e and f overlap in the whole momentum range. The distribution for SC89 has got a similar shape, but the momenta around  $1 \text{ fm}^{-1}$  are slightly more important than in the case of SC97.

Summarizing we found that the  $\Lambda$ ,  $\Sigma$  and nucleon momentum distributions have got very different

	NN		AN		ΣN	
	$s = 0$	$s = 1$	$s = 0$	$s = 1$	$s = 0$	$s = 1$
SC97e+Nijm 93	0.03	99.97	73.21	26.67	0.02	0.10
SC97f+Nijm 93	0.07	99.93	72.37	27.44	0.03	0.17
SC89+Nijm 93	0.31	99.69	71.67	27.84	0.10	0.40
SC89+Bonn B	0.32	99.68	71.84	27.64	0.10	0.41
Λ <sup>-2</sup> H approx.	—	100.00	75.00	25.00	—	—

Table 5.7: Probabilities  $P_s^q$  to find NN, AN and ΣN pairs in spin  $s = 0$  and  $s = 1$  states in  ${}^3_\Lambda\text{H}$ . The probabilities are compared to the analytical results for a simplified  ${}^3_\Lambda\text{H}$  wave function (Λ<sup>-2</sup>H approx., see text) All probabilities are given in %.

shapes. The nucleon distribution is similar in shape to the distribution functions found in  ${}^3\text{H}$  and  ${}^4\text{He}$ . We also emphasize that the Λ momentum distributions are similar to the Λ<sup>-2</sup>H/ ${}^3_\Lambda\text{H}$ -overlap functions. This is a consequence of the high probability to find a deuteron in  ${}^3_\Lambda\text{H}$ . We note that differences of the overlaps and Λ distributions show up for momenta higher than  $1\text{ fm}^{-1}$ .

Now we turn to the correlation functions. Similar to Eq. (4.8) we define probabilities  $P_s^q$  for the different baryon-baryon pairs to be in a spin  $s = 0$  or  $s = 1$  state. The probabilities indicate the importance of different baryon-baryon channels and spin states of the correlation functions. Table 5.7 displays  $P_s^q$  for  $q = \text{NN}, \text{AN}$  and  $\Sigma\text{N}$ . The AN and ΣN probabilities together sum up to 100 %. In the same way the  $P_s^{\text{NN}}$  are normalized.

We compare our results to an analytical estimate based on a very simple hypertriton wave function. For this approximation we assume that the NN pair is in a  $s = 1$  state (like the deuteron) and the total orbital angular momentum is  $L = 0$ . From Tables 5.4 and 5.6 we see that both assumptions are justified. Neglecting the Σ component, one can analytically derive  $P_s^{\text{AN}}$  for  $s = 0$  and  $s = 1$  in this case by recoupling the spin part of the approximated wave function. The result is shown in the last row of Table 5.7. It reasonably agrees with our exact calculations. We emphasize that this relation only holds for the summed up probabilities for all  $s = 1$  and  $s = 0$  states. In the literature (see for example [73]) this relation has very often been applied to the  ${}^1\text{S}_0$  and  ${}^3\text{S}_1$  AN states. From Table 5.5 we know that this is a very pure approximation, because it completely neglects the very important higher partial waves in the relative motion of the Λ and one of the nucleons.

We are ready for a look to correlations now. We start with correlation functions in configuration space. Fig. 5.7 compares the NN correlations for two NN interactions: Bonn B (left hand side) and Nijm 93 (right hand side). The functions are normalized to the same peak height. We show results for  ${}^3_\Lambda\text{H}$  for SC97e (dashed), SC97f (dashed dotted) and SC89 (dotted). Additionally, we show the deuteron predictions obtained from the same NN interactions (solid lines). For interparticle distances below  $r = 2.0\text{ fm}$  the correlations of  ${}^3_\Lambda\text{H}$  and  ${}^2\text{H}$  are identical. In the long range tails we observe slight differences due to the different binding energies predicted by the force models. This confirms our expectation from the high probability for the nucleons to form a deuteron within  ${}^3_\Lambda\text{H}$ .

In Fig. 5.8 the AN correlations are shown. Because the tail in the AN correlations is driven by the very small Λ<sup>-2</sup>H separation energies, they are extremely long ranged. Therefore we chose a logarithmic  $r$ -scale. The functions are again normalized to the same peak height. We present results for SC97e (solid lines), SC97f (dashed lines) and SC89 (dotted lines) in conjunction with the Nijm 93. Results for Bonn B do not differ from the results shown. The left figure shows the  $s = 0$  correlations. We find a similar short



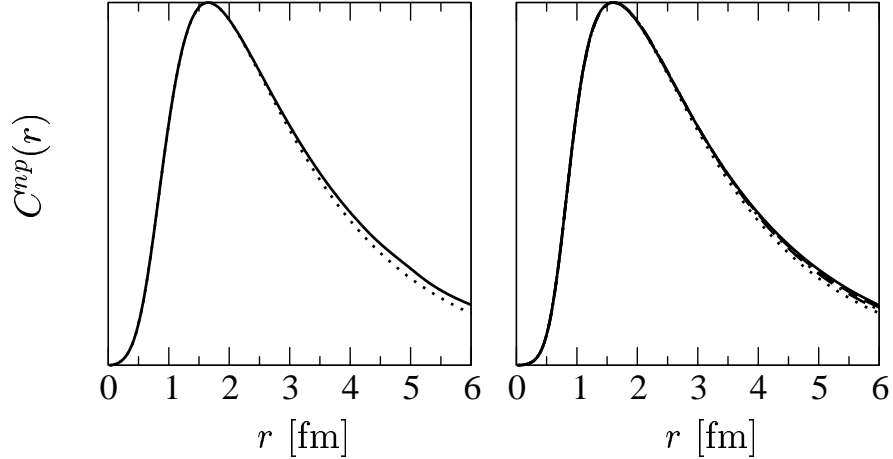


Figure 5.7: np correlations in  ${}^2\text{H}$  and  ${}^3_{\Lambda}\text{H}$  in configuration space. The correlation functions are based on calculations using the Bonn B (left figure) and Nijm 93 (right figure) NN interactions and SC 97e (dashed lines), SC 97f (dashed dotted lines) or SC 89 (dotted lines) YN interactions. The correlations in the deuteron are marked by solid lines. The functions are normalized to the same peak height. They are given in arbitrary units on a linear scale.

range repulsion as in the case of the NN correlations. There is a small dependence of the short range behavior on the YN interaction used. The peak is found at  $\approx 3$  fm. As expected the tail is extremely long ranged and reaches 30 fm to 50 fm. For  $s = 1$  (right hand side) the behavior is very similar. We observe a decreased dependence of the short range behavior on the YN interaction. Peak position and shape are nearly equal.

The  $\Sigma\text{N}$  correlations in Fig. 5.9 are very interesting. Again we found no dependence of the correlation on the NN interaction. Therefore we only show results for Nijm 93. Again the functions are normalized to the same peak height.

For  $s = 1$  (right hand side) the functions are comparable to NN correlations. We find the same repulsive short range behavior. Their shape is very similar for all YN interactions considered. It is remarkable that the  $\Sigma\text{N}$  correlations drop very quickly for higher  $r$ 's. In this point the  $\Sigma\text{N}$  and  $\Lambda\text{N}$  correlations behave differently. It shows that the  $\Sigma\text{N}$  correlations are not driven by the  $\Lambda$ - ${}^2\text{H}$  separation energies, but by the additional mass difference of the  $\Lambda$ - and  $\Sigma$ -particles of about 70 MeV.

In contrast the  $s = 0$   $\Sigma\text{N}$  correlations (left figure) have got a different shape. For all YN interactions we observe two peak structures. The first one for very small distances around 0.3 fm, the second one at roughly 1.5 fm. The relative size of both peaks strongly depends on the YN interaction. For SC89 we find a small peak around 0.3 fm and pronounced peak around 1.5 fm. This is opposite in the case of the SC97 models. Their predictions for the short range peak are identical for SC97e and f, but we find slight deviations for the peak around 1.5 fm. We see that the probabilities to find  $\Lambda$  and  $\Sigma$  particles in the hypertriton in fixed interparticle distances are completely disentangled, because both correlations in configuration space are not comparable. This contradicts the naive expectation that the  $\Sigma$  and  $\Lambda$  distributions are correlated, because  $\Sigma$ -particles are created in the conversion process. We consider the peak for small interparticle distances to be the consequence of the attractive short range behavior of the

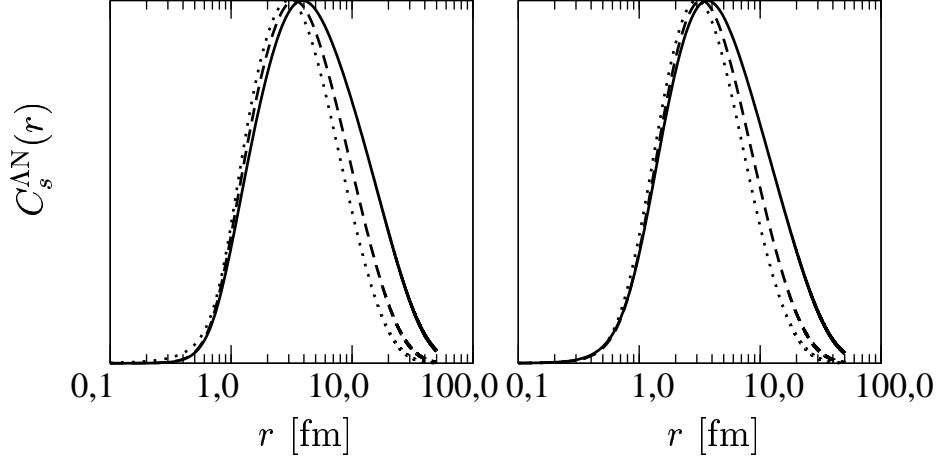


Figure 5.8: AN correlations for  $s = 0$  (left figure) and  $s = 1$  (right figure) in  ${}^3_{\Lambda}\text{H}$  in configuration space. The correlation functions are based on calculations using the Nijm 93 NN interactions and SC 97e (solid lines), SC 97f (dashed lines) or SC 89 (dotted lines) YN interactions. The functions are normalized to the same peak height. They are given in arbitrary units on a linear scale.

OBE YN interaction models. This effect is only seen in the  $s = 0$  channel.

We complete our presentation of correlation functions with momentum space  $\Lambda\text{N}$  and  $\Sigma\text{N}$  correlations in Fig. 5.10. Again we found no NN force dependence and show only results for Nijm 93. As usual we normalize the correlations to

$$\int_0^{\infty} dp C_s^q(p) = \frac{1}{4\pi} \quad \text{for } s = 0, 1 \text{ and } q = \Lambda\text{N and } \Sigma\text{N} \quad (5.2)$$

The two upper figures show the  $\Lambda\text{N}$  correlations for  $s = 0$  (left) and  $s = 1$  (right). We find a very sharp low momentum peak around  $0.1 \text{ fm}^{-1}$ .  $C_s^{\Lambda\text{N}}$  drops very quickly in  $s = 0$  states and more slowly in  $s = 1$  states for higher momenta. The shape of the correlations is very similar for all studied YN interactions. In contrast to the ordinary nuclei presented in Chapter 4, the correlations depend on interaction for small and high momenta. Because this is partly due to the different binding energy predictions and because we do not have a set of trial Hamiltonians to our disposal, which predict the same binding energies, we do not want to compare the correlations in the same detail as in the case of  ${}^3\text{H}$  and  ${}^4\text{He}$ .

Instead we have a look to the  $\Sigma\text{N}$  correlations given in the lower two figures of Fig. 5.10. The shape of  $C_s^{\Sigma\text{N}}$  remarkably differs from the  $\Lambda\text{N}$  correlations. We find a very broad high momentum tail. For  $s = 1$  (right figure) we can distinguish the SC89 (dotted line) and the overlapping SC97 (solid and dashed lines) results. For SC89 we observe a shift to lower momenta, keeping the shape of the correlation.

As expected from the configuration space correlations, the  $s = 0$  (left figure) correlations are visibly different from the  $s = 1$  functions. For SC89 we find a dip structure around  $2 \text{ fm}^{-1}$ . The results for SC97e and f are different for  $s = 0$ . In both cases the high momentum tail is very flat. Starting from  $1.0 \text{ fm}^{-1}$  we find different shapes for both SC97 models.

In summary the NN correlations are very similar to corresponding correlations in  ${}^3\text{H}$  and  ${}^4\text{He}$ . In configuration space the YN models considered predict comparable YN correlations for  $\Lambda\text{N}$  pairs and  $\Sigma\text{N}$

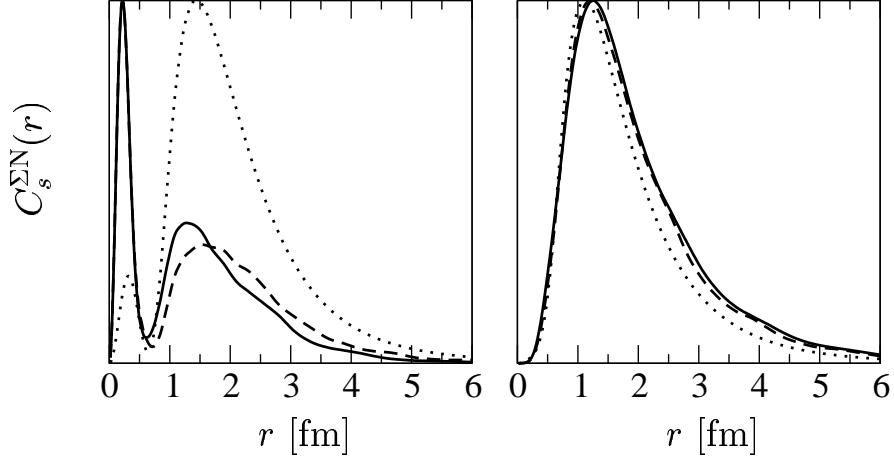


Figure 5.9:  $\Sigma N$  correlations for  $s = 0$  (left figure) and  $s = 1$  (right figure) in  ${}^3_{\Lambda}\text{H}$  in configuration space. The correlation functions are based on calculations using the Nijm 93 NN interactions and SC 97e (solid lines), SC 97f (dashed lines) or SC 89 (dotted lines) YN interactions. The functions are normalized to the same absolute maxima. They are given in arbitrary units on a linear scale.

	$\Lambda N$ - $\Lambda N$			$\Sigma N$ - $\Sigma N$			$\Lambda N$ - $\Sigma N$		
	${}^1S_0$	${}^3S_1$ - ${}^3D_1$	ALL	${}^1S_0$	${}^3S_1$ - ${}^3D_1$	ALL	${}^1S_0$	${}^3S_1$ - ${}^3D_1$	ALL
SC97e+Nijm 93	-0.83	0.07	-0.75	-0.08	0.07	0.00	-0.04	-0.70	-0.75
SC97f+Nijm 93	-1.60	0.12	-1.46	-0.21	0.10	-0.10	-0.16	-1.19	-1.37
SC89+Nijm 93	-1.72	0.02	-1.69	0.03	-0.06	-0.02	-0.41	-1.58	-2.02
SC89+Bonn B	-1.81	0.03	-1.77	0.03	-0.06	-0.02	-0.43	-1.63	-2.09

Table 5.8: Contributions of different partial waves to the expectation value of the YN potential for  ${}^3_{\Lambda}\text{H}$ . We distinguish  ${}^1S_0$ ,  ${}^3S_1$ - ${}^3D_1$  partial waves and the total contribution (ALL) of the  $\Lambda N$ - $\Lambda N$ ,  $\Sigma N$ - $\Sigma N$  and  $\Lambda N$ - $\Sigma N$  potentials. All energies are given in MeV.

pairs in  $s = 1$  states. In  $s = 0$  states the YN models predict very different  $\Sigma N$  correlations. In this state especially the new SC97 models predict a high probability for  $\Sigma N$  pairs with small interparticle distances  $r \approx 0.3$  fm. In this region the two baryons are overlapping. The validity of the OBE interactions for these interparticle distances is questionable.

We end our survey on hypertriton properties with a closer look to the YN potential expectation values in Table 5.8. We give the contributions of the YN potential for  ${}^1S_0$ ,  ${}^3S_1$ - ${}^3D_1$  states and the sum of all partial waves and distinguish the  $\Lambda N$ - $\Lambda N$ ,  $\Sigma N$ - $\Sigma N$  potentials and the  $\Lambda N$ - $\Sigma N$  conversion potentials.

The expectation values slightly depend on the NN interaction. As expected the contribution of the  $\Sigma N$ - $\Sigma N$  potentials is in all cases of minor importance. But we observe an important contribution from the conversion potentials, which are comparable to or bigger than the  $\Lambda N$ - $\Lambda N$  direct interactions. It is remarkable that the direct  $\Lambda N$ - $\Lambda N$  potential is repulsive in  ${}^3S_1$ - ${}^3D_1$  for all YN interactions. We also find that all models predict two major contributions to the total potential energy. The first is from the

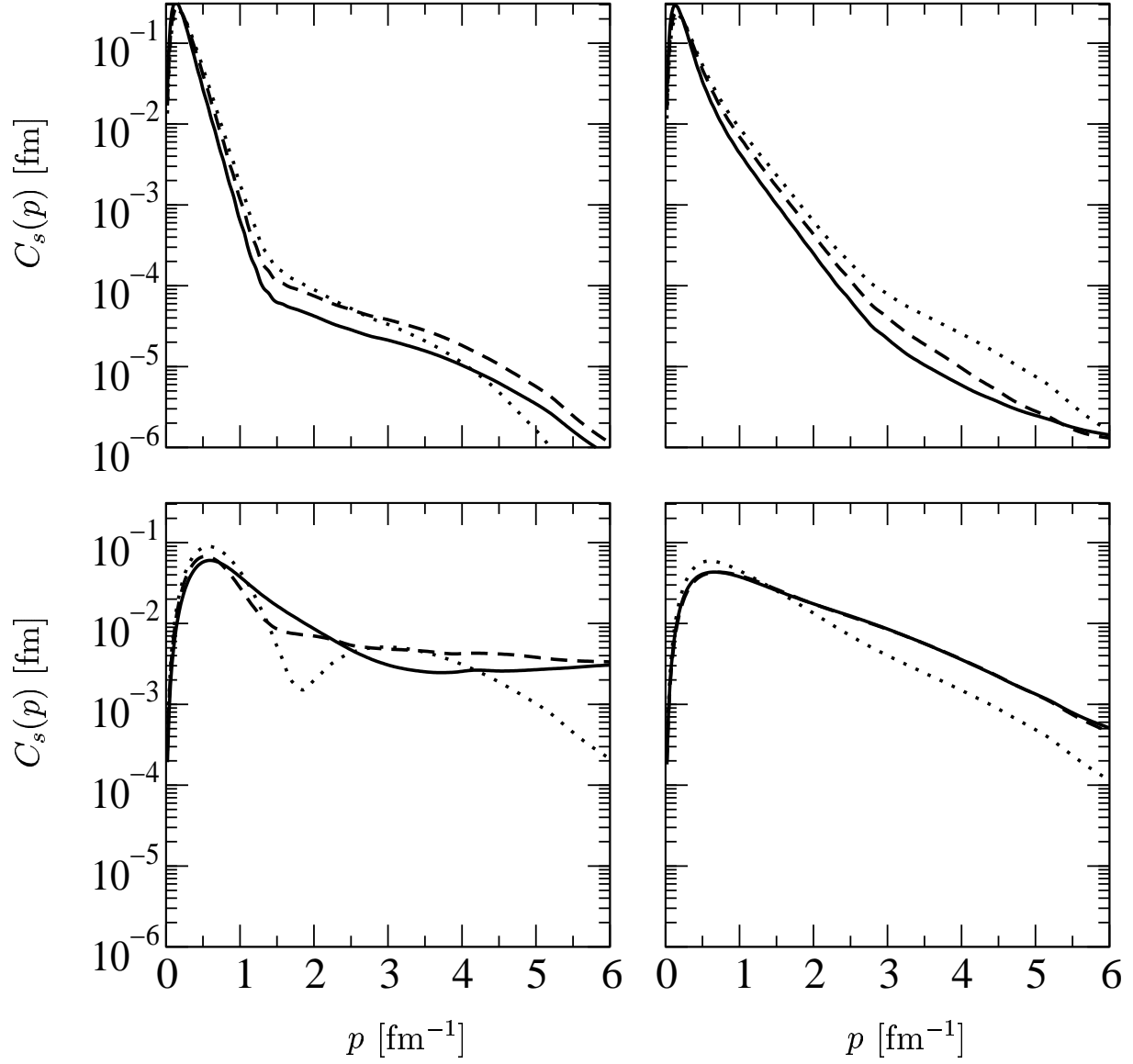


Figure 5.10: AN (upper figures) and  $\Sigma$ N (lower figures) correlations for  $s = 0$  (left figures) and  $s = 1$  (right figures) in  ${}^3_{\Lambda}\text{H}$  in momentum space. The correlation functions are based on calculations using the Nijm 93 NN interactions and SC 97e (solid lines), SC 97f (dashed lines) or SC 89 (dotted lines) YN interactions. The functions are normalized to  $\int C(p)dp = \frac{1}{4\pi}$ .

$^1S_0$  interaction of the direct potential and the second from the  $^3S_1$ - $^3D_1$  interaction of the conversion potential. We note that the conversion potential contributes roughly half of the YN interaction, though the  $\Sigma$  component of the wave function is very small and contributes less than 0.5 %. We also observe that the higher partial waves in the YN subsystem are very important in the wave functions (see Table 5.5), but are less important in the potential energy expectation values. Also for the relative  $S$ -waves we do not see any connection of the relative importance of the partial wave contributions to the wave function and to the potential energy expectation values. Therefore simple rules to estimate the binding energies in different spin states of the ANN system must fail. The spin  $J = \frac{1}{2}$  of the hypertriton is the result of dynamical properties of the interaction, which cannot be summarized in the simplified statement that the  $^1S_0$  interaction is more attractive than the  $^3S_1$ . Complete calculations are necessary to obtain reliable results. Surprisingly for us we found for the Nijmegen SC models SC97 and SC89, that the relative contributions for different partial waves in the direct and the conversion potentials are comparable in  $^3_\Lambda\text{H}$ . This is astonishing to us, because we found a very different behavior of both interactions in the  $^3S_1$ - $^3D_1$  phaseshifts in Figs. 5.3 and 5.4.

This closes our presentation of the properties of hypertriton wave functions. In the next section we turn to the hypernuclear four-body problems. We study the predicted binding energies of the YN interactions, which are to our disposal. Because the  $^4_\Lambda\text{H}$  and  $^4_\Lambda\text{He}$  nuclei have two experimentally settled bound states with different spins, we can expect sensitivity to the spin dependences of the YN interactions.

## 5.4 Four-body hypernuclei

In this section we present our binding energy results for the four-body hypernuclei and compare them to the experimental energies.

We can get much more information from the hypernuclear four-body systems than for example from the  $\alpha$ -particle. This is the consequence of the fact that two states are experimentally settled: a  $J^\pi = 0^+$  ground state and a  $J^\pi = 1^+$  excited state, and this for both hypernuclei,  $^4_\Lambda\text{He}$  and  $^4_\Lambda\text{H}$ . Due to the different spins of both states, we expect valuable information on the spin structure of the YN interactions. Moreover it is known that these hypernuclei form an isospin doublet. The binding energy differences within the multiplet are experimental signatures of CSB in the YN interactions. Therefore the four-body hypernuclei also give important information on CSB effects.

In Section 3.3.2 we performed careful checks of our numerical accuracy. Here we just recall that our most sophisticated calculations truncate the partial wave decomposition with  $l_{sum}^{max} = 8$  for  $J^\pi = 0^+$  states and with  $l_{sum}^{max} = 6$  for  $J^\pi = 1^+$  states. We defined  $\Lambda$  separation energies

$$\begin{aligned} E_{sep}^\Lambda &\equiv E_B(^3\text{He}) - E_B(^4_\Lambda\text{He}) \\ \text{or } E_{sep}^\Lambda &\equiv E_B(^3\text{H}) - E_B(^4_\Lambda\text{H}) \end{aligned} \quad (5.3)$$

which converge faster than the absolute binding energies  $E_B$ . Therefore we present in the following  $E_{sep}^\Lambda$  based on 3N binding energies obtained in a similar partial wave truncation than used for the hypernucleus. For the interaction combination Bonn B and Jülich  $\tilde{\text{A}}$  we found that the  $\Lambda$  separation energies  $E_{sep}^\Lambda$  are converged within 12 keV. We found a slower convergence with respect to the partial wave decomposition in the case of the Nijmegen interactions, but confirmed an accuracy of 50 keV in  $E_{sep}^\Lambda$  for all potential combinations considered. Because we observed a faster convergence for the  $0^+$ - $1^+$  splitting  $\Delta = E_{sep}^\Lambda(0^+) - E_{sep}^\Lambda(1^+)$ , we decided to regard  $\Delta$  based on calculations with  $l_{sum}^{max} = 6$  for both states,  $J^\pi = 0^+$  and  $J^\pi = 1^+$ . This leads to deviations of the differences of  $E_{sep}^\Lambda$  and  $\Delta$  in the tables, but results in more accurate numbers for  $\Delta$ .

${}^4_{\Lambda}\text{He}$	$0^+$		$1^+$		$\Delta$
	$E_B$	$E_{sep}^{\Lambda}$	$E_B$	$E_{sep}^{\Lambda}$	
this work	-9.46	2.32	-7.84	0.74	1.52
CRCGBV [71]	-9.27	2.12	-7.54	0.39	1.74
Brückner-Hartree-Fock [72]	—	2.18	—	0.70	1.48

Table 5.9: Predictions for the  ${}^4_{\Lambda}\text{He}$  binding energy  $E_B$ , the corresponding  $\Lambda$  separation energy  $E_{sep}^{\Lambda}$  and the  $0^+-1^+$  splitting  $\Delta$  for the SC97f-sim YN potential model. Our work and the CRCGBV calculation is based on the AV8' NN interaction. In [72] the NN interaction is not documented. All energies are in MeV.

In the realistic calculations we take the mass differences of the proton and neutron and within the  $\Sigma$  multiplet into account. CSB of the YN interaction and the Coulomb force in pp,  $\Sigma^+p$  and  $\Sigma^-p$  pairs are considered, but we restrict our calculations to total isospin  $T = \frac{1}{2}$  states. We expect that this truncation leads only to minor changes of the binding energies. From the  ${}^3\text{H}$  and  ${}^3\text{He}$  nuclei we learned that this truncation leads to errors of the order 20 keV in the binding energy. This is below our current numerical accuracy. Therefore we claim that our predictions for  $E_{sep}^{\Lambda}$  are correct within 50 keV and allow judgments on the nonrelativistic dynamics of the YN and NN model interactions.

As in the case of the hypertriton we performed benchmark calculations using the SC97f-sim YN interaction in conjunction with the AV8' NN force. Because of the complexity of the problem only a few other calculations are available. For these benchmarks averaged masses for the  $\Sigma$ -particles and the nucleons have been used. Table 5.9 shows predictions for  ${}^4_{\Lambda}\text{He}$  including the Coulomb force. We compare our numbers to predictions using the CRCGBV method, which have been obtained using the same YN and NN interactions [71]. The CRCGBV calculation does not include the Coulomb interaction. We perturbatively estimated the Coulomb contribution based on our wave function and compare to CRCGBV results, to which we added this Coulomb contribution. The CRCGBV result for the  $J^{\pi} = 1^+$  state is not fully converged. We expect a further increase of its binding energy and a reduction of the splitting  $\Delta$  in this case. Unfortunately the agreement is not satisfactory. Also for the  $J^{\pi} = 0^+$  state we find a discrepancy of 200 keV to our calculations. Therefore we carefully checked our results for consistency and calculated the expectation value of the Hamilton operator  $H$ . For  $J = 0^+$  we find  $H = -9.43$  MeV, which compares well with our binding energy result of  $E_B = -9.46$  MeV. The agreement is perfect for  $J = 1^+$ . Our wave function results in an expectation value of  $H = -7.84$  MeV, which is equal to the binding energy given in Table 5.9. We note that the kinetic energy amounts to  $T = 54.62$  MeV. Compared to this number the disagreement of both methods is 0.4 %.

Recently a calculation using the Brückner-Hartree-Fock many-body technique has been published [72]. We are not aware of the NN interaction used in their calculation, but we will show later on that the separation energies are not sensitive to the used NN force. In Table 5.9 we see that this calculation better agrees with our results, especially the  $0^+-1^+$  splitting. In view of the fact that the many-body technique is less accurate than exact few-body methods, we are satisfied with this sort of agreement.

The slight disagreement to CRCGBV has to be clarified in forthcoming studies. We again emphasize that the calculation of the expectation value of the Hamiltonian enables us to perform an independent consistency check of our calculations. We confirmed in this way all results given in this section. The possibility to perform these self-consistency checks is an important feature of our method.

Now we turn to an estimate of systematical errors of the  $\Lambda$  separation energy  $E_{sep}^{\Lambda}$ . We are interested

${}^4_\Lambda\text{He}$	$0^+$		$1^+$		$\Delta$
	$E_B$	$E_{sep}^\Lambda$	$E_B$	$E_{sep}^\Lambda$	
SC97e+Bonn B	-8.92	1.66	-8.04	0.80	0.84
SC97e+Nijm 93	-8.55	1.54	-7.69	0.72	0.79
SC97e+Nijm 93+TM	-9.32	1.56	-8.35	0.70	0.82
SC89+Bonn B	-9.50	2.25	—	—	—
SC89+Nijm 93	-9.14	2.14	-6.99	0.02	2.06
SC89+Nijm 93+TM	-9.95	2.19	—	—	—
Jülich $\tilde{A}$ +Bonn B	-7.75	0.50	-7.78	0.54	-0.05
Jülich $\tilde{A}$ +Nijm 93	-7.40	0.43	-7.45	0.48	-0.05

Table 5.10: NN and 3N interaction dependence of the  ${}^4_\Lambda\text{He}$  binding energy  $E_B$ , the corresponding  $\Lambda$  separation energy  $E_{sep}^\Lambda$  and the  $0^+ - 1^+$  splitting  $\Delta$ . We show results for SC97e, SC89 and Jülich  $\tilde{A}$ . All energies are given in MeV.

in a comparison of  $E_{sep}^\Lambda$  to experimental results. As we already emphasized the binding energies of nuclei strongly depend on the NN interaction models. The same is true for the binding energies  $E_B$  of the four-body hypernuclei (see Table 5.10). In general it is assumed that the difference of the  ${}^4_\Lambda\text{He}$  and 3N binding energies, namely  $E_{sep}^\Lambda$  does not depend on the NN interaction. To check this assumption we performed calculations based on the SC97e, SC89 and Jülich  $\tilde{A}$  interactions in conjunction with Nijm 93 and Bonn B. Additionally we included the TM-3NF in some calculations. The results are shown in Table 5.10.

The table shows that the binding energies  $E_B$  strongly depend on the NN interaction, as expected. The  $\Lambda$  separation energies  $E_{sep}^\Lambda$  have a much smaller dependence on the NN and 3N interaction, nevertheless we still see deviations up to 120 keV. For the Jülich interaction these differences are smaller, around 70 keV. For SC97e and Jülich  $\tilde{A}$  we find that the splitting  $\Delta$  is less dependent on the NN and 3N interactions. In the case of Jülich  $\tilde{A}$  we find no differences at all, but for SC97e 50 keV deviation remains. The situation is very similar for  $0^+$  and  $1^+$  states. We note that the influence of the TM 3NF on  $E_{sep}^\Lambda$  is much smaller than the effect of the NN interaction. The change of binding energy in the 3N system due to the TM force is much bigger than the difference of the binding energy predictions of Bonn B and Nijm 93. Therefore we conclude that  $E_{sep}^\Lambda$  does not scale with the 3N binding energy and is sensitive to details of the NN interaction. Because we chose two very different NN models for our calculations, we expect that these results cover the whole range of possible differences due to the nucleonic interactions. Our estimate of the systematical uncertainty due to the NN force dependence of  $E_{sep}^\Lambda$  is 120 keV. For the energy splitting  $\Delta$  we fix 50 keV uncertainty. This closes the estimate of the uncertainty and reliability of our theoretical calculations. We turn to a comparison of the predictions of several YN interactions to the experimental separation energies now. A comparison to the binding energies  $E_B$  is useless, because of their strong NN force dependence. Therefore we omit the experimental binding energies in the tables and only present experimental separation energies. For the following investigations we chose the Nijm 93 NN interaction.

We start with a comparison of the  ${}^4_\Lambda\text{He}$  binding energies in Table 5.11. First we have a look to the  $J^\pi = 0^+$  ground state. We see that none of the potentials is able to predict the ground state binding energy correctly. The prediction of SC89 is closest to the experimental result. In view of the NN force dependence and numerical and experimental errors SC89 might give a realistic description of the ground

${}^4_{\Lambda}\text{He}$	$0^+$		$1^+$		$\Delta$
	$E_B$	$E_{sep}^{\Lambda}$	$E_B$	$E_{sep}^{\Lambda}$	
SC89	-9.14	2.14	-6.99	0.02	2.06
SC97f	-8.73	1.72	-7.50	0.53	1.16
SC97e	-8.55	1.54	-7.69	0.72	0.79
SC97d	-8.30	1.29	-7.77	0.80	0.47
Jülich $\tilde{A}$	-7.40	0.43	-7.45	0.48	-0.05
SC97e w/o $\Sigma$	-8.13	1.12	-7.76	0.79	0.37
Exp.	—	2.39(3)	—	1.24(5)	1.15

Table 5.11: Predictions for the  ${}^4_{\Lambda}\text{He}$  binding energy  $E_B$ , the corresponding  $\Lambda$  separation energy  $E_{sep}^{\Lambda}$  and the  $0^+-1^+$  splitting  $\Delta$  of the different YN potential models. The calculations are based on the Nijm 93 NN interaction. All energies are in MeV.

state binding energy.

The SC97d-f models clearly underbind the  ${}^4_{\Lambda}\text{He}$ . We emphasize that the SC97f and SC97f-sim (see Table 5.9) results again differ by 600 keV. While SC97f clearly underbinds  ${}^4_{\Lambda}\text{He}$ , the approximated interaction erroneously describes the ground state binding energy. This shows that reliable conclusions on the YN interaction models require non-approximated interactions.

From SC97f to SC97d the ground state separation energies drop. The predictions of the three SC97 interactions deviate in the ground state by 430 keV. Therefore visible differences of the ground state binding energies can be observed though we showed the equivalence of all three interactions for the total  $\Lambda p$  cross sections (see Fig. 5.1). The cross section predictions near  $T_{\Lambda} = 0$  MeV for SC89 are visibly smaller than for SC97d-f. Nevertheless we observe a higher  $\Lambda$  separation energy in the ground state of  ${}^4_{\Lambda}\text{He}$  and in  ${}^3_{\Lambda}\text{H}$  (see Table 5.2) for SC89 than for SC97d-f. Assuming that the binding energies are driven by the low energy behavior of the potentials, this indicates that the strength of the interactions is different in the nuclear medium and in the two baryon system. The last interaction considered is the Jülich  $\tilde{A}$  model. It predicts a tremendous underbinding in the  $J^{\pi} = 0^+$  state.

The Jülich  $\tilde{A}$  interaction even predicts the wrong spin ordering in  ${}^4_{\Lambda}\text{He}$ . For Jülich  $\tilde{A}$   $J^{\pi} = 1^+$  is more bound than the  $J^{\pi} = 0^+$  state. The  $0^+-1^+$  splitting  $\Delta$  has the wrong sign. In addition the experimental  $\Lambda$  separation energy could also not be reached in the  $J^{\pi} = 1^+$  state. Therefore we conclude that the Jülich  $\tilde{A}$  interaction completely fails to describe the light hypernuclei.

While SC89 might be able to describe the ground state realistically, it fails to predict correctly the excited state. The  $0^+-1^+$  splitting  $\Delta$  is nearly twice as large as the experimental value. We find that the  $J^{\pi} = 1^+$  state is hardly bound.

SC97d-f predict more realistic separation energies for the excited states. We observe that they increase going from SC97f to SC97d. This is opposite to the behavior in the ground state. We note that SC97f predicts  $\Delta$  in agreement with the experimental value. The SC97 scattering lengths given in Table 5.1 indicate a loss of strength in the  ${}^1S_0$  channel and a gain in the  ${}^3S_1$  channel going from SC97f to SC97d. From this tendency one can expect that the  $J = 0^+$  state gets less tightly bound and the  $J = 1^+$  more tightly bound changing from SC97f to SC97d (because the weights of spin  $s = 0$  and  $s = 1$  YN pairs should be different in both spin states). Our calculations confirm this behavior. However, the  ${}^3S_1$  scattering length is already bigger than the  ${}^1S_0$  one for SC97d. It has been argued in literature that in this case the  $J^{\pi} = 1^+$  state is more bound than the  $J^{\pi} = 0^+$  state [73]. Our results show that this is not



$J^\pi$		${}^4_\Lambda\text{He}$		${}^4_\Lambda\text{H}$		$\Delta_{CSB}$
		$E_B$	$E_{sep}^\Lambda$	$E_B$	$E_{sep}^\Lambda$	
$0^+$	SC97e	-8.55	1.54	-9.12	1.47	0.07
	SC89	-9.14	2.14	-9.45	1.80	0.34
	Exp.	—	2.39(3)	—	2.04(4)	0.35
$1^+$	SC97e	-7.69	0.72	-8.35	0.73	-0.01
	Exp.	—	1.24(5)	—	1.00(6)	0.24

Table 5.12: CSB splitting of the  ${}^4_\Lambda\text{He}$ - ${}^4_\Lambda\text{H}$  mirror nuclei. We show the binding energies  $E_B$ , the corresponding  $\Lambda$  separation energies  $E_{sep}^\Lambda$  and the CSB splitting  $\Delta_{CSB}$  of SC89 and SC97e potential models. The calculations have been performed with the Nijm 93 NN interaction. The first three rows compare ground state results to the experimental values, the last two excited states results. All energies are given in MeV.

true. SC97d leads to the correct spin ordering.

In summary we find that none of the interactions can predict the size of the  ${}^4_\Lambda\text{He}$  energies correctly. For SC89 we can nearly reach  $\Lambda$  separation energies in the  $J^\pi = 0^+$  state in agreement with the experimental value, but the potential fails to describe the splitting  $\Delta$  correctly. SC97f predicts the experimental value of  $\Delta$ , but leads to visible underbinding in both states. Jülich  $\tilde{A}$  even fails to predict the correct ordering of the excited and ground state. Moreover the  $\Lambda$  separation energies are strongly underpredicted.

In Table 5.11 we also present results of calculations based on a truncated  $t$ -matrix (labeled w/o  $\Sigma$ ). As described in Section 5.2, we solve the Lippmann-Schwinger equation for the full interaction (here SC97e) and restrict the  $t$ -matrix to  $\Lambda\text{N}$ - $\Lambda\text{N}$  matrix elements,  $\Lambda$ - $\Sigma$  conversion is switched off. By analytic continuation to positive energies the truncated  $t$ -matrix (given at negative energies) is linked to  $\Lambda\text{N}$  scattering. By construction it describes  $\Lambda\text{N}$  scattering equivalently to the original  $t$ -matrix. Nevertheless we observe visible separation energy differences. Again we consider this change in the separation energy as a systematic inaccuracy of effective  $\Lambda\text{N}$  interactions without  $\Lambda$ - $\Sigma$  conversion. For SC97e we find significant effects of the order of 400 keV in the ground state, and less important contributions in the excited state. If  $\Lambda$ - $\Sigma$  conversion is not explicitly included, the effects can be simulated by a  $\Lambda\text{NN}$  three-baryon force (3BF). Interestingly, the effect of this 3BF is attractive for  $J^\pi = 0^+$  states and repulsive for  $J^\pi = 1^+$  states. It is strongly spin dependent.

We close with a look to the energies of the  ${}^4_\Lambda\text{H}$  system. Table 5.12 compares the binding and separation energies for  ${}^4_\Lambda\text{He}$  and  ${}^4_\Lambda\text{H}$  using SC97e and SC89 with the experiment. We also give the difference  $\Delta_{CSB}$  of the  ${}^4_\Lambda\text{He}$  and  ${}^4_\Lambda\text{H}$  separation energies.  $\Delta_{CSB}$  is very sensitive to CSB in the YN interaction. The binding energies of  ${}^4_\Lambda\text{He}$  and  ${}^4_\Lambda\text{H}$  differ mostly because of the Coulomb repulsion acting in the pp pair in  ${}^4_\Lambda\text{He}$ . Because roughly the same Coulomb repulsion acts in the  ${}^3\text{He}$  core of  ${}^4_\Lambda\text{He}$ , the separation energy  $E_{sep}^\Lambda = E_B({}^3\text{He}) - E_B({}^4_\Lambda\text{He})$  is nearly independent from this Coulomb effect. Nevertheless it is experimentally found that  $E_{sep}^\Lambda({}^4_\Lambda\text{He})$  and  $E_{sep}^\Lambda({}^4_\Lambda\text{H})$  differ by 350 keV in the ground state and 240 keV in the excited state. This is expected to be an effect of the mass differences in the  $\Sigma$  multiplet and CSB of the strong YN interaction [64, 58]. As outlined at the beginning of the section, we incorporated both ingredients in our calculations.

We find very different predictions for SC89 and SC97e. For the  $J^\pi = 0^+$  ground state, SC89 can accurately describe  $\Delta_{CSB}$ . In contrast we find a too small CSB splitting for SC97e.

From the experimental values we learn that  $\Delta_{CSB}$  is state dependent. For the  $J^\pi = 1^+$  excited state

we performed the same calculations for SC97e only, because it is numerical very demanding to perform exited state calculations for the very loosely bound state predicted by SC89. We see that SC97e also fails to predict the experimental  $\Delta_{CSB}$  in the exited state. For this state even the sign of the experimental datum is not reproduced. In Section 5.6 we investigate perturbatively the origin of the predicted CSB.

In summary current YN interaction models, especially the SC97f interaction, can give a qualitative description of the four-body hypernuclei (correct spin ordering and splitting). Quantitatively all models fail to describe these hypernuclear systems. In SC97f overall binding in both, the ground and the exited state, is missing. We expect that important hints to missing features of the YN interactions arise from the CSB of the separation energies. It is interesting to see that the old SC89 model seems to do a better job for this aspect of the four-body bound states.

For a quantitative analysis of the binding energies an estimate of ANN 3BF due to other mechanisms than  $\Lambda$ - $\Sigma$  conversion is required. Unfortunately, no realistic models are available for numerically founded estimates. We would like to remark that similar mechanisms lead to roughly 10 % more binding in  ${}^3\text{H}$  against break-up in a nucleon and a deuteron. Based on the 2.39 MeV  $\Lambda$  separation energy, we estimate that a similar 10 % contribution of a ANN force to the separation energy of  ${}^4_\Lambda\text{He}$  amounts to 240 keV. This would not solve the underbinding problem for SC97f. We also note that this contribution might be strongly spin dependent. Therefore a similar contribution to the exited state with opposite sign is thinkable. This would wipe out our understanding of the  $0^+-1^+$  splitting. Realistic ANN 3BF, e.g. inspired by chiral perturbation theory, are highly needed to allow judgments of the size and spin dependence of these forces. Such studies are conceptually interesting also for ordinary nuclear physics, because they might clarify the mechanisms leading to 3BF's. In contrast to ordinary nuclear few-body systems, the lightest hypernuclei allow for an investigation of the spin structure of those forces. Such informations can hardly be obtained from the particle-stable nuclear three- and four-body states.

In contrast we also expect from the experience in the 3N and 4N system that these 3BF have only a subtle impact on the structure of the wave functions. The charge-dependence of these 3BF's is certainly small. Therefore the  ${}^4\text{He}$ - ${}^4\text{H}$  binding energy difference can be reliably estimated from our calculations neglecting these 3BF's. In Section 5.6 we will come back to this point and argue that the splitting due to CSB is related to  $\Lambda$ - $\Sigma$  conversion and therefore can give interesting insights into the YN interaction.

In the next section we summarize the most simple properties of the wave functions and reveal the parts of the interaction contributing to the different states of the nuclei. It will also be interesting to see correlations and distributions based on different interactions in comparison to the ones of the hypertriton. We again emphasize that these properties are less dependent on 3BF, at least if one is allowed to generalize our results for 3N and 4N bound states to the hypernuclei.

## 5.5 Properties of the four-body hypernuclear wave functions

In this section we will look to the properties of the  ${}^4_\Lambda\text{He}$  wave functions in more detail.

We will start with a judgment on the accuracy of our  ${}^4_\Lambda\text{He}$  wave functions and continue with a summary of the contributions of different orbital and spin states to the wave function. An emphasis is put on the decomposition of the YN potential expectation values into contributions of different channels. A big part of this section is devoted to a presentation of momentum distributions and correlation functions.

To that aim we created wave functions based on the interaction combinations Nijm 93+SC97d-f, Nijm 93+SC89 and Bonn B+Jülich  $\tilde{\Lambda}$ . The results presented in this section are based on these interaction combinations. Additionally we prepared wave functions for Bonn B+SC89 and Bonn B+SC97e. We found that the wave function properties of the hyperons or YN pairs are only slightly dependent on the NN

interaction. Therefore we omit results based on the wave functions related to Bonn B in the following. We also restrict ourselves to  ${}^4_{\Lambda}\text{He}$  wave functions. In Section 4.4 we investigated the CSB breaking of the 3N wave functions. We found differences, which are below the accuracy of our hypernuclear calculations. Therefore we do not expect new insights from investigations of  ${}^4_{\Lambda}\text{H}$  wave functions.

In Section 3.3.2 we outlined our algorithm to create wave functions from the Yakubovsky components. All results presented in this section are based on wave functions, whose partial wave decomposition is truncated in the same way. For  $J^{\pi} = 0^{+}$  states we restrict the partial wave decomposition by  $l_{sum}^{max} = 14$  and for  $J^{\pi} = 1^{+}$  states by  $l_{sum}^{max} = 10$ . As outlined in Section 3.3.2 we obtain wave functions in all different kinds of Jacobi coordinates.

It is numerically very hard to obtain accurate wave functions for the four-body systems. Only the inclusion of a tremendous number of partial waves led to an accurate description of the hypernuclear four-body bound states. To exemplify our accuracy we compare in Tables 5.13 and 5.14 the expectation values of the Hamilton operator  $H$  to the binding energies  $E_B$  found from the diagonalization of the Yakubovsky equations. We emphasize that  $E_B$  is more accurate than  $H$ , because the representation of the Yakubovsky equations is based on a systematic usage of all different Jacobi coordinates. This leads to an increased speed of convergence. Nevertheless we find that for all interactions and both states  $H$  and  $E_B$  differ at most by 70 keV. Compared to the binding energies this means that we achieve an accuracy of 0.9 % or better for  $H$ . The expectation value  $H$  is the sum of the kinetic energy  $T$  and the YN and NN potential energies  $V_{YN}$  and  $V_{NN}$ . The individual contributions of these parts to  $H$  are also given in the tables. As usual they cancel each other to a great extent. Compared to the kinetic energy  $H$  and  $E_B$  only differ by 0.2 %. This is an indication of the numerical error of the wave functions. We are very satisfied with this agreement and consider it as a good consistency check of our calculations. We remark that our kinetic energies are based on overlaps of the Yakubovsky components (YC) and wave functions as described in Section 3.3.2. This improves the accuracy, because the YC's project the wave function on low momenta. The error in high momentum components is expected to be higher.

Comparing  $V_{NN}$  for the different Nijm 93 calculations in Tables 5.13 and 5.14 we observe a slight dependence of  $V_{NN}$  on the YN interaction and the state of  ${}^4_{\Lambda}\text{He}$ . We conclude that a possible  ${}^3\text{He}$  core in  ${}^4_{\Lambda}\text{He}$  is disturbed by the bound hyperon. But we also note that  $V_{NN}$  only slightly changes. This is an indication for the existence of a core state in  ${}^4_{\Lambda}\text{He}$ . We will clarify this point later on, when we build up  $\Lambda$ - ${}^3\text{He}/{}^4_{\Lambda}\text{He}$  overlaps.

In contrast the YN potential energy  $V_{YN}$  strongly depends on the interaction and the state. We especially note that  $V_{YN}$  for Jülich  $\tilde{A}$  is bigger in the  $J^{\pi} = 0^{+}$  state than in the  $J^{\pi} = 1^{+}$  state. This is remarkable, because the binding energy prediction for this interaction is bigger in the  $J^{\pi} = 1^{+}$  state. Obviously the ordering of the different spin states in  ${}^4_{\Lambda}\text{He}$  is the result of a complicated interplay of different parts of the Hamiltonian. The YN potential expectation values for Jülich  $\tilde{A}$  clearly show, that one cannot conclude from the physical spin ordering of  ${}^4_{\Lambda}\text{He}$  on the strength of parts of the interaction. Such arguments are very often used in literature (see for example [73]). They are based on the assumption that the binding energy and the expectation value of  $V_{YN}$  are correlated. The example of the Jülich  $\tilde{A}$  interaction shows that this correlation is not necessarily true. Therefore we point out that conclusions based on such approximations might be misleading.

In Table 5.15 we present the contributions of different total orbital angular momenta to the wave function. For  $J^{\pi} = 0^{+}$  states we find total orbital  $S$ -,  $P$ - and  $D$ -states in the wave function. Similar to the  $\alpha$ -particle (see Table 4.17), we see that the  $S$ -state dominates the wave function. The  $D$ -state is a visible part of the wave function, but the  $P$ -state contributes only tinily. We note that the  $S$ -wave is even more important in the hypernuclear systems than in the  $\alpha$ -particle. For  $J^{\pi} = 1^{+}$  states total orbital angular momenta up to  $F$ -states can contribute to the wave function. Our results are also shown in

	$E_B$	$H$	$T$	$V_{NN}$	$V_{YN}$
Nijm 93+SC89	-9.14	-9.13	65.34	-53.86	-20.63
Nijm 93+SC97f	-8.73	-8.68	59.76	-52.20	-16.24
Nijm 93+SC97e	-8.55	-8.49	59.26	-52.27	-15.48
Nijm 93+SC97d	-8.30	-8.25	58.15	-52.26	-14.14
Bonn B +Jülich $\tilde{A}$	-7.75	-7.68	49.77	-43.86	-13.59

Table 5.13: Expectation values of the Hamilton operator  $H$ , the kinetic energy  $T$ , the NN potential energy  $V_{NN}$  and the YN potential energy  $V_{YN}$  for the  $J^\pi = 0^+$  state of  ${}^4_\Lambda\text{He}$ . The expectation value of the Hamiltonian  $H$  is compared to the binding energies  $E_B$ . All energies are given in MeV.

	$E_B$	$H$	$T$	$V_{NN}$	$V_{YN}$
Nijm 93+SC89	-6.99	-6.99	45.80	-51.25	-1.55
Nijm 93+SC97f	-7.50	-7.47	52.72	-50.70	-9.49
Nijm 93+SC97e	-7.69	-7.65	54.84	-50.92	-11.57
Nijm 93+SC97d	-7.77	-7.74	55.47	-51.05	-12.16
Bonn B +Jülich $\tilde{A}$	-7.78	-7.72	47.57	-44.56	-10.73

Table 5.14: Expectation values of the Hamilton operator  $H$ , the kinetic energy  $T$ , the NN potential energy  $V_{NN}$  and the YN potential energy  $V_{YN}$  for the  $J^\pi = 1^+$  state of  ${}^4_\Lambda\text{He}$ . The expectation value of the Hamiltonian  $H$  is compared to the binding energies  $E_B$ . All energies are given in MeV.

model	$J^\pi = 0^+$			$J^\pi = 1^+$			
	$S$	$P$	$D$	$S$	$P$	$D$	$F$
SC97f+Nijm 93	90.87	0.11	9.02	90.77	0.08	9.13	0.02
SC97e+Nijm 93	90.85	0.11	9.03	90.63	0.08	9.27	0.03
SC97d+Nijm 93	90.82	0.11	9.06	90.58	0.08	9.31	0.03
SC89+Nijm 93	90.32	0.13	9.55	91.36	0.07	8.57	0.00
Jülich $\tilde{A}$ +Bonn B	92.61	0.07	7.32	92.32	0.06	7.61	0.01

Table 5.15:  $S$ ,  $P$ ,  $D$  and  $F$  state probabilities for the  $J^\pi = 0^+$  and  $J^\pi = 1^+$  state of  ${}^4_\Lambda\text{He}$ . All probabilities are given in %.

Table 5.15. We see that the contributions of the different states are very similar in  $J^\pi = 0^+$  and  $J^\pi = 1^+$  states. The  $F$ -state probabilities are even smaller than the  $P$ -wave contributions. We observe that the small shifts in the probabilities depend on the interaction. For SC97 the  $J^\pi = 0^+$  state has got a higher  $S$ -wave and smaller  $D$ -wave probability than the  $J^\pi = 1^+$  state. For the SC89 and Jülich interactions we observe an opposite behavior. In all cases the  $P$ -wave contribution decreases going from the  $J^\pi = 0^+$  to the  $J^\pi = 1^+$  state.

In Table 5.16 we present the probabilities for different total spin states. The spins of the four spin  $\frac{1}{2}$  fermions can sum up to total spin  $S = 0$ ,  $S = 1$  and  $S = 2$ . The table summarizes the contributions of these spin states to the  $J^\pi = 0^+$  and  $J^\pi = 1^+$  states. For  $J^\pi = 0^+$  states the total spin  $S$  and the orbital angular momentum are equal. Therefore the results of Tables 5.15 and 5.16 agree for this state. We have already seen that the contributions of the orbital angular momenta are very similar for ground and

model	$J^\pi = 0^+$			$J^\pi = 1^+$		
	$S = 0$	$S = 1$	$S = 2$	$S = 0$	$S = 1$	$S = 2$
SC97f+Nijm 93	90.87	0.11	9.02	0.02	95.57	4.41
SC97e+Nijm 93	90.85	0.11	9.03	0.02	95.53	4.45
SC97d+Nijm 93	90.82	0.11	9.06	0.02	95.50	4.48
SC89+Nijm 93	90.32	0.13	9.55	0.02	95.71	4.28
Jülich $\tilde{A}$ +Bonn B	92.61	0.07	7.32	0.01	96.37	3.62

Table 5.16: Total spin state  $S = 0$ ,  $S = 1$  and  $S = 2$  probabilities for the  $J^\pi = 0^+$  and  $J^\pi = 1^+$  state of  ${}^4_\Lambda\text{He}$ . All probabilities are given in %.

	$J^\pi = 0^+$				$J^\pi = 1^+$			
	${}^1S_0$	${}^3S_1$	P	other	${}^1S_0$	${}^3S_1$	P	other
SC97f+Nijm 93	38.67	45.06	9.75	6.51	12.39	58.92	16.48	12.22
SC97e+Nijm 93	38.13	44.57	10.31	7.00	13.09	61.98	14.67	10.26
SC97d+Nijm 93	37.21	43.65	11.34	7.80	13.35	63.04	13.98	9.62
SC89+Nijm 93	39.40	45.91	9.15	5.55	6.10	30.30	24.71	38.89
Jülich $\tilde{A}$ +Bonn B	31.83	37.67	16.50	14.00	12.94	58.33	16.83	11.89

Table 5.17: Probabilities to find a YN pair in a fixed relative partial wave for the  $J^\pi = 0^+$  and  $J^\pi = 1^+$  state of  ${}^4_\Lambda\text{He}$ . We distinguish  ${}^1S_0$ ,  ${}^3S_1$ - ${}^3D_1$ , P-waves ( ${}^3P_0$ ,  ${}^1P_1$ ,  ${}^3P_1$ ,  ${}^3P_2$ - ${}^3F_2$ ) and other partial waves. All probabilities are given in %.

exited states. This indicates that the orbital parts of the wave function are comparable. From the spin probabilities we see that the spin wave functions are very different. In the  $J^\pi = 0^+$  state spin  $S = 0$  is dominant. In contrast the  $S = 1$  spin state dominates the  $J^\pi = 1^+$  states. This confirms the expectation that both hypernuclear states predominately differ in their spin structure and can be seen as spin flip states.

We showed that the total orbital  $S$ -wave is the most important part of the wave function. However, as in the case of the hypertriton the relative motion within a YN pair requires a high number of partial waves. In Table 5.17 we give the contributions of the different partial waves to the relative motion in the YN pairs for the ground and exited states. We distinguish the  ${}^1S_0$  and  ${}^3S_1$ - ${}^3D_1$  states, the  $P$ -waves and other partial waves. In both states, the  $J^\pi = 0^+$  and  $J^\pi = 1^+$ , we see that the  $P$ -waves and higher partial waves always give more than 15 % to the wave function. This contribution is generally higher in the  $J^\pi = 1^+$  state. We observe a correlation of the  $\Lambda$  separation energy and the contribution of the higher partial waves: the smaller the separation energy for the interaction model and the state the higher is the contribution of the higher partial waves. For the extremely loosely bound  $J^\pi = 1^+$  state for SC89 we find a contribution of more than 60 % from these partial waves. For many simple investigations it is assumed that the relative weights of the  ${}^1S_0$  and  ${}^3S_1$ - ${}^3D_1$  states is 1:1 for the  $J^\pi = 0^+$  states and 1:5 for the  $J^\pi = 1^+$  states. We find roughly 1:1.2 and 1:4.9 for these ratios. Though the contributions of the higher partial waves are non-negligible, our ratios of  ${}^1S_0$  and  ${}^3S_1$ - ${}^3D_1$  states are in rough agreement with the simple theoretical predictions.

Experimentally the  $J^\pi = 0^+$  state is the ground state. Because the  ${}^1S_0$  contribution to this state is bigger than in the exited state, it has been argued that the  ${}^1S_0$  YN interaction is more attractive

	AN-AN			$\Sigma N$ - $\Sigma N$			AN- $\Sigma N$		
	$^1S_0$	$^3S_1$ - $^3D_1$	ALL	$^1S_0$	$^3S_1$ - $^3D_1$	ALL	$^1S_0$	$^3S_1$ - $^3D_1$	ALL
SC97f+Nijm 93	-5.92	1.11	-4.66	-0.27	0.93	0.72	-0.28	-11.91	-12.30
SC97e+Nijm 93	-5.30	1.16	-4.04	-0.43	1.18	0.81	-0.17	-11.98	-12.25
SC97d+Nijm 93	-4.53	0.91	-3.54	-0.53	1.10	0.62	-0.07	-11.06	-11.23
SC89+Nijm 93	-5.00	0.14	-4.81	-0.20	-0.47	-0.57	-1.27	-13.78	-15.26
Jülich $\tilde{A}$ +Bonn B	1.78	-2.49	-0.68	-3.93	0.03	-4.01	-7.03	-1.84	-8.90

Table 5.18: Contributions of different partial waves to the expectation value of the YN potential for the  $J^\pi = 0^+$  state of  $^4_\Lambda\text{He}$ . We distinguish  $^1S_0$ ,  $^3S_1$ - $^3D_1$  partial waves and the total contribution (ALL) of the AN-AN,  $\Sigma N$ - $\Sigma N$  and AN- $\Sigma N$  potentials. All energies are given in MeV.

	AN-AN			$\Sigma N$ - $\Sigma N$			AN- $\Sigma N$		
	$^1S_0$	$^3S_1$ - $^3D_1$	ALL	$^1S_0$	$^3S_1$ - $^3D_1$	ALL	$^1S_0$	$^3S_1$ - $^3D_1$	ALL
SC97f+Nijm 93	-1.26	1.36	0.18	-0.06	1.40	1.37	-0.04	-10.89	-11.04
SC97e+Nijm 93	-1.34	1.55	0.29	-0.12	2.00	1.92	-0.03	-13.63	-13.78
SC97d+Nijm 93	-1.28	1.40	0.21	-0.16	2.10	1.98	0.00	-14.21	-14.34
SC89+Nijm 93	-0.20	-0.04	-0.23	0.00	-0.01	-0.01	-0.03	-1.25	-1.31
Jülich $\tilde{A}$ +Bonn B	1.03	-3.76	-2.69	-2.16	0.06	-2.14	-3.58	-2.30	-5.90

Table 5.19: Contributions of different partial waves to the expectation value of the YN potential for the  $J^\pi = 1^+$  state of  $^4_\Lambda\text{He}$ . We distinguish  $^1S_0$ ,  $^3S_1$ - $^3D_1$  partial waves and the total contribution (ALL) of the AN-AN,  $\Sigma N$ - $\Sigma N$  and AN- $\Sigma N$  potentials. All energies are given in MeV.

than the  $^3S_1$ - $^3D_1$  interaction. Is such an argumentation justified? To answer this question we present in Tables 5.18 and 5.19 the contributions of the different partial waves in the YN pairs to the expectation value of the YN potential. The dominant contributions are caused by the  $S$ -waves. Therefore we only distinguish  $^1S_0$  and  $^3S_1$ - $^3D_1$  states. Additionally we give the summed up contribution of all partial waves. To clarify the importance of the conversion potentials we give the expectation values of the AN-AN direct potential, of the  $\Sigma N$ - $\Sigma N$  potential and of the AN- $\Sigma N$  conversion potential.

We start with the group of the Nijmegen SC interactions and for the  $J^\pi = 0^+$  state presented in Table 5.18. For these interactions the most important contributions arise from the  $^1S_0$  AN-AN interaction and the  $^3S_1$ - $^3D_1$  AN- $\Sigma N$  conversion potential. As in the case of the hypertriton we find a repulsive  $^3S_1$ - $^3D_1$  AN-AN interaction. Though we look at the  $J^\pi = 0^+$  states, we see that the summed up expectation values of the  $^3S_1$ - $^3D_1$  potentials are still more than two times as important as the sum of  $^1S_0$  channels. This shows that the  $^3S_1$ - $^3D_1$  interactions are very attractive. Nevertheless the Nijmegen interactions predict the correct spin ordering for  $^4_\Lambda\text{He}$ . We conclude that the relative strength in the  $^1S_0$  and  $^3S_1$ - $^3D_1$  potentials is not decisive for the spin ordering. In this context we refer to the  $\Lambda p$  scattering lengths given in Table 5.1. For SC97d we observe a bigger triplet than singlet scattering length. Nevertheless the  $J^\pi = 0^+$  state is more tightly bound than the  $J^\pi = 1^+$ .

For SC89 we find some interesting differences to the SC97 models. First we observe a visibly less repulsive  $^3S_1$ - $^3D_1$  AN-AN interaction. We also note that the  $\Sigma N$ - $\Sigma N$  interaction is overall attractive for this potential and repulsive for the SC97 models. Additionally we find more attraction in the  $^1S_0$  AN- $\Sigma N$  potential. The origin of these difference has to be clarified. Each difference might explain the stronger binding predicted by SC89 in the ground state and gives hints how to cure the underbinding problem of

SC97 in a future series of model interactions.

In the last section we already emphasized that the Jülich model fails to describe the four-body hypernuclei. Nevertheless it is interesting to see the differences compared to the Nijmegen models. From Table 5.18 we learn that the action of Jülich  $\tilde{\Lambda}$  in  ${}^4_{\Lambda}\text{He}$  tremendously differs from the Nijmegen SC models. For  $\Lambda\text{N}-\Lambda\text{N}$  we see that the  ${}^1\text{S}_0$  interaction is repulsive, whereas the  ${}^3\text{S}_1$ - ${}^3\text{D}_1$  potential is attractive. This is opposite to the SC interactions. We are surprised to find an important  $\Sigma\text{N}-\Sigma\text{N}$  contribution to the potential energy. For this part of the interaction the  ${}^1\text{S}_0$  is attractive and  ${}^3\text{S}_1$ - ${}^3\text{D}_1$  is nearly negligible. Similar to the Nijmegen models, the  $\Lambda\text{N}-\Sigma\text{N}$  interaction is the most important part. In contrast to Nijmegen we see for Jülich that the  ${}^1\text{S}_0$  channel is much more important than the  ${}^3\text{S}_1$ - ${}^3\text{D}_1$  channel for this part. We note that the summed up contribution of the  ${}^1\text{S}_0$  channels is much more attractive than the contribution of the  ${}^3\text{S}_1$ - ${}^3\text{D}_1$  channels. Nevertheless we predict a  $J^\pi = 1^+$  ground state using this interaction. Again the relative strength of the  ${}^1\text{S}_0$  and  ${}^3\text{S}_1$ - ${}^3\text{D}_1$  interactions cannot be deduced from the spin ordering of  ${}^4_{\Lambda}\text{He}$ .

Summarizing the situation in the  $J^\pi = 0^+$  states, we found that the  $\Lambda\text{N}-\Sigma\text{N}$  part of the interactions is always the most important one. We found repulsive  $S$ -wave contributions for all interactions, however for the Jülich and the Nijmegen models these attractive and repulsive channels have different spin. We emphasize that one cannot deduce the relative strength of  ${}^1\text{S}_0$  and  ${}^3\text{S}_1$ - ${}^3\text{D}_1$  interactions from the spin ordering of the ground and excited state of  ${}^4_{\Lambda}\text{He}$ .

With this knowledge we look to the  $J^\pi = 1^+$  state in Table 5.19. In general we observe for all interactions a decrease of the  ${}^1\text{S}_0$  contributions and an increase of the  ${}^3\text{S}_1$ - ${}^3\text{D}_1$  contributions compared to the  $J^\pi = 0^+$  state (except for SC89, this case is special because of its very small  $\Lambda$  separation energy). This also holds for the conversion potential and indicates that the mechanism of  $\Lambda$ - $\Sigma$  conversion suppression [68] is not responsible for the spin ordering in the four-body hypernuclei. For the SC97 models this leads to a repulsive  $\Lambda\text{N}-\Lambda\text{N}$  interaction. For these interactions binding is only provided by the  $\Lambda\text{N}-\Sigma\text{N}$  part. We note that the  $\Sigma\text{N}-\Sigma\text{N}$  interaction is also repulsive and more important than the  $\Lambda\text{N}-\Lambda\text{N}$  potential. For the Jülich model we see that the direct  $\Lambda\text{N}-\Lambda\text{N}$  interaction gets more important now. We know that the  $J^\pi = 1^+$  state is slightly deeper bound than the  $J^\pi = 0^+$  state. We already emphasized that the total potential energy is smaller in the  $J^\pi = 1^+$  state. But we see from the table, that for this state a visible part is contributed by the direct interaction. This is an indication that the  $\Lambda\text{N}-\Lambda\text{N}$  part is more effective for the binding of the hypernuclei. This might be the result of a smaller kinetic energy in these channels (the mass of the  $\Sigma$  particle is much bigger than the  $\Lambda$  mass). We do not give kinetic energies separated for different YN channels here. As described in Section 3.3.2 and shown in Table 3.30 it is mandatory for us to calculate the kinetic energies with the help of Yakubovsky components. Therefore the kinetic energies are calculated simultaneously using all Jacobi coordinates. Because a projection on fixed YN subsystem channels can only be performed in 1C or 2B coordinates, we are not able to project on these YN channels using our way to calculate the kinetic energies. Such an investigation is left for forthcoming studies using an increased number of partial waves and calculating the kinetic energies directly from the wave functions.

Therefore we summarize the results for the  $J^\pi = 1^+$  states. For the Nijmegen interactions, the decrease of the attractive  ${}^1\text{S}_0$  direct  $\Lambda\text{N}-\Lambda\text{N}$  potentials seems to be responsible for the smaller attraction in the excited state. In contrast we find that the direct part gets more attractive for the Jülich interaction in the  $J^\pi = 1^+$ . This might explain the wrong spin ordering predicted by this interaction. For both states and all interactions we found that the  $\Lambda\text{N}-\Sigma\text{N}$  conversion potential is a very important attractive interaction. We confirmed this result from [76] for the four-body system now. Unfortunately the complicated structure of the YN interaction prohibits simple deductions on the strength of different spin states of the YN interaction from the level ordering in the hypernuclei. The  $\Lambda$ - $\Sigma$  conversion seems not to be suppressed

	$P_p$	$P_n$	$P_\Lambda$	$P_\Sigma$	$P_{\Sigma^+}$	$P_{\Sigma^0}$	$P_{\Sigma^-}$	$N_T^\Lambda$
SC97f+Nijm 93	66.31	33.69	98.24	1.76	1.15	0.59	0.02	96.35
SC97e+Nijm 93	66.36	33.64	98.43	1.57	1.02	0.52	0.03	96.78
SC97d+Nijm 93	66.39	33.61	98.51	1.49	0.95	0.50	0.04	97.04
SC89+Nijm 93	65.81	34.19	95.92	4.08	2.67	1.36	0.05	93.20
Jülich $\tilde{A}$ +Bonn B	66.79	33.21	96.71	3.29	0.99	1.10	1.20	96.00

Table 5.20: Probabilities to find a nucleon as proton ( $P_p$ ) or neutron ( $P_n$ ) and a hyperon as  $\Lambda$  ( $P_\Lambda$ ) or ( $P_\Sigma$ ) for the  $J^\pi = 0^+$  state of  ${}^4_\Lambda\text{He}$ . We also distinguish the contributions of  $\Sigma^+$ ,  $\Sigma^0$  and  $\Sigma^-$  to  $P_\Sigma$  ( $P_{\Sigma^+}$ ,  $P_{\Sigma^0}$  and  $P_{\Sigma^-}$ ). The normalization constants  $N_T^\Lambda$  of the  $\Lambda$ - ${}^3\text{He}/{}^4_\Lambda\text{He}$  overlap function are also given. All probabilities are given in %.

	$P_p$	$P_n$	$P_\Lambda$	$P_\Sigma$	$P_{\Sigma^+}$	$P_{\Sigma^0}$	$P_{\Sigma^-}$	$N_T^\Lambda$
SC97f+Nijm 93	66.77	33.23	99.02	0.98	0.41	0.33	0.24	98.08
SC97e+Nijm 93	66.74	33.26	98.92	1.08	0.46	0.36	0.27	97.90
SC97d+Nijm 93	66.72	33.28	98.86	1.14	0.48	0.38	0.28	97.81
SC89+Nijm 93	66.67	33.33	99.75	0.25	0.11	0.08	0.06	99.34
Jülich $\tilde{A}$ +Bonn B	66.40	33.60	97.98	2.02	1.22	0.67	0.13	97.15

Table 5.21: Probabilities to find a nucleon as proton ( $P_p$ ) or neutron ( $P_n$ ) and a hyperon as  $\Lambda$  ( $P_\Lambda$ ) or ( $P_\Sigma$ ) for the  $J^\pi = 1^+$  state of  ${}^4_\Lambda\text{He}$ . We also distinguish the contributions of  $\Sigma^+$ ,  $\Sigma^0$  and  $\Sigma^-$  to  $P_\Sigma$  ( $P_{\Sigma^+}$ ,  $P_{\Sigma^0}$  and  $P_{\Sigma^-}$ ). The normalization constants  $N_T^\Lambda$  of the  $\Lambda$ - ${}^3\text{He}/{}^4_\Lambda\text{He}$  overlap function are also given. All probabilities are given in %.

in the excited state.

Now we turn to the momentum distribution in  ${}^4_\Lambda\text{He}$ .

The  ${}^4_\Lambda\text{He}$  calculations are performed using isospin conservation. The hypernuclear four-body wave functions are restricted to total isospin  $T = \frac{1}{2}$ . In contrast to the hypertriton, the  ${}^4_\Lambda\text{He}$  is not invariant under isospin rotations. Therefore we can distinguish momentum distributions and correlations for particles or pairs of particles with a different magnetic isospin quantum number. We investigated the dependence on the third component of the isospin quantum number. And indeed, as expected, we find visible differences in the probabilities for a nucleon to be in the proton ( $P_p$ ) or neutron ( $P_n$ ) state or for a hyperon to be in a  $\Sigma^+$  ( $P_{\Sigma^+}$ ),  $\Sigma^0$  ( $P_{\Sigma^0}$ ) or  $\Sigma^-$  ( $P_{\Sigma^-}$ ) state (see Tables 5.20 and 5.21). However, we observed that the functional form of the distributions and correlations are qualitatively equal for different orientations in isospin space. Therefore we present in the following only momentum distributions and correlations, which are averaged over the isospin orientations.

For the momentum distributions we distinguish  $D_N$ ,  $D_\Lambda$  and  $D_\Sigma$ , for the nucleon,  $\Lambda$  and  $\Sigma$ , respectively, as we already did for the hypertriton in Section 5.3. The definition of nucleon momentum distributions as given in Eq. (4.2) can be easily generalized to  ${}^4_\Lambda\text{He}$  baryon momentum distributions. We present the functions in the normalization given in Eq. (5.1). The original sizes of  $D_\Lambda$  and  $D_\Sigma$  can be deduced from the  $\Lambda$  and  $\Sigma$  probabilities  $P_\Lambda$  and  $P_\Sigma$  shown in Tables 5.20 and 5.21.

For  ${}^4_\Lambda\text{He}$  we also define overlap functions with  ${}^3\text{He}$ . The definition follows Eq. (4.19). We directly make use of the angular independence of the overlap functions, which also holds for four-body states with non-zero total angular momentum (see Appendix E). In that appendix it is also shown that the overlap



function does not depend on the orientation  $m_t$  of the 3N wave function. Therefore we omit the  ${}^3\text{He}$  angular momentum  $j_t m_t$  in our notation here. Additionally we introduce a projection operator  $P_{\Lambda/\Sigma}(4)$  on the  $\Lambda$  or  $\Sigma$  state of the hyperon. Therefore Eq. (4.19) turns to

$$\mathcal{T}_{\Lambda/\Sigma}(p) = \frac{1}{2J+1} \sum_M \langle \Psi JM | \delta(q_4 - p) P_{\Lambda/\Sigma}(4) | \phi_t \rangle \langle \phi_t | \Psi JM \rangle \quad (5.4)$$

The normalization constant

$$N_T^\Lambda = \int_0^\infty dp \mathcal{T}_\Lambda(p) \quad (5.5)$$

gives the probability to find a  $\Lambda$  particle bound to an undisturbed  ${}^3\text{He}$  core in  ${}^4_\Lambda\text{He}$ . Our results for  $N_T^\Lambda$  are also included in Tables 5.20 and 5.21. In the following figures we present overlap functions  $\mathcal{T}_\Lambda$ , which are normalized to

$$\int_0^\infty dp \mathcal{T}_\Lambda(p) = 1 \quad (5.6)$$

As in the case of the momentum distribution functions, the original sizes can be deduced from the normalization constants  $N_T^\Lambda$ . We omit  $\mathcal{T}_\Sigma$  in our survey, because we only found a negligible contribution from this overlap.

Before we look to these distribution functions we comment on the probabilities given in Tables 5.20 and 5.21.

Neglecting the  $\Sigma$  components of the wave functions, we find the nucleons to 66.67 % in a proton state and to 33.33 % in a neutron state. The small deviations found in the tables are a consequence of  $\Lambda$ - $\Sigma$  conversion, which populates the  $\Sigma^-$  and  $\Sigma^+$  states differently. Therefore this is a property of the underlying YN interaction.

The results for the  $J^\pi = 0^+$  states are summarized in Table 5.20. For the Nijmegen SC models we find a slightly increased neutron probability  $P_n$ . This fits to the observation of a higher  $P_{\Sigma^+}$  than  $P_{\Sigma^-}$ . In contrast the Jülich  $\tilde{A}$  interaction populates the  $\Sigma^-$  component more than the  $\Sigma^+$  component in the  $J^\pi = 0^+$  state. This leads to a decreased neutron probability.

The summed  $\Sigma$  probabilities  $P_\Sigma$  are considerably higher for SC89 and Jülich  $\tilde{A}$  than for the new SC97 models. The conversion process seems to be more pronounced in the case of the older interactions. We see that the normalization constants  $N_T^\Lambda$  are much bigger than corresponding results for the  $\alpha$ -particle (see Table 4.19). Because  $N_T^\Lambda$  is bigger than 93 % in all cases, we note that the  ${}^4_\Lambda\text{He}$  state is to a great extent a  $\Lambda$  particle bound to a  ${}^3\text{He}$  core nucleus. The perturbation of the core nucleus is more visible for SC89 than for the other interactions. We also observe that this perturbation is bigger than the one of the  ${}^2\text{H}$  core in  ${}^3_\Lambda\text{H}$  (see Table 5.6).

For the  $J^\pi = 1^+$  state the observations are very similar. The results are summarized in Table 5.21. Compared to the  $J^\pi = 0^+$  results we see that the  $\Sigma$  probabilities are generally decreased for these states. We also find increased  $N_T^\Lambda$  in  $J^\pi = 1^+$  states. For the Nijmegen SC interactions the  $\Sigma$  components again pronounce the  $\Sigma^+$  state. It is remarkable that the same behavior is found for Jülich  $\tilde{A}$  now. In this point there is a qualitative difference of the  $J^\pi = 0^+$  and  $J^\pi = 1^+$  results for Jülich  $\tilde{A}$ .

For both states the  $\Sigma$  probabilities are visibly bigger than the corresponding  ${}^3_\Lambda\text{H}$  predictions from Table 5.6. We find  $\Sigma$  probabilities up to 4.08 %. This is 8 times the maximum prediction for  ${}^3_\Lambda\text{H}$  from the same interactions. This shows the increased importance of the  $\Sigma$  particle for the four-body hypernuclei.

Now we are ready for a look to the nucleon distributions  $D_N(p)$ . In Fig. 5.11 we present the nucleon distributions for both states of  ${}^4_\Lambda\text{He}$ . For the presentation we compare the results of two interaction combinations (SC97f+Nijm 93 and SC89+Nijm 93) to  $D_N(p)$  in  ${}^3\text{He}$ , which has been obtained using

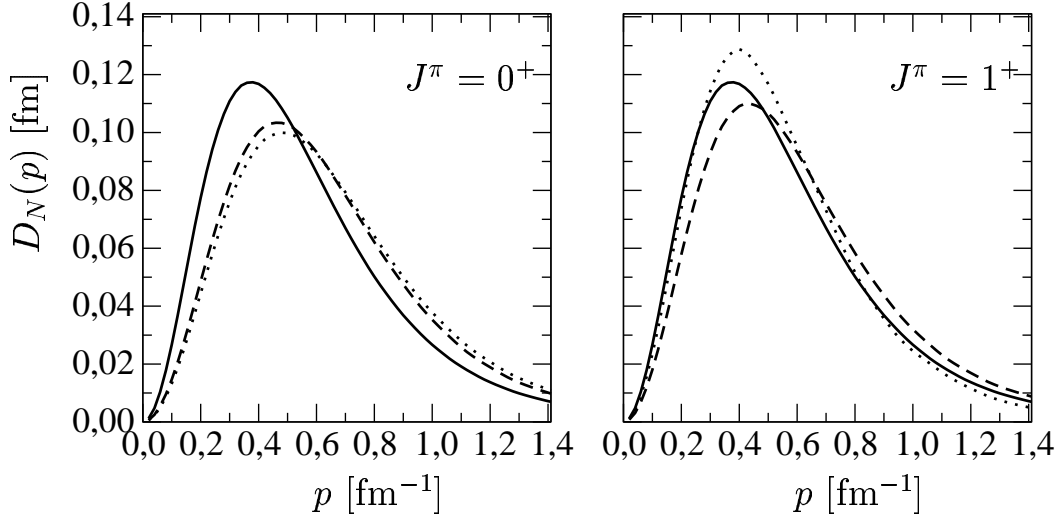


Figure 5.11: Nucleon momentum distributions in the  $J^\pi = 0^+$  (left figure) and  $J^\pi = 1^+$  (right figure) state of  ${}^4_\Lambda\text{He}$ . The distribution functions are based on calculations using the Nijm 93 NN interaction and the SC97f (dashed lines) or SC89 (dotted lines) YN interactions. Additionally the nucleon distribution in  ${}^3\text{He}$  (solid lines) is included based on the Nijm 93 NN interaction. The functions are normalized to  $\int C(p)dp = \frac{1}{4\pi}$ .

the same NN interaction. For these distributions we chose a linear scale, because we are interested in the low momentum region of the interaction. The distributions of  ${}^3\text{He}$  and  ${}^4_\Lambda\text{He}$  differ visibly though we found a quite large  ${}^3\text{He}$  component in the state of the 3N subsystem. We observe a shift of the peak of the  ${}^4_\Lambda\text{He}$  distributions to higher momenta in both states. For  $J^\pi = 0^+$  we see that  $D_N$  for  ${}^4_\Lambda\text{He}$  only slightly depends on the YN interaction. In contrast we find a considerable difference of the distributions for  $J^\pi = 1^+$ . Again we note the anomalously small  $\Lambda$  separation energy prediction for this potential in the excited state.

In Fig. 5.12 we compare the  $\Lambda$  momentum distributions  $D_\Lambda$  to the  $\Lambda$ - ${}^3\text{He}/{}^4_\Lambda\text{He}$  overlap functions  $\mathcal{T}_\Lambda$ . We compare results of Bonn B+Jülich  $\tilde{\Lambda}$ , SC97f+Nijm 93 and SC89+Nijm 93 for  ${}^4_\Lambda\text{He}$ . Due to the much bigger  $\Lambda$  separation energies in the four-body system, we find distributions which are much smoother than the  $\Lambda$  distributions of  ${}^3_\Lambda\text{H}$  shown in Fig. 5.6. Only the very loosely bound excited state for SC89 leads to a sharp peak in  $D_\Lambda$  near  $p = 0$ . As one can expect from the high probabilities to find the three nucleons in a  ${}^3\text{He}$  bound state,  $D_\Lambda$  and  $\mathcal{T}_\Lambda$  are very similar in the low momentum region. This holds for all states and interactions. For both functions we find very similar results for SC89 and SC97f in the ground state. In this state the Jülich potential leads to somewhat different predictions. In contrast for the  $J^\pi = 1^+$  state the Jülich and SC97f predictions are similar. We have already noted the sharp peak predicted by SC89 in this state.

For momenta  $p$  higher than  $1 \text{ fm}^{-1}$  we find visibly differences in  $D_\Lambda$  and  $\mathcal{T}_\Lambda$ . In this region the  $\mathcal{T}_\Lambda$  function has got a dip structure and drops very quickly. In contrast  $D_\Lambda$  has got more high momentum components. For the  $J^\pi = 0^+$  state only  $S$ -waves contribute to the relative motion of the  $\Lambda$  and  ${}^3\text{He}$ . Because this partial wave has got a node, we find a pronounced dip structure in  $\mathcal{T}_\Lambda$  for the  $J^\pi = 0^+$  state.

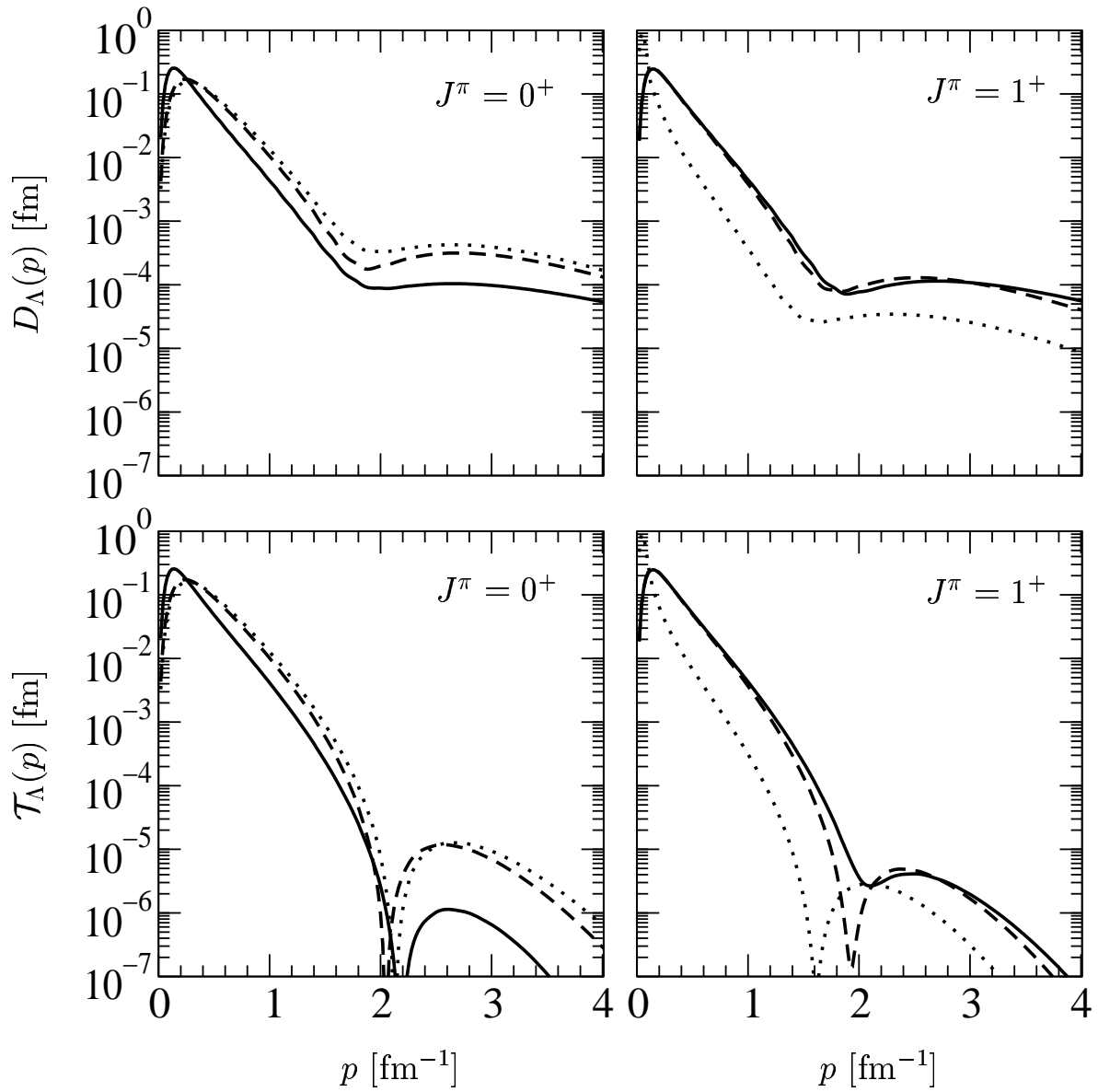


Figure 5.12:  $\Lambda$  momentum distributions (upper figures) and  $\Lambda$ - ${}^3\text{He}/{}^4\text{He}$  overlap functions (lower figures) in the  $J^\pi = 0^+$  (left figures) and  $J^\pi = 1^+$  (right figures) state of  ${}^4_\Lambda\text{He}$ . The distribution functions are based on calculations using Bonn B+Jülich A (solid lines), Nijm 93+SC97f (dashed lines) or Nijm 93+SC89 (dotted lines). The functions are normalized to  $\int C(p)dp = \frac{1}{4\pi}$ .

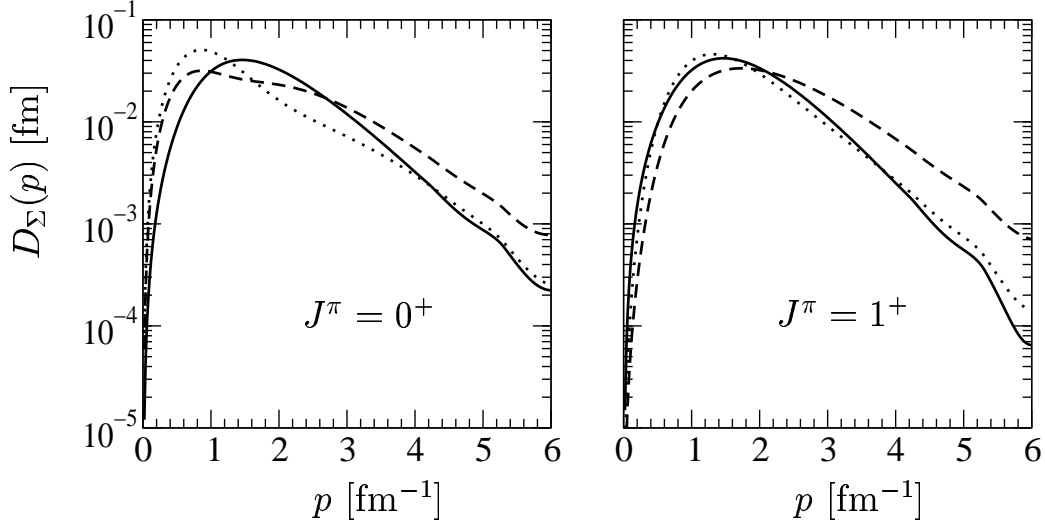


Figure 5.13:  $\Sigma$  momentum distributions in the  $J^\pi = 0^+$  (left figure) and  $J^\pi = 1^+$  (right figure) state of  ${}^4_\Lambda\text{He}$ . The distribution functions are based on calculations using Bonn B+Jülich  $\tilde{A}$  (solid lines), Nijm 93+SC97f (dashed lines) or Nijm 93+SC89 (dotted lines). The functions are normalized to  $\int C(p)dp = \frac{1}{4\pi}$ .

We note that the position of this peak is nearly independent from the YN interaction.

In the excited state  $D$ -waves can also contribute to  $\mathcal{T}_\Lambda$ . This leads to a less pronounced dip. Especially for the Jülich interaction, this structure is nearly removed. We see that the dip position depends on the YN interaction in this state.

We remark that we also looked to the NN interaction dependence of these functions. We found no significant dependence of  $\mathcal{T}_\Lambda$  and  $D_\Lambda$  on the NN interaction. For SC97d-e the results were very similar to SC97f. We note that  $D_\Lambda$  is very similar for the  $J^\pi = 0^+$  and  $J^\pi = 1^+$  state for Jülich  $\tilde{A}$ .

The  $\Sigma$  momentum distributions are shown in Fig. 5.13. We again present results for Jülich  $\tilde{A}$ +Bonn B, SC97f+Nijm 93 and SC89+Nijm 93. A comparison with SC89+Bonn B revealed that the NN force dependence is negligible. For the momentum distribution of  $\Sigma^+$ ,  $\Sigma^0$  and  $\Sigma^-$  we found no significant differences. Therefore we only show the averaged distributions.

We see that all  $\Sigma$  distributions have got a similar functional form. Compared to the  $\Sigma$  distribution in  ${}^3_\Lambda\text{H}$  (see Fig. 5.6), we see that the functions drop more quickly in the four-body hypernuclei. We are astonished to find less important high momentum components in the more tightly bound  ${}^4_\Lambda\text{He}$ .

For the Nijmegen interactions the  $\Sigma$  distributions differ in the ground and the excited state. In contrast the Jülich interaction predicts very similar distribution functions in both cases. It is remarkable that for the Nijmegen interactions the peak moves to higher momenta going from the tightly bound ground state to the less tightly bound excited state. This is opposite to the naive expectation that higher binding energies generally cause bigger high momentum components. For  $J^\pi = 0^+$  the distributions qualitatively differ for the interaction models considered. For the excited state, we observe a similar behavior for SC89 and Jülich  $\tilde{A}$ .

In summary we emphasize that the distribution functions for the hyperons are less sensitive to the

	NN		$\Lambda$ N		$\Sigma$ N	
	$s = 0$	$s = 1$	$s = 0$	$s = 1$	$s = 0$	$s = 1$
SC97f+Nijm 93	45.51	54.49	45.34	52.89	0.33	1.45
SC97e+Nijm 93	45.51	54.49	45.41	53.00	0.27	1.32
SC97d+Nijm 93	45.49	54.51	45.44	53.06	0.26	1.25
SC89+Nijm 93	45.24	54.76	43.97	51.93	1.38	2.72
Jülich $\tilde{\Lambda}$ +Bonn B	46.34	53.66	45.03	51.64	1.59	1.74
$\Lambda$ - $^3$ He approx.	50.00	50.00	50.00	50.00	—	—

Table 5.22: Probabilities  $P_s^q$  to find NN,  $\Lambda$ N and  $\Sigma$ N pairs in spin  $s = 0$  and  $s = 1$  states in the  $J^\pi = 0^+$  state of  $^4_\Lambda\text{He}$ . The probabilities are compared to the analytical results for a simplified  $^4_\Lambda\text{He}$  wave function ( $\Lambda$ - $^3\text{He}$  approx., see text) All probabilities are given in %.

	NN		$\Lambda$ N		$\Sigma$ N	
	$s = 0$	$s = 1$	$s = 0$	$s = 1$	$s = 0$	$s = 1$
SC97f+Nijm 93	45.77	54.23	17.68	81.30	0.16	0.86
SC97e+Nijm 93	45.77	54.23	17.67	81.20	0.17	0.96
SC97d+Nijm 93	45.77	54.23	17.65	81.17	0.18	1.00
SC89+Nijm 93	45.78	54.22	17.83	81.83	0.07	0.27
Jülich $\tilde{\Lambda}$ +Bonn B	45.90	54.10	17.37	80.55	0.92	1.15
$\Lambda$ - $^3\text{He}$ approx.	50.00	50.00	16.67	83.33	—	—

Table 5.23: Probabilities  $P_s^q$  to find NN,  $\Lambda$ N and  $\Sigma$ N pairs in spin  $s = 0$  and  $s = 1$  states in the  $J^\pi = 1^+$  state of  $^4_\Lambda\text{He}$ . The probabilities are compared to the analytical results for a simplified  $^4_\Lambda\text{He}$  wave function ( $\Lambda$ - $^3\text{He}$  approx., see text) All probabilities are given in %.

NN interaction. From the overlap functions we know that the three nucleons are predominately in a  $^3\text{He}$  core state. However, we found visible differences in the momentum distribution of the nucleons. This is remarkable. We would like to add that we expect a scaling behavior with the binding energies for the distribution functions from our investigations in the 3N and 4N system (see Sections 4.3 and 4.6). In future we require phenomenological 3BF or similar mechanisms, which are able to provide the missing binding to  $^4_\Lambda\text{He}$ . This could remove the dependence on binding energies from the distribution functions and might help to pin down a “real” YN force dependence of the distributions.

This closes our look to distribution functions and leads us to correlation functions.

The correlation functions are defined in Eqs. (4.5) and (4.6). These definitions are easily generalized to hyperon-nucleon pairs carefully replacing the isospin projection operators and renumbering the particles. Similar expressions can be obtained for configurations space correlations. As in the case of  $^3_\Lambda\text{H}$  (see Section 5.3) we only look to the angular independent parts  $C_s^q$  for NN,  $\Lambda$ N and  $\Sigma$ N pairs here. Because the functional dependence of these correlations does not significantly change replacing protons by neutrons or changing the charge of  $\Sigma$ 's, we do not distinguish different  $\Sigma$ N,  $\Lambda$ N and NN pairs. In the figures we chose the same normalization for all  $C_s^q$ . The original sizes of the correlation functions can be found from the probabilities  $P_s^q$  (see Eq. 4.8) given in Tables 5.22 and 5.23.

A widely used approximation to the  $^4_\Lambda\text{He}$  wave function is based on the assumption of a  $^3\text{He}$  core

nucleus. The normalization constants of the overlap functions given in Tables 5.20 and 5.21 might justify this approximation. To get analytical insights to the spin structure in hypernuclear systems, one neglects the  $\Sigma$  components and assumes a principal S-state for the core nucleus (from Table 4.8 we know that also this approximation carries an error of roughly 10 %). With the approximation that states with total orbital angular momentum non-zero do not contribute, one concludes that only one spin/isospin state contributes to the 1A representation of the  ${}^4_{\Lambda}\text{He}$  wave function. This state is different for the ground and the excited state. Recoupling the spin/isospin part of the wave function to the 2B representation one analytically finds the  $P_s^q$  labeled by “ $\Lambda$ - ${}^3\text{He}$  approx.” in the tables.

Like in the case of the hypertriton we observe a rough agreement of these predictions with the exact answers from our calculations. We note that already for the NN pairs the approximated  $P_s^q$ 's do not exactly fit to the numerically ones. This is the consequence of admixtures from the  $S'$ -,  $P$ - and  $D$ -waves to the  ${}^3\text{He}$  wave function. The deviations of the AN probabilities from the approximation are in the same order of magnitude. We note that the probabilities are predominately the consequence of the  $\Lambda$ -core nucleus structure of  ${}^4_{\Lambda}\text{He}$ . They are not the result of properties of the YN or NN interactions. The small deviations from the analytical predictions are interaction dependent.

The existence of  $\Sigma\text{N}$  pairs is not considered in the approximated wave functions. They are the consequence of the YN interaction. Therefore we expect that  $P_s^{\Sigma\text{N}}$  are sensitive to the spin dependence of the conversion potential. For both states, the  $J^\pi = 0^+$  and  $J^\pi = 1^+$ , we observe for the SC97 interactions, that the  $s = 1$   $\Sigma\text{N}$  pairs are much more important than the  $s = 0$   $\Sigma\text{N}$  pairs. This unbalance is decreased for the SC89 and Jülich interactions. We are astonished to see no significant shift to  $s = 1$   $\Sigma\text{N}$  pairs in the  $J^\pi = 1^+$  state, though we observe such a shift for  $\Lambda\text{N}$  pairs.

The  $\Sigma$  probabilities  $P_\Sigma$  given in Tables 5.20 and 5.21 can also be found adding  $P_{s=0}^{\Sigma\text{N}}$  and  $P_{s=1}^{\Sigma\text{N}}$ . In Tables 5.20 and 5.21 they were obtained using the more accurate 1A representation, in Tables 5.22 and 5.23 we had to use the 2B representation, which is less accurate (see Table 3.28). A comparison of both results reveals a satisfying agreement in nearly all cases. Only for SC89 in the excited state we found a visible difference in both results. Similar deviations, comparing the results of different representations, have already been found for the kinetic energies (see Table 3.30). They are generally the effect of missing higher partial waves in the representation. We prefer the  $P_\Sigma$  results given in Tables 5.20 and 5.21. We emphasize that we still expect reliable results for  $C^{\Sigma\text{N}}$  in the low momentum region for all interactions and in the ground and the excited state, because we confirmed our accuracy comparing  $E_B$  and  $H$  in Tables 5.13 and 5.14.

We proceed with a look to correlation functions in configuration space. In Fig. 5.14 we begin with the NN correlations. We show results based on the Nijm 93 NN interaction. The figures compare the NN correlations in  ${}^3\text{He}$  to predictions for  ${}^4_{\Lambda}\text{He}$  based on SC89 and SC97f. We find for both spin states  $s = 0$  and  $s = 1$  in the NN pair agreement of the  ${}^3\text{He}$  and the  ${}^4_{\Lambda}\text{He}$  predictions. This holds for the ground and the excited state of the four-body hypernucleus and is independent from the YN interaction. The small deviations in the long range tail can be traced back to binding energy differences. This observations could be expected from the high probabilities to find the three nucleons in a  ${}^3\text{He}$  bound state within  ${}^4_{\Lambda}\text{He}$  (see  $N_T^\Lambda$  in Tables 5.20 and 5.21).

For the  $\Lambda\text{N}$  correlations we find similar shapes for  $C_s^q$  as for the NN correlations. The results are shown in Fig. 5.15. We present correlations for the  $J^\pi = 0^+$  and  $J^\pi = 1^+$  states of  ${}^4_{\Lambda}\text{He}$  for Jülich  $\tilde{\Lambda}$ , SC97f+Nijm 93 and SC89+Nijm 93. We insured that the NN force has only minor effects on this correlations. We remark that the SC97d and e interactions give very similar results to SC97f.

Compared to the NN correlations we observe a shift of the peak to higher interparticle distances. Because the  $\Lambda$  separation energies are considerably smaller than corresponding nucleon separation energies, we observe longer ranged tails in  $C^{\Lambda\text{N}}$  than in  $C^{\text{NN}}$ . This is especially true for SC89 in the  $J^\pi = 1^+$

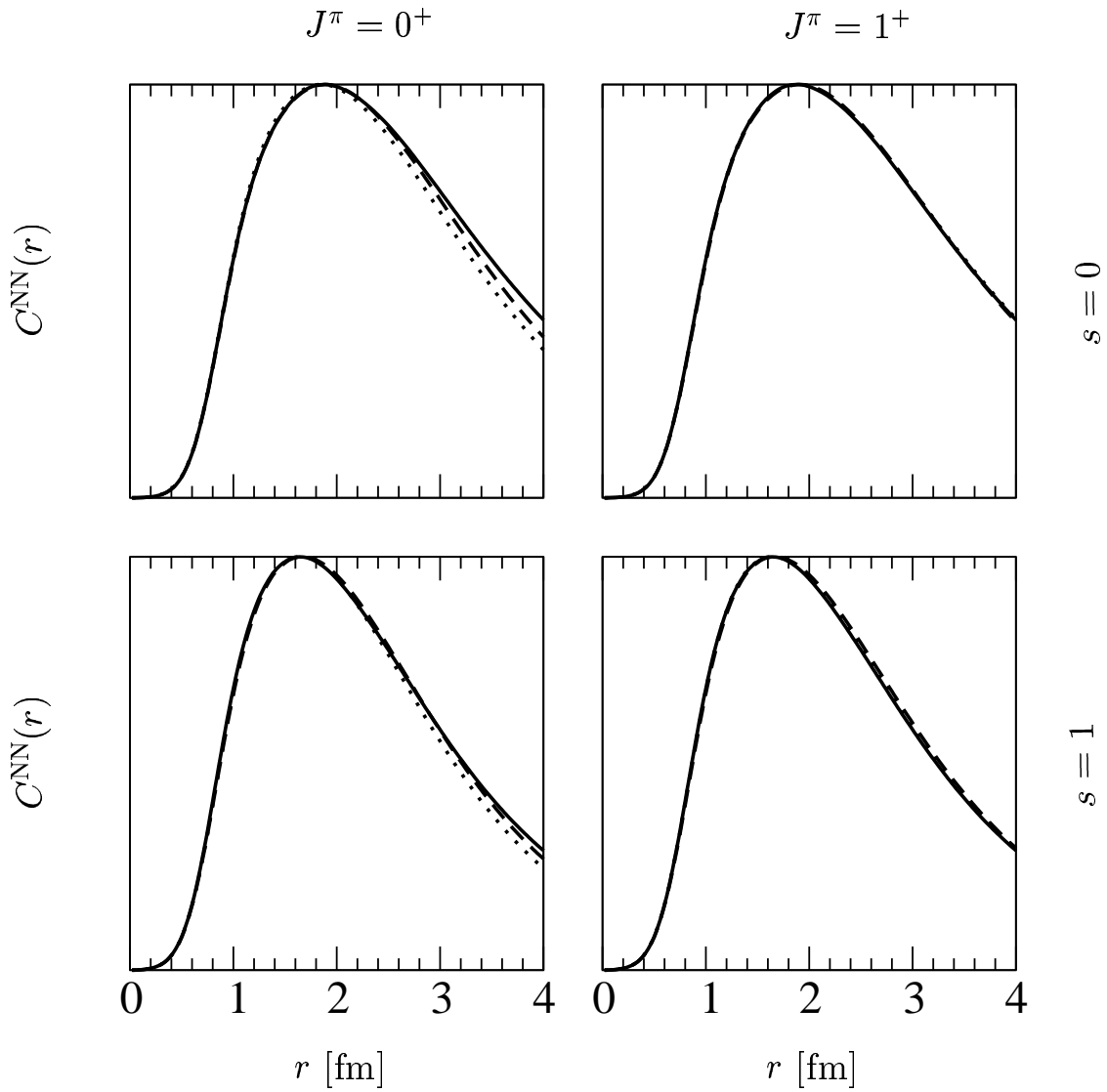


Figure 5.14: NN correlations compared for the  $J^\pi = 0^+$  (left figures) and  $J^\pi = 1^+$  (right figures) states of  ${}^4_\Lambda\text{He}$  for spin  $s = 0$  (upper figures) and  $s = 1$  (lower figures) in configuration space. The correlation functions are based on calculations using Nijm 93+SC97f (dashed lines) and Nijm 93+SC89 (dotted lines). For comparison we also give the NN correlations in  ${}^3\text{He}$  for Nijm 93 (solid lines). The functions are normalized to the same peak height. They are given in arbitrary units on a linear scale.

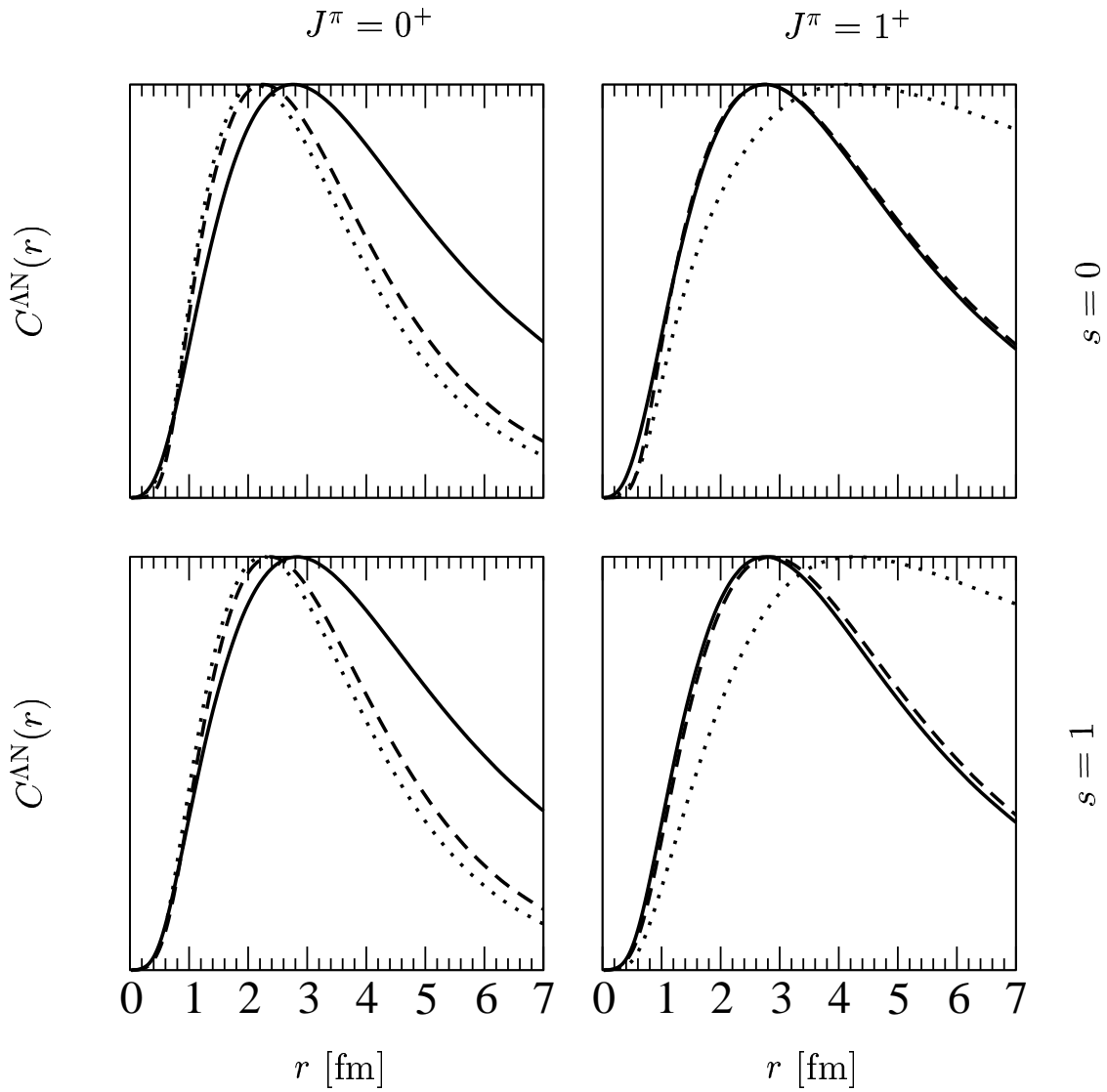


Figure 5.15: AN correlations compared for the  $J^\pi = 0^+$  (left figures) and  $J^\pi = 1^+$  (right figures) states of  ${}^4_\Lambda\text{He}$  for spin  $s = 0$  (upper figures) and  $s = 1$  (lower figures) in configuration space. The correlation functions are based on calculations using Bonn B+Jülich A (solid lines), Nijm 93+SC97f (dashed lines) and Nijm 93+SC89 (dotted lines). The functions are normalized to the same peak height. They are given in arbitrary units on a linear scale.



state. Comparing to the same correlations for  ${}^3_{\Lambda}\text{H}$  (see Fig. 5.8), we see that the increased  $\Lambda$  separation energies lead to a shorter tail in the four-body systems. We observe that the correlations are not  $\Lambda\text{N}$  pair spin dependent. We also note that the correlations for the Jülich  $\tilde{\Lambda}$  interaction in both, the ground and the excited state, are nearly equal. For the other potentials and states, we see that the peak position and the  $\Lambda$  separation energies are correlated. A more tightly bound  $\Lambda$  particle leads to a peak position closer to the origin. As for the momentum distributions, we require additional, maybe phenomenological, ingredients in the Hamiltonians, which are able to cure the underbinding problem. With such an upgraded Hamiltonian it will be easier to distinguish binding energy effects from explicitly interaction dependent properties of the wave function. Such binding energy effects might also explain the surprisingly similar correlations for Jülich  $\tilde{\Lambda}$  and SC97f in the  $J^{\pi} = 1^{+}$  state.

Now we turn to  $\Sigma\text{N}$  correlations in  ${}^4_{\Lambda}\text{He}$ . In Fig. 5.16 we again show the results only for Jülich  $\tilde{\Lambda}$ , SC97f+Nijm 93 and SC89+Nijm 93. There is no NN force dependence for this correlations. We also found only minor differences of the SC97f calculation to SC97d and e. For the  $\Sigma\text{N}$  correlation we found visible dependences on the charge of the  $\Sigma$  particle and the nucleon. But in all cases the correlations qualitatively agree. In view of the strong interaction dependences of the  $\Sigma\text{N}$  correlations we decided to omit the charge-dependences and to present only charge-averaged  $\Sigma\text{N}$  correlations.

Looking to Fig. 5.16 it sticks out that the  $\Sigma\text{N}$  correlations depend less on the kind of  ${}^4_{\Lambda}\text{He}$  state ( $J^{\pi} = 0^{+}$  or  $J^{\pi} = 1^{+}$ ) than on the spin state of the  $\Sigma\text{N}$  pair. This implies that there is obviously no scaling of the peak positions with the  $\Lambda$  separation energies, because of the very different separation energy predictions for the ground and the excited states for the Nijmegen SC models. We find a strong dependence of the correlations on the  $\Sigma\text{N}$  pair spin. Whereas the correlations in  $s = 1$  pairs have got a similar shape as NN correlations, we again observe a peak structure for SC97f and Jülich  $\tilde{\Lambda}$  for very small interparticle distances around 0.3 fm in the  $s = 0$  state. For SC89 such a peak is visible only in the  $J^{\pi} = 1^{+}$  state. In contrast to the results for  ${}^3_{\Lambda}\text{H}$  (see Fig. 5.9), we find a qualitatively similar behavior of SC89 and SC97f also in the  $s = 0$  correlation. For the  $s = 0$  correlations in the four-body system we see that both potentials predict a broad peak around 1.6-2.0 fm and only a smaller peak (or no visible) around 0.2-0.4 fm. But we see that the Jülich interaction leads to very different results. For  $s = 0$  there is only one peak around 0.4 fm. A second peak is missing. We note that for  $s = 1$  the shape of the correlation is similar for all potentials. It is astonishing that in this case the prediction of Jülich indicate quite large  $\Sigma\text{N}$  interparticle distances. In this context it might be interesting that the Jülich  $\tilde{\Lambda}$  interaction predicts a resonance in  ${}^1\text{S}_0$  (see Section 5.1). Is this spurious resonance responsible for the very different behavior in the  $s = 0$   $\Sigma\text{N}$  correlation? Certainly an upgraded version of the Jülich interaction without spurious resonances is required. In the case of the Nijmegen interactions the effect of the attractive short range  $\Sigma\text{N}$  potential seems to be less visible in  ${}^4_{\Lambda}\text{He}$  than in  ${}^3_{\Lambda}\text{H}$ .

Summarizing our findings on correlation functions, we point out that the NN correlations are driven by the behavior in the 3N bound states. The YN interaction does not influence the short range behavior visibly. We found that the  $\Lambda\text{N}$  correlations might scale with the  $\Lambda$  separation energies. Here it is interesting that the dependence on the spin of the  $\Lambda\text{N}$  subsystem is small. In view of this it is remarkable that the  $\Sigma\text{N}$  correlations have got an extremely big baryon-baryon pair spin dependence. In this case we found a dependence on the YN interaction, which can surely not be led back to  $\Lambda$  separation energy differences.

We close the presentation of correlation functions with a brief look to correlations in momentum space. The NN correlations are nearly identical in the whole momentum range to corresponding correlations in  ${}^3\text{He}$  shown in Section 4.3. Therefore we start with  $\Lambda\text{N}$  correlations in Fig. 5.17. We again show results for Jülich  $\tilde{\Lambda}$ , SC97f and SC89.

Compared to the same correlations in  ${}^3_{\Lambda}\text{H}$  (see Fig. 5.10), we see that the peak structure for low

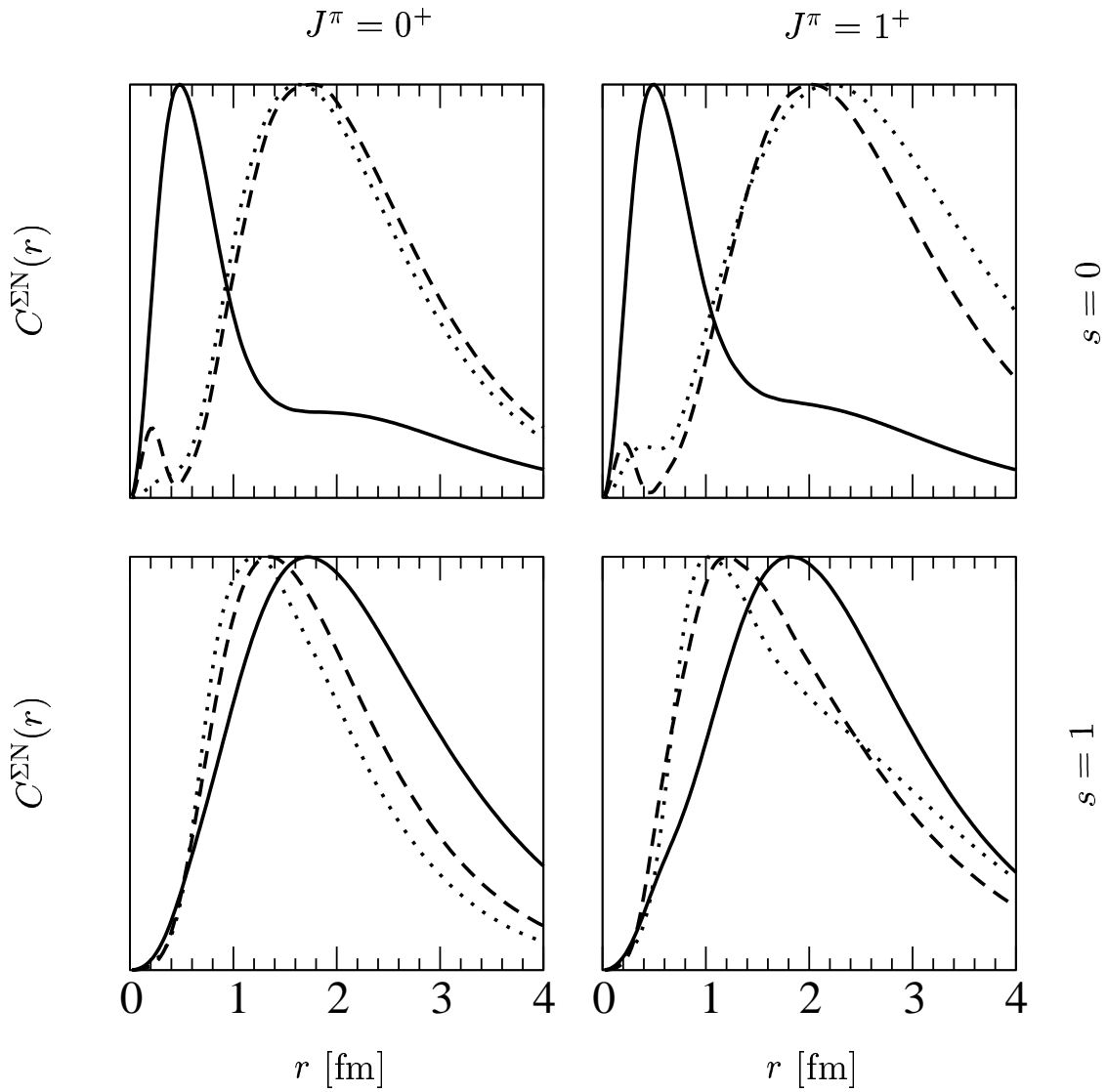


Figure 5.16:  $\Sigma N$  correlations compared for the  $J^\pi = 0^+$  (left figures) and  $J^\pi = 1^+$  (right figures) states of  ${}^4_\Lambda\text{He}$  for spin  $s = 0$  (upper figures) and  $s = 1$  (lower figures) in configuration space. The correlation functions are based on calculations using Bonn B+Jülich Å (solid lines), Nijm 93+SC97f (dashed lines) and Nijm 93+SC89 (dotted lines). The functions are normalized to the same peak height. They are given in arbitrary units on a linear scale.

momenta is less pronounced in the four-body system. As an exception we find a similar sharp peak for the loosely bound excited state using SC89.

We find a dependence of the peak width and height of the correlation on the state of the  ${}^4_{\Lambda}\text{He}$  system ( $J^{\pi} = 0^{+}$  or  $J^{\pi} = 1^{+}$ ). Similar to the differences in the configuration space correlations, this dependence might be linked to the different binding energy predictions. Additionally we see that the high momentum components are also state dependent. Generalizing our experience from the nuclear bound state (see Sections 4.3 and 4.6), we expect no scaling with the separation energies in this momentum region. For these momenta dependences on the pair spin  $s$  become visible. Such dependences were invisible in configuration space correlations.

In Fig. 5.18 we turn to the  $\Sigma\text{N}$  correlations in momentum space. Again we show results for Jülich  $\tilde{\Lambda}$ , SC97f and SC89.

Comparing to the corresponding correlation in  ${}^3_{\Lambda}\text{H}$  in Fig. 5.10, we find similar shapes for the  $s = 1$  pair spin. For  $s = 0$  the correlations differ remarkably.

As in configuration space we observe comparable functional forms in the  $J^{\pi} = 0^{+}$  and  $J^{\pi} = 1^{+}$  states of  ${}^4_{\Lambda}\text{He}$  only for pair spins  $s = 1$ . For  $s = 0$  we find considerable differences in the case of the Nijmegen SC interactions. For  $J^{\pi} = 0^{+}$  SC97f and SC89 lead to a similar low momentum  $\Sigma\text{N}$  correlation for  $s = 0$ . In the excited state the peak is broader for both interactions. For SC97 this effect is more pronounced than for SC89. We also see that in both  ${}^4_{\Lambda}\text{He}$  states the momentum correlations are similar for Jülich  $\tilde{\Lambda}$ . However, the qualitative differences of the Jülich predictions to the SC predictions for the  $s = 0$   $\Sigma\text{N}$  correlations found in configuration space are not similarly concrete in momentum space.

This closes our look to correlations. We end this chapter with a survey on the CSB effects in the four-body hypernuclei in the next section.

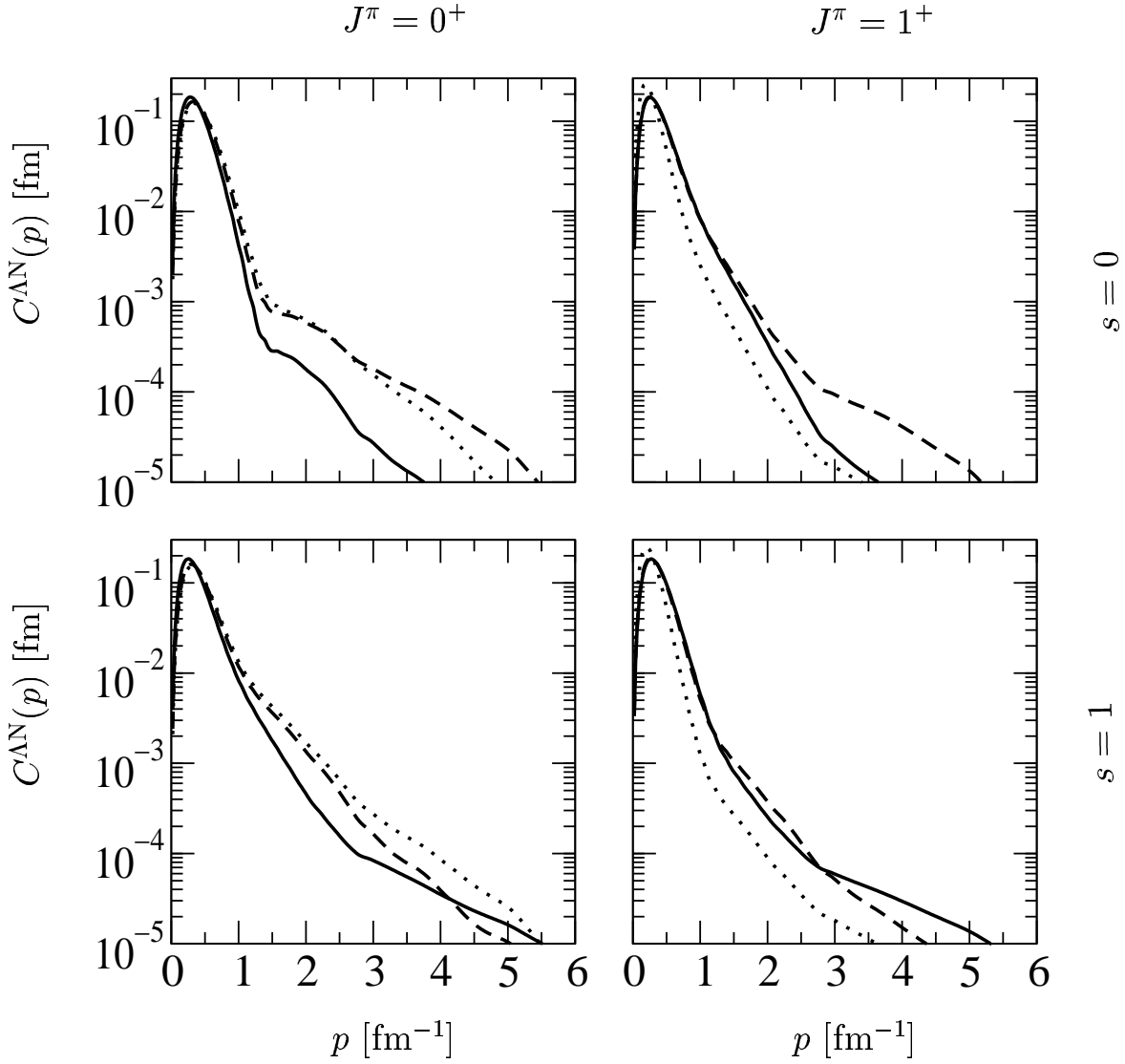


Figure 5.17: AN correlations compared for the  $J^\pi = 0^+$  (left figures) and  $J^\pi = 1^+$  (right figures) states of  ${}^4_\Lambda\text{He}$  for spin  $s = 0$  (upper figures) and  $s = 1$  (lower figures) in momentum space on a logarithmic scale. The correlation functions are based on calculations using Bonn B+Jülich A (solid lines), Nijm 93+SC97f (dashed lines) and Nijm 93+SC89 (dotted lines). The functions are normalized to  $\int C(p)dp = \frac{1}{4\pi}$ .

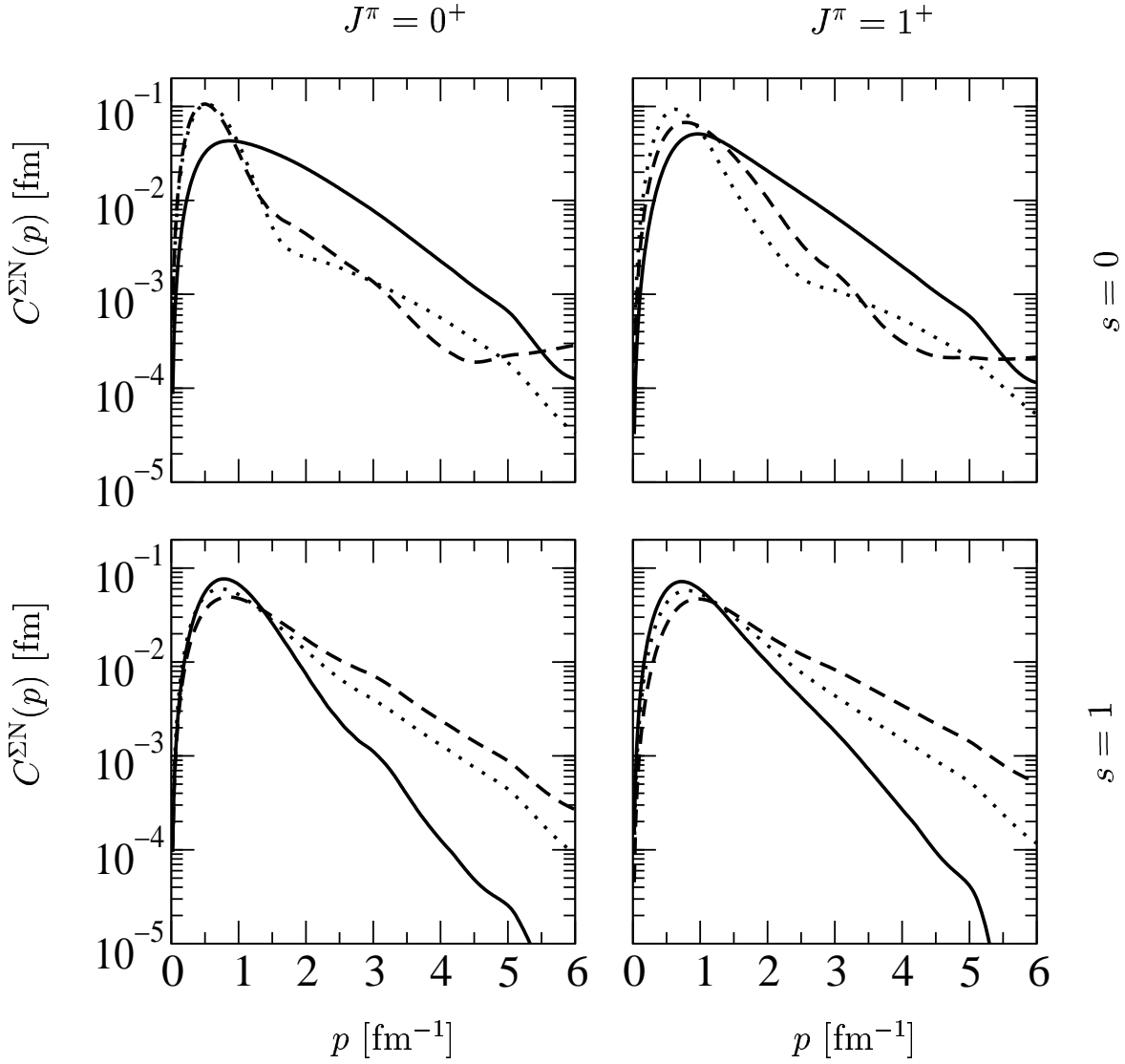


Figure 5.18:  $\Sigma N$  correlations compared for the  $J^{\pi} = 0^+$  (left figures) and  $J^{\pi} = 1^+$  (right figures) states of  ${}^4_{\Lambda}\text{He}$  for spin  $s = 0$  (upper figures) and  $s = 1$  (lower figures) in momentum space on a logarithmic scale. The correlation functions are based on calculations using Bonn B+Jülich Å (solid lines), Nijm 93+SC97f (dashed lines) and Nijm 93+SC89 (dotted lines). The functions are normalized to  $\int C(p)dp = \frac{1}{4\pi}$ .

## 5.6 The origin of the CSB in the $\Lambda$ separation energies

In Section 5.4 we found in our calculations visible CSB of the  $\Lambda$  separation energies for  ${}^4_{\Lambda}\text{He}$  and  ${}^4_{\Lambda}\text{H}$ . Our predictions for the difference  $\Delta_{CSB}$  of the  $\Lambda$  separation energies are model dependent. For the  $J^\pi = 0^+$  state the SC89 model could nearly explain the experimentally found 350 keV.

We already emphasized that there are very likely ANN 3BF missing in our model Hamiltonians. Theoretical models for these interactions are not available. We can expect that the 3BF are strongly spin dependent, but nearly isospin invariant. Because the spin structure of the  $0^+$  and  $1^+$  states are very different, the ANN interactions will presumably act differently in both states and might significantly affect the  $0^+-1^+$  splitting. This means that we have to be very careful in concluding on the YN interactions using our predictions for the  $0^+-1^+$  splitting.

Because of the expected isospin invariance of the 3BF's, their action in  ${}^4_{\Lambda}\text{He}$  and  ${}^4_{\Lambda}\text{H}$  is presumably nearly equal. Therefore  $\Delta_{CSB}$  is not significantly affected by ANN forces and we are able to conclude rather safely on the YN pair interactions from our calculations. This makes the CSB splitting an important observable to pin down failures of the YN two-body interactions.

In the past a few mechanisms have been proposed to explain the experimentally found splitting due to CSB without assuming explicit CSB in the strong YN interaction. Both effects are a consequence of  $\Lambda$ - $\Sigma$  conversion. It is expected (and our results confirm this expectation, see Table 5.20) that the  $\Sigma^+$ ,  $\Sigma^0$  and  $\Sigma^-$  states are not equally populated. Because of the mass difference within the  $\Sigma$  multiplet, this leads to a shift of the kinetic energy in  ${}^4_{\Lambda}\text{He}$ , which is different in  ${}^4_{\Lambda}\text{H}$ . In a very early work [64] it has been shown that this effect provides a contribution to  $\Delta_{CSB}$  with the correct sign and order of magnitude. Additionally,  $\Lambda$ - $\Sigma$  conversion creates charged  $\Sigma\text{N}$  pairs and pp pairs. This leads to additional Coulomb force effects, which, according to Ref. [64], also contribute with the correct sign and order of magnitude.

In Ref. [67] a ‘‘core compression effect’’ has been studied, which leads to a contribution to  $\Delta_{CSB}$  with the wrong sign. The  ${}^3\text{He}$  core in  ${}^4_{\Lambda}\text{He}$  should be slightly compressed because of the increased binding energy. The increased nucleon density should increase the Coulomb repulsion within pp pairs. In Ref. [67] it has been estimated that this effect amounts to 50 keV in the ground state. This means that other mechanisms must explain 50 keV more CSB than experimentally found.

As outlined in Section 5.1 meson exchange models of the YN interaction also include explicit CSB in the strong interaction. The isospin dependence has carefully been taken into account in our calculations. We consider this as an important feature of the calculations, because the contribution of realistic CSB based on meson theoretical models has never been estimated before.

We emphasize that all mechanisms for CSB are related to  $\Lambda$ - $\Sigma$  conversion. This important part of the interaction is still not understood. Therefore the investigation of CSB in the four-body hypernuclei will clarify the correctness of the predicted  $\Lambda$ - $\Sigma$  conversion strength in the YN forces.

The estimates of CSB effects in literature are based on simplified models for the  ${}^4_{\Lambda}\text{He}$  and  ${}^4_{\Lambda}\text{H}$  nuclei. In the following we estimate the contribution of the mentioned mechanisms based on our new wave functions. Our calculations include all dynamical ingredients, which are expected to influence  $\Delta_{CSB}$ :  $\Lambda$ - $\Sigma$  conversion, Coulomb forces, baryon mass differences and the CSB of the strong YN interaction. We think that this is an important step forward to understand the origin of  $\Delta_{CSB}$ .

To this aim we perturbatively study the origin of this splitting in the following. The  $\Lambda$  separation energies are defined as

$$\begin{aligned} E_{sep}^{\Lambda}({}^4_{\Lambda}\text{He}) &= E({}^3\text{He}) - E({}^4_{\Lambda}\text{He}) \\ E_{sep}^{\Lambda}({}^4_{\Lambda}\text{H}) &= E({}^3\text{H}) - E({}^4_{\Lambda}\text{H}) \end{aligned} \tag{5.7}$$

Therefore the CSB splitting is given by

$$\begin{aligned}
\Delta_{CSB} &= E_{sep}^{\Lambda}({}^4_{\Lambda}\text{He}) - E_{sep}^{\Lambda}({}^4_{\Lambda}\text{H}) \\
&= (E({}^3\text{He}) - E({}^3\text{H})) - (E({}^4_{\Lambda}\text{He}) - E({}^4_{\Lambda}\text{H}))
\end{aligned} \tag{5.8}$$

We insert for the binding energies the expectation values of the Hamiltonian  $H$  and make use of the decomposition of  $H$  in kinetic energy  $T$ , strong NN interaction  $V_{NN,nucl.}$ , strong YN interaction  $V_{YN,nucl.}$ , Coulomb interaction in pp pairs  $V_{NN,C}$  and Coulomb interaction in YN pairs  $V_{YN,C}$ . This leads to a decomposition of  $\Delta_{CSB}$  as

$$\begin{aligned}
\Delta_{CSB} &= (T({}^3\text{He}) - T({}^3\text{H})) - (T({}^4_{\Lambda}\text{He}) - T({}^4_{\Lambda}\text{H})) \\
&\quad + (V_{NN,nucl.}({}^3\text{He}) - V_{NN,nucl.}({}^3\text{H})) - (V_{NN,nucl.}({}^4_{\Lambda}\text{He}) - V_{NN,nucl.}({}^4_{\Lambda}\text{H})) \\
&\quad + (V_{NN,C}({}^3\text{He}) - V_{NN,C}({}^3\text{H})) - (V_{NN,C}({}^4_{\Lambda}\text{He}) - V_{NN,C}({}^4_{\Lambda}\text{H})) \\
&\quad - (V_{YN,nucl.}({}^4_{\Lambda}\text{He}) - V_{YN,nucl.}({}^4_{\Lambda}\text{H})) \\
&\quad - (V_{YN,C}({}^4_{\Lambda}\text{He}) - V_{YN,C}({}^4_{\Lambda}\text{H})) \\
&\equiv \Delta T^{CSB} + \Delta V_{NN,nucl.}^{CSB} + \Delta V_{NN,C}^{CSB} + \Delta V_{YN,nucl.}^{CSB} + \Delta V_{YN,C}^{CSB}
\end{aligned} \tag{5.9}$$

In the following we present perturbative estimates based on a  ${}^3\text{He}$  wave function calculated using the Nijm 93 interaction and two different  ${}^4_{\Lambda}\text{He}$  wave functions. For  ${}^4_{\Lambda}\text{He}$  we use the Nijm 93+SC89 and Nijm 93+SC97e interactions. We only look to the  $J^{\pi} = 0^+$  state. Because the Nijm 93 model includes no nn force adjusted to the nn scattering length, we neglect the contribution of  $V_{NN,nucl.}$  in this study. We expect no significant contribution from  $V_{NN,nucl.}$ , because the CSB differences of the NN force are small and nearly equal in the 3N system and in  ${}^4_{\Lambda}\text{He}$  and  ${}^4_{\Lambda}\text{H}$ . Correspondingly to the wave functions we chose SC89 or SC97e as YN interaction to calculate  $\Delta V_{YN,nucl.}^{CSB}$ . The results are presented in Table 5.24. We see that our perturbative estimate for  $\Delta_{CSB}$  agrees within 10 keV with the full calculation presented in Section 5.4. We conclude that the accuracy of the perturbative treatment is sufficient.

As already emphasized the SC89 model predicts  $\Delta_{CSB}$  in agreement with the experiment. SC97e fails to describe  $\Delta_{CSB}$ . We learn from the SC89 and SC97e results, that the Coulomb interaction contributes only a minor part to  $\Delta_{CSB}$ . In this point our findings are different to the predictions in Ref. [64]. We confirm a visible contribution of the  $\Sigma$  mass differences, which shows up in  $\Delta T^{CSB}$ .

The mechanism leading to this effect in the kinetic energy is different to the one observed in the 3N system. Whereas in the nuclear bound state an increased nucleon mass increases the magnitude of the binding energy, we find an opposite behavior for the hypernuclei increasing the  $\Sigma$  masses. The kinetic energy has got a rest mass contribution  $M_R$  and the usually considered momentum dependent part  $\propto \frac{p^2}{M_R}$  (non-relativistic). In first order the first term increases and the second term decreases with increasing rest mass  $M_R$ . The effect on the  $M_R$  term is in general bigger than the effect on  $\frac{p^2}{M_R}$ . For the ordinary nuclei no particle conversion takes place. Therefore the increased particle mass works on the threshold energy for total break-up in the same way as on the rest masses in the kinetic energy. Therefore the smaller effect on the momentum dependent part of the kinetic energy becomes visible in the binding energy relative to the total break-up threshold. For the hypernuclei only the  $\Lambda$  mass affects the threshold. The  $\Sigma$  masses do not affect the threshold, but the rest masses in the kinetic energies. Therefore the mass difference enter through the  $M_R$  term in the binding energies. A careful analysis reveals that the contribution of this part is related to the difference of the  $\Sigma^+$  and  $\Sigma^-$  probabilities  $P_{\Sigma^{\pm}}$  and the  $\Sigma^+$  and  $\Sigma^-$  mass difference.

	Nijm 93+SC89	Nijm 93+SC97e
$\Delta T^{CSB}$	132	47
$\Delta V_{NN,C}^{CSB}$	-9	-9
$\Delta V_{YN,nucl.}^{CSB}$	255	44
$\Delta V_{YN,C}^{CSB}$	-27	-7
$\Delta_{CSB}$	351	75
non-pert (see Section 5.4)	340	70
Exp.	350	350

Table 5.24: Perturbative calculation of the CSB splitting of  ${}^4_{\Lambda}\text{He}$  and  ${}^4_{\Lambda}\text{H}$  separation energies. The perturbative estimates of the contribution of the kinetic energy  $\Delta T^{CSB}$ , the pp Coulomb potential energy  $\Delta V_{NN,C}^{CSB}$ , the YN nuclear potential energy  $\Delta V_{YN,nucl.}^{CSB}$  and the YN Coulomb potential  $\Delta V_{YN,C}^{CSB}$  are given separately (see text for definitions). The results are based on  $J^{\pi} = 0^{+}$   ${}^4_{\Lambda}\text{He}$  and  ${}^3\text{He}$  wave functions. The sums  $\Delta_{CSB}$  are compared to non-perturbatively calculated  $\Lambda$  separation energies and the experimental value. All energies are given in keV.

We find

$$\Delta T_{M_R}^{CSB} = (P_{\Sigma^{+}} - P_{\Sigma^{-}}) (m_{\Sigma^{-}} - m_{\Sigma^{+}}) \quad (5.10)$$

Here the  $\Sigma$  probabilities in  ${}^4_{\Lambda}\text{He}$  enter. Using the mass difference of the  $\Sigma^{+/-}$  particles of 8.1 MeV and the  $\Sigma$  probabilities from Table 5.20, we find for SC97e  $\Delta T_{M_R}^{CSB} = 80$  keV and for SC89  $\Delta T_{M_R}^{CSB} = 210$  keV. Our full results given in Table 5.24 are considerably smaller. We conclude that the contribution of the momentum dependent part of the kinetic energy reduces the estimates from Eq. (5.10) significantly. However, the sign of  $\Delta T^{CSB}$  is driven by the  $M_R$  contribution.

The results of Table 5.24 reveal that an important part of  $\Delta_{CSB}$  arises from CSB of the strong YN interaction. Especially for SC89  $\Delta V_{YN,nucl.}^{CSB}$  is surprisingly important. The Nijmegen interaction models include CSB based mainly on the mass differences of the baryons and mesons and on the  $\Sigma^0$ - $\Lambda$  particle mixing. We switched off all terms arising from  $\Sigma^0$ - $\Lambda$  mixing in the potentials [136]. The results for  $\Delta_{CSB}$  using the truncated interactions are given in Table 5.25. For completeness we include all contributions to  $\Delta_{CSB}$  in the table. Of course only  $\Delta V_{YN,nucl.}^{CSB}$  differs from the results given in Table 5.24. For the truncated interaction the CSB breaking is visibly reduced. We conclude that  $\Sigma^0$ - $\Lambda$  particle mixing is an important contribution to  $\Delta_{CSB}$ .

We also note that the overall contribution from the pp Coulomb interaction  $\Delta V_{NN,C}^{CSB}$  is small for both interaction models. We note that this term includes the contribution from the ‘‘core compression’’ effect and from a change of the average number of pp pairs due to  $\Lambda$ - $\Sigma$  conversion. Both effects tend to cancel each other. The resulting  $\Delta V_{NN,C}^{CSB}$  is negligible. The Coulomb interaction in  $\Sigma N$  pairs  $\Delta V_{YN,C}^{CSB}$  leads in the case of SC89 to a more pronounced contribution with the wrong sign, but also in this part the Coulomb interaction only gives a minor contribution to the splitting.

Summarizing we emphasize that the Coulomb interaction is not an important contribution to  $\Delta_{CSB}$ . Our estimations are driven by the effects on the kinetic energy as well as the explicit CSB in the strong interaction.  $\Delta T^{CSB}$  is directly linked to the  $\Sigma$  probability.

In the 3N system CSB effects of the strong interaction contribute only 60 keV (see e.g. Table 4.12).



	Nijm 93+SC89	Nijm 93+SC97e
$\Delta T^{CSB}$	132	47
$\Delta V_{NN,C}^{CSB}$	-9	-9
$\Delta V_{YN,nucl.}^{CSB}$	52	-1
$\Delta V_{YN,C}^{CSB}$	-27	-8
$\Delta_{CSB}$	148	29
Exp.	350	350

Table 5.25: Perturbative calculation of the CSB splitting of  ${}^4_{\Lambda}\text{He}$  and  ${}^4_{\Lambda}\text{H}$  separation energies. The perturbative estimates of the contribution of the kinetic energy  $\Delta T^{CSB}$ , the pp Coulomb potential energy  $\Delta V_{NN,C}^{CSB}$ , the YN nuclear potential energy  $\Delta V_{YN,nucl.}^{CSB}$  and the YN Coulomb potential  $\Delta V_{YN,C}^{CSB}$  are given separately (see text for definitions). The results are based on  $J^{\pi} = 0^+$   ${}^4_{\Lambda}\text{He}$  and  ${}^3\text{He}$  wave functions. The sums  $\Delta_{CSB}$  are compared to the experimental value. The YN potentials are modified as explained in the text. All energies are given in keV.

Therefore we expect from the big size of the observed CSB splitting in the four-body hypernuclei that a visible contribution of the kinetic energy is necessary to give a realistic description of  $\Delta_{CSB}$ . This prefers predictions with a rather big  $P_{\Sigma}$  probability. In this sense  $P_{\Sigma} = 4.08\%$  of the SC89 model (see Table 5.20) might be realistic. We note that the new SC97 models predict much smaller  $P_{\Sigma}$ .

A completely unsettled contribution arises from the CSB in the strong YN interaction. We emphasize that  $\Delta_{CSB}$  is sensitive to  $\Lambda$ - $\Sigma^0$  mixing in the interaction. As described in Section 5.1 this part is important for the long range  $\Lambda\text{N}$  force, because it leads to  $\Lambda\Lambda\pi$  coupling. This rises the question, whether one has some freedom to adjust the strength of this contribution.

For further investigation it seems to be interesting for us to develop a series of realistic YN models, which cover a wide range of  $\Lambda$ - $\Sigma$  conversion strength (visible in  $P_{\Sigma}$ ). For the SC97 interactions the  $P_{\Sigma}$ 's are very close together. We argued that the predicted  $P_{\Sigma}$  might be too small to explain  $\Delta_{CSB}$ . We would like to understand whether increasing these probabilities changes also  $\Delta V_{YN,nucl.}^{CSB}$ . In the same time one could find out, whether the  $\Sigma$  probabilities systematically affect the  $0^+-1^+$  splitting and the absolute  $\Lambda$  separation energies. Maybe the understanding of the conversion process is the key issue for understanding the YN force. The CSB splitting of the four-body  $\Lambda$  separation energies is very sensitive to the strength of this process.

This concludes the chapter on our results for the few-body hypernuclei. We end this thesis with our conclusions given in the next chapter.

# Chapter 6

## Summary and Conclusions

We studied in this thesis nuclear and hypernuclear few-body bound states. Our numerical calculations were based on realistic models for the NN and YN interaction. We also took 3NF's into account. In Chapter 1 we introduced the physical problem and described the available models for the NN and YN interaction and for 3NF's. We summarized the knowledge on nuclear and hypernuclear few-body bound states obtained in the past and motivated our investigations.

### 6.1 Summary of the technical and formal developments

Our investigations are based on numerical solutions of the non-relativistic Schrödinger equation for the nuclear and hypernuclear systems. Instead of directly solving the Schrödinger equation, we decided to rewrite it into a set of Yakubovsky equations (YE).  ${}^4_{\Lambda}\text{He}$  is the most complex system considered. Therefore we presented a derivation of the YE's for this system in Chapter 2. We obtained a set of five YE's for five independent Yakubovsky components (YC). We considered 3NF's in the derivation. We derived an explicit representation in momentum space, which makes use of a partial wave decomposition. We emphasized that the explicit form of YE's naturally leads to several sets of Jacobi coordinates, which describe the motion of the four baryons. Each of the sets singles out different clusters of particles. Our numerical investigations showed that the systematic usage of all these sets in the YE's is decisive to obtain converged solutions. The full complexity of the four-body system is reflected in the matrix elements of coordinate transformations between different kinds of Jacobi coordinates. The extensive partial wave decomposition of those matrix elements was led back to corresponding matrix elements for three-body systems. In this way we efficiently obtained the necessary expressions in a form, which can numerically be handled on today's supercomputers. We arrived at a representation of the YE's, which includes the  $\Lambda$ - $\Sigma$  conversion as well as the mass differences within the isospin multiplets of the baryons.

Our partial wave decomposition allows to distinguish analytically states with symmetric and anti-symmetric NN subsystems. The restriction to antisymmetric subsystems removed spurious, unphysical solutions from the set of YE's from its eigensystem. Therefore the partial wave decomposition guaranteed physical solutions.

In Chapter 3 we described the computer algorithm, which we implemented for the numerical solution of the YE's. In discretized form, using a realistic number of partial waves and momentum grid points, we obtained a linear eigenvalue equation of the dimension  $10^8 \times 10^8$ . For its solution we used an iterative,

Lanczos-like method. The technical problem reduced to the application of the kernel of the YE's to a set of trial YC's. Because of the huge dimension we need modern massively parallel supercomputers for the solution. Therefore we gave a brief introduction to our implementation on the Cray T3E-1200 of the NIC in Jülich in Chapter 3.

After that we studied the numerical stability of our algorithms and of our partial wave decomposition for  ${}^3_{\Lambda}\text{H}$  and  ${}^4_{\Lambda}\text{He}$ . The numerical solution required no uncontrolled approximation. Therefore we could reliably estimate the uncertainty in our binding energy results. We especially investigated the quality of our representation of the wave functions, which we obtained from the solution set of YC's. The representation of hypernuclear wave functions in momentum space is numerically very demanding. We described an efficient and accurate algorithm to obtain these wave functions. For these wave functions we carried out consistency checks, which confirmed the reliability of our binding energy predictions and wave functions. We showed that it is mandatory to obtain the wave functions in all different Jacobi coordinates.

We established in Chapters 2 and 3 a reliable and feasible method to calculate accurately bound states of three and four nucleons or one hyperon and two or three nucleons. The solutions can be checked for self-consistency. We are not restricted to a special form of the two-body and three-body interactions. We carried out the implementation taking into account the full spin and isospin dependence of the underlying interactions. Therefore we claim that we are able to find accurate solutions of the few-body Schrödinger equations.

## 6.2 3N Model Hamiltonians

In Chapter 4 we applied the developed technique to the bound states  ${}^3\text{H}$ ,  ${}^3\text{He}$  and  ${}^4\text{He}$ . We are interested in model dependences of the predictions. To pin down these model dependences we compared results based on different model Hamiltonians. The basis of these model Hamiltonians are NN pair interactions. Therefore we started with an overview on the modern and realistic NN interactions in Section 4.1. We introduced the most modern NN interactions, which are called “realistic”, because they perfectly describe the pp and np scattering data for low and intermediate energies and the deuteron bound state. Nevertheless their functional form is very different. Therefore they are very valuable for investigations of the strong interaction, because deviations of the predictions for more complex systems are surely not the result of an inaccurate description of the NN data, but are related to the underlying model. The most sophisticated interactions, CD-Bonn [12] and AV18 [9], also include a parameterization of the nn interaction, which is adjusted to the pp data, but refined to predict the experimental nn scattering length.

Based on these interactions we found  ${}^3\text{He}$  and  ${}^3\text{H}$  binding energies in Section 4.2. We confirmed that NN interactions alone visibly underpredict the 3N binding energies. We also confirmed that the underprediction is model dependent. Our fully converged calculations show an underprediction of 500 keV to 800 keV. In spite of the on-shell equivalence of the interactions, we find sizable deviations in their results for the 3N system.

We argued that relativity and 3NF's should cure the underbinding problem. In this work we did not perform relativistic calculations. This is beyond its scope. The effect of relativity on the binding energy is still controversial, but a recent investigation indicated that wave functions are only slightly affected by relativity [95]. This means that our results for the wave functions are good approximations to fully relativistic ones. We emphasize that a study of the wave function properties using our non-relativistic results is meaningful.

In this work we concentrated on 3NF's and applied the TM-3NF [24], a modified version TM'-3NF

[106, 107] and the Urbana IX-3NF [17]. All these models have got a non-trivial spin-isospin structure. We argued that the 3NF models are not settled. Theoretically founded 3NF's are still not available. This justifies a phenomenological adjustment of the TM and TM' interactions. To this aim we combined the 3NF's with the realistic NN interactions and adjusted each combination to predict the experimental  ${}^3\text{H}$  binding energy. For the adjustment we used a parameter of the TM- and TM'-3NF. In this way we established a series of model Hamiltonians, which perfectly describe the NN data and predict by construction the same  ${}^3\text{H}$  binding energies. A similar adjustment has been performed by the Argonne-Urbana collaboration for the combination of Urbana IX and AV18. We also applied this combination in our studies. All this combinations formed a series of model Hamiltonians, which differ in both, the NN and 3N interactions. The differences showed up for example in the unobservable expectation values of the NN and 3N potential energies in  ${}^3\text{H}$ .

We emphasize that this series of model interactions is a very important result of our study. They are indispensable for investigations of the 3N continuum. Therefore we summarized the insights and results, which could be obtained by their application to 3N scattering problems. Many 3N scattering observables are correlated to the binding energy [112, 113]. For those observables the predictions of our Hamiltonians are identical (and in general in good agreement with the experimental data). Therefore they give the same information on the NN interaction as the  ${}^3\text{H}$  binding energy and they are not interesting to pin down model dependences. With the new Hamiltonians observables could be identified, which depend on the 3N interactions used, but not on the NN interaction [22]. These observables are good candidates for experimental investigations of the structure of 3NF's. The results will guide experimental investigations. Therefore these 3N Hamiltonians are an important tool to understand 3NF's. First experimental results showed that the used 3NF's cannot explain all measured observables [25, 26, 27, 28, 114]. The experimental results showed that the 3NF models are not complete. We remark that the calculations for the 3N continuum showed the different action of the available 3NF's and proved that they are not equivalent.

For upcoming, theoretically founded interactions from chiral perturbation theory an adjustment to the 3N binding energies will also be required [13, 14, 15]. With our work we established the technique for the necessary binding energy calculations for these models.

Our series of model Hamiltonians is a valuable tool to recognize model dependences, which are not the consequence of deviations in the description of NN data or 3N binding energies.

### 6.3 Properties of 3N bound states

We continued our investigations applying the adjusted models to the 3N bound state problem.

For the 3N bound states we were interested to pin down model dependences of the wave function. To this aim we looked into the momentum distributions and correlation functions for the  ${}^3\text{H}$  and  ${}^3\text{He}$  bound states in Section 4.3. For the momentum distributions we took over the usual definitions, but for correlation functions we invented a momentum space generalization of the ones usually chosen. Those momentum space correlations are defined as the probability that two nucleons in a fixed spin state have got a given *relative* momentum. We preferred these momentum space correlations, because, in plane wave impulse approximation (PWIA), they are directly linked to observables of nucleon knock-out experiments on  ${}^3\text{He}$ . In those experiments one of the nucleons is knocked out by  $e^-$ -scattering and the relative momentum of the remaining two is detected. We did not predict cross sections for this process, because we cannot judge the validity of the PWIA. But we studied in detail model dependences of the momentum correlations to identify interesting momentum regions.

The results were very similar for momentum correlations and distributions: We found a small or no dependence of these functions below  $1.5 \text{ fm}^{-1}$  on our adjusted Hamilton operators. This was a new insight. It was surprising for us to see this similarity of the predictions also for the momentum correlations for adjusted Hamiltonians, which differ in their NN interactions, because one observes visible differences in their short range configuration space correlations and also in the non-observable kinetic and potential energies.

We also observed that for momenta above  $2 \text{ fm}^{-1}$  in both, the momentum correlations and distributions, sizable differences arise comparing the predictions for the adjusted Hamiltonians based on different NN interactions. Thereby the 3NF's used had no effect on these functions in the entire momentum range.

We conclude that the correlation functions based on the adjusted Hamiltonians are not sensitive to the interaction in the low momentum region. They are influenced by all 3NF's in the same way, but show visible sensitivity to the NN interaction for momenta above  $2 \text{ fm}^{-1}$ . This clear separation of NN interaction sensitive and insensitive regions has never been observed before.

From knock-out experiments we expect information on the high momentum components of the NN interaction. Because of the model independence the low momentum region might be interesting for investigations of the interaction mechanisms, for example for meson exchange (MEC) currents.

Our results also indicate a sizable spin dependence of the correlation functions. We found this spin dependence also in momentum regions, where our results are model independent. For the summed up intrinsic spins  $s = 1$  of two nucleons we could establish a form of the angular dependence of the momentum correlations similar to the one in configuration space [118]. Our calculations showed that the angular dependent part of the correlation is also interaction independent for low momenta. This angular dependent part visibly shows up in correlations for momenta around  $1.5 \text{ fm}^{-1}$ .

$n\text{-}^2\text{H}/^3\text{H}$  overlap functions give the probability to find two nucleons in a deuteron state and the third one with a fixed relative momentum. We learned that n-p pairs in a spin  $s = 1$  state are predominately in a deuteron state. However, the probability for np pairs to be in a  $s = 1$  state is only  $\approx 51 \%$ . The spin structure of the  $^3\text{H}$  or  $^3\text{He}$  bound state is constrained by two requirements: the  $S$ -wave is the most important total orbital angular momentum state and the wave function is spatially symmetric. Both requirements minimize the kinetic energy of the nucleons [137]. They drive the observed spin structure, which favors an equal distribution of nucleon pairs with spin  $s = 0$  or  $s = 1$ .

In Section 4.4 we regarded the binding energy difference of the  $^3\text{H}$  and  $^3\text{He}$  nuclei. Besides the scattering length measurements for the strong pp and nn scattering lengths, this difference is an important experimental indication of CSB in the strong interaction. Model calculations showed that its size cannot completely be explained by the Coulomb interaction and the mass differences of the neutron and proton [31]. Part of the difference is expected to be the result of CSB in the strong interaction.

Our calculations included all dynamical ingredients, which are expected to contribute to the binding energy difference: the Coulomb interaction (or more elaborated electromagnetic interactions), the charge-dependence of the strong interaction and the np mass difference. It is well known that the splitting of the  $^3\text{H}$  and  $^3\text{He}$  binding energy is correlated to the 3N binding energies. Therefore a comparison of the predictions to the experiment required our adjusted 3N Hamiltonians. For these 3N Hamiltonians we model independently underpredicted the experimental value for the splitting by  $\approx 20 \text{ keV}$ . Only the prediction for CD-Bonn 2000 gave a slightly improved description and resulted in an underprediction of  $\approx 10 \text{ keV}$ .

We perturbatively compared the origin of the binding energy differences for the different models. We found that perturbation theory can predict the splitting only to an accuracy of  $10 \text{ keV}$ . In view of the small deviation of experimental and theoretical results the perturbative estimation visibly differed from our full results. But the accuracy was good enough to study possible differences in the origin of the

splitting. We saw that the contribution of the electromagnetic and strong interaction sizably differs for the different NN interaction models. Only the summed up result was equal in all cases. The interaction models give different predictions for CSB in several partial waves [123], only their scattering length predictions in conjunction with their specific electromagnetic interaction are by construction equal. We concluded that the  ${}^3\text{He}$ - ${}^3\text{H}$  binding energy difference is only sensitive to the scattering length difference of the pp and nn system. Neither higher partial waves nor other properties of the interactions seemed to contribute. A similar result was found in Ref. [123]. Moreover, we could trace back the different prediction of CD-Bonn 2000 to a correspondingly different prediction for the nn scattering length. The experimental situation for this scattering length is not clear. We found that a change of the scattering length within the error bar of the currently accepted experimental value [8] cannot resolve the underprediction. Recently a smaller value for the nn scattering length was proposed [6, 7]. We stated that this value would wipe out our understanding of the splitting. But we argued that we cannot propose a reliable estimation of the nn scattering length based on the energy splitting, because we expect that part of the unexplained underprediction is contributed by an unknown CSB in the 3NF.

## 6.4 $\alpha$ -particle binding energies and 4NF's

That study on CSB closed our work on the 3N system and led us to the 4N system in Section 4.5. We could present for the first time completely converged Faddeev-Yakubovsky calculations for the  $\alpha$ -particle. We showed  $\alpha$ -particle binding energies based on all modern realistic NN interactions. Our method enabled us to pin down dependences on the interaction models and to figure out the theoretical uncertainties in the description of the  $\alpha$ -particle due to the differences in the proposed NN interactions. Using only NN interactions we underpredicted the  $\alpha$ -particle binding energies by 2 to 4 MeV. We confirmed a known linear correlation of the  ${}^3\text{H}$  and  ${}^4\text{He}$  binding energies [124] for the new interaction models and extrapolated our results to the experimental  ${}^3\text{H}$  binding energy using a linear fit to our pairs of  ${}^3\text{H}$  and  ${}^4\text{He}$  binding energies. We obtained the so called Tjon-line. The experimental point for the pair of binding energies was situated slightly below this Tjon-line. The application of our properly adjusted model Hamiltonians to the  $\alpha$ -particle was because of the 3NF's a technical demanding, but very important step forward to find a quantitative understanding of the  $\alpha$ -particle. For all NN and 3N force combinations we found an attractive contribution of the 3NF's. The resulting  $\alpha$ -particle binding energies are slightly bigger than the experimental one. (By construction the Hamiltonians correctly predict the  ${}^3\text{H}$  binding energy). For the TM-3NF we found more overprediction for the  $\alpha$ -particle binding energy than for the TM' and Urbana IX 3NF's. The model dependence of our calculation reduces from 2 MeV for pure NN interactions to 800 keV for the adjusted Hamiltonians. We stated an average overprediction of 530 keV. For an estimation of the 4NF strength we assumed that this overprediction is balanced by a repulsive 4N interaction. This are 1.9 % of the  $\alpha$ -particle binding energy. Our results gave an average contribution of 13.8 % of the 3NF's to the  $\alpha$ -particle binding energy. Therefore we concluded that the series of NN, 3N, 4N,... interactions quickly converges. This new insight could only be obtained, because we are able to probe a wide range of NN and 3N interactions in our calculations. It indicates that nuclei can be described in terms of nucleons and interactions deduced in the NN and 3N system. These interactions have got predictive power in more complex systems. This justified the ambitious program from the Argonne-Los Alamos group to deduce the binding energies and low lying spectra of systems with  $A > 3$  from NN and 3N interactions. We note that our predictions showed a visible model dependence of the  $\alpha$ -particle binding energy. An investigation of the model dependence for  $A > 4$  is highly desirable.

## 6.5 Properties of the 4N wave function

In Section 4.6 we presented momentum distributions and correlations for the  $\alpha$ -particle. We again confirmed that these properties are essentially model independent in the low momentum region. The high momentum tail depends on the NN interaction, but we found independence from the 3NF. In comparison to the 3N bound state, we found a shift to higher momenta and a broader peak structure in the momentum correlations and distributions. This is in accordance with our expectation from the higher nuclear density in the  $\alpha$ -particle.

It has been argued that the  $p$ - $^3\text{H}/^4\text{He}$  overlap function gives insights to the short range behavior of the NN interaction [129]. We could obtain realistic overlap functions based on our  $^3\text{H}$  and  $^4\text{He}$  wave functions and studied their model dependence. For the low momenta the functions were again model independent. But for higher momenta around  $2\text{ fm}^{-1}$  we found the expected dip structure. Its position indeed depends on the NN interaction used. We revealed that the dependence on the 3NF is of minor importance. Both findings are very important new insights, which could only be obtained, because we are able to compare the results of various NN and 3N force combinations. Our findings confirmed that the overlap function is only sensitive to the NN interaction. The 3NF's are to a high degree unknown. Investigations on the structure of NN interactions require quantities, which are insensitive to the 3N and sensitive to the NN interaction. The results showed that the overlap functions fulfill both requirements. They can be related to proton knock-out experiments on  $^4\text{He}$ , where  $^3\text{H}$  is observed in the final state. The analysis of first experiments were obscured by FSI and MEC effects [125], but recently a new measurement has been performed in different kinematical regions, where both mechanisms should be suppressed [126]. Our results will enter into a "Generalized Eikonal Approach" (GEA) analysis of these experiments [130, 138].

We closed our investigations on the 3N and 4N systems with a look to the used 3NF's. In the properties of the wave functions presented we could hardly see any 3NF effect. To exemplify the action of 3NF's on the wave function, we presented the contribution of states with different total angular momentum to the expectation value of the 3N potential. We got two insights from this study. Firstly we observed that these matrix elements *qualitatively* differ for different 3NF's. This means that the action of the 3NF's in the  $\alpha$ -particle is very force dependent. This indicated that the considered models cover a wide range of possible 3NF's. Secondly we found tremendously different matrix elements for the wave functions calculated with and without 3NF. The 3NF's visibly changed the wave functions. From our observation that momentum distributions and correlations are not affected by 3NF's, we conclude that the changes in the wave function are very subtle. The pair configurations seem to be determined by the NN interaction. But this left some room for changes in 3N configurations. A forthcoming study should identify changed structures in these "3N correlations".

## 6.6 The hypertriton

In Chapter 5 we turned to hypernuclear physics. As in the case of the NN system, several models have been developed to describe YN scattering. In Section 5.1 we described the most elaborated models available. These are the SC89 [54], the series of SC97a-f [51] and the Jülich  $\tilde{\text{A}}$  [52]. Because the YN scattering data are very scarce, a purely phenomenological approach to YN interactions is impossible. Instead all considered interactions use the OBE mechanism to determine most parameters from the large NN database. Only a few parameters are fitted to the YN data. Because the physical input to the models is quite different, they do not equivalently describe the YN system. We showed the total  $\Lambda p$  cross section, for which the models predict comparable results in the region where data exist. But especially for small

energies we found sizable differences in the predictions for this simplest observable. We exemplified that the predictions for the most important phaseshifts even qualitatively differ. In summary we saw that the YN interaction is to a great extent unknown.

With these YN interactions at our disposal we started an investigation of the simplest hypernuclear bound state, the  ${}^3_{\Lambda}\text{H}$ , in Section 5.2. We continued the work of Miyagawa [75, 76] and confirmed the independence of the binding energy predictions from the NN interactions applied. A benchmark to other calculations [76, 71] established our implementation. We could give the first converged binding energies for the new SC97 models. Our results showed that only SC89 and SC97e-f led to  ${}^3_{\Lambda}\text{H}$  bound states. For SC97a-d and Jülich  $\tilde{\Lambda}$  we confirmed that no bound states exists. The binding energies for SC89 and SC97f are in accordance with the experimental value. SC97e clearly underbinds  ${}^3_{\Lambda}\text{H}$ .

For a simpler approach to the complicated hypernuclear bound states an approximation to the SC97f interaction has been developed (SC97f-sim) [131]. We showed that the binding energy predictions for SC97f and SC97f-sim differ by 109 keV. The approximation is not suitable to predict reliably the binding energy of  ${}^3_{\Lambda}\text{H}$ . For this hypernucleus the full interactions are required to give reliable predictions for the binding energies.

We also checked the possibility to construct effective  $\Lambda\text{N}$  interactions without the explicit  $\Lambda\text{-}\Sigma$  conversion. Therefore we estimated the contribution of the  $\Lambda\text{-}\Sigma$  conversion to the binding energy performing truncated calculations without explicit  $\Sigma$ -degree of freedom. These calculations were based on truncated interactions, which effectively includes the conversion. They are exactly phase equivalent in the  $\Lambda\text{N}$  system to the original interactions. Nevertheless their binding energy predictions differ from the original ones. We led this difference back to missing three-baryon interactions or, in other words, to a medium dependence of the  $\Lambda\text{N}$  interaction due to the eliminated  $\Sigma$ -degree of freedom. For  ${}^3_{\Lambda}\text{H}$  these three-baryon interactions are attractive. We conclude that their 116 keV contribution for SC89 is a realistic measure of the error, which is systematically included in calculations using effective  $\Lambda\text{N}$  interactions in  ${}^3_{\Lambda}\text{H}$ . For  ${}^3_{\Lambda}\text{H}$  the inclusion of  $\Lambda\text{-}\Sigma$  conversion is essential for a reliable prediction of the binding energies.

We presented the properties of the  ${}^3_{\Lambda}\text{H}$  wave functions in Section 5.3. In all cases they showed that the hypertriton can be seen as a  $\Lambda$  loosely bound to a deuteron. Due to  $\Lambda\text{-}\Sigma$  conversion a small  $\Sigma$ -component of 0.1 % to 0.5 % in the wave function arises.

We decomposed the expectation values of the YN interaction in contributions from different channels. This study could not confirm the naive expectation that the  ${}^1\text{S}_0$  potential is stronger than the  ${}^3\text{S}_1\text{-}{}^3\text{D}_1$  potential, which has often been concluded from the experimentally found angular momentum  $J^\pi = \frac{1}{2}^+$  of  ${}^3_{\Lambda}\text{H}$ .

Based on our wave functions we calculated momentum distributions and correlation functions for  ${}^3_{\Lambda}\text{H}$ . We found that both, the correlations and the momentum distributions are quite different for nucleons,  $\Lambda$ - and  $\Sigma$ -particles. Of special interest are the  $\Sigma\text{N}$  correlations, because they qualitatively differ from the usual functions for nuclear systems. The different structure in the  $\Sigma\text{N}$  correlations can be best seen in configuration space. They are extremely spin dependent. For  $s = 1$  we found a similar functional form as for NN correlations. The  $\Sigma$ -particle and the nucleon are well separated. In contrast our calculations showed that for  $s = 0$  both particles are overlapping with a high probability. This seems to be the consequence of the attractive short range behavior in parts of the  $\Sigma\text{N}$  interaction. This behavior is more pronounced for SC97e and f than for SC89.

We again emphasize that we learned from our  ${}^3_{\Lambda}\text{H}$  calculations that  $\Lambda\text{-}\Sigma$  conversion is an essential ingredient to the dynamics. We also state that an approximate treatment of the YN interaction is dangerous and might be misleading. We do not want to conclude on the YN interactions here without the important information from  ${}^4_{\Lambda}\text{He}$  and  ${}^4_{\Lambda}\text{H}$ .



## 6.7 The binding energies of ${}^4_{\Lambda}\text{He}$ and ${}^4_{\Lambda}\text{H}$

Our binding energies for  ${}^4_{\Lambda}\text{He}$  and  ${}^4_{\Lambda}\text{H}$  are presented in Section 5.4. We obtain the first complete solutions for these bound states based on the full, not approximated YN interactions derived from the OBE. This was a very important step forward for the understanding of the YN interaction. We emphasized the high reliability and accuracy of our calculations, because they are the prerequisites for conclusions on the underlying dynamical assumptions. For SC97f-sim we found only an unsatisfying agreement with two existing calculations [71, 72], which are also not in good agreement with each other. Our scheme allows for meaningful self-consistency checks, which confirmed our results. Therefore we claim to give accurate predictions for the binding energies.

Again we learned that the predictions of the approximated and original interaction significantly differ. A complete calculation is indispensable for  ${}^4_{\Lambda}\text{He}$  and  ${}^4_{\Lambda}\text{H}$  to conclude reliably using the results.

Our full calculations confirmed that the  $\Lambda$  separation energies of  ${}^4_{\Lambda}\text{He}$  and  ${}^4_{\Lambda}\text{H}$  allow for a meaningful comparison to the experiment. Our predictions only slightly depend on the nucleonic part of the Hamiltonian. This insight is based on calculations for different NN interactions and even on the application of a 3NF.

Based on the available YN interactions we presented  $\Lambda$  separation energy predictions for the ground and excited state of  ${}^4_{\Lambda}\text{He}$  without any uncontrolled approximation. The results are sensitive to the used YN interactions. The best description of the  $0^+$  state could be obtained for SC89. But the same interaction fails to predict a reasonable  $1^+$   $\Lambda$  separation energy. For this state the new SC97d-f interactions did a better job, but they give a considerably smaller binding energy for the ground state. Using the last considered interaction, Jülich  $\tilde{A}$ , even results in the wrong spin ordering and a too small overall binding in both states.

Very often the correct splitting of the ground and the excited state is seen as the key quantity to make judgments on the quality of the interaction models [72, 51]. We saw that SC97f can predict the correct spin splitting, but we hesitate to conclude that the interaction describes the dynamics correctly. We will come back to this issue below.

As in the case of  ${}^3_{\Lambda}\text{H}$ , we judged on the importance of  $\Lambda$ - $\Sigma$  conversion for the binding energies using a truncated effective  $\Lambda\text{N}$  interaction, which is phase equivalent to SC97e. We found that the medium effect of  $\Lambda$ - $\Sigma$  conversion, which cannot be included in an effective two-body interaction and can be seen as a missing many-body force, is important for the separation energies and their spin splitting. This missing many-body force turned out to be attractive for the ground and repulsive for the excited state. The deviations of the exact and truncated calculations amount to up to 400 keV. The  $\Lambda$ - $\Sigma$  conversion has got a decisive influence on the separation energies. This influence is even more pronounced than in  ${}^3_{\Lambda}\text{H}$ . Therefore also for the four-body hypernuclei an effective  $\Lambda\text{N}$  interaction is not suitable.

We pointed out that SC97d predicts the correct spin ordering, though the scattering lengths indicated a stronger  ${}^3\text{S}_1$ - ${}^3\text{D}_1$  interaction and that SC89 predicts a smaller zero energy cross section than the SC97 models but the highest ground state separation energies. Both facts indicate that a simple relation of the hypernuclear four-body binding energies and the strengths of the YN interactions is not existing. Full calculations are required to make judgments on the YN potentials.

We argued that an interpretation of our binding energies and especially of the predicted  $0^+$ - $1^+$  splitting is very difficult. We can expect from our experience in the 3N and 4N systems, that a three-baryon interaction (3BF) based on the same mechanisms as the 3NF in ordinary nuclear systems contribute roughly 10 % to the separation energies. This means roughly 240 keV. We emphasized that a strong spin dependence of this forces might lead to a tremendous influence of this missing 3BF on the  $0^+$ - $1^+$  splitting. Therefore a judgment on the YN two-body interaction based on this quantity has to be done

very carefully.

## 6.8 The ${}^4_{\Lambda}\text{He}$ wave function

For our further investigations it was an important point that we found in Chapter 4 hardly any effect of 3NF's on most of the wave function properties, especially on the properties of NN pairs. We generalized this experience to the hypernuclear bound states and possible 3BF's, which justifies our studies of the properties of the hypernuclei based on our solutions in Section 5.5. For these studies we created wave functions for  ${}^4_{\Lambda}\text{He}$ . We reached a high accuracy, which has been confirmed comparing the binding energies and the expectation values of the Hamiltonians. As expected we found that the orbital  $S$ -state is the most important part of the wave function in both, the ground and the excited state. For all YN interactions we found the expected spin flip in the spin wave functions going from the ground to the excited state.

From the contributions of different channels to the expectation values of the YN potential we learned that the action of the Jülich interaction qualitatively differs from the Nijmegen SC interactions in the hypernuclei. For the Nijmegen SC interactions we obtained in the  $\Lambda\text{N}$ - $\Lambda\text{N}$  direct potential an attractive contribution in the  ${}^1\text{S}_0$  channel and a repulsive contribution in the  ${}^3\text{S}_1$ - ${}^3\text{D}_1$  channel, which we also observed in  ${}^3_{\Lambda}\text{H}$ . It is remarkable that this is opposite for the Jülich force in  ${}^4_{\Lambda}\text{He}$ . Also the spin structure of the important  $\Lambda$ - $\Sigma$  conversion potential tremendously differs. We generally found a shift from the  ${}^1\text{S}_0$  to the  ${}^3\text{S}_1$ - ${}^3\text{D}_1$  matrix elements comparing the  $0^+$  and  $1^+$  states. However, a simple understanding of the relative strength of the  ${}^1\text{S}_0$  and  ${}^3\text{S}_1$ - ${}^3\text{D}_1$  interactions from the spin ordering in  ${}^4_{\Lambda}\text{He}$  was again impossible. We could also not see a suppression of  $\Lambda$ - $\Sigma$  conversion in the excited state, which has been proposed in Ref. [68] to understand the spin ordering.

The dynamics showed up to be complicated and strongly influenced by  $\Lambda$ - $\Sigma$  conversion as can be seen from the big contribution of the conversion potential to the YN potential energy in both states and for an arbitrary interaction.

The  $\Sigma$ -component was more visible in  ${}^4_{\Lambda}\text{He}$  than in  ${}^3_{\Lambda}\text{H}$ . It amounts up to 4.1 % in the ground state and was generally smaller in the excited state. We could find in both states a big component of an unperturbed bound 3N core state surrounded by a  $\Lambda$ . But we observed that this core- $\Lambda$  component is less important than in  ${}^3_{\Lambda}\text{H}$ .

The momentum distributions are qualitatively similar to the ones for  ${}^3_{\Lambda}\text{H}$ . Again we are especially interested in the  $\Sigma\text{N}$  correlations. The results in configuration space turned out to be more concrete. For the Nijmegen SC models, we found a behavior similar to NN correlations in the  $s = 1$  states. This was in accordance with the results for  ${}^3_{\Lambda}\text{H}$ . For  $s = 0$  the small interparticle distances were less pronounced than in  ${}^3_{\Lambda}\text{H}$ . We considered it important that the Jülich and Nijmegen models predicted comparable  $\Sigma\text{N}$  correlations in the  $s = 1$  channel, but different ones in the  $s = 0$  channel. In the latter channel the probability for overlapping  $\Sigma$ 's and nucleons is very high for Jülich  $\tilde{\Lambda}$ . We argued that a spurious resonance in the  ${}^1\text{S}_0$  channel, which also spoils the prescription of the  $\Lambda\text{N}$  scattering data, might be responsible for this behavior. One highly needs an update of the Jülich interaction for a better understanding.

## 6.9 The CSB in ${}^4_{\Lambda}\text{He}$ and ${}^4_{\Lambda}\text{H}$

We closed our investigations with a look into another, in our opinion important observable in Section 5.6, the binding energy difference of  ${}^4_{\Lambda}\text{He}$  and  ${}^4_{\Lambda}\text{H}$ . We explained that this splitting due to CSB is less obscured by missing 3BF's than the  $0^+$ - $1^+$  splitting and that it is strongly related to  $\Lambda$ - $\Sigma$  conversion. In our

opinion it is the only observable in the  ${}^4_{\Lambda}\text{He}$  and  ${}^4_{\Lambda}\text{H}$  system, from which one can rule out or confirm YN interaction models. The binding energies and spin splittings are always uncertain because of the unknown 3BF effects. We could confirm an important contribution to the  ${}^4_{\Lambda}\text{He}$ - ${}^4_{\Lambda}\text{H}$  splitting from the kinetic energy due to  $\Lambda$ - $\Sigma$  conversion. We found that the Coulomb interaction is less important for this quantity, but the CSB of strong YN interaction visibly shows up. For the SC97e and SC89 interactions we found that the CSB due to  $\Lambda$ - $\Sigma^0$  mixing is an important part of the total CSB in the strong interaction. We rise the question, whether there is freedom in the mixing angle and whether one can sizably tune the CSB using this freedom. For SC89 we found a reasonable agreement with the experimental result in the  $0^+$  state. Unfortunately, this is not true for SC97e. Because of the big size of the experimentally found CSB, we expect that a sizable contribution from the kinetic energy is necessary. Therefore we stated that  $\Sigma$ -contributions of the order 4 % to 5 % are preferred for an understanding of the splitting. In this view the new SC97 models seem to give too small  $\Lambda$ - $\Sigma$  conversion strength. In this point SC89 does a better job. We would like to emphasize that we do not expect that 3BF's can cure the underbinding in the  $1^+$  state for this interaction. We conclude that SC89 is ruled out by its excited state predictions, whereas the new SC interactions can not explain the  ${}^4_{\Lambda}\text{He}$ - ${}^4_{\Lambda}\text{H}$  binding energy difference. The Jülich interaction seems to be also not suitable to explain the experimental  $\Lambda$  separation energies.

We see that the  ${}^3_{\Lambda}\text{H}$  binding energies are less sensitive to the differences of the YN interactions. Moreover the experimental  $\Lambda$  separation energy has got a very big error bar for this hypernucleus. The  ${}^4_{\Lambda}\text{He}$  and  ${}^4_{\Lambda}\text{H}$  nuclei are much more suitable to pin down model dependences especially because of their four experimentally found bound states with different angular momenta and charges. Our results showed that we highly need new YN interaction models to understand completely these hypernuclei.

## 6.10 Outlook for hypernuclear studies

In this thesis we established a technique, which is able to handle hypernuclear few-body bound state problems. In the near future an improved series of Nijmegen SC interactions will appear [136]. It is one step to a better understanding of the YN interaction. We would like to stimulate a series of models, which systematically differ in their  $\Lambda$ - $\Sigma$  conversion strength. This might clarify the role of  $\Lambda$ - $\Sigma$  convergence for the YN interaction, because we will be able to observe its effects on the splitting due to CSB, the  $0^+$ - $1^+$  splitting and the absolute  $\Lambda$  separation energies.

New theoretical developments are badly needed. Recently, interactions based on RGM for quark clusters appeared [57]. An investigation of these models might give new interesting insights. We emphasize that we are not able to judge the influence of a missing 3BF on the binding energies, because there are no 3BF models available. Therefore we would like to encourage the investigation of the YN and YNN system using a generalization of chiral perturbation theory. Recently it was possible to apply interactions derived from chiral perturbation theory to the 3N and 4N system [139]. A transference to hypernuclear physics might lead to a much better understanding of the few-body hypernuclei. We expect that realistic estimates for 3BF effects are possible on this theoretical basis. A generalization of theoretical concepts from nuclear to hypernuclear systems will improve the understanding of the underlying mechanisms also for nuclear systems.

## Appendix A

# Transformation of Jacobi coordinates in arbitrary 3-body systems

In our work we used Jacobi coordinates to describe the motion of the particles. They allow to remove the center of mass motion. The solution of the Yakubovsky equations makes it necessary to transform the different possible sets of Jacobi coordinates into each other. For three particles with momenta  $\vec{k}_i$  and masses  $m_i$  they are defined as

$$\begin{aligned}\vec{p}_{12} &= \frac{1}{m_1 + m_2}(m_2\vec{k}_1 - m_1\vec{k}_2) \\ \vec{q}_3 &= \frac{1}{m_1 + m_2 + m_3}((m_1 + m_2)\vec{k}_3 - m_3(\vec{k}_1 + \vec{k}_2))\end{aligned}\tag{A.1}$$

Analogous expressions exist for the cyclic and anticyclic definition:

$$\begin{aligned}\vec{p}_{23} &= \frac{1}{m_2 + m_3}(m_3\vec{k}_2 - m_2\vec{k}_3) \\ \vec{q}_1 &= \frac{1}{m_1 + m_2 + m_3}((m_2 + m_3)\vec{k}_1 - m_1(\vec{k}_2 + \vec{k}_3))\end{aligned}\tag{A.2}$$

and

$$\begin{aligned}\vec{p}_{31} &= \frac{1}{m_3 + m_1}(m_1\vec{k}_3 - m_3\vec{k}_1) \\ \vec{q}_2 &= \frac{1}{m_1 + m_2 + m_3}((m_3 + m_1)\vec{k}_2 - m_2(\vec{k}_3 + \vec{k}_1))\end{aligned}\tag{A.3}$$

In this vector notation the transformation matrix element of momentum eigenstates  $|\vec{p}_{12}\vec{q}_3\rangle_{(12)3}$  to  $|\vec{p}_{23}\vec{q}_1\rangle_{(23)1}$  is easily obtained:

$${}_{(12)3}\langle\vec{p}_{12}\vec{q}_3|\vec{p}'_{23}\vec{q}'_1\rangle_{(23)1} = \delta^3(\vec{p}'_{23} - \vec{\pi}'_{23}(\vec{p}_{12}\vec{q}_3)) \delta^3(\vec{q}'_1 - \vec{\chi}'_1(\vec{p}_{12}\vec{q}_3))\tag{A.4}$$

Please note the choice of  $\delta$ -functions. Indeed there are several possibilities to choose the arguments. In this case we fix the momenta of the right hand side by the momenta of the left hand side. This choice

breaks the symmetry of the permutation operator. The indices  $(ij)k$  only emphasize the kind of Jacobi coordinate. They will become important later in this appendix.

Instead of these 3-dimensional basis we expand the angular dependence in partial waves. Therefore the momentum eigenstates change to eigenstates of the angular momentum and the momentum magnitude

$$|p_{12}q_3\alpha\rangle_{(12)3} \equiv |p_{12}q_3((l_{12}(j_1j_2)s_{12})j_{12}(l_3j_3)I_3)JM\rangle \quad (\text{A.5})$$

We need the expression of Eq. (A.4) in a partial wave decomposition. The actual derivation follows [140]. The result for arbitrary masses and spins has the same structure like the result of [140].

$${}_{(12)3}\langle p_{12}q_3\alpha|p'_{23}q'_1\alpha'\rangle_{(23)1} = \int_{-1}^1 dx \frac{\delta(p'_{23} - \pi'_{23}(p_{12}q_3x))}{\pi'^2_{23}l'^2_{23}+2} \frac{\delta(q'_1 - \chi'_1(p_{12}q_3x))}{\chi'^{l'_1+2}_1} G_{\alpha\alpha'}(p_{12}q_3x) \quad (\text{A.6})$$

The magnitude of the shifted momenta are derived directly from the 3-dimensional expressions. One expresses the individual momenta by the Jacobi momenta Eq.(A.1) and inserts the result into Eq.(A.2). The angular dependence of the magnitudes is kept in the  $x$  variable, which is the cosine of the angle between  $\vec{p}_{12}$  and  $\vec{q}_3$ .

$$\begin{aligned} \pi'_{23}(p_{12}q_3x) &= \sqrt{\beta^2 p_{12}^2 + \gamma^2 q_3^2 + 2\beta\gamma p_{12}q_3x} \\ \chi'_1(p_{12}q_3x) &= \sqrt{p_{12}^2 + \alpha^2 q_3^2 - 2\alpha p_{12}q_3x} \end{aligned} \quad (\text{A.7})$$

The mass ratios  $\alpha$ ,  $\beta$  and  $\gamma$  are defined as

$$\begin{aligned} \alpha &= \frac{m_1}{m_1 + m_2} \\ \beta &= \frac{m_3}{m_2 + m_3} \\ \gamma &= \frac{m_2(m_1 + m_2 + m_3)}{(m_2 + m_3)(m_1 + m_2)} \end{aligned} \quad (\text{A.8})$$

The  $x$  dependence of the  $G$  function is expanded in Legendre polynomials  $P_k$ . It remains a purely geometrical part  $g$

$$G_{\alpha\alpha'}(p_{12}q_3x) = \sum_k P_k(x) \sum_{\mu_1 + \mu_2 = l'_{23}} \sum_{\nu_1 + \nu_2 = l'_1} (-\beta p_{12})^{\mu_1} (-\gamma q_3)^{\mu_2} p_{12}^{\nu_1} (-\alpha q_3)^{\nu_2} g_{\alpha\alpha'}^{k\mu_1\nu_1\mu_2\nu_2} \quad (\text{A.9})$$

The geometrical part  $g$  is a very complicated function of the angular momentum quantum numbers. It is diagonal in  $J$  and  $M$ , because the total angular momentum cannot depend on the kind of Jacobi coordinate used. Additionally the parity is not changed. Therefore

$$(-1)^{l_{12}+l_3} = (-1)^{l'_{23}+l'_1} \quad (\text{A.10})$$

The explicit form of the  $g$  function is very lengthy

$$g_{\alpha\alpha'}^{k\mu_1\nu_1\mu_2\nu_2} = \delta_{MM'} \delta_{JJ'} \sum_{LS} \sum_{gg'} \frac{\hat{k}}{2} \sqrt{\hat{g}\hat{g}'\hat{s}_{12}\hat{I}_3\hat{j}_{12}} \sqrt{\hat{l}'_{23}\hat{l}'_1\hat{s}'_{23}\hat{I}'_1\hat{j}'_{23}} \hat{L}\hat{S} \sqrt{\frac{\hat{l}'_{23}!\hat{l}'_1!}{(2\mu_1)!(2\mu_2)!(2\nu_1)!(2\nu_2)!}}$$

$$\begin{aligned}
& (-1)^{s'_{23}+2j_1+j_2+j_3+L+g+l_3} \begin{Bmatrix} l_{12} & s_{12} & j_{12} \\ l_3 & j_3 & I_3 \\ L & S & J \end{Bmatrix} \begin{Bmatrix} l'_{23} & s'_{23} & j'_{23} \\ l'_1 & j'_1 & I'_1 \\ L & S & J \end{Bmatrix} \begin{Bmatrix} \mu_1 & \mu_2 & l'_{23} \\ \nu_1 & \nu_2 & l'_1 \\ g & g' & L \end{Bmatrix} \\
& \begin{Bmatrix} j_1 & j_2 & s_{12} \\ j_3 & S & s'_{23} \end{Bmatrix} \begin{Bmatrix} g' & g & L \\ l_{12} & l_3 & k \end{Bmatrix} (\mu_1 \nu_1 g, 00)(\mu_2 \nu_2 g', 00)(gk l_{12}, 00)(g' k l_3, 00) \quad (\text{A.11})
\end{aligned}$$

In these expressions the abbreviation  $\hat{l} = 2l + 1$  is used.

Up to now we did not mention the corresponding expressions for the third kind of Jacobi coordinates Eq.(A.3). The matrix elements  ${}_{(12)3} \langle pq\alpha | p'q'\alpha' \rangle_{(31)2}$  are related to  ${}_{(12)3} \langle pq\alpha | p'q'\alpha' \rangle_{(23)1}$  in our representation. The interchange of the particles of the two-body subsystems leads to well known phases

$$|pq\alpha \rangle_{(ij)k} = (-1)^{l_{ij}+j_i+j_j-s_{ij}} |pq\alpha \rangle_{(ji)k} \quad (\text{A.12})$$

Doing this for the right and left hand side of the matrix element leads immediately to

$$\begin{aligned}
{}_{(12)3} \langle pq\alpha | p'q'\alpha' \rangle_{(31)2} &= (-1)^{l_{12}+j_1+j_2-s_{12}+l_{31}+j_3+j_1-s_{31}} {}_{(21)3} \langle pq\alpha | p'q'\alpha' \rangle_{(13)2} \\
&= (-1)^{l_{12}+j_1+j_2-s_{12}+l_{31}+j_3+j_1-s_{31}} {}_{(12)3} \langle pq\alpha | p'q'\alpha' \rangle_{(23)1} \quad (\text{A.13})
\end{aligned}$$

In the last equality we exchanged the numbers of particles 1 and 2 on both sides of the matrix element.

The isospin matrix element is completely independent from the spin orbital part and factorizes. The explicit expression reads

$$\begin{aligned}
& {}_{(12)3} \langle ((t_1 t_2) t_{12} t_3) T M_T | ((t_2 t_3) t'_{23} t_1) T' M'_T \rangle_{(23)1} \\
&= \delta_{M_T M'_T} \delta_{T T'} (-1)^{t'_{23}+2t_1+t_2+t_3} \sqrt{\hat{t}_{12} \hat{t}'_{23}} \begin{Bmatrix} t_1 & t_2 & t_{12} \\ t_3 & T & t'_{23} \end{Bmatrix} \quad (\text{A.14})
\end{aligned}$$

Again one can show that the matrix element for the anticyclic coordinate transformation is connected to the cyclic one by

$${}_{(12)3} \langle \alpha_T | \alpha'_T \rangle_{(31)2} = (-1)^{2t_1+t_2+t_3-t_{12}-t'_{31}} {}_{(12)3} \langle \alpha_T | \alpha'_T \rangle_{(23)1} \quad (\text{A.15})$$

## Appendix B

# Reduction of the general Yakubovsky equations to more simple physical systems

In this appendix we summarize the dynamical equations for  ${}^3\text{He}$ ,  ${}^3\text{H}$ ,  ${}^4\text{He}$  and  ${}^3_\Lambda\text{H}$ . We will derive a connection between the Faddeev or Yakubovsky equations of these systems and the more general Yakubovsky equations, which we presented in Chapter 2.

### B.1 Faddeev equations for the hypertriton

In Eqs. (2.35) to (2.39) the Yakubovsky equations for  ${}^4_\Lambda\text{He}$  are given. In this formulation the fourth particle is the hyperon. Now we assume that one of the nucleons, for example the third particle, does not interact anymore. The four-body system is then reduced to an interacting three-body system of two nucleons and one hyperon. The third particle is just a non-interacting spectator at rest. Formally this means that the potentials  $V_{i3}$ , the corresponding  $t$ -matrices and the three-nucleon interaction  $V_{123}$  are zero. This implies a reduction of the Yakubovsky components as follows

$$\psi_{1A} \equiv \psi_{(12)3,4} = 0 \quad (\text{B.1})$$

$$\psi_{1B} \equiv \psi_{(12)4,3} = G_0 t_{12} (1 - P_{12}) \psi_{1C} \quad (\text{B.2})$$

$$\psi_{1C} \equiv \psi_{(14)2,3} = G_0 t_{14} (\psi_{1B} - P_{12} \psi_{1C}) \quad (\text{B.3})$$

$$\psi_{2A} \equiv \psi_{(12)34} = 0 \quad (\text{B.4})$$

$$\psi_{2B} \equiv \psi_{(34)12} = 0 \quad (\text{B.5})$$

The third particle does not feel any interaction in this case. Its contribution to the kinetic energy is zero, if its momentum is zero. Therefore we solve Eqs. (B.2) and (B.3) for  $q_3 = 0$ .

It is a nice exercise to show the complete equivalence of these equations with the Faddeev equations derived in Ref. [75]. We use the Schrödinger equation of the hypertriton wave function  $\Psi$

$$\Psi = G_0 V \Psi = G_0 (V_{12} + V_{14} + V_{24}) \Psi \quad (\text{B.6})$$

and insert it into the definition of the Yakubovsky components  $\psi_{1B}$  and  $\psi_{1C}$

$$\begin{aligned}\psi_{1B} &= G_0 t_{12} G_0 (V_{14} + V_{24}) \Psi \\ &= G_0 t_{12} G_0 (V - V_{12}) \Psi \\ &= G_0 V_{12} \Psi\end{aligned}\tag{B.7}$$

and

$$\begin{aligned}\psi_{1C} &= G_0 t_{14} G_0 (V_{12} + V_{24}) \Psi \\ &= G_0 t_{14} G_0 (V - V_{14}) \Psi \\ &= G_0 V_{14} \Psi\end{aligned}\tag{B.8}$$

In the last steps we used the Lippmann-Schwinger equation for the  $t$ -matrix Eq. (2.8) and exactly arrived at the definition of the two independent Faddeev components of the hypertriton. Omitting the third particle reduces the expression Eq. (2.40) for the four-baryon wave function to the one of the hypertriton

$$\Psi = \psi_{1B} + (1 - P_{12})\psi_{1C}\tag{B.9}$$

## B.2 Yakubovsky equations for the $\alpha$ -particle

In this subsection we use the additional symmetry of the  $\alpha$ -particle wave function compared to the  ${}^4_\Lambda\text{He}$  wave function to reduce the number of independent Yakubovsky components. Very similarly to Eq. (2.34) one finds relations between “3+1” YC’s  $\psi_{1B}$ ,  $\psi_{1C}$  and  $\psi_{1A}$  and the “2+2” YC’s  $\psi_{2A}$  and  $\psi_{2B}$ .

$$\begin{aligned}\psi_{1B} &= -P_{34}\psi_{1A} \\ \psi_{1C} &= P_{24}P_{34}\psi_{1A} \\ \psi_{2B} &= P_{13}P_{24}\psi_{2A}\end{aligned}\tag{B.10}$$

In this case two of the Yakubovsky equations are already a closed set of linear equations for the two independent components  $\psi_{1A}$  and  $\psi_{2A}$ .

$$\begin{aligned}\psi_{1A} &\equiv \psi_{(12)3,4} = G_0 t_{12} (P_{13}P_{23} + P_{12}P_{23}) ((1 - P_{34}) \psi_{1A} + \psi_{2A}) \\ &\quad + (1 + G_0 t_{12}) G_0 V_{123}^{(3)} \Psi\end{aligned}\tag{B.11}$$

$$\psi_{2A} \equiv \psi_{(12)34} = G_0 t_{12} P_{13} P_{24} [(1 - P_{34})\psi_{1A} + \psi_{2A}]\tag{B.12}$$

In the same way one finds for the wave function  $\Psi$

$$\Psi = (1 - (1 + P)P_{34})(1 + P)\psi_{1A} + (1 + P)(1 + \tilde{P})\psi_{2A}\tag{B.13}$$

with  $P = P_{12}P_{23} + P_{13}P_{23}$  and  $\tilde{P} = P_{13}P_{24}$

In this form the  $\alpha$ -particle equations were derived in Ref. [36]. The generalization to 3NF’s has already been published in Ref. [109].

## B.3 Faddeev equations for the triton

The well known Faddeev equations of the 3N system (see for example [140]) can be derived from the two Yakubovsky equations for the  $\alpha$ -particle Eqs. (B.11) and (B.12). We omit all interactions and permutations involving the fourth particle and arrive at

$$\psi_{1A} \equiv \psi_{(12)3,4} = G_0 t_{12} (P_{13}P_{23} + P_{12}P_{23}) \psi_{1A}$$



$$+(1 + G_0 t_{12}) G_0 V_{123}^{(3)} \Psi \tag{B.14}$$

$$\psi_{2A} \equiv \psi_{(12)34} = 0 \tag{B.15}$$

The wave function also simplifies in this case to

$$\Psi = (1 + P)\psi_{1A} \tag{B.16}$$

with  $P = P_{12}P_{23} + P_{13}P_{23}$ .

This concludes the short summary of the dynamical equations, which we use in this thesis. The explicit expression can easily be derived using the formulas in Chapter 2.

# Appendix C

## Treatment of the three-nucleon interaction embedded in the four-body Hilbert space

This appendix deals with the representation of 3NF's in a four-body Hilbert space. An explicit form will be given for the Tucson-Melbourne (TM) [24] and Urbana (Urb-IX) [17] 3NF.

The following derivation is based on the partial wave decomposition of TM given in Ref. [82]. But the form derived there turns out not to be applicable to four-body states. The old algorithms require tremendous amounts of memory in the case of the four-body calculations, because they simultaneously need the partial wave decomposed forces for all angular momenta of the three-body subsystems (at least 50 GBytes).

The new feature is a different treatment of the necessary coordinate transformations, which is suitable for an application to four-body states. In this form we are able to generate a 3NF during the iterative solution procedure for the YE's. The memory consuming storage of a full 3NF can be left out. Moreover the algorithm can efficiently be implemented on a massively parallel computer. The solutions of the Yakubovsky equations presented in Chapter 4 and 5 could only be obtained in the form presented here. The appendix consists of four sections. In the first two we concentrate on the TM force. We apply the scheme to the Urbana force in the last two.

### C.1 Separation of the TM force in NN-like potentials

The two 3NF models that we apply in this thesis, the TM model [24] and the Urbana model [17], have got a few common features. They both naturally decompose into three parts, which are identical up to a cyclic or anticyclic permutation of the three interacting particles

$$\begin{aligned} V_{ijk} &= V_{jki}^{(i)} + V_{ikj}^{(j)} + V_{ijk}^{(k)} \\ V_{jki}^{(i)} &= P_{jk} P_{ij} V_{ikj}^{(j)} P_{ij} P_{jk} \end{aligned} \tag{C.1}$$

$4(2\pi)^6 V_0 [m_N^{-2}]$	$a [m_\pi^{-1}]$	$b [m_\pi^{-3}]$	$c [m_\pi^{-3}]$	$d [m_\pi^{-3}]$
179.7	1.13	-2.58	1.0	-0.753

Table C.1: Strength constants of the TM force as given in Ref. [141]. The numbers are in units of the nucleon mass  $m_N$  and the  $\pi$  mass  $m_\pi$

Only one of the three parts enters into the Yakubovsky equation Eq. (2.35). Therefore the problem reduces to the evaluation of the matrix element

$$\langle (12)3, 4 | V_{123}^{(3)} | \Psi \rangle \quad (\text{C.2})$$

where we can assume that the state  $\Psi$  is antisymmetric in the nucleons 123. The fourth particle does not matter. The following derivation is equally valid for an outer nucleon and an outer hyperon.

One distinguishes four terms in the TM force, the so called  $a$ -,  $b$ -,  $c$ - and  $d$ -term which are named by their individual strength constants. These constants are fixed by low energy theorems [24]. The constants are given in Table C.1 together with an overall strength parameter  $V_0$ .

$$\begin{aligned} V_{123}^{(3)} = V_0 ( & a \vec{\tau}_1 \cdot \vec{\tau}_2 W_{23}^a W_{31}^a \\ & + b \vec{\tau}_1 \cdot \vec{\tau}_2 \vec{W}_{23}^b \cdot \vec{W}_{31}^b \\ & + c \vec{\tau}_1 \cdot \vec{\tau}_2 (W_{23}^a W_{31}^c + W_{23}^c W_{31}^a) \\ & + d \vec{\tau}_3 \cdot \vec{\tau}_1 \times \vec{\tau}_2 \vec{W}_{23}^d \cdot \vec{W}_{31}^b) \end{aligned} \quad (\text{C.3})$$

Here we use a form, where we separated the isospin operators, which consist of combinations of the Pauli matrices  $\tau_i$ , and the spin-orbital operators  $W$  of the 3NF.

The  $W$ 's can be read off from the definition of the TM force in momentum space, as given in Ref. [82].

$$W_{23}^a = F(\vec{Q}'^2) \frac{\vec{\sigma}_2 \cdot \vec{Q}'}{\vec{Q}'^2 + m_\pi^2}$$

$$W_{31}^a = F(\vec{Q}^2) \frac{\vec{\sigma}_1 \cdot \vec{Q}}{\vec{Q}^2 + m_\pi^2} \quad (\text{C.4})$$

$$\vec{W}_{23}^b = F(\vec{Q}'^2) \frac{\vec{\sigma}_2 \cdot \vec{Q}'}{\vec{Q}'^2 + m_\pi^2} \vec{Q}'$$

$$\vec{W}_{31}^b = F(\vec{Q}^2) \frac{\vec{\sigma}_1 \cdot \vec{Q}}{\vec{Q}^2 + m_\pi^2} \vec{Q} \quad (\text{C.5})$$

$$W_{23}^c = F(\vec{Q}'^2) \frac{\vec{\sigma}_2 \cdot \vec{Q}'}{\vec{Q}'^2 + m_\pi^2} \vec{Q}'^2$$

$$W_{31}^c = F(\vec{Q}^2) \frac{\vec{\sigma}_1 \cdot \vec{Q}}{\vec{Q}^2 + m_\pi^2} \vec{Q}^2 \quad (\text{C.6})$$

$$\vec{W}_{23}^d = F(\vec{Q}'^2) \frac{\vec{\sigma}_2 \cdot \vec{Q}'}{\vec{Q}'^2 + m_\pi^2} \vec{\sigma}_3 \times \vec{Q}' \quad (\text{C.7})$$

with the momentum transfers (as indicated in Fig. C.1)

$$\vec{Q} = \vec{k}_1 - \vec{k}_1'$$

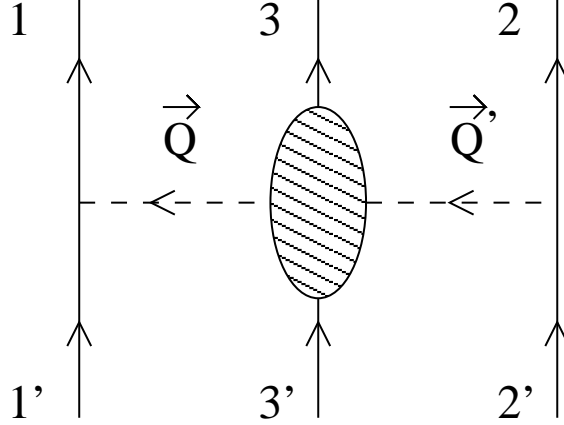


Figure C.1: Symbolic representation of a 3NF like the TM force and the definition of the momentum transfers  $\vec{Q}$  and  $\vec{Q}'$  within the two subsystems

$$\vec{Q}' = \vec{k}_2' - \vec{k}_2 \quad (\text{C.8})$$

$\sigma_i$  are Pauli spin matrices and the form factors  $F$  are chosen to be monopole ones

$$F(\vec{Q}^2) = \frac{\Lambda^2 - m_\pi^2}{\Lambda^2 + \vec{Q}^2} \quad (\text{C.9})$$

In Chapter 4 we investigate the dependence of the triton binding energy on the cut-off parameter  $\Lambda$  and use it to adjust the binding energy to the experimental one.

The momentum space matrix elements of the different terms in Eq. (C.3) have got the form

$$\langle \vec{k}_1 \vec{k}_2 \vec{k}_3 | V_{123}^{(3)} | \vec{k}_1' \vec{k}_2' \vec{k}_3' \rangle = f(\vec{k}_1 - \vec{k}_1') h(\vec{k}_2' - \vec{k}_2) \delta(\vec{k}_1 + \vec{k}_2 + \vec{k}_3 - \vec{k}_1' - \vec{k}_2' - \vec{k}_3') \quad (\text{C.10})$$

Because we can replace the momentum conserving  $\delta$ -function by the integral

$$\int d^3 k_1'' d^3 k_2'' d^3 k_3'' \delta(\vec{k}_1 - \vec{k}_1'') \delta(\vec{k}_2 + \vec{k}_3 - \vec{k}_2'' - \vec{k}_3'') \delta(\vec{k}_2' - \vec{k}_2'') \delta(\vec{k}_1' + \vec{k}_3' - \vec{k}_1'' - \vec{k}_3'') \quad (\text{C.11})$$

We can express Eq. (C.10) as

$$\begin{aligned} & \langle \vec{k}_1 \vec{k}_2 \vec{k}_3 | V_{123}^{(3)} | \vec{k}_1' \vec{k}_2' \vec{k}_3' \rangle \\ &= \int d^3 k_1'' d^3 k_2'' d^3 k_3'' \\ & \quad \delta(\vec{k}_1 - \vec{k}_1'') \delta(\vec{k}_2 + \vec{k}_3 - \vec{k}_2'' - \vec{k}_3'') h(\vec{k}_2'' - \vec{k}_2) \\ & \quad \delta(\vec{k}_2' - \vec{k}_2'') \delta(\vec{k}_1' + \vec{k}_3' - \vec{k}_1'' - \vec{k}_3'') f(\vec{k}_1'' - \vec{k}_1') \\ &\equiv \int d^3 k_1'' d^3 k_2'' d^3 k_3'' \\ & \quad \langle \vec{k}_1 \vec{k}_2 \vec{k}_3 | W_{23} | \vec{k}_1'' \vec{k}_2'' \vec{k}_3'' \rangle \langle \vec{k}_1'' \vec{k}_2'' \vec{k}_3'' | W_{31} | \vec{k}_1' \vec{k}_2' \vec{k}_3' \rangle \end{aligned} \quad (\text{C.12})$$

In this manner we rewrite the 3NF as a consecutive application of NN-like interactions.

In Eq. (C.3) we have already chosen a form which suggests to separate the application of the  $W$ 's and to introduce intermediate states between  $W_{23}$  and  $W_{31}$ . The  $W_{ij}$ 's are operators, which only act on the two particles of the subsystem ( $ij$ ). The third and fourth particle are not affected. In this sense the  $W$ 's are NN interactions. But there are important differences, which are caused by the simple fact that a 3NF is not a consecutive application of NN forces. The common scalar factor  $F(\vec{Q}^2) \frac{\vec{\sigma}_2 \cdot \vec{Q}}{Q^2 + m_\pi^2}$  is odd in the momentum  $\vec{Q}$ . This implies that  $W^a$  and  $W^c$  change the parity. Only the application of both  $W$ 's guarantees the conservation of parity in the TM force. The  $b$ - and  $d$ -operators conserve the parity, but they are vector operators and violate angular momentum conservation. The conservation of the angular momentum is only restored by the application of the second vector potential. Moreover all  $W$ 's are non-symmetric with respect to the interchange of the two particles of the subsystem. Therefore their application necessarily introduces fermion states which are "unphysically" symmetric.

With this important insights in mind, we are ready to compose the TM force from these parts. Applied to a state vector  $\psi$  all four terms have got the form

$$\psi' \sim W_{23} I W_{31} \psi \quad (\text{C.13})$$

where we abbreviated the isospin operators by  $I$ .

We introduce coordinates which are natural for the  $W$  potentials and single out the same subsystem like  $W$ . In this coordinates the matrix elements of  $W$  are very simple. They conserve the momentum and the quantum numbers of the outer particle. The numerical application of this block diagonal structure can quickly be performed. Unfortunately the natural coordinates of  $W_{23}$  and  $W_{31}$  are different. A transformation is required. In this step the three-body character of the force enters. We recognize a structure, which is very similar to the type A transformations derived in Section 2.3. Additionally we need a second transformation, because the full expression is required in (12)3, 4 coordinates in Eq. (2.35). Eq. (C.13) turns into

$$\begin{aligned} \langle (12)3, 4 | \psi' \rangle &\sim \langle (12)3, 4 | (23)1, 4' \rangle \langle (23)1, 4' | W_{23} | (23)1, 4'' \rangle \\ &\langle (23)1, 4'' | I | (31)2, 4''' \rangle \langle (31)2, 4''' | W_{31} | (31)2, 4^* \rangle \langle (31)2, 4^* | \psi \rangle \end{aligned} \quad (\text{C.14})$$

We omitted the integrals and sums over momenta and quantum numbers of the intermediate states to simplify the expressions.  $\psi$  originally enters in (12)3, 4 coordinates. But because of the antisymmetry of  $\psi$  in the (123) subsystem, the (31)2, 4 coordinates are equivalent here. In the following we carefully analyze the part of the Hilbert space, which must be considered in the sums over the intermediate states. The incoming state  $\psi$  has got a fixed four-body total angular momentum and parity,  $J_0^{\pi_0}$ , and is antisymmetric in the subsystem (12). This restricts the quantum numbers of the \*-states. This restriction has to be loosed for the '''-states. First of all the unphysical symmetric states also enter, because of the unsymmetric  $W$ . Depending on the  $W_{31}$ , states with the opposite parity or with total angular momenta  $J = |J - 1|, \dots, J + 1$  contribute. The known expressions for transformation matrix elements are also valid for these quantum numbers. The isospin transformation is replaced by the combined transformation and isospin matrix derived in Ref. [82]. The form of this operators are summarized in the next section. Because the total angular momentum and parity is conserved by transformations, the same states contribute to the ''-sum.

With the knowledge that the complete  $V_{123}^{(3)}$  conserves angular momentum and parity and is symmetric within the (12) subsystem, one concludes that the outgoing states are antisymmetric in (12) and are restricted to  $J_0^{\pi_0}$ . Because we only applied one of the three parts of Eq. (C.1), the antisymmetry with

respect to the third particle is destroyed. This carries over to the  $'$ -states. They have the same angular momentum and parity, but the antisymmetry of the (23) subsystem is not insured.

From the decomposition Eq. (C.14) of the TM force one easily reads off the four necessary steps for an application of the 3NF:

- 1) We apply the NN-like interaction  $W_{31}$  to the incoming state  $\psi$  and create the intermediate state  $\psi'$ . To its partial wave decomposition the unphysical partial waves with changed angular momentum or parity also contribute. This step only requires a minor part of the numerical effort.
- 2) The transformation to (23)1,4-states involves all quantum numbers and momenta of the (123) subsystem. This is the most CPU-time consuming part.
- 3) Similarly to 1), we apply the  $W_{23}$  to the result of the transformation. Actually, we can restrict the result to states with physical parity and angular momentum, but we have to take the symmetric partial waves into account.
- 4) The last step transforms the result to the desired (12)3,4 coordinates. This is again a time-consuming real three-body operation. The result only contains the physical partial waves.

Each of the four steps results in a four-body state vector. The 3NF is never generated in a closed form. This is the main difference to the algorithm described in Ref. [82] where the full three-body operator is calculated first and then applied to the state vectors.

The new algorithm requires only the preparation of NN-like interactions. These interactions need only a tiny storage compared to a full matrix of the three-nucleon subsystem. The three-body structures are the well known coordinate transformations. As described in Section 2.3, they can be put together from a quite small geometrical, momentum independent  $g$  function and polynomials in the momenta. Therefore the memory requirements are also much smaller than for a full 3NF matrix.

In the next section we briefly summarize the results of [82] for the NN-like matrix elements and generalize them to the four-body system.

## C.2 Explicit form of the TM NN-like potentials

In this section we will give the results for the partial wave decomposition of the NN-like potentials. The derivation of the matrix elements has been performed in Ref. [82]. In the following we generalize the expressions to four-body states.

### C.2.1 $a$ -term and $c$ -term

These are the more simple terms, because the NN-like interaction are pseudoscalar operators. In the same way as shown in Ref. [82] one finds in the case of the four-body system

$$\begin{aligned}
& \langle (31)2, 4 | W_{31}^a | (31)2, 4' \rangle \\
&= \frac{\delta(q_4 - q_4')}{q_4 q_4'} \frac{\delta(p_2 - p_2')}{p_2 p_2'} \delta_{I_4 I_4'} \delta_{I_2 I_2'} \delta_{l_4 l_4'} \delta_{l_2 l_2'} \delta_{J J'} \delta_{M M'} \delta_{j_3 j_3'} \delta_{j_{31} j_{31}'} \delta_{|l_{31} - l_{31}'|, 1} \\
& 2\pi\sqrt{6} (-)^{j_{31} + 1 + \max(l_{31}, l_{31}')} \sqrt{\hat{s}_{31} \hat{s}_{31}'} \left\{ \begin{array}{ccc} \frac{1}{2} & \frac{1}{2} & s_{31}' \\ 1 & s_{31} & \frac{1}{2} \end{array} \right\} \left\{ \begin{array}{ccc} l_{31}' & s_{31}' & j_{31}' \\ s_{31} & l_{31} & 1 \end{array} \right\}
\end{aligned}$$

$$\sqrt{\max(l_{31}, l'_{31})} (p_{31} H_{l'_{31}}(p_{31}, p'_{31}) - p'_{31} H_{l_{31}}(p_{31}, p'_{31})) \quad (\text{C.15})$$

The operator has no isospin dependence, therefore it is diagonal in isospin space. The momentum dependence is given in terms of the function  $H$ , which is a combination of Legendre polynomials of the second kind  $Q_l$  and their derivatives  $Q'_l$ .

$$H_l(p, p') = \frac{1}{pp'} (Q_l(B_{m_\pi}) - Q_l(B_\Lambda)) + \frac{\Lambda^2 - m_\pi^2}{2(pp')^2} Q'_l(B_\Lambda) \quad (\text{C.16})$$

with

$$B_{m_\pi} = \frac{p^2 + p'^2 + m_\pi^2}{2pp'} \quad (\text{C.17})$$

and

$$B_\Lambda = \frac{p^2 + p'^2 + \Lambda^2}{2pp'} \quad (\text{C.18})$$

The  $c$ -term looks very similar and follows, if one replaces  $H$  by

$$\tilde{H}_l(p, p') = -\frac{m_\pi^2}{2pp'} (Q_l(B_{m_\pi}) - Q_l(B_\Lambda)) + \frac{\Lambda^2 - m_\pi^2}{2(pp')^2} \Lambda^2 Q'_l(B_\Lambda) \quad (\text{C.19})$$

For our convenience, we used the abbreviation  $\hat{k} = 2k + 1$  here.

Because the  $W_{23}$ - and  $W_{31}$ -operators are equivalent up to a renumbering of the particles, the matrix elements are equal up to a phase factor

Please note here the direction of the transferred momenta in Fig. C.1. Without partial wave decomposition, the momentum transfer operators read in (12)3, 4 coordinates

$$\begin{aligned} \langle (12)3, 4 | \vec{Q} | (12)3, 4' \rangle &= (\vec{p}_{12} - \vec{p}'_{12} - \frac{1}{2}(\vec{p}_3 - \vec{p}'_3))\delta(\vec{p}_{12} - \vec{p}'_{12}) + \frac{1}{2}(\vec{p}_3 - \vec{p}'_3)\delta(\vec{q}'_4 - \vec{q}_4) \\ \langle (12)3, 4 | \vec{Q}' | (12)3, 4' \rangle &= (\vec{p}_{12} - \vec{p}'_{12} + \frac{1}{2}(\vec{p}_3 - \vec{p}'_3))\delta(\vec{p}_{12} - \vec{p}'_{12}) - \frac{1}{2}(\vec{p}_3 - \vec{p}'_3)\delta(\vec{q}'_4 - \vec{q}_4) \end{aligned} \quad (\text{C.20})$$

Because  $P_{12}$  changes the sign of the subsystem momentum  $\vec{p}_{12}$ , the sign of the momentum transfer operator also changes

$$\vec{Q}' = -P_{12} \vec{Q} P_{12} \quad (\text{C.21})$$

This carries over to the  $W$ 's of the  $a$ - and  $c$ -term, because they have an odd number of  $\vec{Q}$ 's. One finds

$$\begin{aligned} \langle (23)1, 4 | W_{23}^{a,c} | (23)1, 4' \rangle &= -\langle (23)1, 4 | P_{12} W_{31}^{a,c} P_{12} | (23)1, 4' \rangle \\ &= -\langle (13)2, 4 | W_{31}^{a,c} | (13)2, 4' \rangle \\ &= (-)^{(31)+(31)'+1} \langle (31)2, 4 | W_{31}^{a,c} | (31)2, 4' \rangle \end{aligned} \quad (\text{C.22})$$

As we already mentioned, we replace the simple isospin transformation matrix element as given in Eq. (A.14) by a combination of the transformation and the isospin operator, which has already been given in Ref. [82]

$$\langle (23)1, 4 | \vec{\tau}_1 \cdot \vec{\tau}_2 | (31)2, 4' \rangle = \delta_{TT'} \delta_{M_T M'_T} \delta_{\tau\tau'} (-6) (-)^{t_{23}} \sqrt{\hat{t}_{23} \hat{t}'_{31}} \begin{Bmatrix} \frac{1}{2} & \frac{1}{2} & t'_{31} \\ \frac{1}{2} & 1 & \frac{1}{2} \\ t_{23} & \frac{1}{2} & \tau \end{Bmatrix} \quad (\text{C.23})$$

### C.2.2 $b$ -term and $d$ -term

These terms are a little bit more complicated, because the NN-like potentials are vector operators now. We define the spherical components of the operators as

$$\begin{aligned} W^1 &= -\frac{1}{\sqrt{2}} (W^x + iW^y) \\ W^0 &= W^z \\ W^{-1} &= \frac{1}{\sqrt{2}} (W^x - iW^y) \end{aligned} \quad (\text{C.24})$$

and use the Wigner-Eckart theorem to separate the matrix element into a Clebsch-Gordan coefficient and a reduced matrix element

$$\langle (31)2, 4 || W_{31}^\mu || (31)2, 4' \rangle = (J'1J, M'\mu M) \langle (31)2, 4 || W_{31} || (31)2, 4' \rangle \quad (\text{C.25})$$

In this form one easily finds that only the reduced matrix elements are important for the application of the NN-like potentials. The scalar product in spherical coordinates reads

$$\vec{W}_{23} \cdot \vec{W}_{31} = \sum_{\mu} (-)^{\mu} W_{23}^{\mu} W_{31}^{-\mu} \quad (\text{C.26})$$

There is no dependence on the third component of the total angular momentum, neither in the transformation matrix elements nor in the incoming state. The application of  $W$  introduces such a dependence, but fortunately this is analytically given by the Clebsch-Gordan coefficients. The transformation from  $(31)2, 4$  to  $(23)1, 4$  coordinates in Eq. (C.14) is diagonal in  $M'''$ . Therefore the double sum over  $\sum_{M''', M''}$  reduces to  $\sum_{M''}$ . Together with the sum over  $\mu$  one obtains

$$\sum_{M''\mu} (-)^{\mu} (J''1J', M''\mu M') (J^*1J'', M^* - \mu M'') = \delta_{J'J^*} \delta_{M'M^*} \sqrt{\frac{\hat{J}''}{\hat{J}'}} (-)^{J''-J'} \quad (\text{C.27})$$

We recover the conservation of the total angular momentum. Additionally we could perform the sums over the third components resulting in a simple factor  $\sqrt{\frac{\hat{J}''}{\hat{J}'}} (-)^{J''-J'}$  and see that the application of the NN-like potentials effectively only requires the application of the reduced matrix elements. The intermediate states are also not  $M$  dependent.

The generalization of the formulas given in Ref. [82] to the four-nucleon system reads

$$\begin{aligned} &\langle (31)2, 4 || W_{31}^b || (31)2, 4 \rangle' \\ &= \frac{\delta(q_4 - q_4')}{q_4 q_4'} \frac{\delta(p_2 - p_2')}{p_2 p_2'} \delta_{I_4 I_4'} \delta_{I_2 I_2'} \delta_{l_4 l_4'} \delta_{l_2 l_2'} (-)^{J'+j_3'+j_3+I_4+I_2+s_{31}+s_{31}'} \sqrt{\hat{J}' \hat{j}_3' \hat{j}_3 \hat{s}_{31}' \hat{s}_{31} \hat{j}_{31}' \hat{j}_{31}} \\ &\quad \left\{ \begin{matrix} j_3' & 1 & j_3 \\ J & I_4 & J' \end{matrix} \right\} \left\{ \begin{matrix} 1 & j_{31} & j_{31}' \\ I_2 & j_3' & j_3 \end{matrix} \right\} \left\{ \begin{matrix} \frac{1}{2} & \frac{1}{2} & s_{31} \\ 1 & s_{31}' & \frac{1}{2} \end{matrix} \right\} \\ &\quad \times \left[ \delta_{l_{31} l_{31}'} \frac{2\pi}{3} \sqrt{6} (-)^{l_{31}+1} \left\{ \begin{matrix} j_{31}' & j_{31} & 1 \\ s_{31} & s_{31}' & l_{31} \end{matrix} \right\} \tilde{H}_{l_{31}}(p_{31} p_{31}') \right. \\ &\quad \left. - 40\pi \sqrt{6} (-)^{s_{31}'+j_{31}} \left\{ \begin{matrix} 2 & 1 & 1 \\ l_{31} & s_{31} & j_{31} \\ l_{31}' & s_{31}' & j_{31}' \end{matrix} \right\} \sum_{\bar{l}} \tilde{H}_{\bar{l}}(p_{31} p_{31}') \right] \end{aligned}$$



$$\times \sum_{a+b=2} \frac{p_{31}^a p_3^b}{\sqrt{(2a)!(2b)!}} \left\{ \begin{matrix} b & a & 2 \\ l'_{31} & l_{31} & \bar{l} \end{matrix} \right\} (a \bar{l} l'_{31}, 00) (b \bar{l} l_{31}, 00) \quad (C.28)$$

and

$$\begin{aligned} & \langle (23)1, 4 || W_{23}^d || (23)1, 4 \rangle' \\ &= \frac{\delta(q_4 - q'_4)}{q_4 q'_4} \frac{\delta(p_1 - p'_1)}{p_1 p'_1} \delta_{I_4 I'_4} \delta_{I_1 I'_1} \delta_{l_4 l'_4} \delta_{l_1 l'_1} (-)^{J'+j'_3+j_3+I_4+I_1+s_{23}+s'_{23}+1} \sqrt{\hat{J}' \hat{j}'_3 \hat{j}_3 \hat{s}'_{23} \hat{s}_{23} \hat{j}'_{23} \hat{j}_{23}} \\ & \quad \left\{ \begin{matrix} j'_3 & 1 & j_3 \\ J & I_4 & J' \end{matrix} \right\} \left\{ \begin{matrix} 1 & j_{23} & j'_{23} \\ I_1 & j'_3 & j_3 \end{matrix} \right\} \\ & \times \left[ \delta_{l_{23} l'_{23}} i 4\pi \sqrt{6} (-)^{l_{23}+s_{23}} \left\{ \begin{matrix} l_{23} & s_{23} & j_{23} \\ 1 & j'_{23} & s'_{23} \end{matrix} \right\} \left\{ \begin{matrix} 1 & 1 & 1 \\ \frac{1}{2} & \frac{1}{2} & s'_{23} \\ \frac{1}{2} & \frac{1}{2} & s_{23} \end{matrix} \right\} \tilde{H}_{l_{23}}(p_{23} p'_{23}) \right. \\ & \quad \left. + i 240\pi \sqrt{6} (-)^{j'_{23}} \sum_{\chi} (-)^{\chi} \hat{\chi} \left\{ \begin{matrix} 2 & \chi & 1 \\ 1 & 1 & 1 \end{matrix} \right\} \left\{ \begin{matrix} 2 & \chi & 1 \\ l'_{23} & s'_{23} & j'_{23} \\ l_{23} & s_{23} & j_{23} \end{matrix} \right\} \left\{ \begin{matrix} 1 & 1 & \chi \\ \frac{1}{2} & \frac{1}{2} & s'_{23} \\ \frac{1}{2} & \frac{1}{2} & s_{23} \end{matrix} \right\} \right] \\ & \times \sum_{\bar{l}} \hat{l} H_{\bar{l}}(p_{23} p'_{23}) \sum_{a+b=2} \frac{p_{23}^a p_{23}^b}{\sqrt{(2a)!(2b)!}} \left\{ \begin{matrix} b & a & 2 \\ l'_{23} & l_{23} & \bar{l} \end{matrix} \right\} (a \bar{l} l'_{23}, 00) (b \bar{l} l_{23}, 00) \quad (C.29) \end{aligned}$$

The momentum dependent functions  $H$  and  $\tilde{H}$  are given in Eqs. (C.16) and (C.19).

As outlined in Eq. (C.22) there is a simple phase relation between the  $W_{23}^b$  and  $W_{31}^b$ . The corresponding expressions for  $W^b$  differ by a minus sign from Eq. (C.22), because the number of  $\bar{Q}$ 's is even now

$$\langle (23)1, 4 || W_{23}^{b,d} || (23)1, 4' \rangle = (-)^{(31)+(31)'} \langle (31)2, 4 || W_{31}^{b,d} || (31)2, 4' \rangle \quad (C.30)$$

The isospin matrix element of the  $d$ -term differs from the one for the  $a$ -,  $b$ - and  $c$ -term given in Eq. (C.23). It reads

$$\begin{aligned} \langle (23)1, 4 || \vec{\tau}_3 \cdot (\vec{\tau}_1 \times \tau_3) || (31)2, 4' \rangle &= \delta_{TT'} \delta_{M_T M'_T} \delta_{\tau\tau'} 24i (-)^{2\tau} \sqrt{\hat{t}_{23} \hat{t}'_{31}} \\ & \sum_{\lambda} (-)^{3\lambda+\frac{1}{2}} \left\{ \begin{matrix} \lambda & \frac{1}{2} & 1 \\ \frac{1}{2} & \frac{1}{2} & t_{23} \end{matrix} \right\} \left\{ \begin{matrix} \tau & \frac{1}{2} & t_{23} \\ \frac{1}{2} & 1 & \lambda \\ t'_{31} & \frac{1}{2} & \frac{1}{2} \end{matrix} \right\} \quad (C.31) \end{aligned}$$

Because many 3NF models are based on a  $2\pi$ -exchange, they have got a similar form as the TM force and can be separated in two NN-like interactions. The scheme which we described above is easily extendible to this kind of forces. We exemplify this in the next section in the case of the Urbana 3NF.

### C.3 Passage to the Urbana 3NF

The Urbana 3NF model is based on the  $2\pi$  exchange mechanism with an intermediate  $\Delta$  excitation originally proposed in Ref. [16]. It is supplemented by a purely phenomenological repulsive short range part. Both parts are adjusted in conjunction with a NN interaction to the experimental  ${}^3\text{H}$  binding energy and the nuclear matter density. The most recent parameter set fits to the AV18 NN interaction and defines the Urbana IX model [17].

Usually one expresses the Urbana interaction in terms of a commutator and anticommutator part. This reads

$$V_{123}^{(3)} = A_{2\pi} [ \{X_{23}, X_{31}\} \{ \vec{\tau}_2 \cdot \vec{\tau}_3, \vec{\tau}_3 \cdot \vec{\tau}_1 \} + \frac{1}{4} [X_{23}, X_{31}] [ \vec{\tau}_2 \cdot \vec{\tau}_3, \vec{\tau}_3 \cdot \vec{\tau}_1 ] ] + U_0 T_\pi^2(r_{23}) T_\pi^2(r_{31}) \quad (\text{C.32})$$

The force is explicitly defined in terms of NN interactions

$$X_{ij} = Y_\pi(r_{ij}) \vec{\sigma}_i \cdot \vec{\sigma}_j + T_\pi(r_{ij}) S_{ij} \quad (\text{C.33})$$

$X_{ij}$  is derived from the  $\pi$  exchange NN force. Therefore it has got a spin-spin part  $\vec{\sigma}_i \cdot \vec{\sigma}_j$  and a tensor part

$$S_{ij} = 3 \vec{\sigma}_i \cdot \hat{r}_i \vec{\sigma}_j \cdot \hat{r}_j - \vec{\sigma}_i \cdot \vec{\sigma}_j \quad (\text{C.34})$$

The radial dependence is given as

$$Y_\pi(r) = \frac{e^{-m_\pi r}}{m_\pi r} (1 - e^{-cr^2})$$

$$T_\pi(r) = \left[ 1 + \frac{3}{m_\pi r} + \frac{3}{(m_\pi r)^2} \right] \frac{e^{-m_\pi r}}{m_\pi r} (1 - e^{-cr^2})^2 \quad (\text{C.35})$$

For the Urbana IX model, which is used in this thesis, the parameters are given as  $A_{2\pi} = -0.0293$  MeV,  $U_0 = 0.0048$  MeV and  $c = 2.1 \text{ fm}^{-2}$  [17].

From the commutator and anticommutator terms it is clear that  $V_{123}^{(3)}$  is symmetrical with respect to an interchange of particles 1 and 2. In the following we would like to derive a form corresponding to Eq. (C.14). Because of the partial wave decomposition we can control the symmetry of the inner subsystem with means of the phases  $(-)^{(ij)}$ . It turns out that we can simplify the interaction in our notation [22].

First we dissolve the commutators and anticommutators. The isospin parts are very similar to the TM ones

$$\begin{aligned} \{ \vec{\tau}_2 \cdot \vec{\tau}_3, \vec{\tau}_3 \cdot \vec{\tau}_1 \} &= 2 \vec{\tau}_1 \cdot \vec{\tau}_2 \\ [ \vec{\tau}_2 \cdot \vec{\tau}_3, \vec{\tau}_3 \cdot \vec{\tau}_1 ] &= -2i \vec{\tau}_3 \cdot \vec{\tau}_1 \times \vec{\tau}_2 \end{aligned} \quad (\text{C.36})$$

We define two isospin operators

$$\begin{aligned} I^- &\equiv 2(\vec{\tau}_1 \cdot \vec{\tau}_2 - \frac{i}{4} \vec{\tau}_3 \cdot \vec{\tau}_1 \times \vec{\tau}_2) \\ I^+ &\equiv 2(\vec{\tau}_1 \cdot \vec{\tau}_2 + \frac{i}{4} \vec{\tau}_3 \cdot \vec{\tau}_1 \times \vec{\tau}_2) \end{aligned} \quad (\text{C.37})$$

and obtain the shorter notation

$$V_{123}^{(3)} = A_{2\pi} I^- X_{23} X_{31} + A_{2\pi} I^+ X_{31} X_{23} + U_0 T_\pi^2(r_{31}) T_\pi^2(r_{23}) \quad (\text{C.38})$$

Because the NN-like interactions in the first two terms occur in a different sequence, we have to introduce different intermediate states. Eq. (C.14) turns for the first term into

$$\langle (12)3, 4 | \psi' \rangle \sim \langle (12)3, 4 | (23)1, 4' \rangle \langle (23)1, 4' | X_{23} | (23)1, 4'' \rangle$$

$$\langle (23)1, 4'' | I^- | (31)2, 4''' \rangle = \langle (31)2, 4''' | X_{31} | (31)2, 4^* \rangle = \langle (31)2, 4^* | \psi \rangle \quad (\text{C.39})$$

and for the second one into

$$\begin{aligned} \langle (12)3, 4 | \psi' \rangle &\sim \langle (12)3, 4 | (31)2, 4' \rangle = \langle (31)2, 4' | X_{31} | (31)2, 4'' \rangle \\ &\langle (31)2, 4'' | I^+ | (23)1, 4''' \rangle = \langle (23)1, 4''' | X_{23} | (23)1, 4^* \rangle = \langle (23)1, 4^* | \psi \rangle \end{aligned} \quad (\text{C.40})$$

In both terms the matrix elements agree up to a renumbering of the particles and some phase factors. For example, we find the  $I^+$  matrix element by renumbering

$$\begin{aligned} \langle (31)2, 4'' | I^+ | (23)1, 4''' \rangle &= \langle (31)2, 4'' | 2(\vec{\tau}_1 \cdot \vec{\tau}_2 + \frac{i}{4} \vec{\tau}_3 \cdot \vec{\tau}_1 \times \vec{\tau}_2) | (23)1, 4''' \rangle \\ &= \langle (32)1, 4'' | 2(\vec{\tau}_2 \cdot \vec{\tau}_1 + \frac{i}{4} \vec{\tau}_3 \cdot \vec{\tau}_2 \times \vec{\tau}_1) | (13)2, 4''' \rangle \end{aligned} \quad (\text{C.41})$$

The first isospin operator is symmetric in (12), whereas the second one is antisymmetric. Together with the phase factors for the interchange within the subsystems, the matrix element turns into the one for  $I^-$

$$\langle (31)2, 4'' | I^+ | (23)1, 4''' \rangle = (-)^{(23)'' + (31)'''} \langle (23)1, 4'' | I^- | (31)2, 4''' \rangle \quad (\text{C.42})$$

In a similar manner the cyclic and anticyclic transformations are connected. The matrix elements for  $X_{ij}$  are equal, and, moreover, they conserve the symmetry of the subsystems, because the NN-like potentials are symmetric in the case of the Urbana force. Therefore both considered terms are equal up to a phase factor, which only depends on the incoming and outgoing quantum numbers. The sum of both terms results in

$$\begin{aligned} \langle (12)3, 4 | \psi' \rangle &\sim \left( 1 + (-)^{(12) + (31)^*} \right) \langle (12)3, 4 | (23)1, 4' \rangle = \langle (23)1, 4' | X_{23} | (23)1, 4'' \rangle \\ &\langle (23)1, 4'' | I^- | (31)2, 4''' \rangle = \langle (31)2, 4''' | X_{31} | (31)2, 4^* \rangle = \langle (31)2, 4^* | \psi \rangle \end{aligned} \quad (\text{C.43})$$

In the phase factor one recovers the symmetry conservation of the (12) subsystem of  $V_{123}^{(3)}$ . We restrict the result to physical states and replace the phase factor by 2. Together with the repulsive part, the Urbana force reads explicitly

$$\begin{aligned} \langle (12)3, 4 | \psi' \rangle &= 2A_{2\pi} \langle (12)3, 4 | (23)1, 4' \rangle = \langle (23)1, 4' | X_{23} | (23)1, 4'' \rangle \\ &\langle (23)1, 4'' | I^- | (31)2, 4''' \rangle = \langle (31)2, 4''' | X_{31} | (31)2, 4^* \rangle = \langle (31)2, 4^* | \psi \rangle \\ &+ U_0 \langle (12)3, 4 | (23)1, 4' \rangle = \langle (23)1, 4' | T_\pi^2(r_{23}) | (23)1, 4'' \rangle \\ &\langle (23)1, 4'' | (31)2, 4''' \rangle = \langle (31)2, 4''' | T_\pi^2(r_{31}) | (31)2, 4^* \rangle = \langle (31)2, 4^* | \psi \rangle \end{aligned} \quad (\text{C.44})$$

Because the NN-like interactions are very simple, the sums include only states with the physical parity and angular momentum. The interactions conserve the symmetry of the subsystem, but, nevertheless, the coordinate transformations introduce unphysically symmetric fermion states in the sums for '' and '''. In the next section we briefly summarize the potential matrix elements.

## C.4 Explicit form of the Urbana-IX NN-like potentials

In this section we briefly summarize the matrix elements of the NN-like interactions  $X_{31}$  and  $T_\pi^2(r_{31})$ . The isospin operators are a combination of Eqs. (C.23) and (C.31) and are not given here.

$X_{31}$  has got the structure of a simplified NN potential. Only the spin-spin and tensor parts of the interaction are non-zero. It is defined in Eq. (C.33) in configuration space and has to be Fourier transformed to obtain the matrix elements in momentum space. The result is

$$\begin{aligned}
& \langle (31)2, 4 | X_{31} | (31)2, 4' \rangle \\
&= \frac{\delta(q_4 - q'_4)}{q_4 q'_4} \frac{\delta(p_2 - p'_2)}{p_2 p'_2} \delta_{I_4 I'_4} \delta_{I_2 I'_2} \delta_{l_4 l'_4} \delta_{l_2 l'_2} \delta_{JJ'} \delta_{MM'} \delta_{j_{31} j'_{31}} \\
& \left[ \tilde{Y}_{l_{31}}(p_{31} p'_{31}) \delta_{l_{31} l'_{31}} \delta_{s_{31} s'_{31}} (-1 + 4s_{31}) + \tilde{T}_{l_{31} l'_{31}}(p_{31} p'_{31}) \delta_{s_{31} s'_{31}} \delta_{s_{31} 1} S_{l_{31} l'_{31} j_{31}} \right] \quad (C.45)
\end{aligned}$$

The tensor operator can be expressed in simple rational functions of the quantum numbers

$$\begin{aligned}
S_{l_{31} l'_{31} j_{31}} = & \begin{matrix} l_{31} = j_{31} - 1 \\ l_{31} = j_{31} \\ l_{31} = j_{31} + 1 \end{matrix} \begin{bmatrix} -2 \frac{j_{31}+2}{2j_{31}+1} & 0 & 6 \frac{\sqrt{j_{31}(j_{31}+1)}}{2j_{31}+1} \\ 0 & 2 & 0 \\ 6 \frac{\sqrt{j_{31}(j_{31}+1)}}{2j_{31}+1} & 0 & -2 \frac{j_{31}-1}{2j_{31}+1} \end{bmatrix} \quad (C.46) \\
& l'_{31} = j_{31} - 1 \quad l'_{31} = j_{31} \quad l'_{31} = j_{31} + 1
\end{aligned}$$

We numerically perform the Fourier transformations

$$\begin{aligned}
\tilde{Y}_{l_{31}}(p_{31} p'_{31}) &= \frac{2}{\pi} \int_0^\infty dr r^2 j_{l_{31}}(p_{31} r) T_\pi(r) j_{l_{31}}(p'_{31} r) \\
\tilde{T}_{l_{31} l'_{31}}(p_{31} p'_{31}) &= (-)^{l_{31}-l'_{31}} \frac{2}{\pi} \int_0^\infty dr r^2 j_{l_{31}}(p_{31} r) T_\pi(r) j_{l'_{31}}(p'_{31} r) \quad (C.47)
\end{aligned}$$

with the usual spherical Bessel functions  $j_l(x)$ .

The short range NN-interactions of the second term are not spin and angular dependent. Their matrix elements are diagonal in the quantum numbers

$$\begin{aligned}
& \langle (31)2, 4 | T_\pi^2(r_{31}) | (31)2, 4' \rangle \\
&= \frac{\delta(q_4 - q'_4)}{q_4 q'_4} \frac{\delta(p_2 - p'_2)}{p_2 p'_2} \delta_{I_4 I'_4} \delta_{I_2 I'_2} \delta_{l_4 l'_4} \delta_{l_2 l'_2} \delta_{JJ'} \delta_{MM'} \delta_{j_{31} j'_{31}} \delta_{l_{31} l'_{31}} \delta_{s_{31} s'_{31}} \bar{T}_{l_{31}}(p_{31} p'_{31}) \quad (C.48)
\end{aligned}$$

with the Fourier transformed potential

$$\bar{T}_{l_{31}}(p_{31} p'_{31}) = \frac{2}{\pi} \int_0^\infty dr r^2 j_{l_{31}}(p_{31} r) T_\pi^2(r) j_{l_{31}}(p'_{31} r) \quad (C.49)$$

Because these NN-like interactions are all symmetric with respect to an interchange of the subsystem particles, the matrix elements for the  $X_{23}$  and  $T^2(r_{23})$  equal those for  $X_{31}$  and  $T^2(r_{31})$ .

This concludes our summary of the NN-like interactions of Urbana IX. The described technique has successfully been applied to the 3N and 4N bound systems. The results and insights are described in Chapter 4. Using the given NN-like interactions the method of [82] has been generalized to the Urbana force. In this form it has been used in the 3N continuum to identify observables, which are sensitive to the spin structure of the 3NF [22].

# Appendix D

## The calculation of the wave function in different Jacobi coordinates

In contrast to the YC's, there are no "natural" coordinates for the wave function. Depending on the information one would like to extract, different kinds of Jacobi coordinates are suitable. Moreover, calculations of expectation values of symmetric operators are more accurate, if one replace the expectation value by mixed overlaps between the YC's and the wave function. These calculations require representations of the wave function in all kinds of Jacobi coordinates. Therefore we give explicit expressions for Eq. (2.40) for the  ${}^4_{\Lambda}\text{He}$  nucleus in this appendix. In the second section we simplify the expressions for using them in four-nucleon and three-body systems.

### D.1 The wave function of ${}^4_{\Lambda}\text{He}$ and ${}^4_{\Lambda}\text{H}$

In the following we will motivate explicit formulas for all different representations of the  ${}^4_{\Lambda}\text{He}$  wave function. In an abstract notation the wave function is given in Eq. (2.40). In this notation the necessary coordinate transformations are hidden. We will transform all YC's to the desired representation now. We do this independently for all YC's and try to avoid intermediate states as far as possible.

#### D.1.1 (12)3, 4 coordinates

The first term of Eq. (2.40) is easily performed

$$\begin{aligned} \langle (12)3, 4 | (1 + P) | \psi_{1A} \rangle &= \langle (12)3, 4 | \psi_{1A} \rangle \\ &+ \langle (12)3, 4 | (23)1, 4' \rangle \langle (12)3, 4' | \psi_{1A} \rangle \\ &+ \langle (12)3, 4 | (31)2, 4' \rangle \langle (12)3, 4' | \psi_{1A} \rangle \end{aligned} \quad (\text{D.1})$$

We applied the permutation operators to the right and replaced them by coordinate transformations. To shorten the notation we omitted the sum and integrals over the ' coordinates. By a renumbering of the particles one easily finds a relationship between both coordinate transformations

$$\langle (12)3, 4 | (31)2, 4' \rangle = (-)^{(12)+(23)'} \langle (12)3, 4 | (23)1, 4' \rangle \quad (\text{D.2})$$

which insures the conservation of the antisymmetry of  $\psi_{1A}$  in the (12) subsystem. We restrict ourselves to antisymmetric outgoing states which fixes the phase factor to 1. Consequently

$$\langle (12)3, 4|(1+P)|\psi_{1A} \rangle = \langle (12)3, 4|\psi_{1A} \rangle + 2 \langle (12)3, 4|(23)1, 4' \rangle \langle (12)3, 4'|\psi_{1A} \rangle \quad (\text{D.3})$$

The  $\psi_{1B}$  requires one intermediate step, because the  $P$  operator cannot be expressed in (12)4,3 coordinates. With the help of Eq. (D.2) one obtains

$$\begin{aligned} \langle (12)3, 4|(1+P)|\psi_{1B} \rangle &= \langle (12)3, 4|(12)4, 3' \rangle \langle (12)4, 3'|\psi_{1B} \rangle \\ &\quad + 2 \langle (12)3, 4|(23)1, 4' \rangle \langle (12)3, 4'|(12)4, 3'' \rangle \\ &\quad \langle (12)4, 3''|\psi_{1B} \rangle \end{aligned} \quad (\text{D.4})$$

The corresponding expressions for the  $\psi_{1C}$  component are a little bit more complicated. Because the natural coordinates of this component are (14)2,3. The change to (12)3,4 requires two steps, if one must avoid a simultaneous change of all three momenta. In Eq. (2.40) the term reads  $(1 - P_{12})(1 + P)\psi_{1C}$ . We can again restrict ourselves to antisymmetric (12) subsystems and replace the transposition  $P_{12}$  by  $-1$ .

$$\begin{aligned} &\langle (12)3, 4|(1 - P_{12})(1 + P)|\psi_{1C} \rangle \\ &= 2 \langle (12)3, 4|(14)2, 3' \rangle \langle (14)2, 3'|\psi_{1C} \rangle \\ &\quad + 2 \langle (12)3, 4|(24)3, 1' \rangle \langle (14)2, 3'|\psi_{1C} \rangle \\ &\quad + 2 \langle (12)3, 4|(34)1, 2' \rangle \langle (14)2, 3'|\psi_{1C} \rangle \end{aligned} \quad (\text{D.5})$$

We interchange the numbers of the particles 1 and 2 in the second term. This leads to a phase  $(-1)$  in the outgoing state

$$\begin{aligned} &\langle (12)3, 4|(1 - P_{12})(1 + P)|\psi_{1C} \rangle \\ &= 2 \langle (12)3, 4|(14)2, 3' \rangle \langle (14)2, 3'|\psi_{1C} \rangle \\ &\quad - 2 \langle (12)3, 4|(14)3, 2' \rangle \langle (14)2, 3'|\psi_{1C} \rangle \\ &\quad + 2 \langle (12)3, 4|(34)1, 2' \rangle \langle (14)2, 3'|\psi_{1C} \rangle \end{aligned} \quad (\text{D.6})$$

The combination of the first and the second term is straight forward. But for the third term we choose a transformation to (34)12 coordinates. The numerical experience tells us that the partial wave decomposition of  $\langle (34)12|(34)1, 2' \rangle$  is rather quickly converging, because the two-body subsystem is untouched. Moreover, the exchange of two subsystems in  $\langle (12)34|(34)12' \rangle$  is diagonal in all orbital angular momentum quantum numbers. There is no loss of accuracy in such a step because of the partial wave truncations. Therefore our choice of the final expression reads

$$\begin{aligned} &\langle (12)3, 4|(1 - P_{12})(1 + P)|\psi_{1C} \rangle \\ &= 2 \langle (12)3, 4|(14)2, 3' \rangle \\ &\quad (\langle (14)2, 3'|\psi_{1C} \rangle - \langle (14)2, 3'|(14)3, 2'' \rangle \langle (14)2, 3''|\psi_{1C} \rangle) \\ &\quad + 2 \langle (12)3, 4|(12)34' \rangle \langle (12)34'|(34)12'' \rangle \\ &\quad \langle (34)12''|(34)1, 2''' \rangle \langle (14)2, 3'''|\psi_{1C} \rangle \end{aligned} \quad (\text{D.7})$$

In a similar manner we find expressions for  $(1 + P)\psi_{2A}$  and  $(1 + P)\psi_{2B}$ . The results are

$$\begin{aligned} &\langle (12)3, 4|(1 + P)|\psi_{2A} \rangle \\ &= \langle (12)3, 4|(12)34' \rangle \langle (12)34'|\psi_{2A} \rangle \end{aligned}$$

$$+2 \langle (12)3, 4|(23)1, 4' \rangle \langle (23)1, 4'|(23)14'' \rangle \langle (12)34''|\psi_{2A} \rangle \quad (\text{D.8})$$

and

$$\begin{aligned} & \langle (12)3, 4|(1+P)|\psi_{2B} \rangle \\ & = \langle (12)3, 4|(12)34' \rangle \langle (12)34'|(34)12'' \rangle \langle (34)12''|\psi_{2B} \rangle \\ & \quad + 2 \langle (12)3, 4|(23)1, 4' \rangle \langle (23)1, 4'|(23)14'' \rangle \\ & \quad \quad \langle (23)14''|(14)23''' \rangle \langle (34)12'''|\psi_{2B} \rangle \end{aligned} \quad (\text{D.9})$$

The wave function in  $(12)3, 4$  coordinates is the sum of Eqs. (D.3), (D.4), (D.7), (D.8) and (D.9).

### D.1.2 $(12)4, 3$ coordinates

The choice for a sequence of transformations is not unique in all representations of the wave function. But the motivations for a certain choice are very much the same in all coordinates. Therefore we will just summarize our final expressions in the following and omit further comments.

$$\begin{aligned} & \langle (12)4, 3|(1+P)|\psi_{1A} \rangle \\ & = \langle (12)4, 3|(12)3, 4' \rangle \langle (12)3, 4'|\psi_{1A} \rangle \\ & \quad + 2 \langle (12)4, 3|(12)3, 4' \rangle \langle (12)3, 4'|(23)1, 4'' \rangle \langle (12)3, 4''|\psi_{1A} \rangle \end{aligned} \quad (\text{D.10})$$

$$\begin{aligned} & \langle (12)4, 3|(1+P)|\psi_{1B} \rangle \\ & = \langle (12)4, 3|\psi_{1B} \rangle \\ & \quad + 2 \langle (12)4, 3|(12)3, 4' \rangle \langle (12)3, 4'|(23)1, 4'' \rangle \\ & \quad \quad \langle (23)1, 4''|(23)4, 1''' \rangle \langle (12)4, 3'''|\psi_{1B} \rangle \end{aligned} \quad (\text{D.11})$$

$$\begin{aligned} & \langle (12)4, 3|(1-P_{12})(1+P)|\psi_{1C} \rangle \\ & = 2 \langle (12)4, 3|(14)2, 3' \rangle \langle (14)2, 3'|\psi_{1C} \rangle \\ & \quad - \langle (14)2, 3'|(14)3, 2'' \rangle \langle (14)2, 3''|\psi_{1C} \rangle \\ & \quad + 2 \langle (12)4, 3|(12)34' \rangle \langle (12)34'|(34)12'' \rangle \\ & \quad \quad \langle (34)12''|(34)1, 2''' \rangle \langle (14)2, 3'''|\psi_{1C} \rangle \end{aligned} \quad (\text{D.12})$$

$$\begin{aligned} & \langle (12)4, 3|(1+P)|\psi_{2A} \rangle \\ & = \langle (12)4, 3|(12)34' \rangle \langle (12)34'|\psi_{2A} \rangle \\ & \quad + 2 \langle (12)4, 3|(12)3, 4' \rangle \langle (12)3, 4'|(23)1, 4'' \rangle \\ & \quad \quad \langle (23)1, 4''|(23)14''' \rangle \langle (12)34'''|\psi_{2A} \rangle \end{aligned} \quad (\text{D.13})$$

$$\begin{aligned} & \langle (12)4, 3|(1+P)|\psi_{2B} \rangle \\ & = \langle (12)4, 3|(12)34' \rangle \langle (12)34'|(34)12'' \rangle \langle (34)12''|\psi_{2B} \rangle \\ & \quad + 2 \langle (12)4, 3|(14)2, 3' \rangle \langle (14)2, 3'|(14)23'' \rangle \langle (34)12''|\psi_{2A} \rangle \end{aligned} \quad (\text{D.14})$$

Again the wave function is given as the sum of Eqs. (D.10)-(D.14).

### D.1.3 (14)2, 3 coordinates

This is the most CPU-time and memory consuming representation. There is no restriction on the symmetry of the (14) subsystem, the antisymmetry of the three nucleons cannot be used for an additional constraint to the partial waves. Therefore the number of partial waves is twice as large as in the other representations.

$$\begin{aligned}
& \langle (14)2, 3|(1+P)|\psi_{1A} \rangle \\
& = \langle (14)2, 3|(12)4, 3' \rangle \langle (12)4, 3'|(12)3, 4'' \rangle \langle (12)3, 4''|\psi_{1A} \rangle \\
& \quad + 2 \langle (14)2, 3|(12)4, 3' \rangle \langle (12)4, 3'|(12)3, 4'' \rangle \\
& \quad \quad \langle (12)3, 4''|(23)1, 4''' \rangle \langle (12)3, 4'''|\psi_{1A} \rangle
\end{aligned} \tag{D.15}$$

$$\begin{aligned}
& \langle (14)2, 3|(1+P)|\psi_{1B} \rangle \\
& = \langle (14)2, 3|(12)4, 3' \rangle \langle (12)4, 3'|\psi_{1B} \rangle \\
& \quad + 2 \langle (14)2, 3|(12)4, 3' \rangle \langle (12)4, 3'|(12)3, 4'' \rangle \langle (12)3, 4''|(23)1, 4''' \rangle \\
& \quad \quad \langle (23)1, 4'''|(23)4, 1^* \rangle \langle (12)4, 3^*|\psi_{1B} \rangle
\end{aligned} \tag{D.16}$$

$$\begin{aligned}
& \langle (14)2, 3|(1-P_{12})(1+P)|\psi_{1C} \rangle \\
& = \langle (14)2, 3|\psi_{1C} \rangle - \langle (14)2, 3|(24)1, 3' \rangle \langle (14)2, 3'|\psi_{1C} \rangle \\
& \quad - \langle (14)2, 3|(14)3, 2' \rangle \langle (14)2, 3'|\psi_{1C} \rangle \\
& \quad + \langle (14)2, 3|(24)1, 3' \rangle \langle (24)1, 3'|(24)3, 1'' \rangle \langle (14)2, 3''|\psi_{1C} \rangle \\
& \quad + \langle (14)2, 3|(14)3, 2' \rangle \langle (14)3, 2'|(34)1, 2'' \rangle \langle (14)2, 3''|\psi_{1C} \rangle \\
& \quad - \langle (14)2, 3|(14)3, 2' \rangle \langle (14)3, 2'|(34)1, 2'' \rangle \\
& \quad \quad \langle (34)1, 2''|(34)2, 1''' \rangle \langle (14)2, 3'''|\psi_{1C} \rangle
\end{aligned} \tag{D.17}$$

$$\begin{aligned}
& \langle (14)2, 3|(1+P)|\psi_{2A} \rangle \\
& = \langle (14)2, 3|(12)4, 3' \rangle \langle (12)4, 3'|(12)34'' \rangle \langle (12)34''|\psi_{2A} \rangle \\
& \quad + \langle (14)2, 3|(14)23' \rangle \langle (14)23'|(23)14'' \rangle \langle (12)34''|\psi_{2A} \rangle \\
& \quad + \langle (14)2, 3|(24)1, 3' \rangle \langle (24)1, 3'|(24)31'' \rangle \\
& \quad \quad \langle (24)31''|(31)24''' \rangle \langle (12)34'''|\psi_{2A} \rangle
\end{aligned} \tag{D.18}$$

$$\begin{aligned}
& \langle (14)2, 3|(1+P)|\psi_{2B} \rangle \\
& = \langle (14)2, 3|(14)23' \rangle \langle (34)12'|\psi_{2B} \rangle \\
& \quad + \langle (14)2, 3|(12)4, 3' \rangle \langle (12)4, 3'|(12)34'' \rangle \\
& \quad \quad \langle (12)34''|(34)12''' \rangle \langle (34)12'''|\psi_{2B} \rangle \\
& \quad + \langle (14)2, 3|(24)1, 3' \rangle \langle (24)1, 3'|(24)31'' \rangle \langle (34)12''|\psi_{2B} \rangle
\end{aligned} \tag{D.19}$$

The sum of Eqs. (D.15)-(D.19) results in the wave function.

### D.1.4 (12)34 coordinates

For the “2+2” representations of the wave function, we choose the transformations following the same scheme.



$$\begin{aligned}
& \langle (12)34|(1+P)|\psi_{1A} \rangle \\
& = \langle (12)34|(12)3, 4' \rangle \langle (12)3, 4'|\psi_{1A} \rangle \\
& \quad + 2 \langle (12)34|(12)3, 4' \rangle \langle (12)3, 4'|(23)1, 4'' \rangle \langle (12)3, 4''|\psi_{1A} \rangle
\end{aligned} \tag{D.20}$$

$$\begin{aligned}
& \langle (12)34|(1+P)|\psi_{1B} \rangle \\
& = \langle (12)34|(12)4, 3' \rangle \langle (12)4, 3'|\psi_{1B} \rangle \\
& \quad + 2 \langle (12)34|(34)12' \rangle \langle (34)12'|(34)1, 2'' \rangle \\
& \quad \quad \langle (34)1, 2''|(31)4, 2''' \rangle \langle (12)4, 3'''|\psi_{1B} \rangle
\end{aligned} \tag{D.21}$$

$$\begin{aligned}
& \langle (12)34|(1-P_{12})(1+P)|\psi_{1C} \rangle \\
& = 2 \langle (12)34|(12)4, 3' \rangle \langle (12)4, 3'|(14)2, 3'' \rangle \\
& \quad (\langle (14)2, 3''|\psi_{1C} \rangle - \langle (14)2, 3''|(14)3, 2''' \rangle \langle (14)2, 3'''|\psi_{1C} \rangle) \\
& \quad + 2 \langle (12)34|(34)12' \rangle \langle (34)12'|(34)1, 2'' \rangle \langle (34)1, 2''|\psi_{1C} \rangle
\end{aligned} \tag{D.22}$$

$$\begin{aligned}
& \langle (12)34|(1+P)|\psi_{2A} \rangle \\
& = \langle (12)34|\psi_{2A} \rangle \\
& \quad + 2 \langle (12)34|(12)3, 4' \rangle \langle (12)3, 4'|(23)1, 4'' \rangle \\
& \quad \quad \langle (23)1, 4''|(23)14''' \rangle \langle (12)34'''|\psi_{2A} \rangle
\end{aligned} \tag{D.23}$$

$$\begin{aligned}
& \langle (12)34|(1+P)|\psi_{2B} \rangle \\
& = \langle (12)34|(34)12' \rangle \langle (34)12'|\psi_{2B} \rangle \\
& \quad + 2 \langle (12)34|(12)4, 3' \rangle \langle (12)4, 3'|(14)2, 3'' \rangle \\
& \quad \quad \langle (14)2, 3''|(14)23''' \rangle \langle (34)12'''|\psi_{2B} \rangle
\end{aligned} \tag{D.24}$$

As usually we find the wave function summing over Eqs. (D.20)-(D.24).

### D.1.5 (34)12 coordinates

This representation completes our set of wave functions. The expressions are very similar to the former ones.

$$\begin{aligned}
& \langle (34)12|(1+P)|\psi_{1A} \rangle \\
& = \langle (34)12|(12)34' \rangle \langle (12)34'|(12)3, 4'' \rangle \langle (12)3, 4''|\psi_{1A} \rangle \\
& \quad + 2 \langle (34)12|(12)34' \rangle \langle (12)34'|(12)3, 4'' \rangle \\
& \quad \quad \langle (12)3, 4''|(23)1, 4''' \rangle \langle (12)3, 4'''|\psi_{1A} \rangle
\end{aligned} \tag{D.25}$$

$$\begin{aligned}
& \langle (34)12|(1+P)|\psi_{1B} \rangle \\
& = \langle (34)12|(12)34' \rangle \langle (12)34'|(12)4, 3'' \rangle \langle (12)4, 3''|\psi_{1B} \rangle
\end{aligned}$$

$$+2 \langle (34)12|(34)2, 1' \rangle \langle (34)2, 1'|(23)4, 1'' \rangle \langle (12)4, 3''|\psi_{1B} \rangle \quad (\text{D.26})$$

$$\begin{aligned} & \langle (34)12|(1 - P_{12})(1 + P)|\psi_{1C} \rangle \\ &= 2 \langle (34)12|(34)1, 2' \rangle \langle (14)2, 3'|\psi_{1C} \rangle \\ & \quad + 2 \langle (34)12|(34)2, 1' \rangle \langle (34)2, 1'|(24)3, 1'' \rangle \\ & \quad (\langle (14)2, 3''|\psi_{1C} \rangle - \langle (24)3, 1''|(24)1, 3''' \rangle \langle (14)2, 3'''|\psi_{1C} \rangle) \end{aligned} \quad (\text{D.27})$$

$$\begin{aligned} & \langle (34)12|(1 + P)|\psi_{2A} \rangle \\ &= \langle (34)12|(12)34' \rangle \langle (12)34'|\psi_{2A} \rangle \\ & \quad + 2 \langle (34)12|(34)1, 2' \rangle \langle (34)1, 2'|(31)4, 2'' \rangle \\ & \quad \langle (31)4, 2''|(31)24''' \rangle \langle (12)34'''|\psi_{2A} \rangle \end{aligned} \quad (\text{D.28})$$

$$\begin{aligned} & \langle (34)12|(1 + P)|\psi_{2B} \rangle \\ &= \langle (34)12|\psi_{2B} \rangle \\ & \quad + 2 \langle (34)12|(34)2, 1' \rangle \langle (34)2, 1'|(24)3, 1'' \rangle \\ & \quad \langle (24)3, 1''|(24)31''' \rangle \langle (34)12'''|\psi_{2B} \rangle \end{aligned} \quad (\text{D.29})$$

The sum of the terms in Eqs. (D.25)-(D.29) results in the wave function.

The speed of convergence of the partial wave decomposition is not unique for the different representations of the wave function. This is outlined in Chapter 3.

In this section, we introduced algorithms to calculate independently the representations from the YC's. A comparison of some of their properties has been performed and we found agreement within the expected accuracy. This is a good check for the consistency of the codes and the algorithm.

In the next section, we will simplify the expressions to the three-body and four-nucleon system.

## D.2 The wave functions for the three-body system and four-nucleon system

In this section we will simplify the expressions from the last section to the more simple systems. For the  $\alpha$ -particle this is straight forward using the known dependences of the YC's. Because of the antisymmetry of the wave function, most representations are equivalent to each other. There are only two independent ones left. For the three-body systems, we omit all parts involving the motion of the outer particle. This reduces the number of particles in the coordinates to three and leads to a enormous simplification of the expressions. Moreover, all coordinate transformations can be done in one step.

### D.2.1 The $\alpha$ -particle

We choose the (12)3, 4 and (12)34 coordinates as independent representations of the wave function. We can lead back all YC's to  $\psi_{1A}$  and  $\psi_{2A}$  as shown in Eq. (B.10) and find for the matrix elements

$$\begin{aligned} \langle (12)4, 3|\psi_{1B} \rangle &= - \langle (12)3, 4|\psi_{1A} \rangle \\ \langle (14)2, 3|\psi_{1C} \rangle &= \langle (12)3, 4|\psi_{1A} \rangle \end{aligned}$$

$$\langle (34)12|\psi_{2B} \rangle = \langle (12)34|\psi_{2A} \rangle \quad (\text{D.30})$$

With the help of this relations we can remove all YC's but the 1A and 2A from Eqs. (D.3), (D.4), (D.7), (D.8) and (D.9) and obtain

$$\begin{aligned} & \langle (12)3, 4|(1+P)|\psi_{1A} \rangle \\ & = \langle (12)3, 4|\psi_{1A} \rangle + 2 \langle (12)3, 4|(23)1, 4' \rangle \langle (12)3, 4'|\psi_{1A} \rangle \end{aligned} \quad (\text{D.31})$$

$$\begin{aligned} & \langle (12)3, 4|-(1+P)P_{34}|\psi_{1A} \rangle \\ & = - \langle (12)3, 4|(12)4, 3' \rangle \langle (12)3, 4'|\psi_{1A} \rangle \\ & \quad - 2 \langle (12)3, 4|(23)1, 4' \rangle \langle (12)3, 4'|(12)4, 3'' \rangle \\ & \quad \langle (12)3, 4''|\psi_{1A} \rangle \end{aligned} \quad (\text{D.32})$$

$$\begin{aligned} & \langle (12)3, 4|(1-P_{12})(1+P)P_{24}P_{34}|\psi_{1A} \rangle \\ & = 2 \langle (12)3, 4|(14)2, 3' \rangle \\ & \quad (\langle (12)3, 4'|\psi_{1A} \rangle - \langle (14)2, 3'|(14)3, 2'' \rangle \langle (12)3, 4''|\psi_{1A} \rangle) \\ & \quad + 2 \langle (12)3, 4|(12)34' \rangle \langle (12)34'|(34)12'' \rangle \\ & \quad \langle (34)12''|(34)1, 2''' \rangle \langle (12)3, 4''|\psi_{1A} \rangle \end{aligned} \quad (\text{D.33})$$

$$\begin{aligned} & \langle (12)3, 4|(1+P)|\psi_{2A} \rangle \\ & = \langle (12)3, 4|(12)34' \rangle \langle (12)34'|\psi_{2A} \rangle \\ & \quad + 2 \langle (12)3, 4|(23)1, 4' \rangle \langle (23)1, 4'|(23)14'' \rangle \langle (12)34''|\psi_{2A} \rangle \end{aligned} \quad (\text{D.34})$$

$$\begin{aligned} & \langle (12)3, 4|(1+P)P_{13}P_{24}|\psi_{2A} \rangle \\ & = \langle (12)3, 4|(12)34' \rangle \langle (12)34'|(34)12'' \rangle \langle (12)34''|\psi_{2A} \rangle \\ & \quad + 2 \langle (12)3, 4|(23)1, 4' \rangle \langle (23)1, 4'|(23)14'' \rangle \\ & \quad \langle (23)14''|(14)23''' \rangle \langle (12)34''|\psi_{2A} \rangle \end{aligned} \quad (\text{D.35})$$

The sum of these terms is the “3+1” representation of the  $\alpha$ -particle wave function.

In the case of the “2+2” coordinates the same replacements in Eqs. (D.20)-(D.24) result in

$$\begin{aligned} & \langle (12)34|(1+P)|\psi_{1A} \rangle \\ & = \langle (12)34|(12)3, 4' \rangle \langle (12)3, 4'|\psi_{1A} \rangle \\ & \quad + 2 \langle (12)34|(12)3, 4' \rangle \langle (12)3, 4'|(23)1, 4'' \rangle \langle (12)3, 4''|\psi_{1A} \rangle \end{aligned} \quad (\text{D.36})$$

$$\begin{aligned} & \langle (12)34|-(1+P)P_{34}|\psi_{1A} \rangle \\ & = - \langle (12)34|(12)4, 3' \rangle \langle (12)3, 4'|\psi_{1A} \rangle \\ & \quad - 2 \langle (12)34|(34)12' \rangle \langle (34)12'|(34)1, 2'' \rangle \\ & \quad \langle (34)1, 2''|(31)4, 2''' \rangle \langle (12)3, 4''|\psi_{1A} \rangle \end{aligned} \quad (\text{D.37})$$

$$\langle (12)34|(1-P_{12})(1+P)P_{24}P_{34}|\psi_{1A} \rangle$$

$$\begin{aligned}
&= 2 \langle (12)34|(12)4, 3' \rangle \langle (12)4, 3'| (14)2, 3'' \rangle \\
&\quad (\langle (12)3, 4''|\psi_{1A} \rangle - \langle (14)2, 3''|(14)3, 2''' \rangle \langle (12)3, 4'''|\psi_{1A} \rangle) \\
&\quad + 2 \langle (12)34|(34)12' \rangle \langle (34)12'|(34)1, 2'' \rangle \langle (12)3, 4''|\psi_{1A} \rangle
\end{aligned} \tag{D.38}$$

$$\begin{aligned}
&\langle (12)34|(1+P)|\psi_{2A} \rangle \\
&= \langle (12)34|\psi_{2A} \rangle \\
&\quad + 2 \langle (12)34|(12)3, 4' \rangle \langle (12)3, 4'|(23)1, 4'' \rangle \\
&\quad \langle (23)1, 4''|(23)14''' \rangle \langle (12)34'''|\psi_{2A} \rangle
\end{aligned} \tag{D.39}$$

$$\begin{aligned}
&\langle (12)34|(1+P)|P_{13}P_{24}\psi_{2A} \rangle \\
&= \langle (12)34|(34)12' \rangle \langle (12)34'|\psi_{2A} \rangle \\
&\quad + 2 \langle (12)34|(12)4, 3' \rangle \langle (12)4, 3'|(14)2, 3'' \rangle \\
&\quad \langle (14)2, 3''|(14)23''' \rangle \langle (12)34'''|\psi_{2A} \rangle
\end{aligned} \tag{D.40}$$

## D.2.2 The hypertriton

In Appendix B.1 the connection between the Faddeev component of the hypertriton and the YC's 1B and 1C is shown. We express the wave function in their natural coordinates dropping the momentum and quantum numbers of the third particle, which is the outer one in 1B and 1C. Especially this means that the cyclic and anticyclic permutations are dropped, because they involve the third particle. Using Eqs. (D.11)-(D.12) one finds for the wave function  $\Psi$  in 1B coordinates

$$\begin{aligned}
&\langle (12)4|\Psi \rangle \\
&= \langle (12)4|\psi_{1B} \rangle \\
&\quad + 2 \langle (12)4|(14)2' \rangle \langle (14)2'|\psi_{1C} \rangle
\end{aligned} \tag{D.41}$$

and from Eqs. (D.16) and (D.17) in 1C representation

$$\begin{aligned}
&\langle (14)2|\Psi \rangle \\
&= \langle (14)2|(12)4' \rangle \langle (12)4'|\psi_{1B} \rangle \\
&\quad + \langle (14)2|\psi_{1C} \rangle - \langle (14)2|(24)1' \rangle \langle (14)2'|\psi_{1C} \rangle
\end{aligned} \tag{D.42}$$

## D.2.3 The 3N system

Here only one Faddeev component enters. From Eq. (D.31) we find omitting the fourth particle the well known expression for the 3N wave function  $\Psi$

$$\langle (12)3|(1+P)|\psi_{1A} \rangle = \langle (12)3|\psi_{1A} \rangle + 2 \langle (12)3|(23)1' \rangle \langle (12)3'|\psi_{1A} \rangle \tag{D.43}$$

## Appendix E

# Partial wave decomposition of correlation and overlap functions

In this appendix we derive explicit expressions for the partial wave decomposed correlation and overlap functions defined in Chapter 4.

### E.1 Correlation functions

In this section we work on the correlation functions as they are defined in Section 4.3. For the sake of simplification we will neglect the isospin dependences introduced by the projector  $P_{12}^T(q)$  in this appendix. The isospin dependences factorize from the spin-orbital part of the correlation. Moreover we have to treat them separately for the 3N and 4N systems and the hypernuclei. The isospin matrix elements have been worked out in the manner shown in Section 2.4 and, therefore, are not presented in this appendix.

In this case the correlation reads

$$C_{s m_s}(\vec{p}) = \frac{1}{2J+1} \sum_M \langle \Psi JM | \delta^3(\vec{p} - \vec{p}_{12}) P_{12}^S(s m_s) | \Psi JM \rangle \quad (\text{E.1})$$

The operator  $\delta^3(\vec{p} - \vec{p}_{12}) P_{12}^S(s m_s)$  acts only on coordinates of the (12) subsystem and conserves the total momentum of (12). We choose coordinates for the description of the  $A$ -body state  $\Psi$ , which single out the subsystem (12) with its momentum  $p_{12}$ , orbital angular momentum  $l_{12}$ , spin  $s_{12}$  and total angular momentum  $j_{12} m_j$ . The relative and internal motion of the  $(A-2)$  subsystem is described with coordinates  $\alpha_{A-2}$  and has got total angular momentum  $J_{A-2} M_{A-2}$ . The angular momenta of the subsystems couple to the total angular momentum  $J M$  of the nucleus. The operator in Eq. (E.1) is independent from  $\alpha_{A-2}$ ,  $J_{A-2}$  and  $M_{A-2}$ . We expand the nuclear wave function in states  $|p_{12} \alpha_{A-2} ((l_{12} s_{12}) j_{12} J_{A-2}) JM \rangle$  and write down the explicit coupling of the (12) and  $(A-2)$  subsystems with the help of Clebsch-Gordan coefficients. Using the independence of the operator on the coordinates of the  $(A-2)$  subsystem, one finds

$$C_{s m_s}(\vec{p}) = \frac{1}{2J+1} \sum_M \sum_{\substack{\alpha_{A-2} \\ J_{A-2} M_{A-2}}} \sum_{\substack{l_{12} l'_{12} s_{12} s'_{12} \\ j_{12} j'_{12} m_j m'_j}} \int dp_{12} p_{12}^2 \int dp'_{12} p'_{12}{}^2$$

$$\begin{aligned}
& (j_{12}J_{A-2}J, m_j M_{A-2}M) (j'_{12}J_{A-2}J, m'_j M_{A-2}M) \\
& \langle \Psi JM | p_{12} \alpha_{A-2} ((l_{12}s_{12})j_{12}J_{A-2})JM \rangle \langle p'_{12} \alpha_{A-2} ((l'_{12}s'_{12})j'_{12}J_{A-2})JM | \Psi JM \rangle \\
& \langle p_{12}(l_{12}s_{12})j_{12}m_j | \delta^3(\vec{p} - \vec{p}_{12}) P_{12}^S(s m_s) | p'_{12}(l'_{12}s'_{12})j'_{12}m'_j \rangle
\end{aligned} \tag{E.2}$$

We define the (12) matrix element by

$$M_{12} = \langle p_{12}(l_{12}s_{12})j_{12}m_j | \delta^3(\vec{p} - \vec{p}_{12}) P_{12}^S(s m_s) | p'_{12}(l'_{12}s'_{12})j'_{12}m'_j \rangle \tag{E.3}$$

The matrix element  $\langle p_{12} \alpha_{A-2} ((l_{12}s_{12})j_{12}J_{A-2})JM | \Psi JM \rangle$  of the wave function of the nucleus is independent from  $M$ . We set  $M = J$  and carry out the  $M$  and  $M_{A-2}$  summation using orthogonality relations of the Clebsch-Gordan coefficients.

$$\begin{aligned}
C_{s m_s}(\vec{p}) &= \sum_{\alpha_{A-2} J_{A-2}} \sum_{\substack{l_{12}l'_{12}s_{12}s'_{12} \\ j_{12}j'_{12}m_j m'_j}} \int dp_{12} p_{12}^2 \int dp'_{12} p_{12}'^2 \frac{1}{2j_{12} + 1} \delta_{j_{12}j'_{12}} \delta_{m_j m'_j} \\
&\langle \Psi JJ | p_{12} \alpha_{A-2} ((l_{12}s_{12})j_{12}J_{A-2})JJ \rangle \langle p'_{12} \alpha_{A-2} ((l'_{12}s'_{12})j'_{12}J_{A-2})JJ | \Psi JJ \rangle M_{12} \\
&= \sum_{\alpha_{A-2} J_{A-2}} \sum_{\substack{l_{12}s_{12}j_{12} \\ l'_{12}s'_{12}}} \int dp_{12} p_{12}^2 \int dp'_{12} p_{12}'^2 \frac{1}{2j_{12} + 1} \sum_{m_j} M_{12} \\
&\langle \Psi JJ | p_{12} \alpha_{A-2} ((l_{12}s_{12})j_{12}J_{A-2})JJ \rangle \langle p'_{12} \alpha_{A-2} ((l'_{12}s'_{12})j_{12}J_{A-2})JJ | \Psi JJ \rangle
\end{aligned} \tag{E.4}$$

This shows that the averaging over  $M$  restricts the quantum numbers on both sides of  $M_{12}$  to  $j_{12} = j'_{12}$  and  $m_j = m'_j$ . This tremendously simplifies the angular dependence of  $M_{12}$ .

We also see that there exists a common structure for all nuclei, which describes the correlation function in terms of the angular momenta of the two-body subsystem. This is an important feature of the definition proposed in [118]. It is the result of the way to introduce an angular dependence. One does not fix the polarization of the nucleus, but fixes the polarization of the spins in the subsystem. This can be done for all nuclei in the same way. It can also be performed for nuclei like the  $\alpha$ -particle with total angular momentum  $J = 0$ .

It remains to work out the matrix element of the two-body correlation operator

$$\mathcal{M} \equiv \frac{1}{2j_{12} + 1} \sum_{m_j} M_{12} \tag{E.5}$$

We insert a complete set of  $|\tilde{p}\rangle$  states and decouple the orbital angular momentum and spin

$$\begin{aligned}
\mathcal{M} &= \frac{1}{2j_{12} + 1} \sum_{m_j} \sum_{\mu\mu'} \int d^3\tilde{p} \\
&\langle p_{12}l_{12}\mu | \langle s_{12}m_j - \mu | \delta^3(\vec{p} - \tilde{p}) P_{12}^S(sm_s) | \tilde{p}\rangle \langle \tilde{p} | s'_{12}m_j - \mu' \rangle | p'_{12}l'_{12}\mu' \rangle \\
&(l_{12}s_{12}j_{12}, \mu m_j - \mu) (l'_{12}s'_{12}j_{12}, \mu' m_j - \mu')
\end{aligned}$$

$$\begin{aligned}
&= \delta_{s_{12}s'_{12}} \delta_{s_{12}s} \frac{\delta(p_{12}-p)}{p_{12}p} \frac{\delta(p'_{12}-p)}{p'_{12}p} \frac{1}{2j_{12}+1} \sum_{m_j} \\
&\quad (l_{12}s j_{12}, m_j - m_s \ m_s) (l'_{12}s j_{12}, m_j - m_s \ m_s) Y_{l_{12}m_j - m_s}^*(\hat{p}) Y_{l'_{12}m_j - m_s}(\hat{p}) \quad (\text{E.6})
\end{aligned}$$

In the second step we used the projection operator  $P_{12}^S(sm_s)$  to fix the spin quantum numbers  $s_{12} = s'_{12} = s$  and their third components. This removes the  $\mu$  and  $\mu'$  summations. With standard techniques one recouples the angular momenta in the Clebsch-Gordan coefficients (see for example [80, 140]) leading to an expression, which separates the coupling of the spins and of the orbital angular momenta

$$\begin{aligned}
\mathcal{M} &= \delta_{s_{12}s'_{12}} \delta_{s_{12}s} \frac{\delta(p_{12}-p)}{p_{12}p} \frac{\delta(p'_{12}-p)}{p'_{12}p} \sum_f (-)^{s-j_{12}} (-)^{l_{12}+l'_{12}-f} \sqrt{\frac{2f+1}{2s+1}} \left\{ \begin{matrix} s & l_{12} & j_{12} \\ l'_{12} & s & f \end{matrix} \right\} \\
&\quad (s \ f \ s, m_s \ 0) \sum_{m_j} (l_{12}l'_{12}f, -m_j + m_s \ m_j - m_s) (-)^{m_j - m_s} Y_{l_{12}m_j - m_s}^*(\hat{p}) Y_{l'_{12}m_j - m_s}(\hat{p}) \quad (\text{E.7})
\end{aligned}$$

and recognizes in the last line a coupled spherical harmonic  $\mathcal{Y}_{l_{12}l'_{12}}^{f0}(\hat{p}\hat{p})$  with magnetic quantum number zero and two identical arguments  $\hat{p}$ . Because of the relation

$$\mathcal{Y}_{l_{12}l'_{12}}^{f0}(\hat{p}\hat{p}) = \sqrt{\frac{(2l_{12}+1)(2l'_{12}+1)}{(2f+1)4\pi}} (l_{12}l'_{12}f, 00) Y_{f0}(\hat{p}) \quad (\text{E.8})$$

we obtain

$$\begin{aligned}
\mathcal{M} &= \delta_{s_{12}s'_{12}} \delta_{s_{12}s} \frac{\delta(p_{12}-p)}{p_{12}p} \frac{\delta(p'_{12}-p)}{p'_{12}p} \sum_f (-)^{s-j_{12}} (-)^{l_{12}+l'_{12}-f} \sqrt{\frac{2f+1}{2s+1}} \left\{ \begin{matrix} s & l_{12} & j_{12} \\ l'_{12} & s & f \end{matrix} \right\} \\
&\quad (s \ f \ s, m_s \ 0) \sqrt{\frac{(2l_{12}+1)(2l'_{12}+1)}{(2f+1)4\pi}} (l_{12}l'_{12}f, 00) Y_{f0}(\hat{p}) \quad (\text{E.9})
\end{aligned}$$

In the last step we use

$$Y_{f0}(\hat{p}) = \sqrt{\frac{2f+1}{4\pi}} P_f(x) \quad (\text{E.10})$$

where  $x = \hat{e}_z \cdot \hat{p}$  and obtain the final expression

$$\begin{aligned}
\mathcal{M} &= \delta_{s_{12}s'_{12}} \delta_{s_{12}s} \frac{\delta(p_{12}-p)}{p_{12}p} \frac{\delta(p'_{12}-p)}{p'_{12}p} \sum_f (-)^{s-j_{12}} (-)^{l_{12}+l'_{12}-f} \sqrt{\frac{(2l_{12}+1)(2l'_{12}+1)(2f+1)}{2s+1}} \\
&\quad \left\{ \begin{matrix} s & l_{12} & j_{12} \\ l'_{12} & s & f \end{matrix} \right\} (s \ f \ s, m_s \ 0) (l_{12}l'_{12}f, 00) \frac{1}{4\pi} P_f(x) \quad (\text{E.11})
\end{aligned}$$

Because  $s$  is restricted to 0 and 1, the order of the Legendre polynomial  $f$  can only take the values 0, 1 and 2. Parity conservation fixes the phase  $(-)^{l_{12}+l'_{12}} = 1$ . Therefore the Clebsch-Gordan coefficient  $(l_{12}l'_{12}f, 00)$  demands even  $f$ 's. Because of this the expansion of the angular dependence contains only

two Legendre polynomials:  $P_0(x)$  and  $P_2(x)$ . This proves the form of Eq. (4.6). From the explicit form of  $\mathcal{M}$  one also reads off, that the  $m_s$  dependence is given by an overall Clebsch-Gordan coefficient. This justifies that we only present results for  $m_s = 0$  in Chapters 4 and 5. We also see that the  $f = 0$  part of  $\mathcal{C}$  is independent of  $m_s$ . Finally, we would like to note that the expressions are also valid in configuration space, replacing the momenta by corresponding distances.

## E.2 Overlap functions

In this section we summarize the partial wave expansion for the  ${}^2\text{H}$ -baryon and  ${}^3\text{H}/{}^3\text{He}$ -baryon overlap functions in the three-body and four-body nuclei. The derivation follows the one sketched in the preceding section. Here we only give final expressions.

The  ${}^2\text{H}$ -baryon overlap function of the three-body bound state  $|\Psi JM\rangle$  is given by

$$\hat{D}_{m_j}(\vec{p}) = \frac{1}{2J+1} \sum_M \langle \Psi JM | \delta^3(\vec{p}_3 - \vec{p}) | \phi_d j m_j \rangle \langle \phi_d j m_j | \Psi JM \rangle \quad (\text{E.12})$$

The calculation of this expectation value requires the partial wave representation of the deuteron projection operator and of the momentum  $\delta$ -function. Again the matrix elements of the wave function are independent from  $M$  and we can fix  $M = J$ . Therefore we need the evaluation of the matrix element

$$\mathcal{M} = \frac{1}{2J+1} \sum_M \langle p_{12} p_3 \alpha | \delta^3(\vec{p}_3 - \vec{p}) | \phi_d j m_j \rangle \langle \phi_d j m_j | p'_{12} p'_3 \alpha' \rangle \quad (\text{E.13})$$

for the usual set of three-body quantum numbers  $\alpha$  and  $\alpha'$ . The deuteron angular momentum  $j = 1$  is fixed. Its third component defines the quantization axis and introduces the angular dependence. Our result is

$$\begin{aligned} \mathcal{M} = & \frac{\delta(p_3 - p)}{p_3 p} \frac{\delta(p'_3 - p)}{p'_3 p} \delta_{j_{12}1} \delta_{j'_{12}1} \delta_{t_{12}0} \delta_{t'_{12}0} \sum_f (-)^{2I'_3} (-)^{I_3 + I'_3 + j - J + \frac{1}{2} + l'_3 + f} \\ & \left\{ \begin{matrix} I_3 & j & J \\ j & I'_3 & f \end{matrix} \right\} \left\{ \begin{matrix} l_3 & f & l'_3 \\ I'_3 & \frac{1}{2} & I_3 \end{matrix} \right\} (2f+1) \sqrt{\frac{(2I_3+1)(2I'_3+1)(2l_3+1)}{2j+1}} \\ & (j f j, m_j 0) (l_3 f l'_3, 00) \frac{1}{4\pi} P_f(x) \phi_d^{l_3 l'_3}(p_{12}) \phi_d^{l'_3 l_3}(p'_{12}) \end{aligned} \quad (\text{E.14})$$

$\mathcal{M}$  restricts the quantum numbers of the two-body subsystem to  $l_{12}, l'_{12} = 0, 2$ ,  $s_{12} = s'_{12} = 1$  and  $j_{12} = j'_{12} = 1$ . The angle is given by  $x = \hat{e}_z \cdot \hat{p}$ .  $\phi_d^{l_3 l'_3}(p_{12})$  is the deuteron wave function in momentum space.

The expression proves the angular dependence as given in Eq. (4.13). The fixed deuteron spin  $j = 1$  restricts  $f = 0, 1, 2$ . Parity conservation and the Clebsch-Gordan  $(l_3 f l'_3, 00)$  coefficient demands even  $f$ 's. Therefore only the Legendre polynomials  $P_0(x)$  and  $P_2(x)$  contribute.

The  ${}^3\text{H}/{}^3\text{He}$ -baryon overlap function is angular independent. Because we think that this is not clear at all in advance for the excited state of  ${}^4_\Lambda\text{He}$  with  $J = 1$ , we define the overlap correspondingly to Eq. (E.12)

$$\hat{T}_{m_t}(\vec{p}) = \frac{1}{2J+1} \sum_M \langle \Psi JM | \delta^3(\vec{q}_4 - \vec{p}) | \phi_t j_t m_t \rangle \langle \phi_t j_t m_t | \Psi JM \rangle \quad (\text{E.15})$$



We project the four-body bound state  $|\Psi JM\rangle$  to the 3N wave function  $|\phi_t j_t m_t\rangle$  and fix the momentum of the fourth particle.

A derivation similar to the one of the preceding section reveals an overlap operator given in usual “3+1” Jacobi coordinates as

$$\begin{aligned}
\mathcal{M} &= \frac{1}{2J+1} \sum_M \langle p_{12} p_3 q_4 \alpha | \delta^3(\vec{q}_4 - \vec{p}) | \phi_t j_t m_t \rangle \langle \phi_t j_t m_t | p'_{12} p'_3 q'_4 \alpha \rangle \\
&= \frac{\delta(q_4 - p)}{q_4 p} \frac{\delta(q'_4 - p)}{q'_4 p} \phi_t(p_{12} p_3 \alpha_3) \phi_t(p'_{12} p'_3 \alpha_3) \\
&\quad \sum_f (-)^{l_4 + l'_4 + I_4 + I'_4 + \frac{1}{2} + j_t + J} \sqrt{\frac{(2I_4 + 1)(2I'_4 + 1)(2f + 1)(2l_4 + 1)(2l'_4 + 1)}{(2j_t + 1)}} \\
&\quad \left\{ \begin{array}{ccc} l_4 & f & l'_4 \\ I'_4 & \frac{1}{2} & I_4 \end{array} \right\} \left\{ \begin{array}{ccc} f & I'_4 & I_4 \\ J & j_t & j_t \end{array} \right\} (f j_t j_t, 0 m_t) (l_4 l'_4 f, 00) \frac{1}{4\pi} P_f(x) \quad (\text{E.16})
\end{aligned}$$

$x$  corresponds to the angle of  $\hat{p}$  to the quantization axis. The 3N wave function  $\phi_t$  depends on the momenta  $p_{12}$  and  $p_3$  and the subset  $\alpha_3$  of quantum numbers of the three-body subsystem of the “3+1” coordinates. Only partial waves contribute, which are consistent with the fixed angular momentum  $j_t = \frac{1}{2}$  of the 3N bound state. The explicit expression shows that  $f$  is restricted to  $f = 0, 1$  by the Clebsch-Gordan coefficient  $(f j_t j_t, 0 m_t)$ . Parity conservation and the second Clebsch-Gordan coefficient requires  $f$  to be even. Therefore only  $f = 0$  remains.  $\hat{T}$  is angular and  $m_t$  independent. This holds for arbitrary  $J$ .

# Bibliography

- [1] B. Gabioud *et al.*, Phys. Rev. Lett. **42**, 1508 (1979).
- [2] D.E. González Trotter *et al.*, Phys. Rev. Lett. **83**, 3788 (1999).
- [3] O. Schori *et al.*, Phys. Rev. **C 35**, 2252 (1987).
- [4] I. Šlaus, Y. Akaishi, H. Tanaka, Phys. Rep. **173**, 259 (1989).
- [5] C. R. Howell *et al.*, Phys. Lett. **B444**, 252 (1998).
- [6] V. Huhn, L. Wätzold, Ch. Weber, A. Siepe, W. von Witsch, H. Witała, W. Glöckle, Phys. Rev. **C 63**, 014003 (2000).
- [7] V. Huhn, L. Wätzold, Ch. Weber, A. Siepe, W. von Witsch, H. Witała, W. Glöckle, Phys. Rev. Lett. **85**, 1190 (2000).
- [8] G.A. Miller, B.M.K. Nefkens, and I. Šlaus, Phys. Rep. **194**, 1 (1990).
- [9] R.B. Wiringa, V.G.J. Stoks, and R. Schiavilla, Phys. Rev. **C 51**, 38 (1995).
- [10] V.G.J. Stoks, R.A.M. Klomp, C.P.F. Terheggen, and J.J. de Swart, Phys. Rev. **C 49**, 2950 (1994).
- [11] R. Machleidt, Adv. Nucl. Phys. **19**, 189 (1989).
- [12] R. Machleidt, F. Sammarruca, and Y. Song, Phys. Rev. **C 53**, R1483 (1996).
- [13] E. Epelbaum, W. Glöckle, Ulf-G. Meißner, Nucl. Phys. **A637**, 107 (1998).
- [14] E. Epelbaum, W. Glöckle, Ulf-G. Meißner, Nucl. Phys. **A671**, 295 (2000).
- [15] U. van Kolck, Phys. Rev. **C 49**, 2932 (1994).
- [16] J. Fujita, H. Miyazawa, Progress of Theor. Phys. **17**, 360 (1957).
- [17] B.S. Pudliner *et al.*, Phys. Rev. **C 56**, 1720 (1997).
- [18] A. Stadler, W. Glöckle, and P.U. Sauer, Phys. Rev. **C 44**, 2319 (1991).
- [19] A. Nogga, D. Hüber, H. Kamada, and W. Glöckle, Phys. Lett. **B409**, 19 (1997).
- [20] E. Epelbaum, Ph.D. thesis, Ruhr-Universität, Bochum, 2000.

- [21] W. Glöckle, H. Witała, D. Hüber, H. Kamada, and J. Golak, *Phys. Rep.* **274**, 107 (1996).
- [22] H. Witała, W. Glöckle, J. Golak, A. Nogga, H. Kamada, R. Skibiński and J. Kuroś-Żolnierczuk, *Phys. Rev. C* **63**, 024007 (2001).
- [23] R.B. Wiringa, *Nucl. Phys.* **A401**, 86 (1983).
- [24] S.A. Coon, M.D. Scadron, P.C. McNamee, B.R. Barrett, D.W.E. Blatt, and B.H.J. McKellar, *Nucl. Phys.* **A317**, 242 (1979).
- [25] E.J. Stephenson, H. Witała, W. Glöckle, H. Kamada, A. Nogga, *Phys. Rev. C* **60**, 061001 (1999).
- [26] R. Bieber *et al.*, *Phys. Rev. Lett.* **84**, 606 (2000).
- [27] H. Sakai *et al.*, *Phys. Rev. Lett.* **84**, 5288 (2000).
- [28] R.V. Cadman *et al.*, *Phys. Rev. Lett.* **86**, 967 (2001).
- [29] P.U. Sauer, *Prog. Part. Nucl. Phys.* **16**, 35 (1986).
- [30] J.L. Friar, G.L. Payne, V.G.J. Stoks, and J.J. de Swart, *Phys. Lett.* **B311**, 4 (1993).
- [31] Y. Wu, S. Ishikawa, and T. Sasakawa, *Few-Body Systems* **15**, 145 (1993).
- [32] A. Kievsky, M. Viviani, and S. Rosati, *Phys. Rev. C* **52**, R15 (1995).
- [33] R.B. Wiringa, Steven C. Pieper, J. Carlson, V.R. Pandharipande, *Phys. Rev. C* **62**, 014001 (2000).
- [34] A.C. Fonseca, *Phys. Rev. C* **40**, 1390 (1989).
- [35] W. Schadow, W. Sandhas, J. Haidenbauer, A. Nogga, *Few Body Systems* **28**, 241 (2000).
- [36] H. Kamada and W. Glöckle, *Nucl. Phys.* **A548**, 205 (1992).
- [37] N.W. Schellingerhout, J.J. Schut, and L.P. Kok, *Phys. Rev. C* **46**, 1192 (1992).
- [38] F. Ciesielski, J. Carbonell, and C. Gignoux, *Phys. Lett.* **B 447**, 199 (1999).
- [39] Y. Suzuki and K. Varga, *Phys. Rev. C* **52**, 2885 (1995).
- [40] Y. Suzuki, K. Varga, *Stochastic variational approach to Quantum-Mechanical Few Body Problems*, Vol. m54 of *Lecture Notes in Physics* (Springer-Verlag, Berlin, 1998).
- [41] H. Kameyama, M. Kamimura, and Y. Fukushima, *Phys. Rev. C* **40**, 974 (1989).
- [42] E. Hiyama, Ph.D. thesis, Kyushu University, 1997.
- [43] E. Hiyama, M. Kamimura, T. Motoba, T. Yamada, Y. Yamamoto, *Nucl. Phys.* **A639**, 169c (1998).
- [44] M. Viviani, A. Kievsky, and S. Rosati, *Nuovo Cimento* **631**, 111c (1992).
- [45] M. Viviani, *Nucl. Phys. A* **631**, 111c (1998).
- [46] P. Navrátil, G. P. Kamuntavičius, B.R. Barrett, *Phys. Rev. C* **61**, 044001 (2000).

- [47] M. M. Nagels , T. A. Rijken, and J.J. de Swart, Phys. Rev. **D 15**, 2547 (1977).
- [48] H. Yamamura, K. Miyagawa, T. Mart, C. Bennhold, H. Haberzettl, W. Glöckle, Phys. Rev. **C 61**, 014001 (1999).
- [49] J. Reinhold, *et. al.*, Nucl. Phys. **A684**, 470c (2001).
- [50] D.E. Groom *et al.* (Particle Data Group), European Physical Journal **C15**, 1 (2000).
- [51] Th. A. Rijken, V.G.J. Stoks, and Y. Yamamoto, Phys. Rev. **C 59**, 21 (1999).
- [52] B. Holzenkamp, K. Holinde, and J. Speth, Nucl. Phys. **A500**, 485 (1989).
- [53] M. M. Nagels , T. A. Rijken, and J.J. de Swart, Phys. Rev. **D 20**, 1633 (1979).
- [54] P. M. M. Maessen, Th. A. Rijken, and J.J. de Swart, Phys. Rev. **C 40**, 2226 (1989).
- [55] V.G.J. Stoks and Th. A. Rijken, Phys. Rev. **C 59**, 3009 (1999).
- [56] K. Holinde, Nucl. Phys. **A547**, 255c (1992).
- [57] Y. Fujiwara, T. Fujita, M. Kohno, C. Nakamoto, Y. Suzuki, Few Body Systems Suppl. **311**, 2000 (1989).
- [58] B. F. Gibson, I. R. Afnan, J. A. Carlson, and D. R. Lehman, Prog. of Theor. Phys., Suppl. **117**, 339 (1994).
- [59] B. F. Gibson and E.V. Hungerford III, Phys. Rep. **257**, 349 (1995).
- [60] M. Jurič, G. Bohm, J. Klabuhn, U. Krecker, F. Wysotzki, G. Coremans-Bertrand, J. Scaton, G. Wilquet, T. Cantwell, F. Esmael, A. Montwill, D.H. Davis, D. Kielczewska, T. Pniewski, T. Tymieniecka, J. Zakrzewski, Nucl. Phys. **B52**, 1 (1973).
- [61] A. Bamberger, M.A. Faessler, U. Lynen, H. Piekarz, J. Piekarz, J. Pniewski, B. Povh, H.G. Ritter, V. Soergel, Nucl. Phys. **B60**, 1 (1973).
- [62] M. Bedjidian, E. Descroix, J.Y. Grossiord, A. Guichard, M. Gusakow, M. Jacquin, M.J. Kudła, H. Piekarz, J. Piekarz, J.R. Pizzi, J. Pniewski, Phys. Lett. **83B**, 252 (1979).
- [63] D.H. Davis , in *AIP Conf. Proc. 224*, edited by B.F. Gibson, W.R. Gibbs, and M.B. Johnson (AIP, New York, 1991), p. 38.
- [64] B. F. Gibson, A. Goldberg, and M. S. Weiss, Phys. Rev. **C 6**, 741 (1972).
- [65] B. F. Gibson and D. R. Lehman, Nucl. Phys. **A329**, 308 (1979).
- [66] L.H. Thomas, Phys. Rev. **47**, 903 (1935).
- [67] A.R. Bodmer and Q.N. Usmani, Phys. Rev. **C 31**, 1400 (1985).
- [68] B. F. Gibson and D. R. Lehman, Phys. Rev. **C 37**, 679 (1988).
- [69] Y. Yamamoto and H. Bandō, Progress of Theor. Phys. **83**, 254 (1990).

- [70] E. Hiyama, M. Kamimura, T. Motoba, T. Yamada, Y. Yamamoto, Nucl. Phys. **A684**, 227c (2001).
- [71] E. Hiyama, private communication.
- [72] Y. Akaishi, T. Harada, S. Shinmura, Khin Swe Myint, Phys. Rev. Lett. **84**, 3539 (2000).
- [73] H. Nemura, Y. Suzuki, Y. Fujiwara, Choki Nakamoto, Progress of Theor. Phys. **103**, 929 (2000).
- [74] S. B. Carr, I. R. Afnan, and B. F. Gibson, Nucl. Phys. **A 625**, 143 (1997).
- [75] K. Miyagawa, W. Glöckle, Phys. Rev. **C 48**, 2576 (1993).
- [76] K. Miyagawa, H. Kamada, W. Glöckle, V. Stoks, Phys. Rev. **C 51**, 2905 (1995).
- [77] O. Yakubovsky, Sov. J. Nucl. Phys. **5**, 937 (1967).
- [78] H. Kamada, private communication.
- [79] L.D. Faddeev, Sov. Phys. JETP **12**, 1014 (1961).
- [80] A. R. Edmonds, *Drehimpulse in der Quantenmechanik* (BI Hochschultaschenbücher, Mannheim, 1964).
- [81] W. Saake, master thesis, Ruhruniversität Bochum, 1992.
- [82] D. Hüber, H. Witala, A. Nogga, W. Glöckle, H. Kamada, Few Body Systems **22**, 107 (1997).
- [83] For a technical description of the T3E installation of the NIC see: [http://www.kfa-juelich.de:80/zam/CompServ/services/sco.crayT3E\\_1200.html](http://www.kfa-juelich.de:80/zam/CompServ/services/sco.crayT3E_1200.html).
- [84] Marc Snir, Steve Otto, Steven Huss-Lederman, David Walker, Jack Dongarra, *MPI: The Complete Reference* (MIT Press, Cambridge, Massachusetts, 1996).
- [85] W. Glöckle, in *Computational Nuclear Physics*, edited by K. Langanke, J.A. Maruhn, S. E. Koonin (Springer-Verlag, Berlin, 1991), Chap. 8.
- [86] V.G.J. Stoks, R.A.M. Klomp, M.C.M. Rentmeester, and J.J. de Swart, Phys. Rev. **C 48**, 792 (1993).
- [87] R. Machleidt, private communication.
- [88] G.Q. Li and R. Machleidt, Phys. Rev. **C 58**, 1393 (1998).
- [89] George Rupp and J.A. Tjon, Phys. Rev. **C 45**, 2133 (1992).
- [90] F. Sammarruca, D.P. Xu, and R. Machleidt, Phys. Rev. **C 46**, 1636 (1992).
- [91] A. Stadler, F. Gross, M. Frank, Phys. Rev. **C 56**, 2396 (1997).
- [92] A. Stadler, F. Gross, Phys. Rev. Lett. **78**, 26 (1997).
- [93] P.A.M. Dirac, Rev. Mod. Phys. **21**, 392 (1949).
- [94] W. Glöckle, T. S. H. Lee, F. Coester, Phys. Rev. **C 33**, 709 (1986).

- [95] J. L. Forest, V. R. Pandharipande, A. Arriaga, Phys. Rev. C **60**, 014002 (1999).
- [96] J. V. Carlson, V.R. Pandharipande, and R. B. Wiringa, Nucl. Phys. **A401**, 59 (1983).
- [97] M. R. Robilotta, H. T. Coelho, Nucl. Phys. **A460**, 645 (1986).
- [98] B.H.J. McKellar and W. Glöckle, Nucl. Phys. **A416**, 435c (1984).
- [99] A. Picklesimer, R.A. Rice, and R. Brandenburg, Phys. Rev. Lett. **68**, 1484 (1992).
- [100] A. Bömelburg, Phys. Rev. C **34**, 14 (1986).
- [101] J.L. Friar, B. F. Gibson, G.L. Payne, and S. A. Coon, Few Body Systems **5**, 13 (1988).
- [102] T. Sasakawa and S. Ishikawa, Few Body Systems **1**, 3 (1986).
- [103] S.A. Coon and M.T. Pena, Phys. Rev. C **48**, 2559 (1993).
- [104] A. Stadler, J. Adam Jr., H. Henning, and P.U. Sauer, Phys. Rev. C **51**, 2896 (1995).
- [105] J.A. Eden and M.F. Gari, Phys. Rev. C **53**, 1510 (1996).
- [106] J.L. Friar, H. Hüber, U. van Kolck, Phys.Rev. C **59**, 53 (1999).
- [107] D. Hüber, J.L. Friar, A. Nogga, H. Witała, U. van Kolck, Few Body Systems **30**, 95 (2001).
- [108] H. Kamada, D. Hüber, A. Nogga, Few Body Systems **30**, 121 (2001).
- [109] A. Nogga, H. Kamada, W. Glöckle, Phys. Rev. Lett. **85**, 944 (2000).
- [110] S.A. Coon and H.K. Han, Few Body Systems **30**, 131 (2001).
- [111] A. Kievsky, private communication.
- [112] D. Hüber, H. Witała, H. Kamada, A. Nogga, W. Glöckle, Nucl. Phys. **A 631**, 663c (1998).
- [113] H. Witała, W. Glöckle, J. Golak, D. Hüber, H. Kamada, A. Nogga, Phys. Lett. B **447**, 216 (1999).
- [114] K. Ermisch *et. al.*, accepted for publication.
- [115] J. Golak, private communication.
- [116] G. Derrick and J.M. Blatt, Nucl. Phys. **8**, 310 (1958).
- [117] R. Schiavilla, V. G. J. Stoks, W. Glöckle, H. Kamada, A. Nogga, J. Carlson, R. Machleidt, V. R. Pandharipande, R. B. Wiringa, A. Kievsky, S. Rosati, M. Viviani, Phys. Rev. C **58**, 1263 (1998).
- [118] J. L. Forest, V. R. Pandharipande, J. Carlson, R. Schiavilla, Phys. Rev. C **52**, 576 (1995).
- [119] J. Golak, H. Witała, H. Kamada, D. Hüber, S. Ishikawa, W. Glöckle, Phys. Rev. C **52**, 1216 (1995).
- [120] R. Schiavilla, R. B. Wiringa, J. Carlson, Phys. Rev. Lett. **70**, 3856 (1993).
- [121] J.L. Friar, B. F. Gibson, and G.L. Payne, Phys. Rev. C **35**, 1502 (1987).

- [122] S.C. Pieper, private communication.
- [123] R. Machleidt and H. Mütter, nucl-th/0011057.
- [124] J.A. Tjon, Phys. Lett. B **56**, 217 (1975).
- [125] J.J. van Leeuwe *et. al.*, Phys. Rev. Lett. **80**, 2543 (1998).
- [126] TJLab, Experiment E97-111, (spokespeople J. Templon, J.Mitchell).
- [127] S. A. Sofianos, G. Ellerkmann, W. Sandhas , nucl-th/9909063.
- [128] O. Benhar, N.N. Nikolaev, J. Speth, A.A. Usmani, B.G. Zakharov, Nucl. Phys. **A673**, 241 (2000).
- [129] H. Morita and T. Suzuki, Prog. of Theor. Phys. **86**, 671 (1991).
- [130] L.L. Frankfurt, M.M. Sargsian, M.I. Strikman, Phys. Rev. C **56**, 1124 (1997).
- [131] S. Shinmura, private communication.
- [132] B. Sechi-Zorn, B. Kehoe, J. Twitty, R.A. Burnstein, Phys. Rev. **175**, 1735 (1968).
- [133] G. Alexander, U. Karshon, A. Shapira, G. Yekutieli, R. Engelmann, H. Filthuth, W. Lughofer, Phys. Rev. **173**, 1452 (1968).
- [134] R.B. Wiringa, R.A. Smith, and T.L. Ainsworth, Phys. Rev. C **29**, 1207 (1984).
- [135] K. Miyagawa, private communication.
- [136] T. Rijken, private communication.
- [137] C.G. Bao, Nucl. Phys. **A637**, 520 (1998).
- [138] M.M. Sargsian, private communication.
- [139] E. Epelbaum, H. Kamada, A. Nogga, H. Witała, W. Glöckle, Ulf-G. Meissner, accepted for publication in Phys. Rev. Lett.
- [140] W. Glöckle, *The Quantum Mechanical Few-Body Problem* (Springer-Verlag, Berlin, 1983).
- [141] S.A. Coon and W. Glöckle, Phys. Rev. C **23**, 1790 (1981).

## Acknowledgment

First of all I would like to thank Prof. Glöckle for giving me the subject and continuously supporting my work. I am also very grateful for his help to get in contact with many scientists and for giving me the possibility to present and discuss my work on conferences and workshops.

Further I acknowledge the strong financial support from the DFG.

I thank Dr. Kamada for his helpful support and many useful discussions.

Dr. Hüber introduced me in the techniques to evaluate 3NF's and provided me with his codes. I am very thankful to him.

For the many interesting discussions, for their kindness and helpfulness I thank my colleagues from the AGR "Kernphysik" in Bochum, namely Dr. Epelbaum, I. Fachruddin, Dr. Golak, Dr. Krüger, G. Ziemer and especially E. Hannes.

Moreover I am grateful to Prof. Witala, who helped me to establish the 3NF codes, and supported an interesting stay in Krakau.

I enjoyed a very instructive visit at the "Argonne Theory Institute on Advanced Computational Methods in the Nuclear Many-Body Problem" in Argonne and at the University of Ohio in Athens with Prof. Elster.

For providing benchmarks, which were indispensable to establish my codes, I thank Prof. Miyagawa, Dr. Kievsky, Dr. Pieper and Dr. Hiyama.

For the help managing the potential codes I thank Prof. Rijken.

Last, but not least, I thank the NIC and ZAM from the FZ Jülich for their continuous support and for providing the necessary computational resources for the calculations. I am very grateful for all the help from Dr. Attig.



# Lebenslauf

## Persönliche Daten

Name: Andreas Nogga  
Geburtsdatum: 25.05.1970  
Geburtsort: Hagen  
Nationalität: deutsch  
Familienstand: verheiratet  
zwei Kinder (4 und 7 Jahre)

## Ausbildungsverlauf

1976 - 1980 Besuch der Grundschule Kückelhausen in Hagen-Haspe  
1980 - 1989 Besuch des Christian-Rohlf-Gymnasiums, Hagen  
dort blieb ich bis zum Abitur (Durchschnitt 1.2)  
1989 Beginn des Physikstudiums an der Ruhr-Universität Bochum  
4/92 Vordiplomsprüfung  
abgeschlossen mit "sehr gut"  
2/94 Diplomprüfungen  
2/94 - 11/95 Diplomarbeit in der theoretischen Kernphysik  
Thema: Inklusive Elektronenstreuung an  $^3\text{He}$  und  $^3\text{H}$   
11/95 Abschluß des Studiums durch das Diplom  
Ergebnis: "mit Auszeichnung"  
seit 11/95 Promotion über gebundene Systeme aus wenigen Nukleonen  
und Hyperonen  
Ich habe seitdem eine Stelle  
in der Arbeitsgruppe von Herrn Prof. Glöckle

Andreas Nogga  
Hagen, den 16.05.2001